Development of Lithium-Drifted Silicon Detectors and Investigation of Cosmic Antihelium Sensitivity for the GAPS Experiment — an Indirect Search for Dark Matter

Nathan Arnett Saffold

Submitted in partial fulfillment of the
requirements for the degree of
Doctor of Philosophy
under the Executive Committee
of the Graduate School of Arts and Sciences

COLUMBIA UNIVERSITY

2021

Abstract

Development of Lithium-Drifted Silicon Detectors and Investigation of Cosmic Antihelium Sensitivity for the GAPS Experiment — an Indirect Search for Dark Matter

Nathan Arnett Saffold

Uncovering the nature of dark matter is one of the most pressing problems in 21st century cosmology. Despite overwhelming evidence that dark matter exists and vigorous experimental efforts to detect it, dark matter has evaded detection and its fundamental nature remains shrouded in mystery. Indirect dark matter detection experiments search for Standard Model byproducts of dark matter annihilation or decay. At low energies, cosmic antideuterons provide an especially clean dark matter signature, since the production of low-energy antideuterons from conventional astrophysical processes is highly suppressed.

The General Antiparticle Spectrometer (GAPS) is an Antarctic balloon experiment designed to search for low-energy cosmic antinuclei as signatures of dark matter. GAPS is optimized to detect low-energy antideuterons, as well as to provide unprecedented sensitivity to low-energy antiprotons and antihelium nuclei. GAPS uses a novel approach to detect antinuclei, based on the formation, decay, and annihilation of exotic atoms. At least three GAPS long-duration balloon (LDB) flights are planned, with the first launch date anticipated for December 2022. The core of the GAPS instrument is a particle tracker, comprised of >1000 lithium-drifted silicon (Si(Li)) detectors, that provides particle tracking and X-ray spectroscopy capabilities. In order to preserve the long-term performance of the tracker, the Si(Li) detectors require a surface passivation coating to protect against environmental contamination.

In this thesis, I cover four main areas of my research: prototype Si(Li) detector fabrication and performance evaluation; development of a surface passivation technique to ensure the long-term stability of GAPS flight detectors; calculation of the GAPS antihelium sensitivity using particle tracking; and prediction of the antihelium exotic atom X-ray energies and yields for future identification studies. I discuss the prototype fabrication work that was carried out at Columbia, which led to the successful mass-production of large-area Si(Li) detectors for the GAPS LDB flights. I report the research and development of a surface passivation method to protect the GAPS flight detectors from environmental contamination. I then describe the calibration scheme for the GAPS Si(Li) detectors, and a simulation study that I conducted to disentangle the contribution of Compton scattering and intrinsic detector performance on the observed spectra. I then move on to discuss the simulation studies used to determine the performance capabilities of GAPS. I describe the benchmarking of the hadronic annihilation products in antinucleus-nucleus annihilations in Geant4. I review the exotic atom cascade model used to determine the X-rays produced by antiprotonic and antideuteronic exotic atoms, and discuss my work extending this model to describe the de-excitation of antihelium exotic atoms. Finally, I present the first GAPS antihelium nuclei sensitivity study, based on full instrument simulation, event reconstruction, and realistic atmospheric influence simulations.

Table of Contents

Acknowledgments x

Dedication xii

Chapter 1: Dark Matter and Dark Energy – The Big Questions 1

1.1 Evidence for Dark Matter 2

1.1.1 Dynamical Evidence 2

1.1.2 Weak Gravitational Lensing 3

1.1.3 Numerical Simulations 4

1.1.4 Cosmological Probes 6

1.2 Dark Matter Candidates 8

1.2.1 Weakly Interacting Massive Particles (WIMPs) 9

1.2.2 Hidden Sector Dark Matter 13

1.2.3 Axion and Axion-like Dark Matter 13

Chapter 2: Dark Matter Searches 18

2.1 Accelerators 19

2.2 Direct Dark Matter Detection 19

2.3 Indirect Dark Matter Detection 24

2.3.1 Antinuclei from Dark Matter 28

Chapter 3: The GAPS Experiment 35
3.1 Overview 35
3.2 Detection Concept 36
3.3 The GAPS Instrument 38
3.3.1 Balloon Requirements 38
3.3.2 Time of Flight (TOF) and Trigger 39
3.3.3 Si(Li) Tracker 40
3.3.4 Detector Electronics and Data Acquisition (DAQ) System 43
3.3.5 Thermal System 43
3.4 GAPS Project Timeline 44

Chapter 4: Lithium-drifted Silicon (Si(Li)) Detectors – Fabrication 45
4.1 Theory of Operation 46
4.1.1 Semiconductor Detectors 46
4.1.2 Detector Efficiency 50
4.1.3 Signal Formation 53
4.1.4 Ballistic Deficit 55
4.2 Description of Fabrication Procedure 56
4.2.1 Overview of Si(Li) Fabrication Method 56
4.2.2 Development of GAPS Prototype Si(Li) Detectors 61
4.3 Conclusions 71

Chapter 5: Si(Li) Detector Passivation 73
5.1 Si(Li) Passivation Review & Requirements 74

5.2 Mechanical Testing 76
5.2.1 Motivation 76
5.2.2 Sample Preparation 77
5.2.3 Adhesion Testing & Results 80
5.2.4 Thermal Testing & Results 81
5.3 Noise Testing 82
5.3.1 Motivation 82
5.3.2 Detector Preparation 83
5.3.3 Noise Testing Setup 84
5.3.4 Noise Testing Results 87
5.4 Effectiveness in Protecting Detectors 89
5.4.1 Motivation 89
5.4.2 Accelerated Humidity Exposures 90
5.4.3 Accelerated Organics Exposures 92
5.4.4 Long-Term Monitoring 94

Chapter 6: Detector Response Simulation 96
6.1 Simulation Framework 97
6.1.1 Simulation Tools 98
6.1.2 Charge Collection Efficiency 100
6.1.3 Simulating Spectral Response 101
6.2 Comparison of Experimental and Simulated Spectra 103
6.3 Conclusions and Outlook 104

Chapter 7: Benchmarking of Hadronic Annihilation Products 105

7.1 Properties of Antinucleus-nucleus Annihilation at Rest 105

7.2 Antiproton-proton Annihilation in Hydrogen 107

7.3 Hadronic Products of Antiproton, Antideuteron, and Antihelium-3 Annihilations . . 110

7.3.1 Motivation 110

7.3.2 Simulation Setup 110

7.3.3 Antiproton and Antineutron Annihilation Properties 111

7.3.4 Antideuteron and Antihelium-3 Annihilation Properties 113

7.4 Conclusions and Outlook 116

Chapter 8: Cascade Model of Exotic Atom De-excitation 117

8.1 Overview of Cascade Model 118

8.1.1 Auger Transitions 120

8.1.2 Radiative Transitions 122

8.1.3 Nuclear Capture 122

8.2 Modifications to Cascade Model for Antihelium Nuclei 123

8.2.1 Initial Principal Quantum Number 124

8.2.2 Auger Transitions 124

8.2.3 Radiative Transitions 125

8.2.4 Optical Potential for Nuclear Capture 125

8.3 Exotic Atom X-rays from Antihelium-3 126

8.4 Integration of Antiprotonic and Antideuteronic Exotic Atoms into Geant4 128

8.5 Conclusions and Future Work 130

Chapter 9: Antihelium Sensitivity Study 131

9.1 Simulation Framework 133

9.2 Particle Identification 134

9.2.1 Event Reconstruction 134

9.2.2 Analysis Preselection 135

9.2.3 Identification Analysis 137

9.3 Sensitivity Calculation 140

9.3.1 Atmospheric Simulations 140

9.3.2 Sensitivity Estimate 141

9.3.3 Future Work 142

9.4 Conclusion and Outlook 143

References 167

List of Figures

1.1 Composition of our universe 1

1.2 Relic density 10

2.1 Visualization of dark matter search techniques 18

2.2 ATLAS upper limits on spin-dependent and spin-independent WIMP-nucleon cross section 20

2.3 Exclusion limits on the spin-independent WIMP-nucleus scattering cross section from direct detection experiments 22

2.4 Fluxes at production of Standard Model particles produced by dark matter annihilation 26

2.5 Status of low-energy antiproton/proton ratio measurements in 1997 27

2.6 Schematic of dark matter annihilating into antinuclei 28

2.7 Expected antideuteron flux from dark matter and secondary sources 34

3.1 Example of typical antideuteron event topology in the GAPS instrument 36

3.2 Schematic of GAPS antinucleus identification concept 37

3.3 Mechanical drawing of the GAPS payload 38

3.4 Time-of-flight system summary 40

3.5 GAPS Si(Li) detector module 42

3.6 Large-scale Si(Li) detector calibration results 42

4.1 Schematic of reverse-biased *p-i-n* junction 50

4.2 Schematic of X-ray scattering and absorption processes 52
4.3 Overview of pulse-mode readout 53
4.4 Equivalent noise circuit of detector and preamplifier readout chain 54
4.5 Schematic of the lithium drifting process 58
4.6 Schematic of detector geometry with drifting groove and guard ring 60
4.7 Lithium evaporator used for Si(Li) fabrication 64
4.8 Lithium drifting apparatus used for prototype Si(Li) fabrication 65
4.9 Example of prototype detector drift profile 66
4.10 Ultrasonic Impact Grinder used for prototype Si(Li) fabrication 67
4.11 Cross section of prototype Si(Li) detector after copper staining 68
4.12 Effect of etching on groove profile 69
4.13 Observed groove profile of Si(Li) detectors 70
4.14 Flight Si(Li) detector geometry 72

5.1 Effect of thermal cycling on polyimide coatings 83
5.2 Energy resolution measurements of prototype detector and the effect of silane cure temperature on detector performance 88
5.3 Results of polyimide passivation validation study 90
5.4 Effect of humidity exposures on detector leakage current 92
5.5 Detector energy resolution before and after accelerated exposure to organics 94
5.6 Long-term monitoring of detector energy resolution 95

6.1 Example spectra of GAPS Si(Li) detector response to radioactive calibration sources 97
6.2 Image of detector in calibration mount compared to simulated detector geometry in Geant4 99
6.3 Electric field as a function of position in GAPS Si(Li) detector, based on electrostatic model 100
6.4 Example of charge collection efficiency determination using electrostatic model . . 101

6.5 Example of simulated detector spectra . . . 103
6.6 Comparison of experimental and simulated spectra . . . 104

7.1 Event display of simulated antiproton annihilation in hydrogen and silicon . . . 108
7.2 Experimental and simulated branching fraction of final states in antiproton annihilation in hydrogen . . . 109
7.3 Charged pion multiplicity per event for antiproton and antineutron annihilation in hydrogen . . . 111
7.4 Charged pion multiplicity per annihilation for antiproton and antineutron annihilation in deuterium . . . 112
7.5 Charged pion multiplicity in antiproton annihilations in silicon, aluminum, and carbon . . . 113
7.6 Charged pion multiplicity in antideuteron annihilations . . . 114
7.7 Charged pion multiplicity in antihelium-3 annihilations . . . 115

8.1 Schematic of the cascade model . . . 120
8.2 Observed energies and yields of 0–120 keV photons produced in simulated antiproton and antideuteron annihilations in aluminum and silicon . . . 129

9.1 Schematic of GAPS instrument and example of antihelium-3 nucleus event topology 135
9.2 Identification variable used for $\mathrm{d}E/\mathrm{d}x$ cut . . . 136
9.3 GAPS acceptance for antiprotons and antihelium-3 nuclei for events passing trigger, stopping, and preselection criteria . . . 137
9.4 Example of two identification variables: the number of reconstructed tracks and the truncated primary mean energy deposition . . . 138
9.5 GAPS acceptance for antihelium-3 nuclei after preselection and identification cuts . 141
9.6 GAPS sensitivity to antihelium-3 nuclei and expected primary and secondary fluxes of antihelium-3 nuclei at the top of atmosphere . . . 143

List of Tables

3.1 Mass and power requirements of the GAPS payload 39

4.1 Specifications of the Si crystal used for GAPS Si(Li) detector fabrication 63

5.1 Sample preparation and cleaning protocols for adhesion and thermal testing samples 78

5.2 Polyimide application parameters used to prepare adhesion and thermal test samples 80

7.1 Fraction of antideuteron annihilation events that breakup into constituent antinucleons in various target materials 115

7.2 Fraction of antihelium-3 annihilation events that breakup into constituent antinucleons in various target materials 116

8.1 X-ray yields from the cascade of antihelium-3, varying the parameter α 126

8.2 X-ray yields from the cascade of antihelium-3, varying the parameter W 127

8.3 X-rays from de-excitation of antihelium-3 exotic atom, as predicted by the cascade model with optimized parameters 127

8.4 Expected and simulated X-ray energies and yields of antiprotonic and antideuteronic exotic atom X-rays produced in aluminum and silicon targets 129

Acknowledgements

First and foremost, I thank my advisor, Professor Charles Hailey, for his invaluable mentorship throughout my time at Columbia. He was always there for me, looking out for my best interests, and his guidance kept me on track. Thank you for challenging me and encouraging me to rise to the occasion. Thank you for believing in my potential as a scientist, and helping me overcome self-doubt.

I am very grateful for the members of the GAPS collaboration, who welcomed me into the group and fostered my growth. Professor Kerstin Perez played a pivotal role in my research on Si(Li) detector fabrication and passivation, generously lending her expertise and providing creative solutions whenever I reached an impasse. Professor Tsuguo Aramaki introduced me to Geant4 early in my graduate career and provided a calm, reassuring voice that helped me keep things in perspective. Professor Philip von Doetinchem helped me immensely with my GAPS simulation work, in particular the antihelium sensitivity study. Professor Hide Fuke and Kozai were a valuable resource on Si(Li) detector fabrication techniques, and taught me a lot about scientific ballooning during our time in Ft. Sumner. I would also like to thank Professor Rene Ong, Mirko Boezio, and Lorenzo Fabris for their valuable input. I must also acknowledge Professor Steve Boggs and Alex Lowell, who introduced me to particle astrophysics eight years ago as an REU student, and set me on the path I walk today.

I would also like to thank my colleagues and fellow students who helped me along my journey. Field, you have been my sounding board for much of my work on GAPS, and I cannot thank you enough for the useful discussions, editing assistance, and generally being a good

friend. Cassia and Jason, thank you for showing me the ropes in the lab, and giving me the confidence to run the lab after you moved on. Evan and Derik, I enjoyed mentoring you and tried to teach you everything I know; thank you for running with the ball at Nevis, taking some of the weight off my shoulders, and enabling me to focus on the tasks I needed to accomplish to graduate. Mengjiao, I have been glad to have you on my team; thank you for all your help with detector testing and troubleshooting. Achim, thank you for all your help managing the GAPS simulation code. Kaya Mori, thank you for looking out for me, providing me with useful advice, and helping me stay fit with early-morning soccer games. To all the undergraduates that I mentored, thank you for your time and effort.

I would also like to acknowledge the people at Columbia who supported me. The professors who instructed me and gave me a strong foundation upon which to embark on my research. The Physics Department staff, particularly Randy Torres, Michael Adan, and Carl Petitfrere, who helped me navigate the Columbia bureaucracy and enriched my days with coffee, cookies, and good conversation. My fellow graduate students, Joey Howlett, Albert Law, Steve Harrellson, Rainer Corley, Ari Brill, and many more, who provided a supportive community and made me feel like I belonged. During those late nights working on problem sets or studying for Quals, it helped having good friends as comrades-in-arms. To the Students of Color Alliance, thank you for providing a safe space for me to blow off steam after a long day in the lab.

Finally, I want to thank my parents, sisters, family, and friends. You have been my biggest cheerleaders and have sustained me through difficult times. To my mother, Carol, thank you for your constant support and lifting me up when I was down. To my father, Gene, thank you for all the lessons you taught me, and providing an example of how to simultaneously work hard and enjoy life. Jessica and Christine, you are the best sisters I could ever ask for, and I am excited to continue ‘growing up’ alongside you. Rich, thank you for always being one call away. Alex, thank you for your patience, love, and support.

Dedication

To my mother and father,

who gave me roots and wings.

Chapter 1: Dark Matter and Dark Energy – The Big Questions

Since ancient times, natural philosophers have pondered the constituents of the Universe and their properties. Over the course of the past century, high-energy particle physics has emerged at the forefront of these efforts, culminating in the Standard Model of particle physics which predicts the results of electromagnetic, strong, and weak interactions with incredible precision.

However, the Standard Model picture — leptons, baryons consisting of quarks, and bosons mediating the fields by which they interact — can not describe the Universe in its entirety. There is overwhelming evidence from independent observations that the Standard Model can only account for approximately 5% of the energy density of the Universe. Cosmological measurements have provided a precise measure, indicating that the Universe's energy density is composed of 4.9% baryonic matter, 26.8% dark matter, and 68.3% dark energy [1, 2], as shown in Fig. 1.1.

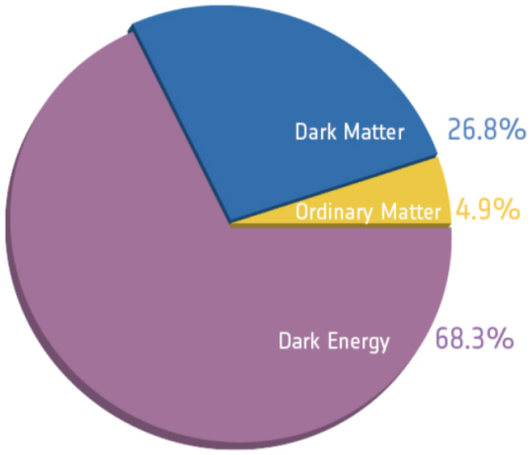

Figure 1.1: Composition of our universe [1].

Despite overwhelming evidence for dark matter and dark energy, their nature and origin remain unknown, and uncovering them is one of the great cosmological problems in 21st century physics. This chapter will provide a brief review of dark matter. Section 1.1 surveys the experimental results

that point to the existence of dark matter. Section 1.2 describes the well-motivated theoretical dark matter candidates that have been invoked to solve this cosmological quandary.

1.1 Evidence for Dark Matter

1.1.1 Dynamical Evidence

Although dark matter (DM) has not been detected, its existence has been inferred based on its gravitational influences. Astronomers in the 19th century discussed dark matter in the form of dark stars, dark planets, dark clouds, or dark nebulae, invoking dark or faint objects to explain anomalies in the motion of visible objects. Lord Kelvin was among the first to attempt a dynamical estimate of the amount of dark matter in the Milky Way. He argued that if stars can be described as a gas of particles acting under the influence of gravity, a relationship between the size of the system and the velocity dispersion of the stars can be established [3].

Using this technique, the first observational evidence of dark matter was found by Fritz Zwicky, based on measurements of the velocity dispersion in the Coma cluster. By estimating the total mass and physical size of the Coma cluster, Zwicky determined the potential energy of the system. Zwicky then imposed the virial theorem to calculate the expected average kinetic energy. He found that, based on the virial theorem, the Coma cluster should exhibit a velocity dispersion of 80 km/s. In contrast, the observed velocity dispersion was approximately 1000 km/s. From this comparison, Zwicky deduced “the surprising result that dark matter is present in much greater amount than luminous matter" in the Coma cluster [4, 5].

Subsequent work found similar evidence of dark matter, but a scientific consensus did not emerge until the 1970s with the observation of approximately “flat” rotation curves at large distances from the center of galaxies. The rotational velocity of an object in a circular orbit can be estimating using Newton’s law of gravitation

$$\frac{mv^2}{r} = G\frac{M(r)m}{r^2}. \tag{1.1}$$

Here, m and v are the mass and translational velocity of the object, r is the distance from the center of the galaxy, and $M(r)$ is the mass enclosed inside the object's orbital radius. In a typical spiral galaxy such as Andromeda, most of the luminous matter exists in the central region. Based on the luminous matter, the expected rotational speed as a function of r would be approximately proportional to $r^{-1/2}$. Once the requisite advances in imaging technology were made, this relationship was tested. In the 1960s, Kent Ford developed an image tube spectrograph that Vera Rubin and he used to perform spectroscopic observations of the Andromeda Galaxy. Rubin and Ford produced a rotation curve of M31 indicating that its rotational velocities are not proportional to $r^{-1/2}$, but approximately flat out to 24 kpc [6]. Furthermore, their optical data was compatible with radio measurements previously obtained in 1966 [7]. This indicated that the mass of M31 was much larger and extended out to larger radii than expected from observations of the stars and gas.

1.1.2 Weak Gravitational Lensing

As the evidence for dark matter in galaxies and galaxy clusters accumulated, astronomers and astrophysicists contemplated what could make up this missing mass. One possible solution was that the missing mass consists of faint compact objects including planets, dwarf stars, neutron stars, and black holes, which are referred to in this context as Massive Astrophysical Compact Halo Objects (MACHOs). Gravitational lensing observations provide a way to search for compact objects in the "dark halo" of galaxies. If a galactic halo consists entirely of MACHOs, then any star in a nearby galaxy has a $\sim 10^{-6}$ probability of being microlensed at any time [8]. A microlensing event would be evident through the variations in brightness of a source star. The search for microlensing events motivated the MACHO, EROS, and OGLE Collaborations to conduct large microlensing surveys to test the hypothesis that the Milky Way's dark halo consisted of MACHOs. Ultimately, the EROS Collaboration set an upper limit of 8% of the halo mass fraction from MACHOs [9]. This limit was further supported by measurements of the cosmological baryon density (see Sec. 1.1.4).

Another alternative to dark matter arose in the early 1980s, when Milgrom proposed Modified

Newtonian Dynamics (MOND) [10]. MOND offered the possibility that using a modified version of Newtonian dynamics to describe the motion of bodies in a gravitational field could account for the observational results of the motions of stars and gas within galaxies without needing to invoke missing mass. The main assumption of MOND is that in the limit of small acceleration ($a \ll a_0 \sim 1.2 \times 10^{-10}\,\mathrm{m/s^2}$), the force due to gravity scaled as $F = ma^2/a_0$, as opposed to the familiar $F = ma$. Even today, MOND appears to be compatible with the observed rotation curves of hundreds of spiral galaxies [11]; however it has not been successful on the scale of galaxy clusters.

Observations of gravitational lensing in the Bullet Cluster – two colliding galaxy clusters – played a crucial role in determining that MOND cannot fully account for observational evidence of dark matter. A map of the gravitational potential in the Bullet Cluster was constructed using weak gravitational lensing. This technique measures the distortion of images of background galaxies caused by the gravitational deflection by the cluster's mass [12]. The observation of the merging clusters indicated that the distribution of mass in the system based on the gravitational lensing analysis is spatially distinct from the distribution of baryonic matter observed by an X-ray telescope [13, 14]. This observation is impossible to reconcile solely with MOND, and was interpreted as direct empirical proof of the existence of DM [14].

1.1.3 Numerical Simulations

Computer simulations made large contributions to the current understanding of the structure and evolution of dark matter halos in the Universe. By the 1970s, computer technology had progressed to enable numerical simulations of the dynamics of galaxies. These early simulations found rotationally supported galaxies consisting of a stellar disk to be unstable, in contradiction with observations [15, 16]. Jerry Ostriker and Jim Peebles proposed a solution to this problem in 1973, recognizing that a rotationally supported stellar disk could be stable if it is embedded within a massive spherical halo [17].

On larger scales, numerical simulations are used to solve the formation and evolution of cosmo-

logical structure. These cosmological simulations are mostly independent of what the dark matter consists of, but are sensitive to the initial velocity distribution of the dark matter particles [18]. This provides a way to discriminate between relativistic, or "hot," and non-relativistic, or "cold," dark matter candidates. Although at the largest scales (galaxy clusters and superclusters), the structure predicted by cosmological simulations is independent of the initial dark matter velocity, at smaller scales density fluctuations can be washed out by the random thermal motion of individual dark matter particles. If the dark matter particles are relativistic, numerical simulations predict that the formation of small scale structure is suppressed [19]. This prediction was compared to experimental data provided by the CfA survey [20] — the first extensive 3D survey of galaxies in the local Universe. CfA identified significant structure on sub-cluster scales, conflicting with the numerical predictions of structure formation with hot dark matter [21]. The first simulations including clumps of cold dark matter in galactic halos were compatible with the results of the CfA survey [22]. Therefore, the emergence of numerical simulations of cosmological structure formation and galaxy surveys ruled out hot dark matter as the dominant form of dark matter.

A decade later, cosmological simulations focused on determining the shapes of the cold dark matter halos. Based on an analysis of the cold dark matter halos generated in their simulations, Julio Navarro, Carlos Frenk, and Simon White found that the mass density of all halos could be fit by scaling a simple universal profile [23]

$$\rho_{NFW} = \rho_s \frac{r_s}{r}\left(1 + \frac{r}{r_s}\right)^{-2}. \tag{1.2}$$

Their fitting formula (Eq. 1.2) became known as the Navarro-Frenk-White (NFW) profile, and is still widely used today to describe the dark matter distribution in galaxies. The scale radius r_s and halo density ρ_s are normalized such that the local DM density is $\sim 0.4\,\mathrm{GeV/cm^3}$ at the distance of the Sun from the Galactic Center $r_\odot \approx 8.33\,\mathrm{kpc}$ (as determined in [24]).

1.1.4 Cosmological Probes

The "standard model" of cosmology describes the evolution of the Universe from the Big Bang $\sim 10^{10}$ years ago, to the current epoch and beyond. This cosmological model is rooted in astrophysical observations of an expanding universe [25] and the cosmic microwave background (CMB) radiation [26]. The model assumes that the Universe is homogeneous and isotropic on large scales, which is supported by the nearly isotropic CMB and the fact that galaxies seem to be distributed homogeneously on scales larger than $\sim 100\,\mathrm{Mpc}$. In this cosmological model — called the ΛCDM model — the Universe contains a cosmological constant, Λ, representing the dark energy component, a matter component consisting of baryonic matter and cold dark matter (CDM), and a radiation component consisting of relativistic particles. The evolution of these components over time is described by the Friedmann equation:

$$H^2 \equiv \left(\frac{\dot{a}}{a}\right)^2 = \frac{8\pi G\rho}{3} - \frac{k}{a^2} \tag{1.3}$$

where $a(t)$ is a dimensionless scale factor (with $a = 1$ being the scale factor today), $H(t) \equiv \frac{\dot{a}}{a}$ is known as the Hubble parameter, G is Newton's gravitational constant, ρ is the energy density, and k is related to the curvature of the Universe. The Hubble parameter at the present time is called H_0,[1] and is estimated to be $67.4 \pm 0.5\,\mathrm{km\,s^{-1}Mpc^{-1}}$ from observations of the CMB [1].[2] The energy density consists of matter (ρ_m), radiation (ρ_r), and vacuum energy (ρ_Λ) — for which the term 'dark energy' is commonly used. The energy density can be expressed as

$$\rho = \rho_m + \rho_r + \rho_\Lambda. \tag{1.4}$$

[1] Traditionally, the unitless parameter h is defined such that $H_0 \equiv 100h\,\mathrm{km\,s^{-1}Mpc^{-1}}$.

[2] Currently, there is tension between the value of H_0 obtained from early Universe probes and late (or local) Universe estimations that find a higher value of H_0. This discrepancy has been interpreted as a potential sign of new physics. For a review on this subject see Ref. [27].

The Friedmann equation can be written in terms of the critical density $\rho_{crit} \equiv \frac{3H^2}{8\pi G}$ as

$$1 - \underbrace{\frac{\rho_m}{\rho_{crit}}}_{\Omega_m} + \underbrace{\frac{\rho_r}{\rho_{crit}}}_{\Omega_r} + \underbrace{\frac{\rho_\Lambda}{\rho_{crit}}}_{\Omega_\Lambda} = -\frac{k}{a^2 H^2} \tag{1.5}$$

where Ω_m, Ω_r, Ω_Λ are the density parameters for matter, radiation, and dark energy. Astrophysical observations constrain these cosmological parameters, finding a flat Universe ($k = 0$) that is expanding at an increasing rate [28] due to dark energy [1].

Parameterized by the ΛCDM model, modern cosmology provides an empirical measure of DM's contribution to the energy density of the Universe and helps constrain viable DM models. The theory of Big Bang nucleosynthesis provides direct constraints on the baryon content of the Universe, indicating that a large component of the matter content of the Universe is non-baryonic [29]. Another cosmological probe of DM comes from the study of large-scale structure formation in the Universe. Temperature anisotropies in the CMB carry a record of inhomogeneities in the photon (and baryon) distribution at the time of recombination, when baryons decoupled from photons. The extent of nonlinear structure in today's Universe would require much more collapsed structure in matter at the time of recombination than is observed in the baryons at that time [30]. Dark matter reconciles these observations by decoupling earlier than baryons and collapsing into halos, providing the initial conditions to produce the large-scale structure observed in the Universe today.

Based on this large body of evidence, it is considered an empirical fact that the majority of the matter in the universe is non-baryonic DM. The ΛCDM model fits DM into the grander scheme of the beginning and evolution of the Universe that is observed today. However, the nature of DM is still unknown, and there are many potential theories that could explain it. The following section will discuss well-motivated DM candidates.

1.2 Dark Matter Candidates

Any viable DM candidate must satisfy a substantial list of criteria. Cosmological probes indicate that DM is predominantly non-baryonic. Astrophysical observations and direct detection exclusion limits indicate that DM does not interact via the electromagnetic or strong forces. Nevertheless, DM does interact via the gravitational force, as evidenced by galactic rotation curves and gravitational lensing measurements. To exist today, DM must be stable on cosmological timescales. It also must be non-relativistic (cold) to enable the formation of large-scale structure in the Universe that is observed today.

Based on cosmological constraints, the most favorable DM candidates are non-baryonic, and baryonic DM scenarios such as MACHOs are strongly disfavored. Primordial black holes (PBHs) provide a potential DM candidate without requiring new physics. Since PBHs were formed in the radiation-dominated era, they are classified as non-baryonic and are not subject to the Big Bang nucleosynthesis constraint on the baryonic energy density. PBHs will evaporate through Hawking radiation, and their evaporation can be probed indirectly, with recent limits set using gamma-ray [31, 32], positron [33], and radio [34] observations. Recently, gravitational microlensing data [35] and the observed stability of neutron stars [36] have largely excluded PBHs as DM candidates. For a detailed review of PBHs as dark matter, see Ref. [37].

Within the Standard Model, neutrinos are the only particles that are stable, electrically neutral, and not strongly interacting, but they have been ruled out as major contributors to DM due to their small mass. The search for DM candidates is not confined to Standard Model particles. Sterile neutrinos with keV-scale masses are one hypothetical DM candidate that would provide a simple explanation for neutrino oscillations via the seesaw mechanism; however, sterile neutrino dark matter in this mass range is disfavored due to constraints from X-ray observations and measurements of the Lyman-α forest [38]. Today, the most prevalent DM candidates are weakly interacting massive particles, hidden sector DM, and wave dark matter such as axions and axion-like particles. These DM candidates arise out of theoretical extensions to the Standard Model, as discussed below.

1.2.1 Weakly Interacting Massive Particles (WIMPs)

The leading candidates for DM are weakly interacting massive particles (WIMPs). If a stable WIMP exists that is sufficiently massive ($\gtrsim$100 keV), it would naturally produce a relic density consistent with the observed DM density in the Universe. Due to a stroke of serendipity called the 'WIMP miracle,' there are a number of beyond the Standard Model theories that posit new massive particles that interact on the weak-scale, in particular Supersymmetry (SUSY) and Kaluza-Klein theory which are discussed below.

1.2.1.1 Thermal Evidence

At early times, the Universe was dense and hot, and most of the constituents of the Universe were in thermal equilibrium. When the Universe cooled to temperatures T below the mass m_χ of particle χ, the particle became non-relativistic and its number density was Boltzmann suppressed, dropping exponentially as $e^{-m_\chi/T}$. This cooling effect alone would drive the number of sufficiently massive, non-relativistic DM particles to zero. However, since the Universe was expanding as it cooled, the Universe eventually became so large that the DM particles were so dilute that they could not find each other to annihilate. The DM particles then "froze out," and their number density asymptotically approached a constant, their thermal relic density (see Fig. 1.2).

This process is described by the Boltzmann equation

$$\frac{dn_\chi}{dt} = -3Hn_\chi - \langle\sigma v\rangle[n_\chi^2 - (n_\chi^{EQ})^2], \tag{1.6}$$

where n_χ is the comoving number density of DM particle χ, n_χ^{EQ} is the DM comoving number density in thermal equilibrium, H is the Hubble parameter, and $\langle\sigma v\rangle$ is the thermally-averaged annihilation cross section. On the right-hand side of Eq. (1.6), the first term accounts for the dilution due to expansion, the n_χ^2 term arises from DM destruction via annihilation $\chi\chi \rightarrow$ SM SM, and the $(n_\chi^{EQ})^2$ term corresponds to the reverse process SM SM $\rightarrow \chi\chi$, which creates DM particles.

By numerically solving the Boltzmann equation and requiring that the predicted relic density of

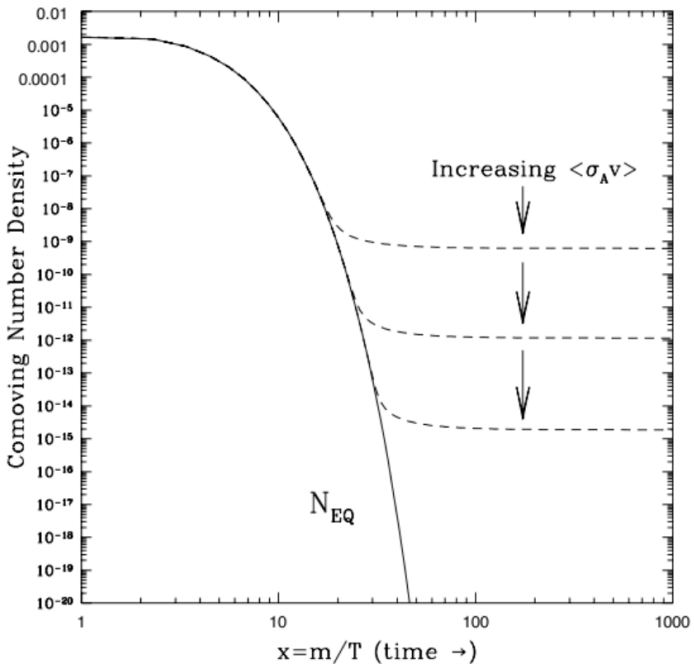

Figure 1.2: WIMP comoving number density as a function of $x \equiv m_\chi/T$. The equilibrium abundance is shown as a solid curve. The freeze out and thermal relic abundance is show as dashed curves. Figure from [39].

DM is consistent with the observed non-baryonic dark matter density parameter, the approximate value of the annihilation cross section can be found:

$$\Omega_\chi \sim \frac{0.1}{h^2}\left(\frac{3\times 10^{-26}\,\mathrm{cm^3 s^{-1}}}{\langle\sigma v\rangle}\right). \tag{1.7}$$

With the current DM density parameter and Hubble constant, $\Omega_\chi h^2 \sim 0.12$, the interaction cross section $\langle\sigma v\rangle$ is predicted to be on the weak scale.

The fact that the DM energy density today could be explained by a GeV-scale particle that interacts on the weak scale is called the "WIMP miracle," and is especially compelling in conjunction with well-motivated DM candidates that would exhibit weak interactions. WIMP-like particles are predicted by supersymmetric extensions of the Standard Model, as well as the Universal extra dimensions (UED) models, as discussed below.

1.2.1.2 Supersymmetric Dark Matter Candidates

The theory of Supersymmetry (SUSY) arose as a potential solution to the gauge hierarchy problem, but its cosmological implications were quickly recognized. SUSY proposes a spacetime symmetry called "supersymmetry." For each Standard Model particle, SUSY introduces a "superpartner" that has the same quantum numbers, but opposite spin statistics. Therefore, SUSY predicts the existence of several new particles that are electrically neutral and do not interact via the strong force, including the superpartners of the neutrinos, photon, Z boson, Higgs boson, and graviton. If any of these superpartners are stable, they could be cosmological DM.

In early SUSY models gravitinos were primarily considered as potential cosmological relics, but the advent of the minimal supersymmetric standard model (MSSM) [40] opened the door to considering neutralinos as a DM candidate. In the MSSM, the superpartners of the photon, Z^0, and Higgs boson mix to form four eigenstates of the mass operator called neutralinos.

Neutralinos are one of the most well-studied DM candidates to date. However, in order for neutralinos to be cosmological DM, something must stabilize the lightest neutralino and prevent it from decaying. In most SUSY models, the conservation of R-parity guarantees that the lightest supersymmetric particle (LSP) is stable. The R-parity P_R of a particle is defined as:

$$P_R = (-1)^{2s+3B+L} \tag{1.8}$$

where s is the spin of the particle, and B and L are the particle's baryon number and lepton number, respectively. Following this definition, Standard Model particles have positive R-parity, $P_R = +1$, whereas all of their superpartners have $P_R = -1$. This parity ensures that superpartners can only be created or destroyed in pairs. A heavy superpartner can decay into a lighter superpartner, but the lightest of the superpartners can not decay. Therefore, R-parity stabilizes the LSP, allowing it to be a viable dark matter candidate.

SUSY WIMPs have masses on the order of 100 GeV, motivating experiments to search for SUSY DM particles in this relatively high mass range. The absence of evidence for SUSY at

the Large Hadron Collider has inspired theoretical efforts to go beyond the MSSM, and consider MSSM extensions with R-parity violation [41]. In these models, the LSP can decay, so it can only be a feasible candidate for cosmological DM if its decay time is greater than the Hubble time.

1.2.1.3 Kaluza-Klein Dark Matter Candidates

In the 1920s, Kaluza and Klein proposed that gravitation and electrodynamics might be unified as a pure gravitational theory in five dimensions. In later years, it was realized that theories with Universal extra dimensions (UED) could resolve the gauge hierarchy problem. Such models also provide stable Kaluza-Klein (KK) particles, viable DM candidates that generically have the desired cosmlogical relic density [42, 43].

UED models postulate that all Standard Model fields may propagate in one or more extra dimensions. The extra dimensions are assumed to be "compactified" on a circle with a radius $R \sim 10^{-18}$ m. At lowest order, the KK particle masses are simply the momenta, and the mass eigenstates are quantized as $m \sim n/R$, where n is the KK number. UED models introduce a KK parity, defined as $(-1)^n$, that is conserved, which implies that the lightest KK particle (LKP) can not decay into Standard Model modes and is stable.

The most promising candidates arising from UED are the KK photon, $B^{(1)}$, and the KK neutrino, $\nu^{(-1)}$. Typically, the KK photon $B^{(1)}$ is considered to be the lightest KK particle (LKP), since it receives negative radiative corrections. The $B^{(1)}$ mass is expected to lie in the range of 300–1000 GeV if it is to account for DM [42]. A second class of Kaluza-Klein DM candidates arises under Z_3 symmetry in the Randall-Sundrum model [44]. The lightest Z_3 particle (LZP) is stable, and is associated with a KK Dirac right-handed neutrino. LZPs can generate the observed DM relic density in two mass ranges: near the Z-resonance ($m_{LZP} \approx 35-50$ GeV) and for considerably higher masses, above several hundred GeV [45, 46].

1.2.2 Hidden Sector Dark Matter

WIMP-type thermal relics have been studied extensively as DM candidates. However, many examples of such candidates have been excluded by direct detection experiments [47, 48] and collider searches [49] (see Refs. [50, 51]). Despite this, there are several ways to reconcile WIMP DM with present-day constraints, including hidden sector dark matter. Hidden sector dark matter is a class of models where DM does not couple directly to Standard Model particles, but instead annihilates to lighter hidden sector particles that in turn couple to the Standard Model through a small "portal" interaction. The natural mass range for hidden sector DM is wider than for WIMPs, extending from $\mathcal{O}(1\,\mathrm{keV})$ up to $\mathcal{O}(100\,\mathrm{TeV})$ [52].

In light of the stringent experimental constraints, an enticing feature of hidden sector models is that DM elastic scattering with nuclei and DM production at colliders are highly suppressed. Therefore, hidden sector models are naturally concealed from collider and direct detection searches. However, since the portal coupling does not suppress the annihilation rate, hidden sector models are well-suited for indirect detection searches. A variety of hidden sector portals and their prospects for detection are discussed in Ref. [53].

One particularly well-motivated hidden sector DM candidate is dark photon DM. The dark photon is identified as the boson of an extra U(1) symmetry, and it is linked to the visible sector through a vector portal. In this model, the dark photon has independent couplings to DM and Standard Model particles, allowing WIMP DM with a thermal relic abundance to evade direct detection and accelerator constraints. If the dark photon mass is less than the DM mass, the DM can annihilate directly into dark photons that subsequently decay, producing Standard Model particles and providing a potential signature that is advantageous to search for with indirect detection experiments.

1.2.3 Axion and Axion-like Dark Matter

Ultralight DM is a general class of DM candidates that are bosonic particles with sub-keV masses. The lower limit for fermionic DM is around a few keV, with these constraints set by

Lyman-alpha forest measurements on substructure formation [54]. For DM masses $m_\chi \lesssim 30\,\text{eV}$, the de Broglie wavelength of the particle exceeds the inter-particle separation. At such light DM masses, the allowed candidates are necessarily bosonic due to the Pauli exclusion principle.

Bosonic DM models cover a wide mass range and a majority are beyond the scope of this thesis (see Ref. [52] for a thorough review). The following section will highlight the most prevalent bosonic DM candidates, the QCD axion and axion-like particles.

1.2.3.1 QCD Axion

The axion is a hypothetical particle that was first proposed to resolve the "strong CP problem," the apparent but unexpected conservation of charge-parity (CP) symmetry in strong interactions [55]. Quantum chromodynamics (QCD) has been incredibly successful in describing the strong force, but the absence of observable CP-violation remains an unsolved problem. QCD gives a CP-violating term in the Standard Model Lagrangian

$$\mathcal{L}_{SM} = \cdots + \frac{\bar{\theta} g^2}{32\pi^2} G^a_{\mu\nu} \widetilde{G}^{a\mu\nu}, \tag{1.9}$$

where $G^a_{\mu\nu}$ is the gluon field strength tensor, g is the QCD coupling constant, and $\bar{\theta}$ parameterizes the magnitude of CP-violating effects and must be experimentally determined. If $\bar{\theta}$ were of order unity, this term would give rise to large CP-violating effects, notably a measurable neutron electric dipole moment. However, the current best upper limit on the neutron electric dipole moment is $|d_n| < 1.8 \times 10^{-26}\, e \cdot \text{cm}$ [56], which constrains the magnitude of the CP-violating term $|\bar{\theta}| < 10^{-11}$. In essence, the strong CP problem lies in explaining why the value of $\bar{\theta}$ is so small.

Peccei and Quinn introduced a promising solution to this problem, interpreting $\bar{\theta}$ as a dynamic field, and introducing a new global $U(1)_{PQ}$ symmetry that is spontaneously broken at an unknown energy scale f_a, known as the PQ energy scale. The axion is the pseudo-Nambu-Goldstone boson resulting from such symmetry breaking. The modified Lagrangian including the spontaneous

breaking of $U(1)_{PQ}$ symmetry gives

$$\mathcal{L}_{SM+a} = \cdots + (\frac{a}{f_a} + \bar{\theta})\frac{g^2}{32\pi^2} G^a_{\mu\nu}\widetilde{G}^{a\mu\nu}, \tag{1.10}$$

where a is the axion field, and f_a is the axion decay constant. When considering this Lagrangian, an effective potential for the axion field arises that is periodic and minimized when $\langle a(x) + f_a\bar{\theta}\rangle = 0$. Therefore, the expectation value of the axion field cancels out the $\bar{\theta}$ term in the Standard Model Lagrangian, eliminating the CP-violating term. The axion mass is given in terms of f_a by

$$m_a \simeq 6\,\text{eV}\frac{10^6\,\text{GeV}}{f_a}. \tag{1.11}$$

Along with potentially resolving the strong CP problem [57, 58], a sufficiently light axion is an excellent DM candidate [59, 60]. The axion energy density relative to the critical density of the Universe is given by [61]

$$\Omega_a \sim 0.1\left(\frac{6\,\mu\text{eV}}{m_a}\right)^{\frac{7}{6}} \tag{1.12}$$

Therefore, an axion of $m_a \approx 20\,\mu\text{eV}$ would account for the entire DM density of the Universe. Cosmological and astrophysical measurements impose limits on the axion mass, with strict limits arising from stellar evolution [62]. Traditionally, the $10^{-6} - 10^{-2}$ eV range has been considered the open mass window for axions [61].

Using the modified Lagrangian, the axion coupling to Standard Model particles can be found. In particular, the axion coupling to two photons is

$$\mathcal{L}_{a\gamma} = -g_\gamma\frac{\alpha}{\pi}\frac{a}{f_a}\vec{E}\cdot\vec{B} \tag{1.13}$$

where α is the fine-structure constant, g_γ is a model-dependent coefficient of order unity, and $\vec{E}$ and $\vec{B}$ are the electric and magnetic fields, respectively. Axion experiments exploit the coupling of the axion to the electromagnetic field, searching for axion-to-photon conversion in strong magnetic fields via the Primakoff effect [63] (Sec. 2.2).

1.2.3.2 Axion-like Particles

The QCD axion is just one instance of an axion-like particle. Generally, periodic spin-zero fields with an approximate shift symmetry are called axion-like fields, and the corresponding particles produced in symmetry breaking are called axion-like particles. Axion-like particles (ALPs) are a generic prediction of many high-energy physics models, including string theory. Akin to the QCD axion, ALPs are expected to couple to photons, and their coupling constant $g_{a\gamma}$ can be probed similarly through the use an external magnetic field.

One particularly compelling ALP is fuzzy dark matter (FDM). FDM is expected to have a mass in the range $m_\chi \sim 10^{-22} - 10^{-21}$ eV to match observational constraints. With such a light mass, FDM's de Broglie wavelength exceeds the average inter-particle spacing in the Galaxy [64, 65]

$$\lambda_{DB} \equiv \frac{2\pi}{m_\chi v} = 0.48\,\mathrm{kpc}\left(\frac{10^{-22}\,\mathrm{eV}}{m_\chi}\right)\left(\frac{250\,\mathrm{km/s}}{v}\right) . \tag{1.14}$$

The average number of particles in de Broglie volume λ_{DB}^3 is given by [65]

$$N_{DB} \sim \left(\frac{34\,\mathrm{eV}}{m_\chi}\right)^4\left(\frac{250\,\mathrm{km/s}}{v}\right)^3 . \tag{1.15}$$

For sub-eV particles, the occupancy N_{DB} is so large that they can be described by a classical field equation. The Schrödinger-Poisson equation for this system can be solved numerically, providing its eigenstates ψ_n. Only the $n = 0$ ground state — called a "soliton" — is stable and time-independent. The n^{th} excited state has n unstable modes that decay to the ground state.

FDM could resolve outstanding issues in the ΛCDM model, notably the "missing satellite" and "cusp-core" problems (for a recent review on these issues see Ref. [66]). Simulations predict that DM will form into halos that have "cuspy" DM distributions, with the density increasing steeply at small radii, whereas rotation curves of galaxies suggest that the DM density distribution resembles the NFW profile and is flat at small radii (resembling a 'core'). This discrepancy is known as the "cusp-core" problem. For FDM, the central density and half-mass radius of each

eigenstate can be calculated. A key result of FDM is that the FDM halo resembles the NFW profile. The solitonic state provides a central core that is consistent with the observed central densities of dwarf spheroidal galaxies in the Local Group, although these observations are not conclusive (e.g. Refs. [67–69]).

The "missing satellite" problem arises from the inconsistency between the expected small-scale structure from CDM clustering and observations. CDM structure formation demands a self-similar hierarchy of DM sub-halos within halos — starting with the galactic halo working downwards. However, at scales $\lesssim 10\,\mathrm{kpc}$, ΛCDM is inconsistent with observations, predicting more low-mass halos than are observed. FDM predicts fewer low-mass sub-halos than CDM [64], providing a potential resolution to the "missing satellite" problem, although it could also be resolved by baryonic physics [66, 70]. For a recent review of FDM, its implications, and potential observables, see Ref. [65].

Chapter 2: Dark Matter Searches

The preceding section laid out the case that dark matter exists and understanding the nature of dark matter requires beyond the Standard Model physics. This section will describe the experimental efforts that search for dark matter (DM).

Dark matter experiments are typically classified into three categories, direct detection, indirect detection, and collider searches. Each search method relies on the existence of interactions between the DM and Standard Model particles, and a schematic of the interactions probed by each search method is shown in Fig. 2.1. Direct detection experiments search for DM scattering or absorption. Indirect detection experiments search for DM annihilation or decay into Standard Model particles. Collider experiments search for DM created in energetic collisions at particle accelerators. Employing experiments with different detection methods and backgrounds is crucial to uncover the nature of dark matter.

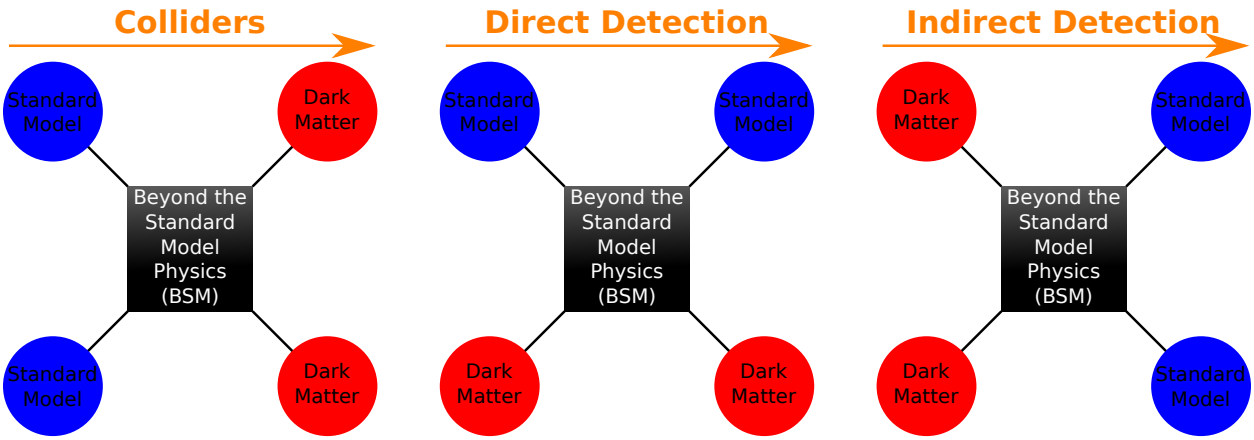

Figure 2.1: Visualization of three different dark matter search techniques. Colliders search for DM produced in energetic collisions at particle accelerators. Direct detection search for DM scattering interactions in a target material. Indirect detection experiments search for DM annihilation or decay into Standard Model particles, with this schematic showing DM annihilation.

2.1 Accelerators

Particle colliders have confirmed the Standard Model of particle physics, and are used to search for physics beyond the Standard Model. The Large Hadron Collider (LHC) [71] is currently the world's premier particle collider, colliding protons at a center-of-mass energy of 13 TeV. Collider DM searches look for DM created in these energetic collisions.

Since WIMPs are not believed to interact via the electromagnetic or strong nuclear forces, if they are produced in colliders they will traverse the detector layers without leaving a signal. However, due to the hermiticity of the experiments, dark matter could be identified by imposing energy and momentum conservation on the collision. Typically, the transverse missing energy E_T^{miss} is used to search for DM particles.[1]

One advantage of collider DM searches is that their limits are independent of the uncertainties in DM halo model parameters; however studying DM with colliders has its own challenges. Mainly, there is no direct verification that any new particle discovered actually comprises cosmological DM. As such, collider searches are considered a complementary strategy to direct detection, both setting corresponding limits on the coupling of DM to Standard Model particles [73]. At the LHC, CMS and ATLAS have produced competitive limits on the WIMP-nucleon cross section for spin-dependent interactions, and modest limits for spin-independent interactions [74], as shown in Fig. 2.2.

2.2 Direct Dark Matter Detection

Direct detection experiments search for scattering of DM particles off atomic nuclei. These interactions are expected to be very rare, with the rate dependent on the local density and velocity profile of the Galactic dark matter halo. In particular, WIMPs are expected to scatter elastically off nuclei. The coupling between WIMPs and Standard Model particles is typically characterized in terms of spin-independent (SI) and spin-dependent (SD) cross-sections, and direct DM searches

[1] Colliders can also search for charged DM candidates using a different technique, e.g. [72].

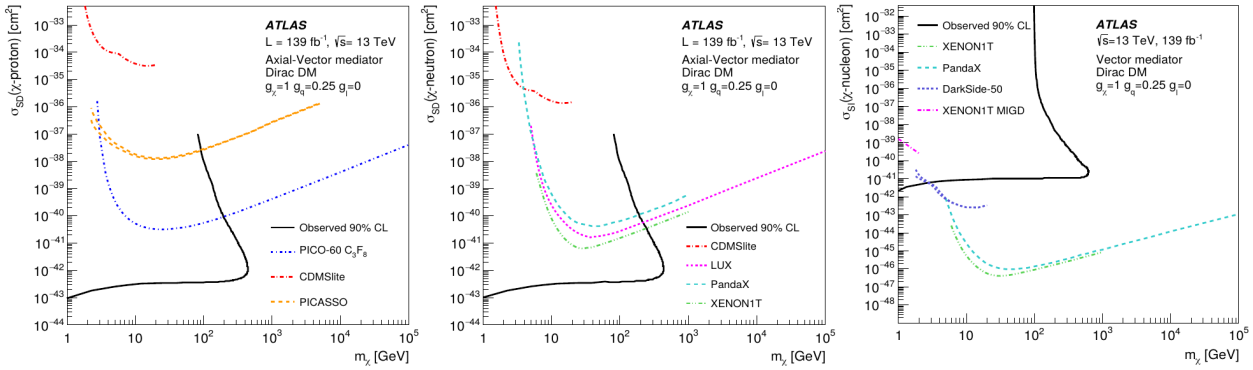

Figure 2.2: ATLAS 90% CL exclusion limit on the χ-proton spin-dependent scattering cross section (left), χ-neutron spin-dependent scattering cross section (center), and χ-nucleon spin-independent scattering cross section (right). Results at 90% CL from direct detection searches are also shown. Figure from [74].

probe both SI and SD couplings. Since DM scattering is a rare event and there are many potential background sources, direct detection experiments are typically installed underground with passive and active shielding.

Direct detection experiments measure the recoil energy of a target atom induced by the interaction with a WIMP. The maximum energy transfer in an elastic collision two-body collision is

$$\Delta E_{max} = \frac{2\mu^2 v_\chi^2}{m_T} \tag{2.1}$$

$$\approx \frac{2m_\chi^2 v_\chi^2}{m_T} \; (m_\chi \ll m_T) \tag{2.2}$$

$$\approx 2m_T v_\chi^2 \; (m_\chi \gg m_T), \tag{2.3}$$

where m_χ is the mass of the DM particle, m_T is the target mass, μ is the reduced mass of the DM particle and-target, and v_χ is the velocity of the incoming WIMP. A 100 GeV DM particle with a $v_\chi \sim 0.001c$, characteristic of galactic speeds, will typically deposit a few tens of keV when scattering off of nuclei. By contrast, the same DM particle scattering off an electron would deposit less than 1 eV. Therefore, the energy depositions from ~100 GeV DM particles scattering off electrons are below the energy threshold of many experiments, and these experiments focus

their search on WIMP-induced nuclear recoils.

There are a few different detector technologies that are used in direct dark matter searches. These experiments typically discriminate nuclear recoils from electronic recoils by measuring two quantities of deposited energy. XENON, LZ, and DarkSIDE deploy dual-phase liquid-gas noble targets (xenon or argon) in time projection chambers (TPCs). TPCs are instrumented with electrodes to apply a bias voltage and an array of photomultiplier tubes to detect scintillation light. The recoil produces prompt scintillation light (S1) and ionization (S2). The ionized electrons drift in the electric field, and some recombine with xenon or argon ions producing more scintillation light. The electrons that do not recombine drift into a high-field gas region, creating a proportional scintillation signal (S2). The dominant background in these experiments are electronic recoils produced by natural radioactivity in the experimental apparatus and environment, so it is imperative to distinguish nuclear and electronic recoils. Since the scintillation and ionization yields for nuclear and electronic recoils are different, the nature of the interaction can be inferred from the energy partition between S1 and S2. For the same energy deposition, a larger S2/S1 ratio is observed in electronic recoils, providing strong discrimination power to reject electronic recoils [75]. In noble TPC experiments optimized to identify nuclear recoils, neutrons are the most deadly background since they can't be easily rejected. To reject neutron events, the outer veto detector vessel is typically loaded with gadolinium to enhance its neutron capture cross section.

Semiconductor detectors are also used to search for dark matter, providing a lower energy threshold than noble TPC experiments, and therefore sensitivity to lower dark matter masses. The Super Cryogenic Dark Matter Search (SuperCDMS) uses germanium and silicon detectors operated at milli-Kelvin temperatures. Particle interactions within the detector produce phonon (S1) and ionization (S2) signals, which are measured using superconducting transition edge sensors (TES) and charge electrodes, respectively. Similar to noble TPC experiments, semiconductor-based experiments used the S1/S2 ratio to discriminate nuclear and electronic recoils.

Ultralow-noise silicon CCDs are used by the DAMIC and SENSEI experiments to search for DM. These experiments are optimized for light DM ($m_\chi < \mathcal{O}(1\,\mathrm{GeV})$), that scatter off bound

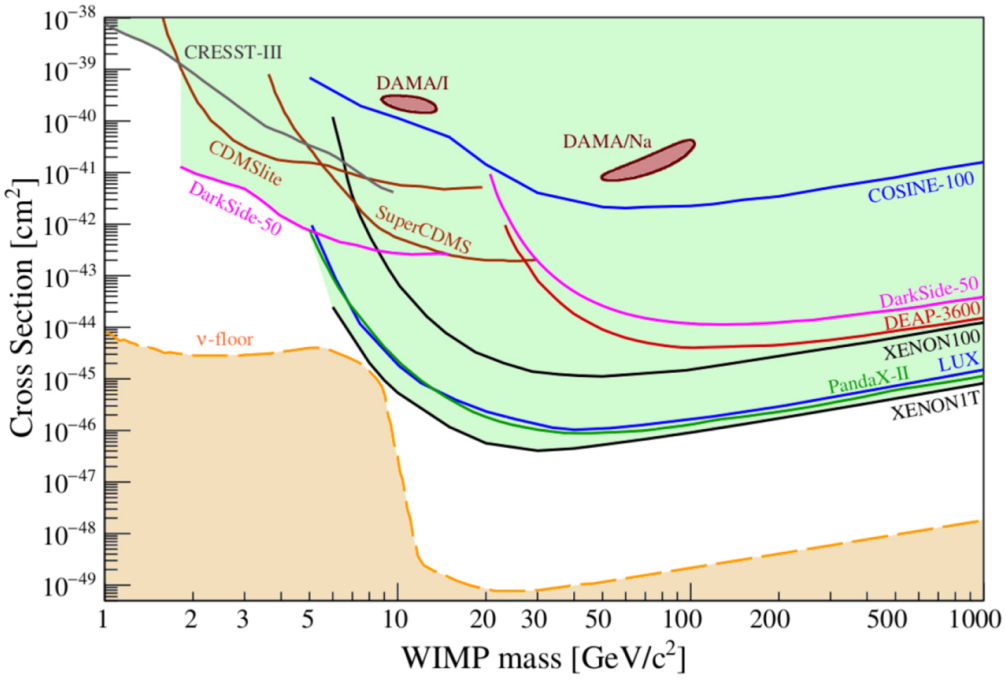

Figure 2.3: Current status of searches for spin-independent elastic WIMP-nucleus scattering. The dashed line limiting the parameter space from below represents "neutrino floor" due to coherent neutrino-nucleus scattering, an irreducible background for WIMP searches. Figure from [76].

electrons in the CCD through the exchange of a dark photon [77]. These CCDs deliver sub-electron readout noise, making them capable of measuring individual electrons, providing a low threshold energy to search for DM-electron scattering. In a recent analysis run, SENSEI set world-leading constraints for DM-electron scattering for DM masses below 10 MeV using a single 2 g CCD [78].

Other experiments use bubble chambers containing a superheated liquid target to detect nuclear recoils from WIMPs. PICO, the current state-of-the-art bubble chamber experiment, uses a fluorocarbon (C_3F_8) target, because fluorine is one of the most favorable nuclei for direct detection of SD interactions [79, 80]. The chamber is visually and acoustically monitored for energy depositions that nucleate bubbles. In order to trigger bubble nucleation, a critical amount of energy has to be deposited within a critical length, which enables the rejection of particles with insufficient ionization density to trigger bubble formation, such as cosmic muons, gamma-rays and electrons. Using a bubble chamber filled with 52 kg of C_3F_8 in the SNOLAB underground laboratory, PICO-60 set world-leading limits on the SD WIMP-proton cross section for WIMP masses below ~50 GeV [81].

The sensitivity of rare event searches are limited by their backgrounds, for instance neutrons and coherent neutrino-nucleus scattering in WIMP-nucleon searches (see Fig. 2.3). Each of these backgrounds give rise to nuclear recoils that cannot be rejected by pulse-shape discrimination, and the neutrino background cannot be shielded against nor mitigated by improving the radiopurity of the instrument. One solution to this limitation is to search for an annual variation in the rate of DM induced events, as predicted from the combination of the Earth's motion around the Sun, and the Sun's motion through the Galactic DM halo. The most well-known group to employ this technique DAMA/NaI Collaboration (and later DAMA/LIBRA), deploying thallium-doped sodium iodide (NaI(Tl)) scintillator crystals deep underground at Gran Sasso Laboratory. Their first published results reported the observation of an annually modulating rate consistent with DM scattering [82]. Although DAMA's signal has persisted and become increasingly statistically significant as more data was collected [83, 84], it is hard to reconcile DM interpretations of the DAMA/LIBRA signal with null results from other DM searches. Furthermore, a similar NaI(Tl) based experiment, ANAIS, recently reported no significant detection of modulation, incompatible with DAMA/LIBRA's result [85].

Axion searches rely on the axion to two-photon coupling (see Eq. (1.13)). Using a technique first proposed by Sikivie [86], it is possible to directly search for axions by exploiting the conversion of axions into photons in an external magnetic field. This process is the inverse of the Primakoff effect [63]. Axion searches can be classified into three categories: *haloscopes* look for relic axions potentially composing the Galactic DM halo, *helioscopes* search for axions produced at the core of the sun, and *light-shining-through-wall* (LSW) experiments [87] aim to produce and detect axions entirely in the laboratory.

Axion haloscopes use the microwave cavity technique, producing a strong electromagnetic field within the cavity, with a frequency related to the size of the cavity. For a given frequency, there exists a narrow range of axion masses that would interact with the electromagnetic field and convert into a light pulse that would be detected by a receiver. The resonance frequency of the cavity can be tuned to search for a range of axion masses. ADMX has probed a significant

part of the the theoretical parameter space and excluded realistic axion DM models for masses ranging from 1.9 μeV to 3.52 μeV [88], with even more stringent limits in the 2.66 to 3.31 μeV mass range [89].

Axion helioscopes typically consist of a superconducting magnet coupled to X-ray optics and a detector module. They take advantage of the fact that the mean energy of solar axions is around 4 keV, implying that in the presence of the strong magnetic field, solar axions would convert into low-energy X-rays. CERN Axion Solar Telescope (CAST) is the most sensitive axion helioscope in use, and has placed stringent constrains on $g_{a\gamma}$, setting $g_{a\gamma} < 0.66 \times 10^{-10}\,\mathrm{GeV}^{-1}$ at 95% confidence level for $m_a \lesssim 0.02\,\mathrm{eV}$ [90]. The next-generation International Axion Observatory (IAXO) will refine this technique, and plans to improve the axion-photon coupling exclusion limit by an order of magnitude [91, 92].

LSW experiments search for photon regeneration arising from the axion-photon coupling. A polarized laser beam propagating in a transverse magnetic field is blocked by a thick absorber that would block all laser light. On the other side of the absorber, there is a second magnetic field region and a detector that for photons of the same wavelength as the laser beam. If photons in the laser beam convert into axions in the magnetic field, the axions would travel through the wall with little absorption and be reconverted into photons in the second magnetic field. LSW experiments are able to set limits on more general models in which photons couple to axion-like particles (ALPs).

2.3 Indirect Dark Matter Detection

Indirect dark matter detection experiments search for Standard Model particles produced in DM annihilations or decays. The annihilation of dark matter into gamma rays was first discussed in 1978 [93, 94]. In the following decade, cosmic-ray (CR) antiprotons and positrons were also proposed as signals of annihilating dark matter particles [95], as well as neutrinos produced from dark matter annihilating in the core of the sun [96] and earth [97, 98]. X-ray observations provide methods to probe the decay of sterile neutrinos with masses in the range of ∼1–100 keV [99], as well as the existence of axions and axion-like particles (ALPs) [100].

Each indirect DM probe has its own advantages and disadvantages. Charged cosmic rays are deflected by magnetic fields, bending their trajectories as they propagate, washing out any directional information on the CR's origin. Contrastingly, gamma-rays and neutrinos trace back to the DM annihilation event making them a less 'indirect' probe, and enabling analysis techniques that exploit the directional information. Each indirect DM probe is also produced in conventional astrophysical processes, and understanding these background processes is paramount to properly interpret any potential DM signal. Although there are many different avenues to indirectly search for dark matter, the search results are complementary and the resulting exclusion limits must be considered en masse.

The prompt spectrum of DM annihilation or decay products is determined by a few physics parameters. The magnitude of the flux depends on the annihilation or decay rate. Due to energy conservation, the kinetic energies of the final-state particles are less than the mass of the DM particle. The shape of the energy spectra of the final-state particles depends on the annihilation or decay channel. Figure 2.4 shows the final yield of several particle species produced in $\chi\chi \rightarrow q\bar{q}$ (left) and $\chi\chi \rightarrow W^+W^-$ (right). These particles primarily originate from the hadronization and cascade decays of jets initiated by the final state q and $\bar{q}$, or directly from the prompt decay modes of the W. Fig. 2.4 demonstrates the complementarity of the various indirect detection probes, and how measurements of different final-state particles can be used to probe the same DM models.

Recently, there have been tantalizing hints of dark matter signatures in cosmic antiprotons [102], positrons [103–105], and gamma-rays [106–109]. Gamma-ray observations have focused on the Galactic center and dwarf galaxies to search for evidence of dark matter annihilations. Observations of dwarf galaxies using the Fermi Large Area Telescope have provided the strongest limits on the dark matter annihilation cross-section to date, constraining WIMPs lighter than ∼100 GeV [110]. Gamma-ray observations of the Galactic Center identified a significant excess of GeV-scale gamma-rays, consistent with the annihilation of ∼50 GeV DM [107, 111]. However, the Galactic Center excess could also be caused by an unresolved population of millisecond pulsars, and debate on how to interpret the purported gamma-ray excess is ongoing.

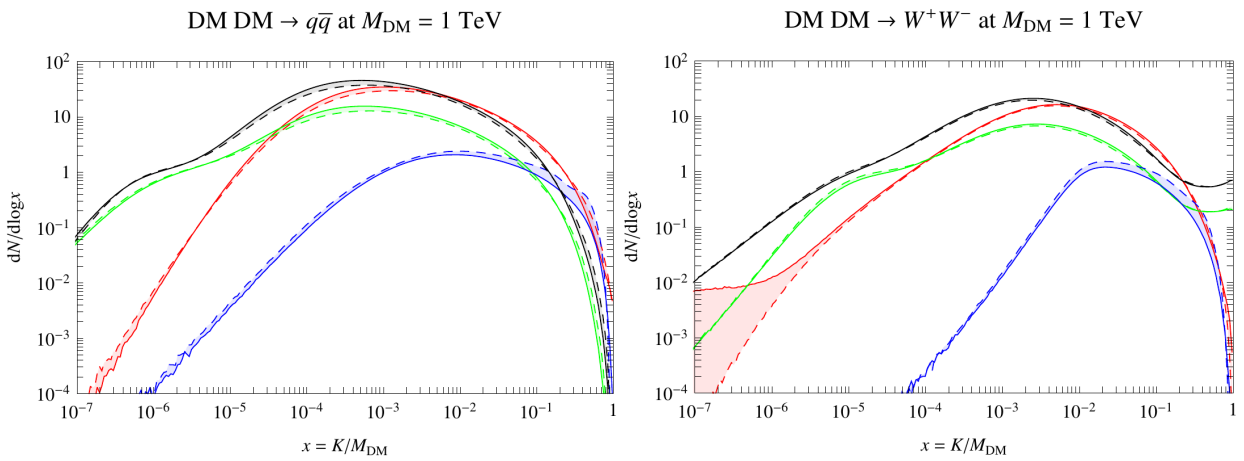

Figure 2.4: The differential photon (red lines), $e^{\pm}$ (green lines), neutrino (black lines), and $\bar{p}$ yield from dark matter pair-annihilation into a $q\bar{q}$ pair (left) and W^+W^- (right). Yields are shown as a function of $x = K/M_{DM}$, where K is the kinetic energy of the final-state particle and M_{DM} is the DM mass. Figure from Ref. [101]

Measurements of the cosmic-ray positron spectrum indicate an excess of positrons at energies above ∼10 GeV, relative to the expectation from standard secondary production. The first hints of this positron excess was found by the HEAT experiment in the 7–20 GeV range [112], and subsequent observations by PAMELA [113] and AMS-02 [103, 104] significantly detected the excess up to higher energies. The positron fraction rises above 10 GeV and peaks at ∼100 GeV, and could be caused by TeV-scale dark matter, but requires leptophilic annihilation with an enhanced cross section to avoid antiproton bounds. The main difficulty with the dark matter interpretation is that there are many conventional sources that can produce positrons in this energy range, including pulsars [114]. Recent HAWC measurements of diffusion around two nearby pulsars, Geminga and PSR B0656+14, indicates that diffusion of particles away from the pulsars is slower than previously expected, supporting the notion that the positron excess is due to dark matter [115]. However, subsequent analyses found that pulsars could still supply the positron excess if one assumes that diffusion is not uniform throughout the local interstellar medium [116, 117].

Since being proposed as a potential dark matter signal, the cosmic antiproton spectrum has been measured with increasing precision by a series of space-based experiments. The detection of cosmic antiprotons was first reported in 1979 [118, 119], and shortly after Buffington et al measured

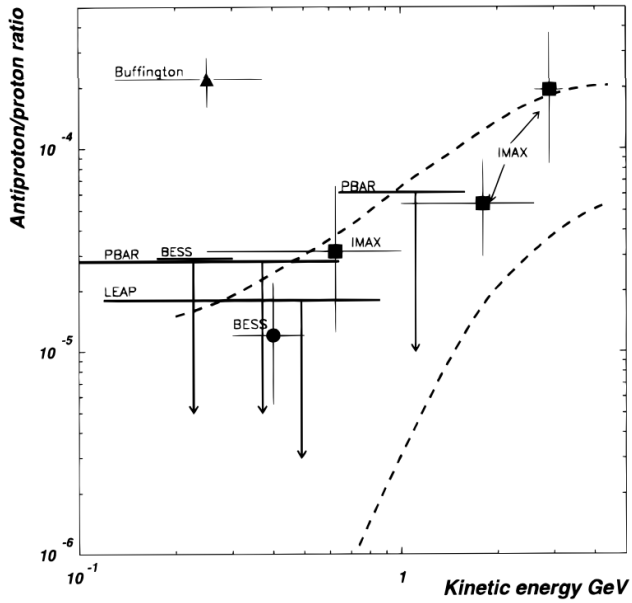

Figure 2.5: Status of low-energy antiproton/proton ratio measurements in 1997, from [121]. The tantalizingly high antiproton/proton ratio measured by Buffington et al [120] was not confirmed by subsequent experiments.

an unexpectedly large antiproton flux in the 130–230 MeV range [120]. Subsequent measurements made in this energy range failed to verify this claim, as shown in Fig. 2.5. Subsequent antiproton measurements by BESS [122, 123], CAPRICE98 [124], PAMELA [102, 125], and AMS-02 [126] have been used to deliver leading constraints on DM models, as well as astrophysical production and propagation. When these measurements are combined with the current understanding of cosmic-ray production (Sec. 2.3.1.1), Galactic propagation (Sec. 2.3.1.2) and Solar modulation (Sec. 2.3.1.3), they indicate that cosmic antiprotons originate largely from conventional secondary production, although a contribution from dark matter remains a possibility. Recent studies of the AMS-02 antiproton spectrum indicate an excess consistent with ~20–80 GeV dark matter [127–129], invoking some of the same models that could explain the Galactic Center gamma-ray excess [130]. However, interpretation of the antiproton excess is inconclusive due to astrophysical uncertainties, and recent analyses show that experimental correlations could reduce the significance of the excess [131, 132].

These indirect dark matter searches have provided some alluring hints of dark matter, but are plagued by astrophysical uncertainties. In the next section, I will introduce indirect dark mat-

ter searches with antinuclei, especially low-energy antideuterons, which can provide an ultra-low background signature of dark matter annihilation or decay.

2.3.1 Antinuclei from Dark Matter

2.3.1.1 Production of Antinuclei

The flux of antinuclei due to dark matter annihilation and decay can be estimated based on dark matter density profiles in the Galaxy, dark matter annihilation and decay channels, and hadronization, coalescence, and Galactic propagation models. A schematic of the production and propagation of antinuclei from DM annihilation is shown in Fig. 2.6.

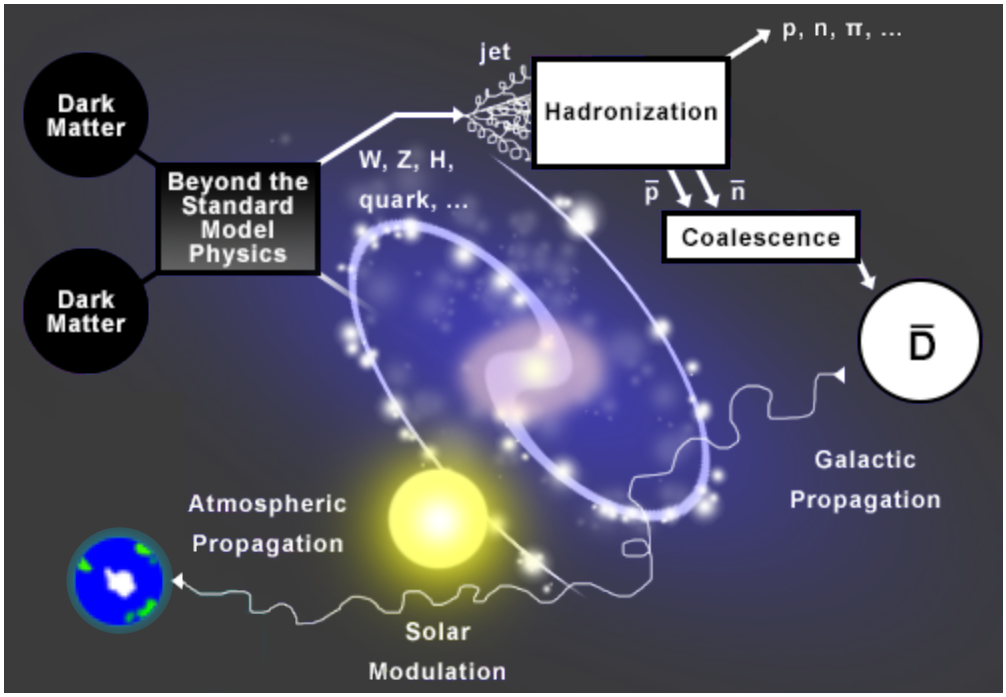

Figure 2.6: Schematic of DM annihilating, highlighting the primary channels that would produce antinuclei. The DM particles annihilate into bosons or quarks that in turn generate a jet whose subsequent fragmentation and hadronization yields antiprotons ($\bar{p}$) and antineutrons ($\bar{n}$). The $\bar{p}$ and $\bar{n}$ can then coalesce to produce and antideuteron, and even antihelium with the coalescence of more antinucleons. After formation, the antinucleus must propagate through the Galaxy, heliosphere, and atmosphere until it reaches an experimental apparatus near Earth. Image credit: J. Ryan, UCLA.

DM annihilations are parameterized by the DM-DM annihilation cross section σv, whereas DM decays are described by the DM decay rate $\Gamma = 1/\tau$. The primary channels for DM annihila-

tion or decay are into quarks, leptons, or bosons. The source term of a particle i produced in DM annihilation or decay is given by

$$Q_i = \frac{1}{2}\left(\frac{\rho(\vec{x})}{m_{DM}}\right)^2 f_{inj}^{ann}, \quad f_{inj}^{ann} = \sum_f \langle\sigma v\rangle_f \frac{dN_i^f}{dE} \quad \text{(annihilation)} \tag{2.4}$$

$$Q_i = \left(\frac{\rho(\vec{x})}{m_{DM}}\right) f_{inj}^{dec}, \quad f_{inj}^{dec} = \sum_f \Gamma_f \frac{dN_i^f}{dE} \quad \text{(decay)}, \tag{2.5}$$

where f runs over all the annihilation or decay channels with the respective thermally averaged cross sections $\langle\sigma v\rangle_f$ or decay rate Γ_f, and dN_i^f/dE_i is the energy spectrum of particle i per annihilation event. The factor of 1/2 in Eq. (2.4) corresponds to a self-conjugate DM particle. For $\rho(\vec{x})$ the NFW profile shown in Eq. (1.2) is often assumed. The energy spectrum of particle i at its production point is obtained by simulating the parton showering and hadronization of the prompt annihilation products using Monte Carlo simulation programs such as PYTHIA [133] or HERWIG [134].

The calculation of the source spectrum for the primary antideuteron flux originating from DM annihilation is based on three hypotheses [135]:

(1) the probability of producing a pair of antinucleons is given by the product of producing a single antinucleon (*factorization*),

(2) the antineutron production cross section is equal to the antiproton production cross section (*isospin invariance*), and

(3) the formation of an antideuteron can be described by the *coalescence model*.

The coalescence model describes the formation of antinuclei from a process that produces antiprotons and antineutrons, including CR spallation off the ISM [136] and DM annihilation [137, 138]. In this model, the individual antinucleons will coalesce if their relative momentum is small enough to allow the formation of a bound state. This threshold momentum value is called the coalescence momentum p_0.

The coalescence momentum is a key parameter because it enters to the third power and sixth power for antideuteron and antihelium-3 production, respectively, and directly scales the yield. It is determined by adapting the coalescence model to antinuclei production at accelerators and can also be assessed using Monte Carlo simulations. The coalescence momentum for (anti)deuterons is fairly well constrained by data from $e^+e^- \rightarrow \bar{D}$ from ALEPH at the Z^0 resonance, which gives the coalescence momentum $p_0 \sim 160\,\mathrm{MeV}$ [139]. Assuming a larger coalescence momentum of 248 MeV, as recently suggested by ALICE measurements [140], would increase the expected antideuteron flux by a factor of four.

In searches for antinuclei signatures of dark matter, the main background is antinuclei produced by cosmic-ray spallation. These background antinuclei are produced through spallation of CR protons, helium, and antiprotons on interstellar hydrogen and helium (e.g. [141]). To first approximation, the CR energy spectrum is a rapidly falling power law in energy, e.g. $\frac{dN}{dE} \propto E^{-\alpha}$ with $\alpha \sim 2.7$. The ISM consists mostly of hydrogen and helium with a constant density of about $1\,\mathrm{cm}^{-3}$ and $0.1\,\mathrm{cm}^{-3}$ in the Galactic disk, respectively [138].

The dominant source of secondary antiprotons is proton-proton collisions, in the reaction

$$p + p \rightarrow \bar{p} + p + p + p \tag{2.6}$$

which can be written as $p\,p \rightarrow \bar{p}\,X$ where X stands for the sum of the remaining final particle states. Since spallation reactions must conserve baryon number, antinucleons will be produced with a corresponding nucleon, i.e. in a nucleon-antinucleon ($N\bar{N}$) pair. The antiproton production cross section in proton-proton collisions is determined by accelerator experiments at a range of center-of-mass energies $\sqrt{s}$. Cross section uncertainties are at the level of 10–20% in the AMS-02 energy range, with higher uncertainties for lower energies [142]. Collisions of CR protons with helium ($p\,He$) and CR helium with protons ($He\,p$), will also make a considerable contribution to the secondary antiproton flux.

Secondary Galactic antideuterons are produced cosmic-ray spallation via the coalescence of

antinucleons that arise from $N\bar{N}$ pairs generated in the collision. At energies above 1 GeV/n, the dominant antideuteron production processes are $p\,p$, $p\,He$, and $He\,p$ reactions. In this case, the formation of an antideuteron requires the production of two antinucleon-nucleon pairs, imposing a higher energy threshold on the incident CR [135].

A competing antideuteron production mechanism is from the $\bar{p}\,p$ and $\bar{p}\,He$ collisions, which dominates the expected secondary antideuteron flux between 0.3–1 GeV/n. Although the CR antiproton flux is much lower than the proton and helium flux, this reaction must be considered since only one $N\bar{N}$ pair has to be produced to create an antineutron that can coalesce with the incident antiproton. The maximum value of the differential cross sections for $\bar{p}\,p \rightarrow \bar{d}\,X$ reactions are about four orders of magnitude higher than for $p\,p \rightarrow \bar{d}\,X$ reactions and peak at lower energies due to the lower production threshold (e.g. [141]).

At low energies, the flux of antideuterons produced in cosmic-ray spallation is suppressed due to kinematical considerations. The production threshold for antideuterons in $p\,p$ collisions in the center-of-mass frame is $\sqrt{s} \geq 6m_p$, and consequently $E \geq 17m_p$ in the laboratory frame, much larger than the corresponding antiproton production threshold ($E \geq 7m_p$). Since the flux of CRs approximately drops as $\sim E^{-2.7}$, there are fewer cosmic-rays with sufficient energy to produce a secondary antideuteron. Furthermore, spallation reactions have relatively high center-of-mass energy, compared to DM annihilations that occur essentially at rest. When boosting to the laboratory frame, the flux of low-energy secondary antideuterons is extremely suppressed.

2.3.1.2 Galactic Propagation

Most cosmic-ray measurements are made deep inside the heliosphere, at or near earth. A key component of determining the expected flux of cosmic-rays detected by an instrument is modeling their propagation through the Galaxy and heliosphere. Analytically, the propagation of nuclei in the Galaxy is described by the Galactic diffusion equation. The transport equation for any nuclear species with number density n can be written in terms of the CR differential density $dn/dE \equiv f$. Assuming steady-state ($\frac{\partial f}{\partial t} = 0$), the Galactic diffusion equation is expressed as [143]:

$$-\vec{\nabla}[K\vec{\nabla}f - \vec{V}_c f] + \frac{\partial}{\partial E}[b(E)f] = Q_{source} - \Gamma_{ine} f. \tag{2.7}$$

Here, the left-hand side describes the spatial diffusion (K), convection ($\vec{V}_c$), and energy transport which includes contributions from ionization, Coulomb, and adiabatic losses, as well as first order reacceleration. On the right-hand side, the first term corresponds to the primary, secondary, and tertiary source terms, and the second term accounts for the spallative destruction or fragmentation of nuclei species. For antideuterons the collision rate is

$$\Gamma_{ine} = \sigma_{\bar{d}_H} v_{\bar{d}} n_H, \tag{2.8}$$

where $\sigma_{\bar{d}_H}$ is the total antideuteron interaction cross section with protons, $v_{\bar{d}}$ denotes the velocity, and $n_H = 1\,\mathrm{cm}^{-3}$ is the average hydrogen density in the Galactic disk.

The estimated fluxes after Galactic propagation depend on the parameter choices, notably of the diffusion coefficient, its rigidity dependence, and the Galactic halo size [144]. Fits of cosmic-ray nuclei data for secondary-to-primary ratios (e.g. B/C) are important to constrain Galactic propagation parameters, in particular the effective column density traversed during propagation [145]. Conventionally, three benchmark choices of Galactic propagation parameters have been deemed the MIN, MED, and MAX models [144], with the MAX model yielding the highest fluxes. Positron measurements have excluded the MIN model [146], so recent antinuclei flux predictions account for Galactic propagation uncertainty using the MED and MAX models as lower and upper bounds, respectively.

2.3.1.3 Solar Modulation

Solar modulation affects the spectra of cosmic-rays below 50 GV, with the amount of modulation depending on the solar activity, configuration, and polarity of the solar magnetic field. Cosmic-ray propagation through the heliosphere can be described by the Parker equation, which gives the equation of transport of Galactic CRs in the heliosphere as [147]

$$\frac{\partial f}{\partial t} = -\underbrace{\boldsymbol{V}\cdot\nabla f}_{\text{a}} + \underbrace{\nabla\cdot(\boldsymbol{K}\cdot f)}_{\text{b}} - \underbrace{\langle \boldsymbol{v_D}\rangle\cdot\nabla f}_{\text{c}} - \underbrace{\frac{1}{3}(\nabla\cdot\boldsymbol{V})\frac{\partial f}{\partial \ln R}}_{\text{d}} + \underbrace{Q,}_{\text{e}} \tag{2.9}$$

where $f(\boldsymbol{r}, R)$ is the omni-directional Galactic CR distribution function at position $\boldsymbol{r}$ and rigidity R, and the terms on the right-hand side describe:

(a) convection by the solar wind speed $\boldsymbol{V}$,

(b) diffusion on heliospheric magnetic field irregularities,

(c) gradient and curvature drifts in the heliospheric magnetic field,

(d) adiabiatic energy losses due to the divergence of the expanding solar wind, and

(e) local sources such as particles accelerated at the Sun.

The full three-dimensional Parker equation can not be solved analytically, and sophisticated numerical models have been developed for the task. However, these models are complicated, and a much simpler description of the solar modulation process based on the force-field approximation [148] is routinely adopted instead. By assuming that there is no local source of cosmic rays ($Q = 0$), a steady state ($\partial f/\partial t = 0$), spherical symmetry, an adiabatic energy loss rate, and no drifts, Eq. 2.9 yields an analytical solution with only one free parameter, the modulation potential ϕ. Even though the force-field approximation can fit the observed data quite well, it has no predictive power, is not applicable for very low energies, and cannot account for charge-sign effects.

High precision data from recent space missions — PAMELA and AMS-02 — combined with observations by Ulysses and Voyager 1 and 2 that probe the outer reaches of the heliosphere, have enabled more sophisticated three-dimensional modeling of heliospheric propagation [149, 150]. Their data taken at different solar activity levels and magnetic field polarities enable a derivation of the local interstellar (LIS) spectra of cosmic-rays, and a more reliable calculation of the solar-modulated spectra. The solar activity level affects the solar-modulated flux, particularly at lower energies where a model predicts the antiproton flux below ~200 MeV is a factor of two larger at solar minimum than at solar maximum [151].

2.3.1.4 Predicted Antinuclei Flux from Dark Matter

Combining the production and propagation of antinuclei, the flux of antinuclei produced from DM and secondary processes can be estimated at the Earth's top-of-atmosphere (TOA). Due to the kinematical arguments presented in Sec. 2.3.1.1, low-energy antideuterons have ultra-low background from conventional astrophysical processes, and provide a promising avenue to search for dark matter. A variety of dark matter models predict antideuteron fluxes [135, 137, 143, 152] orders of magnitude above the astrophysical background in the energy range below approximately 1 GeV/n. Fig. 2.7 shows the predicted flux of antideuterons from a dark matter, as well as secondary and tertiary production. The DM model shown is motivated by the AMS-02 antiproton excess, which indicated a generic 71 GeV DM particle annihilating into $b\bar{b}$, with a thermally averaged cross section near the weak scale [153].

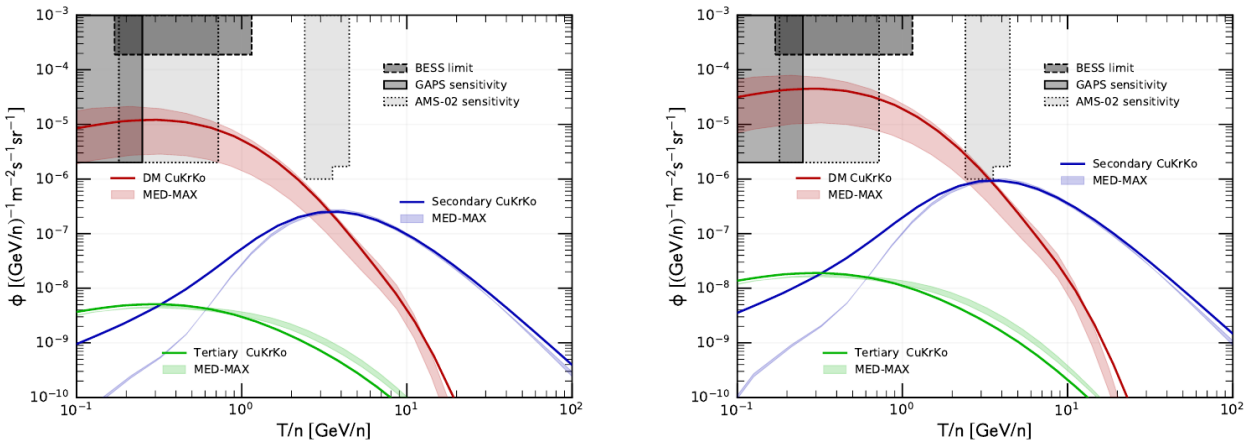

Figure 2.7: Antideuteron fluxes for a potential DM signal and secondaries produced in CR spallation on the ISM. All fluxes are derived using the analytic coalescence model with $p_0 = 160$ GeV (left panel) and $p_0 = 248$ GeV (right panel). Solar modulation was trated in the force-field approximation with the potential $\phi = 400$ MV. Also, the current BESS experimental limit (95% CL) [154], the AMS-02 sensitivity [155], and the expected GAPS sensitivity (99% CL) [156] are displayed. Figure from [138].

Chapter 3: The GAPS Experiment

3.1 Overview

The General Antiparticle Spectrometer (GAPS) is an Antarctic balloon experiment designed for low-energy (0.1–0.3 GeV/n) cosmic antinuclei as signatures of dark matter annihilation or decay. GAPS is optimized to detect low-energy antideuterons, as well as to provide unprecedented sensitivity to low-energy antiprotons and antihelium nuclei. GAPS was first proposed by Hailey and Mori in 2002 as the Gaseous AntiParticle Spectrometer [157], aiming to identify antinuclei through the characteristic X-rays emitted when they form exotic atoms in a gaseous target. In 2004, the measurement of X-ray yields from antiprotonic exotic atoms in liquid and solid targets [158–160] demonstrated the feasibility of a solid target material for exotic atom formation. A solid target provides more stopping power to slow incoming antinuclei, greatly simplifies the needed payload mass and complexity of the instrument, and enables the use of a tracking geometry.

Since its conception, the GAPS experiment has undergone significant R&D, and design and construction for the first GAPS long-duration balloon flight is nearly completed. Although the detection concept (Sec. 3.2) remains the same, the instrument now uses a particle tracker based on lithium-drifted silicon (Si(Li)) detectors as the target material for exotic atom formation. The particle tracker is enclosed in a plastic scintillator time-of-flight (TOF) system (Sec. 3.3.2), and the Si(Li) detectors (Sec. 3.3.3) are cooled by an oscillating heat pipe (OHP) cooling system (Sec. 3.3.5). The Si(Li) detectors are read out using a custom application-specific integrated circuit (ASIC) that is described in Sec. 3.3.4. The key detector and thermal technologies were validated in a prototype GAPS (pGAPS) flight from Hokkaido, Japan in 2012 [161–163], and piggyback flights from Ft. Sumner in 2018 and 2019. GAPS plans for at least three Antarctic long-duration balloon (LDB) flights, with the first flight scheduled for the austral summer of 2022-2023. The

GAPS project schedule is detailed in Sec. 3.4.

3.2 Detection Concept

GAPS uses a novel approach based on the formation and de-excitation of exotic atoms to identify antinuclei, providing greater identification power for these rare event signatures than previous magnetic spectrometer experiments. Fig. 3.1 shows a typical antideuteron event topology inside the GAPS instrument. The incident primary particle traverses the TOF system, which triggers

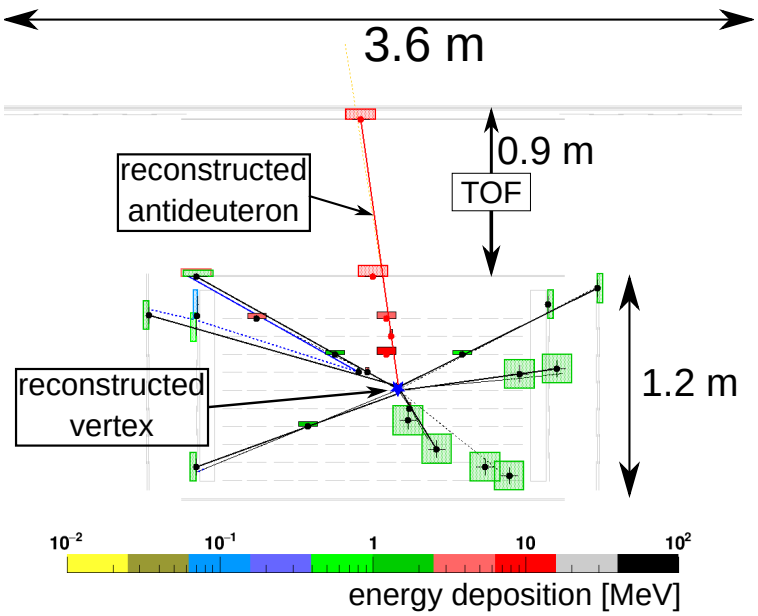

Figure 3.1: Typical antideuteron event topology in the GAPS instrument: the orange dashed line indicates the primary antideuteron and the red line indicates the reconstructed primary antideuteron. The black solid (dashed) lines represent secondary π^+ (π^-) emerging from the stopping vertex, and the blue solid (dashed) lines represent secondary positrons (electrons). The colored boxes show the energy depositions of the registered hits. The color of the box indicates the amount of energy deposited, and the size of the boxes correspond to the estimated error in position.

the instrument readout. The TOF also timestamps the energy depositions in the scintillator paddles, which enables the measurement of the primary particle's velocity β. Afterward, the particle continues into the Si(Li) tracker, where it slows down through ionization losses ($\mathrm{d}E/\mathrm{d}x$) in the tracker material. The Si(Li) detectors measure the energy depositions on the track, which increase as approximately Z^2/β^2 as the particle slows, where Z refers to the primary particle's charge.

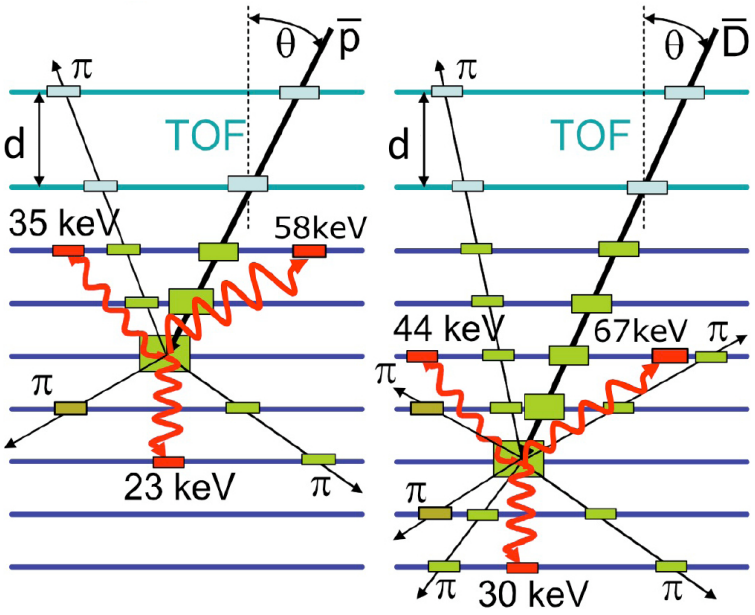

Figure 3.2: Antiprotons are a main background for antideuteron identification. GAPS distinguishes antideuterons from antiprotons using (1) depth sensing, (2) exotic atom X-ray energies, (3) multiplicity of secondary pions emerging from the vertex [156].

When the kinetic energy of an antinucleus is comparable to the binding energy of a target atom, the antinucleus is captured by the target material with near-unity probability, forming an exotic atom in a highly excited state. Within O(1 ns), the exotic atom de-excites, emitting Auger electrons and X-rays with characteristic energies that depend on the reduced mass of the antinucleus and the target material nucleus (see Ch. 8). Finally, the antinucleus annihilates with the target material, producing pions and protons. The lower-energy radiative transitions are in the 20–100 keV range and can be detected with the Si(Li) detectors [160]. The charged-particle annihilation products (primarily pions) can be tracked with both the tracker and the TOF, enabling energy deposition and velocity measurements. The number of pions emerging from the stopping vertex scales with the number of antinucleons in the annihilating antinucleus, which helps distinguish antinuclei event signatures (see Sec. 7.3). Fig. 3.2 compares antiproton and antideuteron event topologies in the GAPS instrument. The antiprotonic and antideuteronic exotic atom X-rays are separated by at least 5 keV, which motivates the requirement that the Si(Li) detectors deliver $\lesssim 4$ keV (FWHM) energy resolution to 20–100 keV X-rays.

3.3 The GAPS Instrument

The GAPS instrument is unique in the landscape of particle astrophysics experiments, being the first balloon-borne instrument with a large-area pixellated Si(Li) detector array and TOF system without a pressure vessel. An engineering drawing of the GAPS payload is shown in Fig. 3.3. The TOF system measures the incoming particle's velocity, and provides high-speed trigger and veto capabilities. The TOF system encapsulates a Si(Li) tracker that consists of ten layers of ~100 eight-strip Si(Li) detectors. Si(Li) detector strips in adjacent tracker layers are oriented orthogonally, providing three-dimensional tracking capabilities. The Si(Li) detectors are cooled to an operational temperature of –43 °C using an OHP system coupled to a radiator.

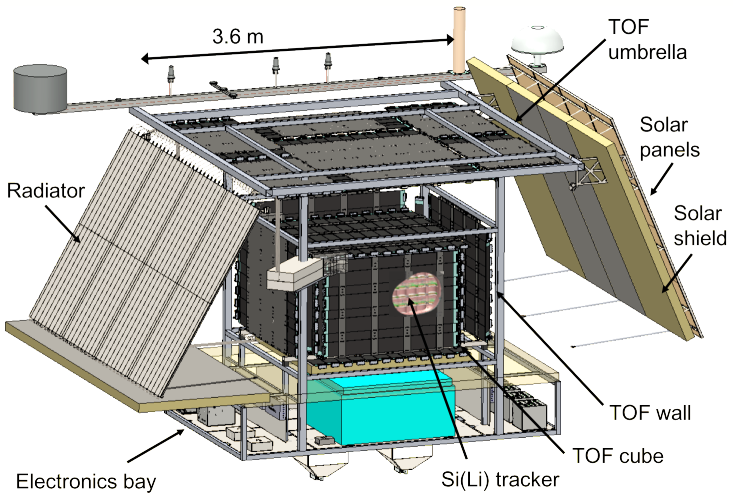

Figure 3.3: Detailed mechanical drawing of the GAPS payload. Two layers of plastic scintillator form the inner TOF "cube" and the outer TOF "umbrella" and "wall." The inner TOF cube encapsulates a tracker composed of 1000 Si(Li) detectors. A rotator is used to keep the radiator pointing to the anti-sun side, enabling cooling with the OHP system.

3.3.1 Balloon Requirements

The GAPS experiment plans to fly on a long-duration balloon from McMurdo Station in Antarctica in late 2022. To reach the desired float altitude of 120 kft, the payload must weigh $\lesssim 2500$ kg. During the flight, the instrument is powered by solar panels, which limits the available power to $\lesssim 1.2$ kW. Many of the design decisions for the GAPS instrument were made to meet

the unique requirements of balloon-borne operation. The mass and power requirements for each subsystem are listed in Table 3.1.

Table 3.1: The GAPS instrument's mass and power requirements.

Item	Mass [kg]
Si(Li) Tracker	472
TOF System	618
Power System	113
Gondola System	34
OHP Cooling System	194
Insulation/Shields	166
Gondola Structure	306
Crush pad	38
Science Subtotal	1942
System-level margin	22%
Science Allocation	2492

Item	Power [W]
ASIC (for 360 modules)	127
Digital Interface Board	10
Tracker Digital Backend	73
Tracker HV/LV Power	60
TOF System	475
CPU, Enet, GPS, Housekeeping	64
Thermal System	220
Science Subtotal	1029
System-level margin	20%
Science Allocation	1292

3.3.2 Time of Flight (TOF) and Trigger

The TOF system plays a crucial role in the GAPS identification scheme through its measurement of the particle β, $\mathrm{d}E/\mathrm{d}x$, and trajectory. The TOF also provides the primary trigger and serves as a shield/veto for the tracker. The TOF system is required to provide a time-of-flight resolution <400 ps, position resolution <6 cm per layer, and sufficient hermeticity to register >98% of tracks entering the tracker.

The TOF system consists of ~160 plastic scintillator paddles arranged into an outer umbrella and wall, and an inner cube. The inner cube is separated from the outer umbrella and wall by a minimum distance of about 0.95 m and 0.3 m, respectively. Each plastic scintillator paddle is 6.35 mm thick and 16 cm wide. The umbrella consists of 1.8 m long paddles, whereas the cube and wall use 1.8 m, 1.56 m, and 1.1 m lengths. The scintillation light is collected by silicon photomultipliers (SiPMs) coupled to each end of the scintillor paddles via optical silicone cookies. A preamplifier board incorporates six SiPMs, providing a bias voltage and high-speed signal amplification, and producing output signals for the waveform digitizer and trigger.

Prototype construction and testing of the TOF paddles and SiPM preamps has been completed, as shown in Fig. 3.4. The prototype TOF paddles have demonstrated a time-of-flight resolution <300 ps, significantly better than the requirement [164].

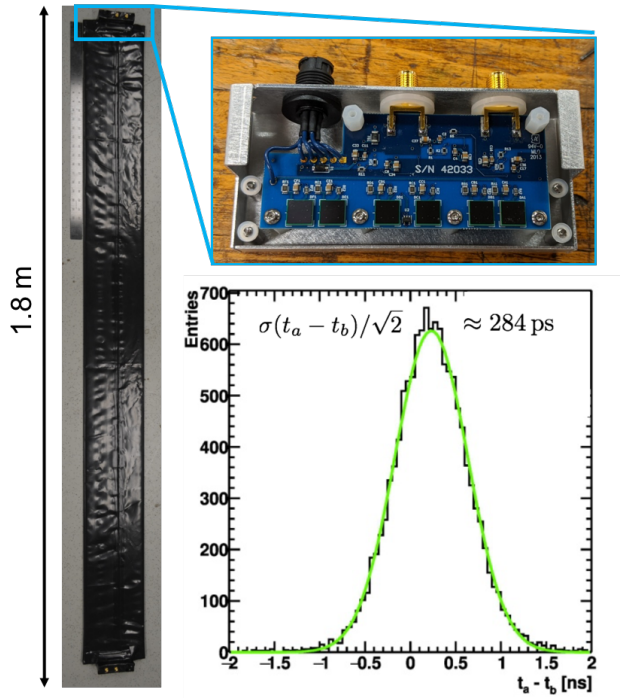

Figure 3.4: *Left:* Full-length (1.8 m x 0.16 m), light-tight TOF paddle. *Top right:* Open enclosure showing SiPM preamplifier and six SiPMs. *Bottom right:* Time difference distribution for vertical muon tracks in a full-length paddle, providing the inferred timing resolution of 284 ps [164].

3.3.3 Si(Li) Tracker

The Si(Li) tracker must provide the stopping power, energy resolution, tracking efficiency, and active area necessary to identify cosmic antinuclei. All of these requirements must be delivered within the temperature, power, and cost constraints of an Antarctic long-duration balloon flight. An energy resolution $\lesssim$4 keV (at –37 °C and 250 V bias) is required to distinguish the exotic atom X-rays from different antinuclei, as shown in Fig. 3.2.

A custom Si(Li) fabrication method was successfully developed at Columbia University and MIT to produce large-area detectors that satisfy the GAPS requirements. I played a pivotal role in this effort, executing the fabrication protocol from end to end and optimizing it, ultimately

producing prototype detectors with low leakage current, which is discussed in Chapter 4. The prototype procedure was transferred to Shimadzu Corporation, a commercial producer of Si(Li) sensors, to mass-produce the ∼1000 detectors for the initial GAPS science flight. Shimadzu Corporation provided large-scale facilities and trained technical staff for the mass-production effort. To preserve the long-term performance of the mass-produced detectors, I developed a custom passivation protocol that protects the exposed Si surfaces from humidity and organic contaminants, which is discussed in detail in Chapter. 5. The Si(Li) fabrication scheme demonstrates the required performance, as summarized in a series of publications [165–168].

These 10 cm-diameter, 2.5 mm-thick Si(Li) detectors provide the active area, X-ray absorption efficiency, energy resolution, and tracking capability necessary for the GAPS identification technique. The 2.5 mm depth is thick enough to stop low-energy antinuclei within ten layers, but thin enough that 20–100 keV exotic atom X-rays can escape from the stopping vertex and be detected in another detector layer. Each Si(Li) detector's active region is segmented into eight single-sided strips of equal area, providing sufficient spatial resolution to distinguish an incoming antinucleus from nuclear annihilation products and a per-strip capacitance that is low enough to operate with a low-power ASIC.

A detector module frame provides the mechanical, electrical, and thermal interface for the detectors (Fig. 3.5). It isolates the detectors from stray noise, transfers heat to the OHP system, and protects the detectors from mechanical shocks during the balloon flight. Four detectors are assembled into each module and the detector strips are wirebonded to the ASIC. Aluminized polypropylene windows are installed on both sides of the module, providing an additional layer of environmental protection while maintaining high X-ray transmission efficiency. In the GAPS flight configuration, each tracker plane will consist of 36 detector modules in a 6×6 array.

Low-temperature calibration of the detector modules is ongoing at MIT and University of Hawaii using low-noise preamplifiers. The energy resolution of all tested detectors is shown in Fig. 3.6. A noise model is used to characterize each detector and identify each noise source that contributes to the overall energy resolution of the detector. The model determines if the noise

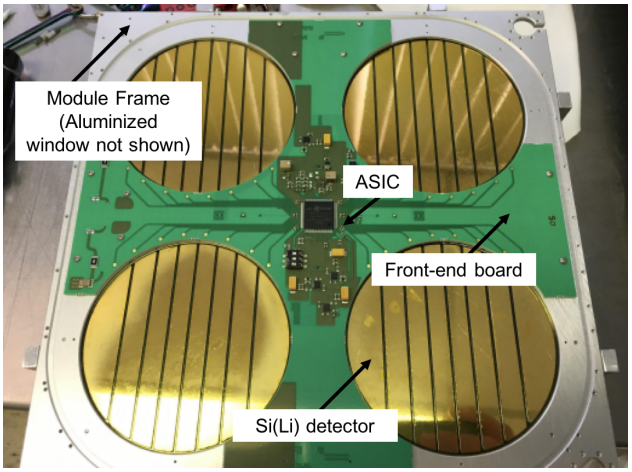

Figure 3.5: GAPS flight module with four Si(Li) detectors wire-bonded to a prototype ASIC front-end board.

arises from intrinsic detector performance or from the readout chain, and enables predicting the final detector performance when read out with the flight ASIC. Detector performance is categorized as 'X-ray' or 'Tracking' quality based on the number of strips delivering $\lesssim$4 keV (FWHM) energy resolution. After calibration, the ASIC front-end boards are mounted in the module and wire-bonded to the detectors at Nevis Laboratories using a K&S 4123 Wirebonder.

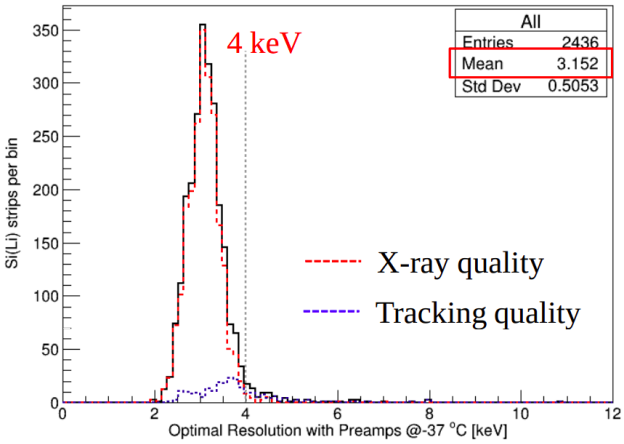

Figure 3.6: Distribution of X-ray energy resolution for strips of all 346 detectors calibrated to date, at the optimal peaking time and –37 °C. The black line represents all calibrated detectors, the red line indicates calibrated detectors categorized as X-ray quality, and the blue line indicates detectors deemed tracking quality.

3.3.4 Detector Electronics and Data Acquisition (DAQ) System

The Si(Li) tracker electronics consist of three main subsystems: front-end electronics, back-end electronics, and a power system. Since the GAPS Si(Li) tracker is designed to simultaneously detect atomic X-rays and track charged particles, the front-end electronics must handle a large range of signal amplitudes. Specifically, the detector readout electronics must provide high-resolution X-ray spectroscopy (< 4 keV FWHM energy resolution with $\sim$40 pf capacitance and < 10 nA leakage current) in the 20–100 keV energy range, and tracking capabilities to detect 1–100 MeV energy depositions from charged particles. To meet power constraints, it must operate at < 10 mW/channel.

Each detector module is read out by a custom 32-channel ASIC, requiring much less power than discrete preamplifiers. The ASIC has been designed, prototyped, and validated to meet the unique requirements of GAPS. A front-end board hosts the ASIC and its connection to the detector module. A back-end electronics board configures, controls, and acquires data from the front-end boards. Each tracker plane is controlled by one six-channel FPGA-based DAQ box, and one back-end channel controls a chain of six detector modules and ASICs through a SPI interface. The front-end board propagates the signals through one tracker row, and also houses a temperature sensor and electronics calibration system. A custom power system has been designed to supply the bias voltage to the detector modules and low-voltage to the front-end ASIC boards. For more details on the front-end electronics and power system see Ref. [169].

3.3.5 Thermal System

A novel Oscillating Heat Pipe [170, 171] (OHP) system has been developed at JAXA that delivers the $\lesssim$–37 °C Si(Li) operational temperature. The OHP system consists of capillary tubes with an inner diameter of 1 mm filled with a two-phase (gas-liquid) working fluid. This system can passively transfer up to 300 W of heat from the Si(Li) tracker to a $\sim$9 m^2 radiator oriented on the anti-solar side of the payload. The pressure balance between the vapor and liquid excites a self-oscillating flow, expanding into vapor in the warm section (tracker) and contracting into liquid in the cool section (radiator). The OHP system does not require a mechanical pump, which reduces

the power and mass consumption of the flight system, although a backup pump has been added to jump-start the OHP system and provide redundancy. The thermal profile of the payload has been modeled and validated in multiple test flights, including pGAPS [162, 172] and two piggyback balloon flights at Ft. Sumner that I participated in. Additionally, a flight-scale OHP system has been environmentally tested at JAXA and has shown the requisite $\lesssim$–37 °C performance.

3.4 GAPS Project Timeline

By late 2021, the construction of individual sub-system components will be completed. To validate the performance of the integrated system, we are currently building a GAPS functional prototype (GFP), consisting of ~10% of the Si(Li) tracker and TOF systems, along with supporting electronics. The GFP will allow full operation of key system interfaces, including triggering and reconstruction of cosmic muon tracks and measurements of X-ray calibration sources.

Full payload integration and testing (I&T) will begin in Fall 2021 and extend through mid-2022. First, the inner payload — including the Si(Li) tracker, OHP, TOF cube and wall, electronics, and back-end DAQ — will be integrated into the gondola frame at Space Sciences Laboratory (SSL). In March 2022, this assembly will be shipped to NASA's Plum Brook Facility and integrated with the radiator for thermal vacuum (TVAC) testing. The TVAC test will demonstrate the performance of all instrument sub-systems, and serves as a gate for GAPS's flight readiness. After TVAC testing, the assembly will be shipped to Columbia Scientific Balloon Facility (CSBF), where it will be integrated with the TOF umbrella and solar panel array, and a CSBF compatilibity test will be performed. The payload will then be partially disassembled and shipped to Antarctica, arriving at McMurdo Station in late Fall 2022. There, the payload will be reassembled and tested in preparation for a Flight 1 readiness date of December 2022. After returning from the first flight campaign, the data will be analyzed and the payload will be refurbised in preparation for the second flight, with a planned launch date of December 2024.

Chapter 4: Lithium-drifted Silicon (Si(Li)) Detectors – Fabrication

The GAPS experiment uses a tracker based on lithium-drifted silicon (Si(Li)) detectors to identify cosmic antinuclei, as described in Sections 3.2 and 3.3.3. Si(Li) detectors were selected for the GAPS tracker for a few key reasons. To achieve the requisite stopping power, it is advantageous use solid-state radiation detectors to form the particle tracker. Due to the thermal requirements of the balloon payload, silicon detectors are preferable to germanium detectors, because silicon's larger band gap facilitates operating at higher temperatures. Furthermore, silicon is relatively easy and inexpensive to procure compared to germanium. Si(Li) detectors have been used extensively for X-ray spectroscopy since the late 1960s. In modern particle physics experiments, most silicon tracking detectors are fabricated from high-resistivity silicon, without the use of lithium compensation. However, high-resistivity silicon detectors are not suitable for GAPS, which requires ~2.5 mm thick detectors to stop incoming antinuclei and have high detection efficiency for exotic atom X-rays. At 2.5 mm, high-resistivity silicon requires large bias voltages to fully deplete, and the resulting power drain is excessive for implementation on a balloon payload. Through lithium compensation, GAPS is able to produce 2.5 mm thick Si(Li) detectors that are fully depleted at modest reverse-bias voltages.

Si(Li) detectors are the heart of the GAPS identification concept, providing the grammage to stop low-energy antinuclei, and the tracking and energy resolution to identify exotic atom X-rays and nuclear annihilation products. GAPS developed a cost-effective method to produce the >1000 large-area Si(Li) detectors that will populate the tracker, providing high acceptance to incoming cosmic antinuclei. The GAPS research program has demonstrated that the Si(Li) detectors meet the requirements for deployment on a long-duration balloon (LDB) — specifically that they provide ≤4 keV energy resolution during operation at relatively high temperature (–37 °C) and low bias voltage (250 V).

This chapter will discuss the prototype fabrication work that I contributed to, which led to the mass-production of Si(Li) detectors for the first GAPS science flight. Section 4.1 reviews the theoretical underpinnings of semiconductor detectors and the principles of detector operation, with a focus on the results that are applicable to Si(Li) detector fabrication. Section 4.2 describes the Si(Li) fabrication process, and the prototype work that led to the mass-production fabrication protocol.

4.1 Theory of Operation

4.1.1 Semiconductor Detectors

Semiconductor detectors are used widely in (astro)particle physics and astrophysics to detect high-energy radiation and provide tracking arrays to identify event signatures in experiments. Silicon and germanium are the most prevalent semiconductors used to fabricate radiation detectors. Each silicon and germanium atom is tetravalent (four valence electrons) and forms valency bonds oriented equally in space with its four neighbor atoms. The outer shell atomic levels exhibit an energy band structure. This structure consists of a valence band, an energy gap, and a conduction band. In the energy band model, electrons are excited from the valence band to the conduction band due to ionizing events in the crystal as well as thermal excitation. The thermally excited electrons and holes contribute to the detector's noise, and generate a current that is conventionally called "leakage current."

A pure semiconductor crystal (without impurities) is called 'intrinsic'. In an intrinsic semiconductor there is an equal number of negatively charged electrons (n_e) and positively charged holes (n_h) in the crystal. The equilibrium concentration n_i of conduction electron-hole pairs in an intrinsic semiconductor ($n_i = n_e = n_h$) due to thermal excitation is given by:

$$n_i = \sqrt{N_c N_v} e^{-E_g/(2kT)} = AT^{\frac{3}{2}} e^{-E_g/(2kT)} \tag{4.1}$$

where N_c and N_v are the number of states in the conduction band and valence band, respectively, A

is a constant for a given material, T is the temperature in Kelvin, E_g is the band gap energy, and k is the Boltzmann constant [173, 174]. Once an electron is excited to the conduction band, it moves under the influence of the electric field in the semiconductor.

The drift velocity of electrons ($\mathbf{v_e}$) and holes ($\mathbf{v_h}$) through a semiconductor can be expressed as

$$\begin{aligned} \mathbf{v_e} &= -\mu_e \mathbf{E} \\ \mathbf{v_h} &= \mu_h \mathbf{E}, \end{aligned} \tag{4.2}$$

where $\mathbf{E}$ is the electric field and μ_e and μ_h are the mobilities of the electrons and holes, respectively. Combining the currents due to electrons and holes, the current density is given by

$$\mathbf{J} = q n_i (\mu_e + \mu_h) \mathbf{E}, \tag{4.3}$$

where q is the elementary charge. Comparing Ohm's law ($\mathbf{J} = \sigma \mathbf{E}$, where σ is the conductivity) to Eq. 4.3 gives the following relation for an intrinsic semiconductor's conductivity

$$\sigma = q n_i (\mu_e + \mu_h). \tag{4.4}$$

The resistivity ρ is the inverse of the conductivity, and is expressed as [173]

$$\rho = (q n_i (\mu_e + \mu_h))^{-1}. \tag{4.5}$$

The resistivity is one of the crucial parameters that determines the performance of a semiconductor detector because it is a driver on the amount of noise due to leakage current during operation.

The discussion above focuses on the properties of intrinsic semiconductors; however, 'extrinsic' semiconductors are more prevalent in detector applications. In extrinsic semiconductors the conduction is dominated by electrical carriers introduced by impurities that increase the electron or hole concentration in the crystal. These impurities (or dopants) are often deliberately added to the crystal during detector fabrication in a process called "doping." Dopants are classified as

'donors' or 'acceptors' based on the mobile charge carrier that they give rise to in the semiconductor, which depends on the impurity's valence structure. Donor impurities (e.g. phosphorous, arsenic, lithium) add excess electrons to the crystal, whereas acceptor impurites (e.g. boron) add excess holes. Doped semiconductors in which electrons are the majority charge carriers are called *n*-type; when positive holes are the majority charge carriers, the semiconductor is called *p*-type.

In most cases, semiconductor detectors are based on the formation of a *p*-*n* junction — the interface between a *p*-type and an *n*-type region in a semiconductor crystal. A *p*-*n* junction behaves like a diode, allowing a large current under forward bias and acting as a rectifier under reverse-bias. Due to the difference in the concentration of electrons and holes at either side of the junction, there is a diffusion of electrons towards the *p*-type region and holes toward the *n*-type region. The recombination of the diffusing electrons and holes causes an accumulation of charge at either side of the junction, which creates an electric field gradient across the junction. The electric field gradient eventually stops the diffusion process, leaving a region of immobile space charge called the depletion region. The depletion region has no mobile charge carriers, and any electron or hole that enters the depletion region will be swept out in the electric field. In semiconductor detectors, the depletion region provides the active volume for radiation detection — ionizing radiation that enters this zone will create electron-hole pairs that are subsequently swept out by the electric field [173, 174].

The depletion region will extend from the junction into the *n*-side and the *p*-side of the crystal. For an unbiased junction, the depth of the depletion zone on either side of the junction can be expressed as [174]

$$x_n = \sqrt{\frac{2\epsilon V_0}{qN_D(1 + N_D/N_A)}} \quad , \quad x_p = \sqrt{\frac{2\epsilon V_0}{qN_A(1 + N_A/N_D)}} \tag{4.6}$$

where x_n denotes the extent of the depletion zone on the *n*-side, x_p is the depth on the *p*-side, N_A is the acceptor concentration on the *p*-side, N_D is the donor concentration on the *n*-side, V_0 is the built-in junction potential ($V_0 \sim 0.7$ V for Si, 0.3 V for Ge), and ϵ is the dielectric constant. From

Eq. 4.6, it is evident that if one side of the *p*-*n* junction is more heavily doped than the other, then the depletion zone will extend farther into the lightly doped side.

With the introduction of a reverse bias, the mobile charge carriers are moved away from the *p*-*n* junction, increasing the width of the depletion region. The width of the depletion region with an externally applied reverse-bias voltage can be calculated from Eq. 4.6 by replacing V_0 with $V_0 + V_b$, where V_b is the reverse-bias voltage. In the case where $N_D \gg N_A$ and the junction is reverse-biased, the width of the depletion region $W \simeq x_p$ is given by

$$W = \sqrt{\frac{2\epsilon(V_b + V_0)}{qN_{eff}}} \tag{4.7}$$

where ϵ is the dielectric constant of the material and N_{eff} is the net density of electrically active centers in the p-type region. This case applies to almost all radiation detector situations, and is directly applicable to Si(Li) detectors where the *n*-side is more heavily doped.

Eq. 4.7 can be re-arranged to find the depletion voltage — the voltage required to deplete a detector of width W. Assuming that $V_b \gg V_0$, the depletion voltage V_d is given by

$$V_d = \frac{qN_{eff}W^2}{2\epsilon} \tag{4.8}$$

Examining Eq. 4.7 and Eq. 4.8, there are two ways to create wider depletion regions in a semiconductor detector: increasing the bias voltage (V_b) or decreasing the net density of electrically active centers in the p-type region (N_{eff}). The bias voltage can only be increased to a certain degree until the resulting electric field in the semiconductor causes secondary ionization and avalanche breakdown. For GAPS, the operating bias voltage is ultimately limited by the power constraints of the balloon payload.

Reducing N_{eff} can be achieved by using higher resistivity substrates or compensating the *p*-type region with *n*-type impurities to reduce the net density of electrically active centers. If both *n*-type and *p*-type impurities are added to the semiconductor, the net concentration $N_{eff} = |N_D - N_A|$. The reduction of the net concentration by adding equal amounts of acceptor and donor impurities

is called ‘compensation’. The advent of the compensation using the lithium drifting process helped achieve detectors with wider depletion regions without requiring exceedingly high bias voltages. Compensated junction diodes are often referred to as *p*-*i*-*n* junctions, where the ‘*i*’ indicates a thick compensated region as shown in Fig. 4.1.

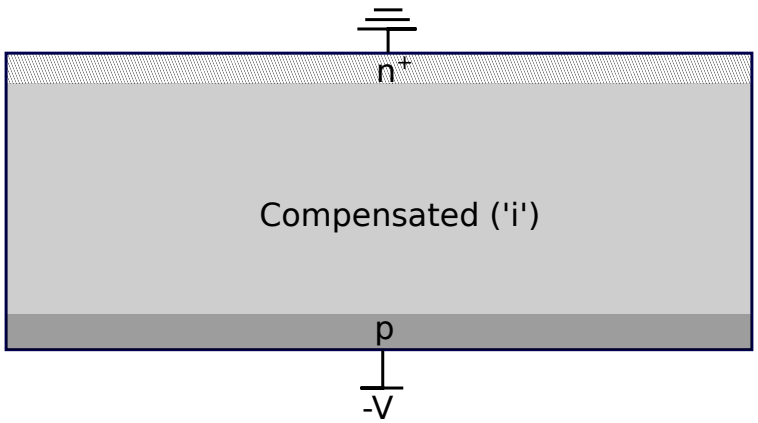

Figure 4.1: Diagram of reverse-biased *p*-*i*-*n* junction. The n^+ designation indicates that the *n*-side of the junction is more highly doped than the *p*-side.

It is important to note that a *p*-*i*-*n* junction is composed of two reasonably conductive regions separated by an insulating depletion region. Thus, the junction resembles a parallel-plate capacitor and has an associated capacitance

$$C = \epsilon \frac{A}{W}, \tag{4.9}$$

where A is the area of the depletion region and W is its width, which increases with increasing reverse-bias voltage until the entire compensated region is depleted. Thus, measuring a junction’s capacitance as a function of voltage provides an empirical method to assess the voltage required to fully deplete the junction.

4.1.2 Detector Efficiency

Radiation detectors can detect ionizing radiation from charged particles and photons. Charged particles lose energy as a result of the excitation and ionization of atoms, with the energy loss per unit path length ($\mathrm{d}E/\mathrm{d}x$) described by the Bethe-Bloch formula (see Ref. [174], Sec. 2.2.2 for functional form). In photon interactions an incident photon can be absorbed or scattered, with the

energy deposition confined to the interaction site. A photon beam will be attenuated following the Beer-Lambert law:

$$I(x) = I_0 \exp(-\mu x) \tag{4.10}$$

where I_0 is the incident beam intensity, x is the thickness of the detector, and μ is the attenuation coefficient. The attenuation coefficient represents the probability per unit length of an interaction that would remove the photon from the incident beam. The attenuation coefficient consists of a number of interaction cross sections. For a molecule consisting of atoms of type j with n_j atoms per molecule, the attenuation coefficient can be expressed as

$$\mu = \frac{\rho N_a}{M_r} \sum_j n_j \sum_i \sigma_{i,j} \tag{4.11}$$

where $\sigma_{i,j}$ is the cross section for process i in atom j, N_a is Avogadro's number, and ρ and M_r are the molecule's density and molecular weight, respectively. In the X-ray band, the main processes of interest are inelastic 'Compton' scattering (σ_{cs}), elastic 'Thomson' scattering (σ_e), and the photoelectric effect (σ_p). The photoelectric effect fully absorbs the photon and its energy, whereas a scattering process redirects the photon. Thomson scattering dominates at low energies with respect to the electron mass ($E_\gamma \ll m_e c^2$), and the photon does not lose energy in the interaction. Compton scattering dominates at high energies with respect to the electron mass ($E_\gamma \gg m_e c^2$), and the interaction shifts the photon's energy downward.

The full-energy peak efficiency (ϵ_P) describes the proportion of photons that are detected in the main photopeak that corresponds to the line energy E_l of a calibration source. The full-energy peak efficiency is defined

$$\epsilon_P(E_l) = \frac{N_P}{N_s(E_l)} \tag{4.12}$$

where N_P is the number of counts in the full-energy peak corresponding to E_l and $N_s(E_l)$ is the number of photons with energy E_l emitted by the source [175]. $\epsilon_P(E_l)$ depends on the geometry of the detector and calibration source, the detector's material properties and charge collection

characteristics, as well as the energy of the incident photons.

To properly calibrate a detector and assess its full-energy peak efficiency, it is imperative to understand the interplay of the photoelectric effect and Compton scattering in the detector and calibration chamber. Fig. 4.2 presents a schematic of the dominant X-ray interactions in a planar *p-i-n* diode. The junction diode is reverse-biased, and the photon interactions occur in the depletion region. In Compton scattering, the photon deposits a small amount of energy at the interaction site, and the amount of energy deposited is related to the scattering angle. In photoelectric interactions, there is a chance that the X-ray ionizes a silicon K shell electron, which results in the emission of a Si-K_α photon that is emitted isotropically with E_k=1.74 keV. If this photon escapes from the detector without being absorbed, it results in an 'escape peak' in the spectrum at $E_l - E_k$. However, the Si fluorescence yield ω_k is small ($\omega_k \sim 0.05$) [176] and a 1.74 keV photon has a relatively high photoelectric cross section so this rarely results in an escape peak in GAPS Si(Li) detectors.

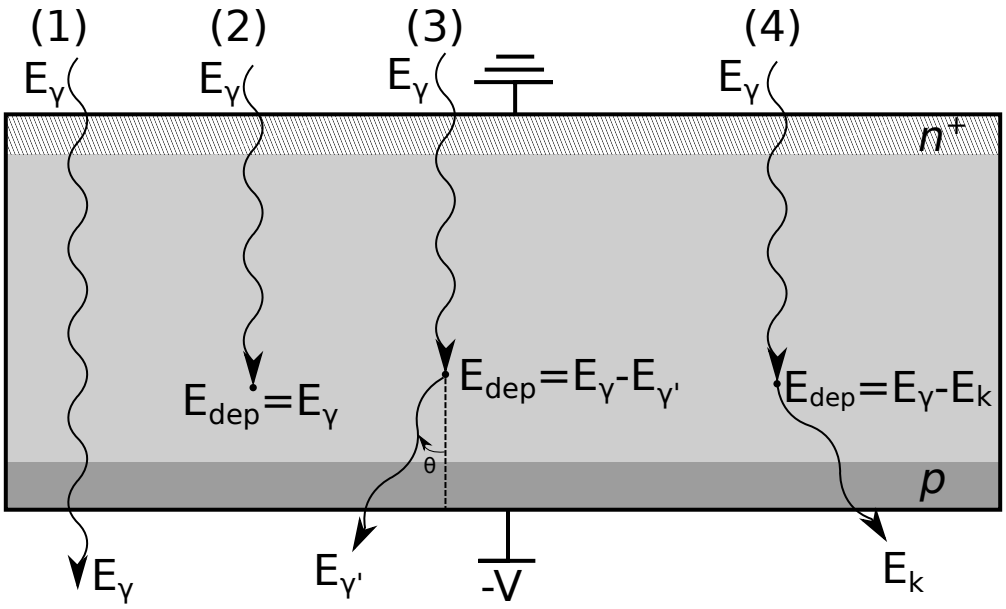

Figure 4.2: Schematic of the dominant X-ray processes. The photon can be (1) transmitted without interaction, (2) fully absorbed by the photoelectric effect, (3) Compton scattered, leaving a relatively small energy deposition at the scattering site, and (4) photoelectrically absorbed with the production of a fluorescence K_α photon. The scattered and fluorescence photons have a probability of escaping the detector, resulting in the full energy of the initial photon not being measured; however, if they are subsequently absorbed via the photoelectric effect, the full energy is recovered.

In efficiency calculations, the n^+ layer and p material on either end of the diode are typically

referred to as ‘dead layers’. Due to the high charge concentration in these regions, the electric field in these layers is reduced, and the charge collection for ionization events that originate in these regions is poor. For thin dead layers, it is likely that ionization events in the dead layers will diffuse out and be swept out in the electric field of the depletion region, but the pulse height of these events can exhibit a ballistic deficit due to the time required for all charges to diffuse out of the dead layer (see Sec. 4.1.3).

4.1.3 Signal Formation

The energy deposited in the detector is registered by measuring the amplitude of individual pulses using a readout scheme known as pulse-mode readout. A schematic of this readout scheme is shown in Fig. 4.3. When an ionizing event occurs in the depletion region, electron-hole pairs

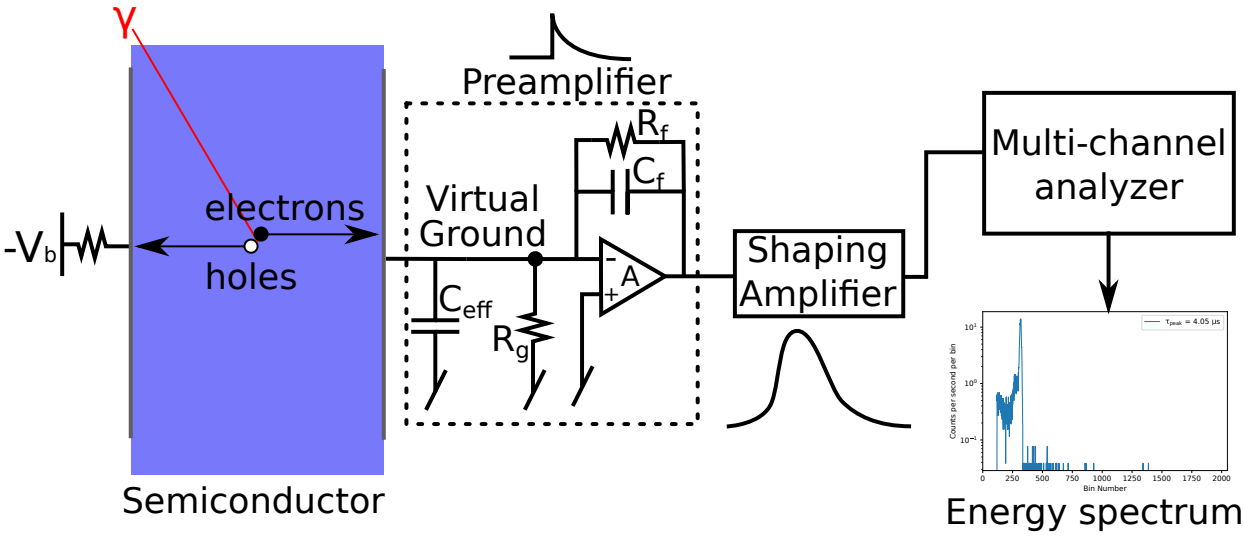

Figure 4.3: Equivalent circuit of detector and readout chain used to produce a spectra from a semiconductor detector. Ionizing events creates mobile electron-hole pairs that drift in the electric field. The movement of charge in the electric field creates a current pulse, that is converted to a voltage pulse by the preamplifier. In this diagram, the effective input capacitance C_{eff} includes the detector capacitance C_{det}, any stray capacitance C_{stray}, and any inter-electrode capacitance C_{int}. The shaping amplifier narrows the bandwidth of the preamplifier output signal. The multi-channel analyzer determines the height of the shaped voltage pulse for each event during a data-taking run to create an energy spectrum.

are excited into the conduction band, and they move towards the electrodes under the influence of the electric field. Both the positive and negative charges couple to the electrodes and induce mirror

charges on the electrodes, creating a measurable current. For a given detector geometry and electric field configuration, the Shockley-Ramo theorem [177, 178] is used to calculate the instantaneous induced current on an electrode as the electrons and holes are swept out of the depletion region. A key parameter in the Shockley-Ramo theorem is the 'weighting potential,' which is calculated for each electrode, and the charge induced on an electrode is proportional to the work done on the electrons and holes as they drift through the electrode's weighting potential. A detailed review of the Shockley-Ramo theorem is presented in [179].

The readout electrode is instrumented with a charge-sensitive preamplifier that produces a voltage pulse with a height proportional to the amount of charge induced on the electrode. The equivalent noise circuit of the detector and preamplifier is shown in Fig. 4.4.

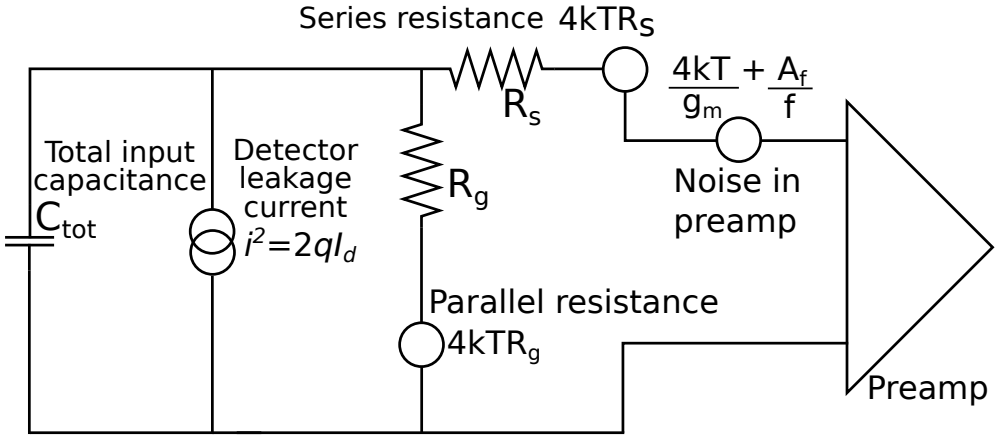

Figure 4.4: Equivalent noise circuit of detector and preamplifier readout chain.

The height of the voltage pulse is used to determine the amount of charge produced in the ionizing event, and subsequently the amount of energy deposited. The preamplifier must be designed to achieve a suitable rise and fall time for the voltage pulse. The voltage pulse is fed into a shaping amplifier that narrows the bandwidth of the signal, thereby reducing the noise and improving the precision of the pulse height measurement. A multi-channel analyzer senses the maximum voltage of the shaped pulse, digitizes the measured value, and fills a histogram for each radiation event to produce an energy spectrum for all registered events in a data run.

4.1.4 Ballistic Deficit

The energy measured by a radiation detector is determined by the pulse height of the recorded event and there are several effects that can cause "ballistic deficit" — a systematic reduction of the measured pulse height. During calibration, ballistic deficit can cause events where the measured energy is lower than the deposited energy, creating a low-energy tail skewing the main photopeak to lower energies and thus degrading the energy resolution. Events that Compton scatter in passive material in the calibration chamber and are subsequently photoelectrically absorbed in the detector will also create a low-energy tail, so it is imperative to disentangle these two effects when analyzing spectra. Ballistic deficit can be caused by attributes of the detector and pulse shaping system, and the contribution of these effects to the detector performance must be understood. As part of my work of GAPS, I studied the effect of ballistic deficit on GAPS Si(Li) detector spectra, which is detailed further in Ch. 6.

Within the detector, incomplete charge collection can be caused by charge trapping and inter-electrode charge collection. Charge trapping is caused by impurities in the crystal that give rise to trapping sites, that assist in the recombination of mobile electrons and holes. Inter-electrode charge collection is caused by charge collection to the gap between the electrodes. If the inter-electrode surface does not have sufficient resistivity to electrically separate the electrodes, the electric field lines can terminate on the inter-electrode surface. Charge carriers traveling on these electric field lines will be collected directly to the inter-electrode surface, and will not drift through the maximum weighting potential of any electrode, resulting in a deficit [180].

In the pulse shaping system, ballistic deficit can arise due to the interplay of finite charge collection times in the detector and the time constants of the amplifier [181]. Fluctuations in the profile of the induced current on the electrode are caused by the initial position of the charge within the detector volume, electric field inhomogeneities, or charge trapping. The peaking time of the pulse shaping network should be greater than the peaking time of the detector's current pulse, but not so large that it leads to pile-up. Simulation studies to disentangle the contribution of ballistic deficit and Compton scattering to the low-energy tail in GAPS Si(Li) detector spectra are presented

in Ch. 6.

4.2 Description of Fabrication Procedure

The basic process to fabricate Si(Li) detectors was developed by the Berkeley Group, and is described in [182]. The Si(Li) detectors used for pGAPS were developed by the now-defunct SEMIKON Detector GmbH [183–185]. A key challenge for GAPS was developing a cost-effective technique to produce large-area Si(Li) detectors. Prototype Si(Li) fabrication work was conducted at Columbia and MIT and is outlined in [165]. The mass-production Si(Li) fabrication procedure was developed in collaboration with Shimadzu Corporation [167]. This section will review the general procedures performed during Si(Li) fabrication, report the fabrication of prototype Si(Li) detectors for GAPS, and highlight the prototype fabrication results that contributed to the protocol ultimately used for mass-production.

4.2.1 Overview of Si(Li) Fabrication Method

Si(Li) detector fabrication aims to reduce the effective charge concentration in p-type silicon by compensation with positive lithium atoms. Si(Li) fabrication relies on two key characteristics of lithium: it is an easily ionized donor atom in Si (0.033 eV) and its ions have high mobility in the silicon lattice that increases with temperature [173]. Si(Li) detectors are fabricated by diffusing lithium into p-type silicon to form a p-n junction. Even at room temperature (average thermal energy ~25 meV) most of the lithium is ionized, leaving abundant positive lithium atoms that can compensate the negatively charged boron acceptor sites in the p-type bulk [186].

After lithium diffusion, the lithium distribution in the silicon can be expressed as [187]

$$N_D = N_0 \operatorname{erfc}\left(\frac{x}{2\sqrt{D(T)t}}\right) \tag{4.13}$$

where N_D is the lithium concentration at depth x from the surface, N_0 is the lithium surface concentration, t is the duration of diffusion, and $D(T)$ is the diffusion constant at the diffusion temper-

ature T. The diffusion constant of lithium in a silicon crystal with ~1000 Ω·cm resistivity is given by [187]

$$D(T) = 6 \times 10^{-4} \exp\left(\frac{-0.61q}{kT}\right) \ [\mathrm{cm}^2/\mathrm{s}] \tag{4.14}$$

The *p*-*n* junction is defined as the location where $N_D = N_A$, where N_A is the acceptor concentration in the *p*-type material. Plugging into Eq. 4.13, the *p*-*n* junction will be at depth x_0 given by

$$N_A = N_0 \,\mathrm{erfc}\left(\frac{x_0}{2\sqrt{D(T)t}}\right) \tag{4.15}$$

Solving for x_0, the *p*-*n* junction depth is

$$x_0 = 2\sqrt{D(T)t}\,\mathrm{erfc}^{-1}\left(\frac{N_A}{N_0}\right) \tag{4.16}$$

After diffusion, a reverse bias is a applied to the *p*-*n* junction and the temperature of the wafer is increased, so that the positive lithium ions 'drift' from the *n*-side of the junction to the p-side, compensating the acceptor atoms in the *p*-type bulk. Only moderate temperatures are needed to give the positive lithium ions sufficient mobility to drift in the electric field. The drift must be carried out in darkness to reduce photocurrents. The drift creates an effectively intrinsic compensated region of width W that can be expressed as [173]

$$W = \sqrt{2V\mu_L(T)t} \tag{4.17}$$

where V is the applied reverse-bias voltage during drifting, t is the drift time, and $\mu_L(T)$ is the temperature-dependent mobility of the lithium ions in silicon. The lithium ion mobility μ_L is related to the diffusion constant D by the Einstein relation

$$D(T) = \mu_L(T) \times \frac{kT}{q} \tag{4.18}$$

Pell [187] gave the following empirical formula for the lithium ion mobility

$$\mu_L = \frac{26.6}{T}\exp(\frac{-7500}{T})\ [\mathrm{cm^2\,V^{-1}\,s^{-1}}] \tag{4.19}$$

The lithium drift technique enables the creation of large effectively intrinsic (charge carrier-free) regions. For thick wafers, either a circular groove or a 'top hat' structure is machined into the *n*-side of the wafer before drifting as shown in Fig. 4.5. These geometries allow the drifting bias to be applied only to the interior of of the lithium-diffused layer, establishing an electric field that drifts the lithium ions through the *p*-type bulk, and not along the side, of the detector.

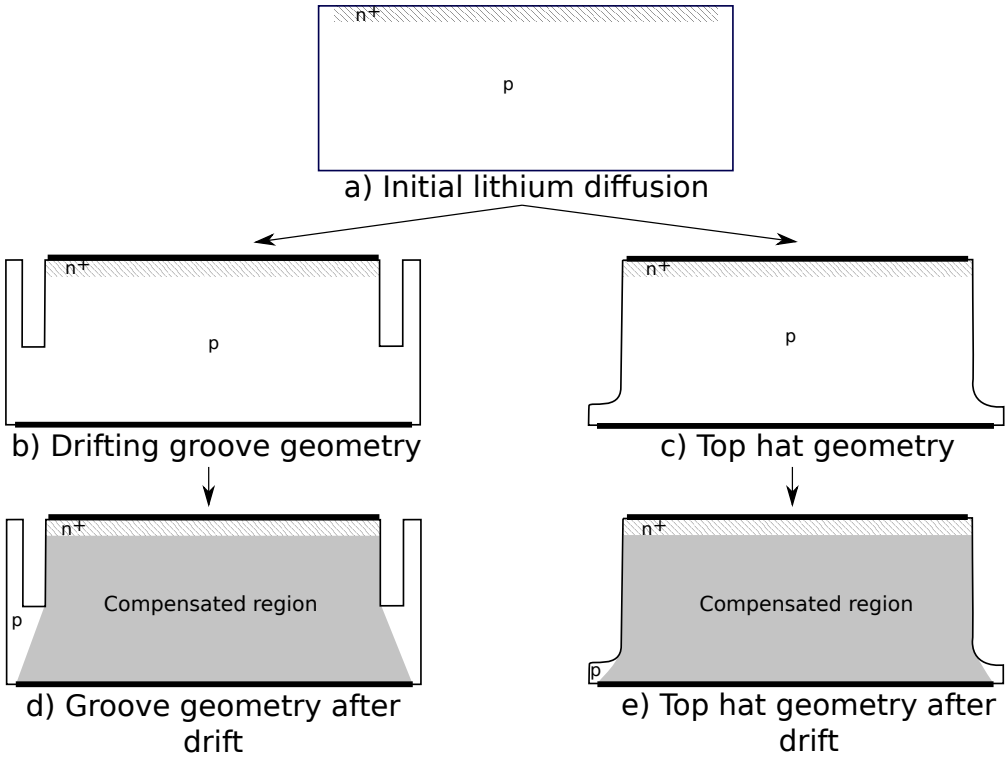

Figure 4.5: Schematic of the lithium drifting process. Lithium is diffused into a *p*-type silicon wafer, creating a highly doped n^+ layer, shown as single hatching in (a). Prior to drifting, a circular groove (b) or top hat structure (c) is contoured into the wafer. The post-drift lithium profile for each geometry is shown in (d) and (e). This geometry ensures that the positive lithium ions do not drift along the side of the wafer, improving the uniformity of the resulting compensated region.

The drifting procedure critically affects the final detector performance, including both the charge collection efficiency and bulk leakage current. There are a wide array of methods used

to indicate the successful end of the drift, including monitoring the diode's leakage current, capacitance, and resistivity. Some methods end the drift after a time that would produce the desired drifted depth, calculated using Eq. 4.17. One reliable indication that the lithium drifted region is approaching the *p*-side is a sharp increase in leakage current, and the drift can be terminated when the leakage current exceeds a pre-defined set point [188, 189].

After the initial drift, an additional 'cleanup' drift at a lower temperature can be performed to make the compensation more uniform. This process allows the positive lithium ions to redistribute, reducing any localized charge over-densities [190]. This also reduces the over-density of positive lithium ions that diffuse below the lithium-diffused n^+ layer during the drift, known as the lithium "tail."

One component of my research was determining the optimal drift and post-drift processing to produce detectors with low leakage current, which is reported in Sec. 4.2.2.3. In conventional Si(Li) fabrication protocols, any undrifted layer is removed after the drift via lapping with an abrasive and chemical etching so that the lithium reaches the face of the *p*-side, creating a compensated region that 'punches-through' the *p*-type bulk. Over-drifted material is also removed, since any excess of lithium on the *p*-side causes high leakage current. Unless a rectifying barrier is introduced on the *p*-side, punch-through detectors exhibit excessive leakage current due to charge injection. For pGAPS, large-area punch-through detectors were successfully fabricated by applying boron-implanted p^+ contacts on the *p*-side before drifting [185]. In this case, the completion of the drift was determined by the detection of full-energy signals from α-particles impinging on the boron-implanted contact, and it was not necessary to remove over-drifted material [185, 191]. The boron-implanted layer acts as a non-injecting contact during the drift and in the final detector.

A guard ring geometry (see Fig. 4.6) is crucial to reduce noise due to surface leakage current in large-area Si(Li) detectors [173, 192]. The guard ring groove must be sufficiently deep to penetrate through the lithium-diffused layer and electrically isolate the guard ring from the active area. During operation, the guard ring is held at the same bias potential as the active area. By chemically treating the surface of the groove to make it lightly *n*-type, the leakage current in the

active region can be made very small. At high bias voltages, a depletion region forms along the groove between the guard ring and active area and the interelectrode impedance becomes very large (~1000 MΩ) [173]. In this configuration, only surface currents that originate in the guard ring groove can enter the readout system, significantly reducing detector noise.

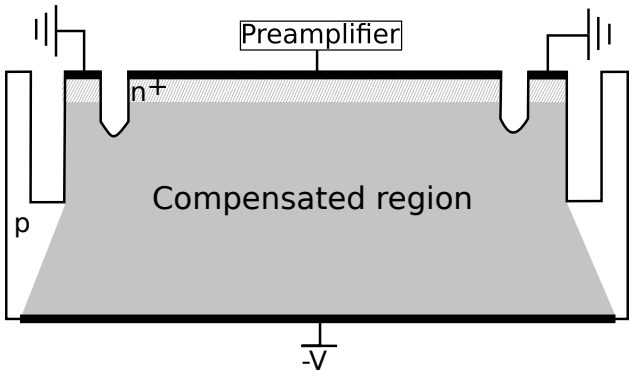

Figure 4.6: Schematic of detector geometry with drifting groove and guard ring. Grounding of the guard ring during operation reduces the surface leakage current in the device.

For a successful drift, a thick initial lithium-diffused n^+ layer is necessary to provide sufficient positive lithium ions compensate the full detector volume. However, the n^+ layer may be regarded as a dead layer, and thinner lithium-diffused contacts can be implemented after the drift and before segmenting position-sensitive structures. The thin lithium-diffused layer is realized by removing the initial n^+ layer entirely and diffusing a thinner n^+ layer [191], or by successively thinning the initial lithium layer via lapping and measuring the layer's sheet resisitivity to determine its thickness, as was done for pGAPS detectors [185]. The primary motivation for the thinner n^+ layers is to allow using relatively shallow grooves (~30 μm) to penetrate the lithium-diffused layer and segment readout strips, which would reduce the dead volume and increase detector efficiency.

Lastly, electrodes are applied to the *n*-side and *p*-side of the detector. On the *n*-side, a non-rectifying (Ohmic) contact is applied to the detector and guard ring to provide good charge collection and low series resistance. On the *p*-side, a Schottky barrier contact is necessary to prevent charge injection from the metal contact into the depletion region.

In developing a Si(Li) fabrication protocol, it is crucial to verify that the fabrication techniques produce the desired lithium distribution in the crystal. Copper staining provides a diagnostic tool to

identify the location of the *p*-*n* junction and the distribution of lithium in the crystal [193]. Copper staining involves the preparation of a copper sulphate solution with a small amount of HF to remove the native silicon oxide layer. The detector is diced before staining to view the cross-section of the detector bulk. The solution is applied onto the detector's surface and illuminated with a bright white light. The Cu^{2+} ions preferentially coat the *n*-type region. The higher the concentration of free electrons in the region, the brighter the copper plating appears. Copper staining a Si(Li) detector clearly shows the lithium diffused n^+ layer and the compensated volume, and is used as a diagnostic to check the lithium distribution in the crystal.

4.2.2 Development of GAPS Prototype Si(Li) Detectors

The SEMIKON Si(Li) detectors used for pGAPS represent the state-of-the-art Si(Li) fabrication procedure, including a boron-implanted p^+ contact, thinned lithium n^+ layer, and fine position elements defined using photolithography and plasma etching. A key challenge for GAPS was to develop a cost-effective fabrication method to produce lithium-drifted silicon detectors that meet the tracker's performance requirements. To meet the budgetary and time constraints of the GAPS research program, the Si(Li) fabrication process needed to produce detectors for 10% of the cost of pGAPS detectors, and to be capable of mass-production on the scale of 1000 detectors per year (whereas SEMIKON produced ~3 detectors per year). In formulating this procedure, we attempted to combine the best practices of over 50 years of research on Si(Li) detector fabrication.

This section will summarize the optimal fabrication methods that were determined during prototype Si(Li) R&D, and the key results that I contributed to the mass-production fabrication protocol. My research contributions demonstrated that GAPS could successfully drift detectors using a cost-effective Si substrate, developed a lithium-diffusion procedure to produce thin n^+ layers, determined the effect of chemical etching on groove shape, and investigated the effect of guard ring groove shape on charge collection. For more details on the fabrication process see Refs. [165–167].

At Columbia, the GAPS prototype detectors are fabricated from 2"-diameter and ~1.75 mm-

thick p-type wafers. The finished detectors have a guard-ring geometry with a single readout strip on a 1.25"-diameter active area. All fabrication procedures were performed in the Columbia Nano Initiative cleanroom, the CCNY Advanced Science Research Center Nanofabrication Facility cleanroom, or a lab space on Columbia's campus. Detector testing and assessment was performed in a lab space at MIT and at the MIT Microsystems Technology Laboratories cleanroom. In conjunction with the prototype fabrication work at Columbia, prototype 4"-diameter and 2.5 mm-thick detectors were fabricated by Shimadzu Corporation, using a flight-geometry 8-strip design and an alternate 4-strip design.

4.2.2.1 Substrate Selection

I led the prototype fabrication of Si(Li) detectors at Columbia using a newly-developed silicon substrate, providing proof-of-concept for the large-scale fabrication process. A main difficulty in producing Si(Li) detectors is finding a suitable substrate, particularly due to defects and contaminants in the crystal, such as oxygen and carbon. These behave as traps for lithium ions, making it challenging to uniformly drift. SEMIKON produced large-area Si(Li) detectors using wafers procured from Topsil Semiconductor Materials [183–185], the premier detector-grade Si supplier. However, the Topsil substrates are expensive and difficult to procure, and thus not suitable for the GAPS science flight. Recently, SUMCO Corporation developed a similar floating-zone p-type substrate which costs ~5 times less than a Topsil substrate, and is therefore much more suitable for a large-scale experiment. At Columbia, I successfully drifted and produced detectors with low leakage current characteristics using SUMCO substrates. The specifications of the SUMCO silicon are presented in Table 4.1.

4.2.2.2 Lithium diffusion

For my research, I used a custom Li evaporation system shown in Fig. 4.7 to evaporate lithium n^+ layers. I evaporated the initial ~150 μm thick n^+ layers, and developed a second lithiation protocol to diffuse thin ~30 μm n^+ layers into the SUMCO Si substrates. During the Li evaporation

Table 4.1: Specifications of the Si crystal used for GAPS Si(Li) detector fabrication. The minority carrier lifetime is the typical lifetime of electrons in the conduction band before they recombine with holes in the valency band, and is an indicator of crystal defects and contaminants.

Fabrication Method	Floating zone
Dopant	Boron
Crystal orientation	<111>
Oxygen concentration	$< 1 \times 10^{16}$ atoms/cm^3
Carbon concentration	$< 2 \times 10^{16}$ atoms/cm^3
Resistivity	$\sim 1000\,\Omega \cdot$ cm
Minority carrier lifetime	~1 ms
Diameter (prototype)	~50 mm
Diameter (mass-production)	~100 mm

process, the silicon wafer is set at the top of a vacuum chamber, sandwiched between a heater plate and a lower mask. A lithium pellet is thermally evaporated from a tungsten crucible below the wafer. The condition for evaporation requires that the pressure in the chamber is lower than lithium's vapor pressure at the temperature of the crucible. Practically, this requires high vacuum ($P \sim 10^{-5}$ Torr) and a high crucible temperature ($T \sim 400\,^{\circ}$C).

For the initial lithium diffusion, the chamber is pumped to 10^{-5} Torr, and the heater is set to 300 °C. After evaporating the lithium, the wafer is kept at 300 °C for a total of 30 minutes, as measured from the beginning of the evaporation, and then the wafer is rapidly cooled using a ice water circulation system. Using this procedure, I diffused ~150 μm lithium n^+ layers into the SUMCO substrates, as verified with copper staining by colleagues at MIT.

I developed a second lithium evaporation process that was incorporated into the final prototype fabrication protocol. By diffusing lithium into SUMCO substrates held at 140 °C for 30 minutes, I produced ~30 μm Li diffused layers, as verified with copper staining. The ultimate purpose of this second lithium evaporation is to allow for shallow segmentation of the active area and guard ring. Future work plans to entirely remove the initial ~150 μm thick Li diffused layer via lapping and etching, and apply a new thinner Li diffused layer. However, in the prototype detectors I only removed ~30 μm from the *n*-side after drifting because the wafers become too fragile if a

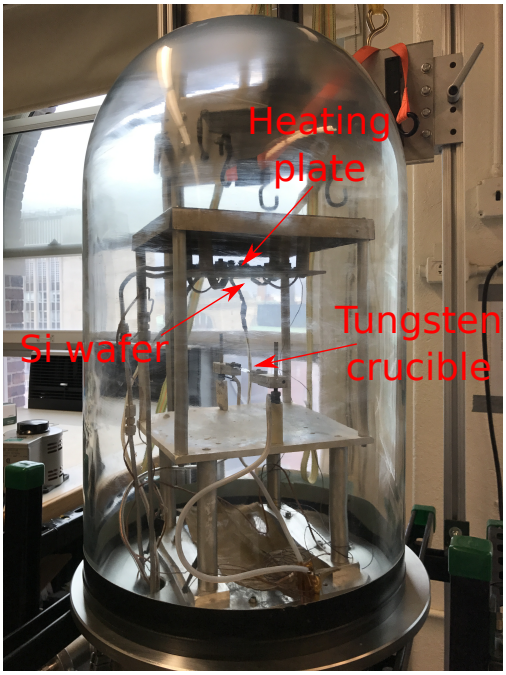

Figure 4.7: The custom Li evaporator consists of a bell jar instrumented with a heater plate to heat the wafer to its diffusion temperature, and a tungsten crucible to resistively heat and evaporate a Li pellet.

substantial thickness of material is removed. Thus, the procedure I developed mainly serves to validate that we can consistently produce very thin n^+ layers.

4.2.2.3 Lithium drift

I was responsible for drifting the prototype detectors, and my work demonstrated that the SUMCO substrates could be drifted to produce Si(Li) detectors with low leakage current and good charge collection characteristics. The SEMIKON detectors used a boron-implanted p^+ contact to prevent charge injection from the p-side surface into the depletion region; however boron-implantation proved too costly for mass-production. Without a p^+ barrier, we found that drifting to punch-through resulted in detectors with unacceptably high leakage current. I studied the effect of the drift termination condition and p-side Schottky barrier contact on detector performance in order to find a drift process that reproducibly produces detectors with low leakage current.

I used a custom drifting station to perform the Li drift, as shown in Fig. 4.8. The drifting station consists of a Au-coated Cu plate that is heated by a heating element to achieve the drift temperature.

Figure 4.8: Custom Li drifting apparatus used to drift 2”-diameter prototype Si(Li) detectors.

A pressure-mounted electrode presses down on the *n*-side of the wafer while the *p*-side is grounded to the plate. A Labview program controls the applied voltage and temperature, while logging detector's leakage current during the drift. The drift commences at room temperature, the bias voltage is raised to 250 V, and if the leakage current is stable at $\leq 100\,\mu$A, the temperature is increased gradually up to 100 °C and held there for the duration of the drift. At the end of the drift, the bias voltage is held at 250 V as the wafer cools down to room temperature, and then the bias is decreased as shown in Fig. 4.9.

I varied the drift termination conditions, drifting based on time or using a pre-defined leakage current set point to trigger the shutdown of the drift. I confirmed that drifting the Li all the way to the *p*-side and applying a Ni Schottky barrier contact resulted in detectors with excessively high leakage current at room temperature and at ~ -35 °C. This result implies that a large-area Schottky barrier contact easily breaks down at the GAPS operating temperature, which is significantly higher than that of conventional Si(Li) detector applications. I found that leaving a thin $\sim 100\,\mu$m undrifted layer suppresses charge injection from the *p*-side and results in devices with much lower leakage current, which was confirmed in mass-production work [167]. Additionally, I demonstrated that terminating the drift based on time reproducibly achieves a thin undrifted layer. Fig. 4.9 shows

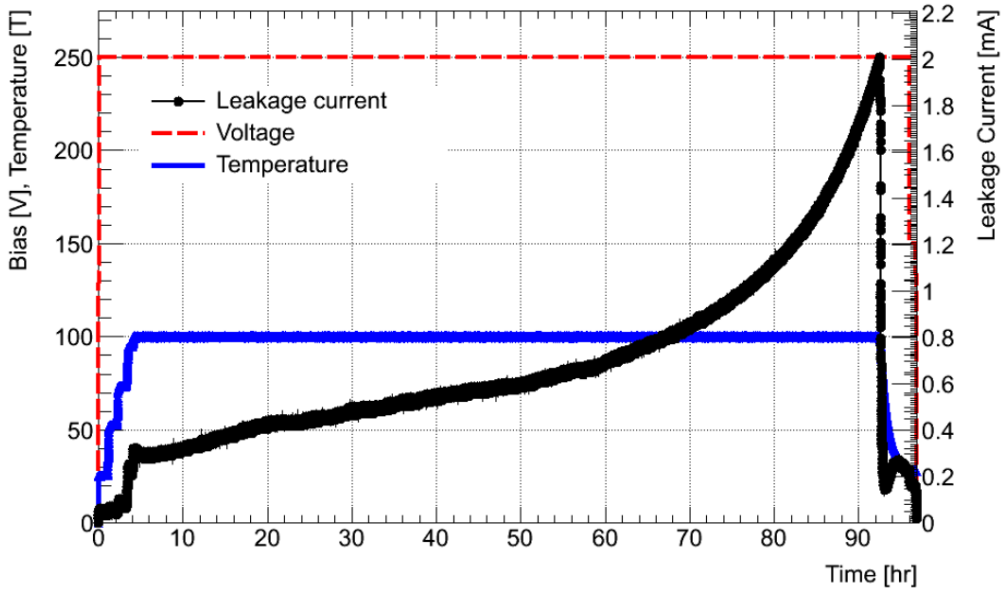

Figure 4.9: Bias voltage, temperature, and leakage current of prototype detector TD0093 during the drift. The sharp increase in leakage current indicates the the Li is reaching the *p*-side.

the drift profile of TD0093, a prototype detector that I successfully drifted. TD0093 was drifted for 88.5 hours at 100 °C and 250 V, producing a 1.45 mm drifted width while leaving a ~100 um undrifted layer.

4.2.2.4 Contouring of grooves

I investigated the effect groove shape on detector performance in order to demonstrate that ultrasonic impact grinding (UIG) is acceptable for mass-production of Si(Li) detectors. The profile of the groove segmenting the active area and guard ring is important to ensure that the electrodes are electrically isolated. Ideally, the groove should be as square as possible to allow high electric field "pinch points" to form, which increase the effective resistance between the active area and guard ring [194].

To assess the feasibility of UIG for large-scale fabrication, I cut grooves into prototype detectors and mechanical test samples using a Raytheon Model 2-334 ultrasonic impact grinder shown in Fig. 4.10. Since the initial Li diffused layer is not fully removed, >200 µm deep grooves are required penetrate through the n^+ layer. Due to this groove depth requirement and cost, the plasma

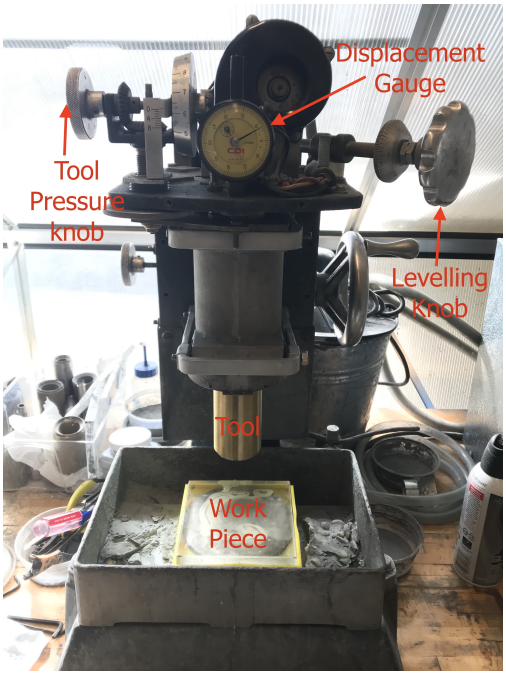

Figure 4.10: Raytheon Model 2-334 ultrasonic impact grinder used to cut grooves segmenting the active area and guard ring in prototype Si(Li) detectors.

etching process used for pGAPS detectors [183] is not feasible as it can not produce such deep features without unreasonably thick Al masking electrodes.

To assess the groove depth and shape imparted by UIG, I cut ~350 µm deep grooves into mechanical test samples. During the UIG process, a displacement gauge shown in Fig. 4.10 is used to determine the depth of the groove. After cutting the grooves, I measured the depth and shape of the grooves using an optical profilometer and by inspecting the cross-sections of a diced test wafer under a microscope. These studies indicate that it is crucial to replace the tool head of the ultrasonic impact grinder periodically to avoid excessive tool wear that results in rounded groove profiles (see Fig. 4.11).

4.2.2.5 Etching and its effect on groove shape

I studied the effect of etching on groove shape, and the effect of groove shape on detector performance. After cutting the grooves with UIG, a wet etching process is necessary to clean, chemically polish, and set the surface state of the grooves. Previous work indicated that it is dif-

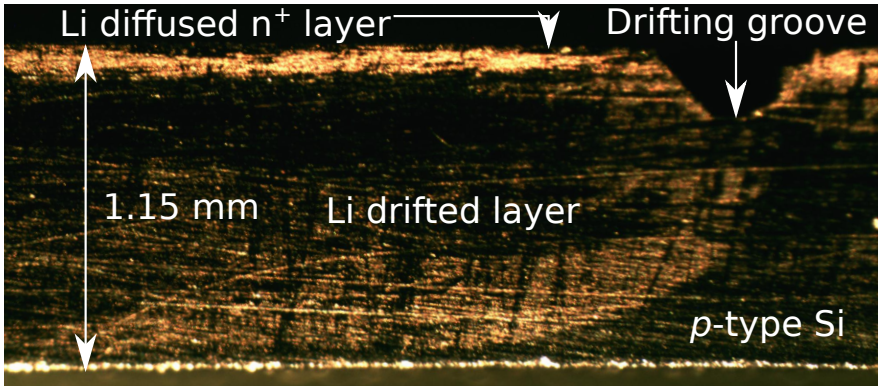

Figure 4.11: The cross section of a prototype detector, TD0082, after copper staining. The heaviest copper staining indicates the n^+ Li diffused layer. The lighter copper plating indicates the Li drifted region. Due to tool wear on the UIG tool head, the groove shape is rounded and shallow, which led to poor detector performance.

ficult to uniformly etch narrower grooves, because the bubbles generated in the chemical reaction stick to the groove surface, inhibiting the etching process (M. Yamada 2016, personal communication). I found that for $\gtrsim$500 µm wide grooves, the GAPS etching process uniformly etches the grooves.

The wet etching process that entails immersing the wafer in a liquid etchant solution. We use the common silicon etchant 'HNA,' a mixture of concentrated nitric acid (HNO_3), hydrofluoric acid (HF), and glacial acetic acid (CH_3COOH). The reaction is carried out in a chemical-resistant polytetrafluoroethylene (PTFE or 'Teflon') beaker. Surfaces that do not require etching (e.g. electrodes) are masked using 'picein' (Apiezon-W) wax that is dissolved into a non-polar solvent, specifically hexane or xylene, for application to the substrate. The wafer is placed in Teflon basket and submerged in the etchant, while gently agitating the basket and periodically (every ~30 seconds) lifting the basket to drain the etchant. The agitation and draining allows bubbles that form on the surface of the wafer to escape, helping ensure that the etchant uniformly contacts the wafer's surface. After etching, the masking wax is removed by immersing the substrate in the hexane or xylene. We found that xylene better dissolves the picein wax, provides more thorough removal of the picein after etching, and prevents staining on the electrode surface.

After segmenting the the guard ring from the active area, the electrodes are masked with picein,

and the grooves and sidewalls are etched in HNA. This final etching is crucial to chemically polish the grooves and set their surface state to be lightly *n*-type. In prototype detector fabrication, I etched the grooves for ~5 minutes, whereas the mass-production studies found that 15 minutes of etching in two discrete etching procedures reduced the detector leakage current and produced smooth, glassy groove surfaces.

I conducted a study to assess the effect of these etchings on the groove profile. I monitored the groove depth and width as a function of etch time and found that the etch rate in the horizontal and vertical direction are consistent within experimental error — indicating that the grooves are etched isotropically. When etching the grooves with a picein mask applied to the *n*-side, the groove depth and width increase at approximately the same rate, reducing the active volume of the sensor and rounding the groove profile, as shown in Fig. 4.12.

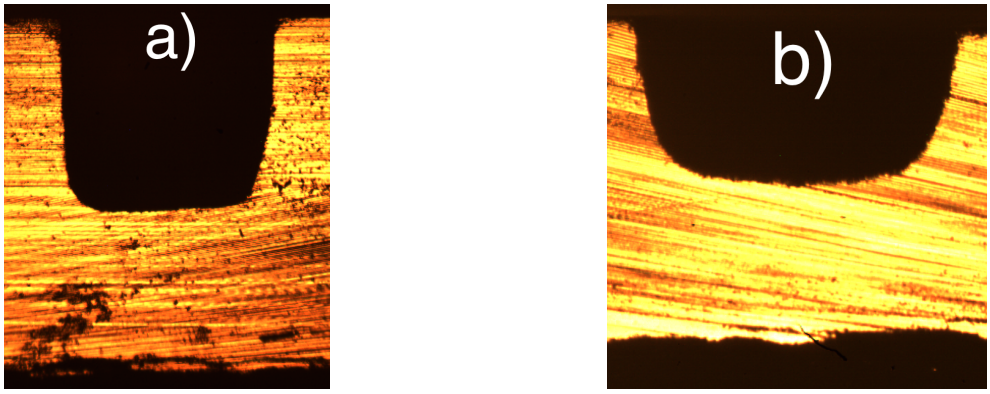

Figure 4.12: a) Image of groove segmented with UIG without any etching. This represents a typical CU UIG deep groove without etching b) Image of a test wafer's groove after 14 minutes of etching. Note that this groove groove is slightly more rounded than the groove in (a).

The mass-production protocol adopted a 15 minute etch time, since it was the minimal etch time that would smooth the groove surfaces while mitigating the rounding of the groove profile and growth of the groove width and depth [167]. We found empirically that detectors with rounded guard ring grooves delivered the requisite leakage current and energy resolution performance for implementation in the GAPS tracker (Fig. 4.13). I also developed an electrostatic simulation to compare the effect of rounded groove shapes on a detector's bulk electric field and charge collection properties, which is reported in Sec. 6.1.

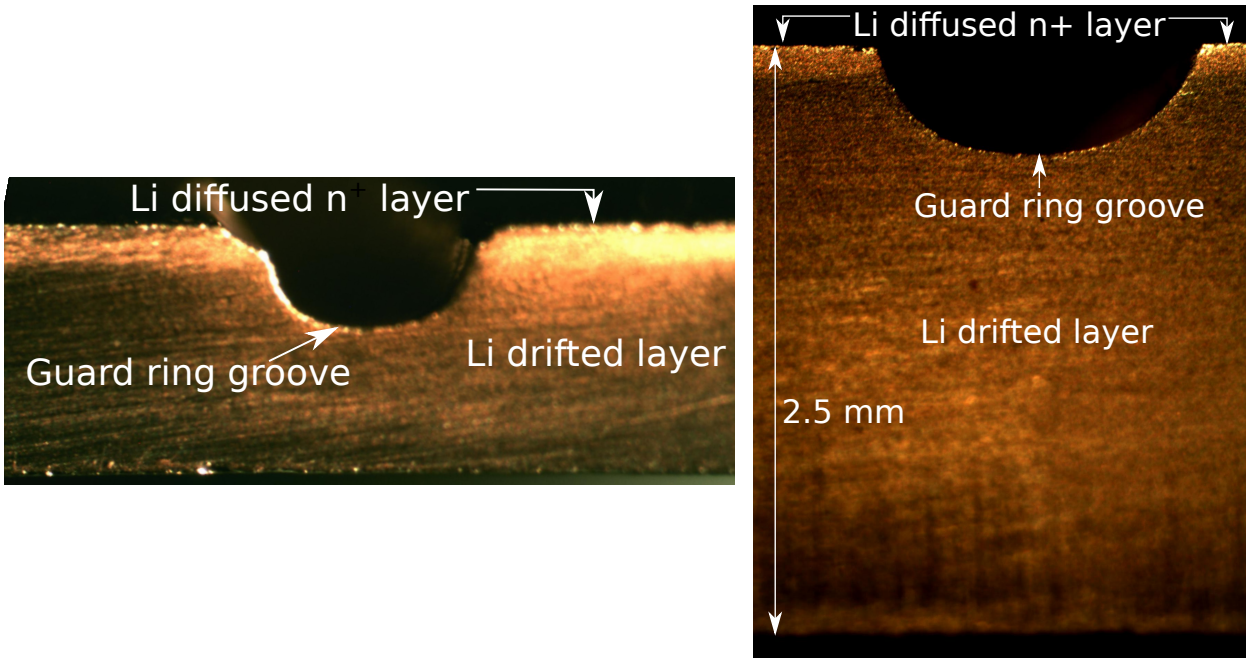

Figure 4.13: The cross section of two prototype detectors after copper staining. The heaviest copper plating indicates the n^+ Li diffused layer. The lighter copper plating illustrates the Li drifted region. Both detectors demonstrated $\lesssim 4$ keV energy resolution at the optimal peaking time, despite the rounded groove shape. *Left:* TD0043, fabricated at Columbia using the prototype fabrication protocol. *Right:* Sh0036, fabricated by Shimadzu using the mass-production fabrication protocol.

4.2.2.6 Strip segmentation

There were a few key considerations when determining the how to segment the detector's active area to the GAPS requirements. Segmenting strips necessarily removes active material from the bulk of detector, so it is preferable to have fewer, narrower, shallower grooves for the sake of detector efficiency (see Sec. 4.1.2). The position resolution of the detector depends on the size, and hence the number, of the strips that are segmented into the wafer. Additionally, limitations on the readout chain's input current and capacitance determine the size of the strips, since a strip's capacitance and bulk leakage current are proportional to the area of the strip.

Both 4- and 8-strip detector geometries were developed in prototype mass-production work. The 8-strip detector geometry was selected for the GAPS flight as it offers several advantages. The smaller strip area results in smaller per-strip leakage current and capacitance, two of the dominant contributions to the overall noise (See Sec. 5.3.3 and Eq. 5.1). 8-strip detectors with per-strip

leakage current <5 nA can meet the energy resolution requirement using a custom ASIC for pulse shaping and detector readout. The ASIC requires less power than a discrete-component design, reducing the thermal load on the cooling system and enabling the detectors to operate at lower temperatures. Additionally, the 8-strip design provides better particle tracking performance, as it delivers finer spatial resolution and its compatibility with ASIC readout reduces the amount of passive material in the tracker.

4.3 Conclusions

Based on the prototype fabrication work, large-area Si(Li) detectors satisfying the unique performance requirements of the GAPS experiment have been developed in partnership with Shimadzu Corporation and validated by the GAPS collaboration. A schematic of the GAPS flight-geometry detectors is shown in Fig. 4.14. The mass-production procedure did not apply a passivation coating. To ensure the long-term stability of the detectors, I developed a surface passivation method, which is outlined in Chapter 5. For further details on the mass-production protocol and validation, see Refs. [166, 167].

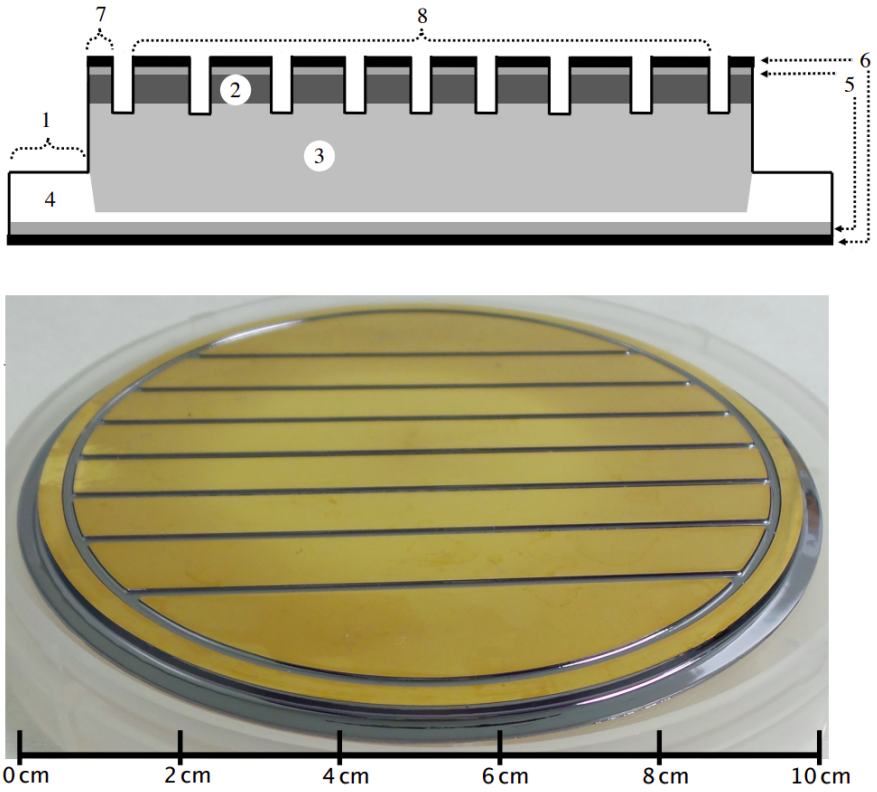

Figure 4.14: *Top*: Diagram of the cross-section of an 8-strip GAPS detector (not to scale). 1) The top hat geometry is defined using Ultrasonic Impact Grinding to remove the top perimeter of the Si wafer, leaving a ~ 1 mm deep, ~ 3 mm wide top hat. 2) Li ions in the $\sim 100\,\mu$m diffused n^+ layer. 3) Li ions drifted into p-type bulk to create compensated active volume. 4) The Si in the top hat 'brim' remains uncompensated. Electrodes consist of ~ 20 nm of Ni (5) and ~ 100 nm of Au (6). ~ 1 mm wide and ~ 0.3 mm deep grooves separate the guard ring (7) from the active area (8). *Bottom*: Photograph of 8-strip GAPS flight detector with ruler for scale. The groove and top hat surfaces require passivation to ensure long-term stability, as described in Chapter 5. Figure from Ref. [166].

Chapter 5: Si(Li) Detector Passivation

The most significant contribution I made to the GAPS hardware R&D was developing a procedure to passivate the Si(Li) detectors to protect them against environmental contamination. GAPS's particle identification capabilities hinge upon Si(Li) detectors that stably deliver $\lesssim 4$ keV (FWHM) energy resolution and <5 nA leakage current per strip. Although we found a method to successfully fabricate Si(Li) detectors that meet the GAPS requirements, the surface passivation of the detectors was an unsolved problem, and previous passivation attempts within the GAPS collaboration were unsuccessful. The unpassivated detectors delivered the requisite noise performance for the GAPS science goals, as presented in [166]. However, these measurements were made in a humidity-controlled lab environment, and we found that it was necessary to clean the detectors immediately before testing to achieve satisfactory results. A Si(Li) surface passivation technique was essential to ensure the success of the experiment; as such, the passivation R&D that I led was on the critical path of the GAPS experiment.

Si(Li) detectors have been used extensively on ground-based experiments, but have only been used twice in space-borne or balloon-borne experiments. Si(Li) detectors formed the X-ray spectrometer array on BBXRT [195], which flew on the space shuttle Columbia as part of the ASTRO-1 payload. These detectors required operation at almost liquid nitrogen temperatures with no reported passivation coating. The only previous balloon-borne experiment to use Si(Li) detectors is the prototype GAPS (pGAPS) experiment. Compared to the Si(Li) detectors mass-produced for the upcoming GAPS flight, the pGAPS Si(Li) detectors were fabricated using a different, more costly process, with much narrower grooves and less exposed silicon surface area. The pGAPS detectors were not passivated, but were held in an environmental enclosure to mitigate humidity, which is not feasible for the GAPS science flight due to the increased mass and complexity of the instrument. A major challenge in the passivation R&D was demonstrating a passivation method for space-based

applications, within the power and thermal requirements of the GAPS balloon payload. All previously reported Si(Li) passivation methods were demonstrated at cryogenic temperatures (e.g. [196, 197]) much lower than the GAPS tracker's operating temperature.

In developing a passivation method for the GAPS Si(Li) detectors, I reviewed the literature to select viable surface passivation candidates, designed application protocols to engender ease of application, and assessed the robustness of the passivation coatings to thermal and mechanical stresses. After finding a protocol that met the mechanical and thermal requirements, I applied passivation coatings to prototype GAPS detectors and further refined the application protocols to produce detectors with low leakage current and no degradation in energy resolution. After finding a passivation method delivering the requisite noise performance, I assessed the passivation coating's effectiveness in protecting the detector performance using accelerated lifetime testing and long-term stability monitoring.

This chapter reports on the R&D effort to develop and select a passivation method for the GAPS Si(Li) detectors. Si(Li) passivation techniques and GAPS requirements for selecting a passivation method are reviewed in Sec. 5.1. Adhesion and thermal testing of passivation candidates are described in Sec. 5.2. In Sec. 5.3, I outline the noise testing conducted to assess passivated detector performance. Accelerated lifetime testing and long-term monitoring of passivated detectors are reported in Sec. 5.4.

5.1 Si(Li) Passivation Review & Requirements

The GAPS flight-geometry Si(Li) detectors fabricated by Shimadzu Corp. are shown in Fig. 4.14. Detector performance is sensitive to the surface state of the exposed silicon of the grooves and top hat [173]. Specifically, the detectors are vulnerable to humidity and organic contaminants adsorbing onto the bare Si surface, and particulate matter (metal flakes from electrode, dust) that can fall into the grooves that segment the strips and guard ring. In order to achieve the GAPS goals on successive balloon flights, the detector performance must be stable over multiple years, so it was necessary to find a passivation method to protect the bare Si surfaces.

GAPS requires a passivation candidate that provides a barrier to environmental contaminants and is robust to thermal cycling and mechanical shock. The passivation coating must protect the detector from its ambient environment and prevent the deleterious effects of surface contamination which can produce high leakage current and 1/f noise. The passivation process must be performed at low enough temperatures to avoid Li diffusion effects. Specifically, the Li in the n^+ layer (Fig. 4.14, #2) must not extend below the detector grooves, which would effectively shunt the strips. Furthermore, the heating involved in the process must not cause significant decompensation of the positive Li ions in the p-type bulk, which could cause poor charge collection from the detector's active volume and increase the voltage required to deplete and operate the detector [173]. The passivation procedure must be adaptable to the geometrical constraints of GAPS, and be routinely applied by technicians to passivate the > 1000 detectors needed for the GAPS flight.

The most commonly used passivation material for silicon radiation detectors is thermally grown silicon dioxide. However, optimal SiO_2 layers are typically obtained at high temperatures ($T >$ 1000 °C) in atmospheres of dry oxygen, wet oxygen or steam. Due to the high temperatures required, SiO_2 was not explored. SiN, TaN, and TiN are often used as passivation coatings for Si substrates, and are typically produced using chemical vapor deposition (CVD), atomic layer deposition (ALD), or sputtering. These materials were not explored because the deposition techniques are not suitable for this work. CVD and ALD of SiN, TaN, and TiN typically require high substrate temperatures (> 300 °C), and sputtering is difficult to confine to the bare Si surfaces with high reproducibility [198–200]. Another common method for passivation of silicon detectors is silicon monoxide. However, high temperature treatments are often necessary to produce optimal SiO films. Furthermore, previous studies indicate that devices passivated with SiO have higher leakage currents and additional 1/f noise [201]. Thus SiO was not explored. Previous work demonstrated successful passivation of Si(Li) detectors using hydrogenated amorphous silicon (α-Si:H) [197]. α-Si:H is typically deposited by RF sputtering onto the detector. Amorphous silicon passivation was not explored because 1) the deposition process is complicated and reproducibility is poor, 2) the heat involved in the RF sputtering process can have an effect on Li compensation, and 3)

GAPS operates Si(Li) detectors at higher temperatures than this previous study, and in this temperature range α-Si coated detectors have reported higher leakage current characteristics than bare detectors [197].

Based on previous work, we chose to focus passivation R&D on polymers, specifically polyimides and Parylene-C [196]. Previous work reports successful passivation of Si(Li) detectors using polyimides [196, 202] and Parylene-C [196]. However, these detectors were operated at cryogenic temperatures much lower than the GAPS operating temperature, where different noise components dominate. Since the bulk leakage current drops exponentially with temperature, at LN2 temperature the leakage current is greatly suppressed, whereas at $\sim$–37 °C leakage current is a major driver on the detector noise. This work evaluates the viability of polyimide (PI) and parylene-C for passivation of Si(Li) detectors operated well above cryogenic temperatures. Adhesion and thermal testing of passivation candidates are described in Sec. 5.2. In Sec. 5.3, I outline the noise testing conducted to assess passivated detector performance. Accelerated lifetime testing and long-term monitoring of passivated detectors are reported in Sec. 5.4.

5.2 Mechanical Testing

5.2.1 Motivation

In order for a passivation method to be viable for the GAPS experiment, the passivation coating must adhere to the Si surfaces. Polymer coatings typically fail due to cracking and/or delamination, and these failures are directly related to the state of stress in the coating. The stress is due to a combination of the material properties of the coating, the processing conditions used to produce the coating, and the environment. If the stress exceeds the ultimate strength of the coating, the coating fails by cracking. If the stored energy in the coating exceeds the work of adhesion to the substrate, the coating can delaminate. Furthermore, a mismatch in the coefficient of thermal expansion (CTE) between the polymer and the substrate can lead to delamination/cracking during temperature cycling [203].

In order to test the mechanical properties of the coatings, adhesion and thermal testing was

performed. Adhesion performance was assessed using a 180° pull test, following the ASTM D3359 standard (see Sec. 5.2.3.1). Thermal testing consisted of cycling the detector between room temperature and −50 °C, and visually inspecting the polymer coatings under a microscope (see Sec. 5.2.4.1).

5.2.2 Sample Preparation

5.2.2.1 Wafer Cleaning and Preparation

Test-grade Si wafers[1] were prepared for adhesion testing and thermal cycling studies. For adhesion testing studies, adherence to the ASTM D3359 standard required applying the polymer to a planar wafer surface. For thermal cycling studies, it was desired to apply the polymer to a sample geometry that is analogous to a detector, specifically to grooves that have been chemically polished to smoothness. Therefore, grooves were cut into thermal cycling samples using Ultrasonic Impact Grinding (UIG) before cleaning, etching, and applying the polymer (see Table 5.1).

Thermal Sample UIG protocol: Using UIG, 1 mm wide, 350 μm deep grooves were cut into wafers. The groove depth and width were chosen to be analogous to the grooves segmenting the GAPS Si(Li) detectors. After UIG, the samples were cleaned ultrasonically in ACS-grade hexane to remove any wax and abrasive slurry from the UIG process. After ultrasonic cleaning with hexane, the following sample preparation was performed.

Thermal & Adhesion Test Sample Preparation: A 3-step cleaning process was performed on all wafers, consisting of ultrasonic cleanings in ACS-grade acetone, methanol and DI water. All samples were etched in an HNA (20 mL 49% Hydrofluoric Acid, 35 mL 60% Nitric Acid, 55 mL Glacial Acetic Acid) solution for 10 minutes. The etching process chemically polishes the Si surfaces, in particular the groove surfaces, which are left rough from the UIG process. With the etchant formulation used, a 10 minute etch was sufficient to produce the smooth and glassy groove surfaces typical of the GAPS Si(Li) detectors [167]. These smooth surfaces presented an adhesion challenge, as rougher surfaces are typically better for polymer adhesion. After cleaning and

[1] Test-grade Si wafers were procured from Addison Engineering and Wafer World

etching, Polyimide or parylene-C was applied to the wafers. Adhesion and thermal testing was performed for two polyimides and Parylene-C, with and without an adhesion promoter.

Table 5.1: Sample preparation and cleaning protocols for adhesion and thermal testing samples. 3-step cleaning entails ultrasonic cleaning a wafer in acetone, methanol, and DI for 5 minutes each, followed by drying with N2. Passivation coatings were applied to samples after etching.

Sample Code	UIG	Hexane	3-Step Clean	Etch
Adhesion	✗	✗	✓	✓
Thermal	✓	✓	✓	✓

5.2.2.2 Polyimide Application

Two polyimide (PI) precursors, VTEC PI-1388 and Ube U-Varnish-S, were used for the following studies. VTEC PI-1388 was selected due to its relatively low cure temperature ($\sim 250\,^{\circ}\text{C}$ for full imidization), while Ube U-Varnish-S was selected because its CTE is a close match to silicon (~ 3 ppm/°C). PI was applied by painting a polyimide precursor onto the wafer surface, and curing the polyimide in a Vulcan 3-1750 furnace. Each polyimide precursor is manufactured by combining a diamine and a dianhydride in a high polarity carrier solvent, typically N-Methyl-2-Pyrrolidine (NMP). The curing process drives the carrier solvent (NMP) out of the PI precursor, and facilitates the imidization (cyclization) of the diamine and dianhydride to form a PI. The final coating quality is extremely sensitive to the cure conditions, specifically the cure temperature and the heating rate. High cure temperatures ($T \geq 250\,^{\circ}\text{C}$) are desired to fully drive out the solvent and imidize the PI, but are not feasible for Si(Li) substrates because of high lithium mobility in silicon. To avoid movement of Li in the n^+ layer and compensated region, we did not use cure temperatures exceeding $210\,^{\circ}\text{C}$.

The following processing parameters were varied between PI samples: cure temperature, cure time, heating rate, use of silane adhesion promoter, and dilution of polyimide (see Table 5.2). These processing parameters were tuned to produce PI coatings robust to mechanical and thermal stresses. Previous Si(Li) passivation literature suggested 'soft-baking' the polyimide at $120\,^{\circ}\text{C}$ for 25 minutes [196, 202], which drives most of the solvent from the PI precursor, but leaves the

degree of imidization relatively low [196]. This soft-bake was used as a baseline cure condition, but further optimization was necessary based on adhesion and thermal testing results. 'Rapid curing', by placing a substrate with PI into a pre-heated oven set to the cure temperature, was compared to 'slow curing', by placing the substrate with PI into an oven at room temperature, and ramping the temperature to the cure temperature with a specified heating rate. For slow curing, a heating rate of 5 °C/min was used. This heating rate was chosen based on a previous study that found that heating rates < 10 °C/min lead to a higher degree of solvent removal and imidization [204]. To test the effect of silane on polyimide adhesion, γ-Aminopropyltriethoxysilane (APS), was applied to some etched wafers before applying the PI. A 0.1% (v/v) solution of APS was prepared in DI water and mixed for 1 hour on a hot plate with a magnetic stir bar. The APS solution was then applied by hand to the clean wafer surfaces, and baked on a hot plate at 85 °C for 30 minutes. This APS application protocol was based on a previous study, which demonstrated that APS increased the adhesion strength of the PI-silicon interface by a factor of 25 [203]. The PI precursor was either applied to the substrate 'neat' as it arrived from the manufacturer, or in a 1:1 dilution of PI precursor and pure NMP. Diluting the PI precursor solution decreases its viscosity, and enables application with a pipette.

5.2.2.3 Parylene-C Application

Parylene-C was applied in a vapor deposition chamber (SCS Labcoter 2, PDS 2010). The deposition process conformally coats the substrate with a Parylene-C film. For a given deposition chamber, the resulting film thickness is proportional to the mass of the dimer that is vaporized, so that for the chamber employed in this study 1 g of dimer resulted in a 1 μm thick coating. For all parylene-C samples, 5 g of dimer was used to produce 5 μm thick coatings. For some samples, a silane adhesion promoter (A-174) was applied before parylene-C deposition, to assess the silane's impact on coating adhesion. For adhesion and thermal testing studies, samples were conformally coated.

In preparation for noise testing, a method to mask the readout strips was developed. Selective

Table 5.2: PI application parameters were optimized to provide a coating with good adhesion and thermal properties. Initial samples (Sample code 1A) were 'rapidly cured' by placing them in an oven pre-heated to the cure temperature; however, it was quickly determined that 'slow curing' by ramping the oven temperature from room temperature to the cure temperature yielded better coatings. The final PI passivation protocol is highlighted in gray.

Sample Code	Cure Temperature	Cure Time	Heating Rate	APS	Dilute PI
1A	120 °C	25 mins	None	✗	✗
1B	120 °C	25 mins	5 °C/min	✗	✗
2A	180 °C	10 mins	5 °C/min	✗	✗
2B	180 °C	10 mins	5 °C/min	✓	✗
2C	180 °C	10 mins	5 °C/min	✗	✓
2D	180 °C	10 mins	5 °C/min	✓	✓
3A	180 °C	25 mins	5 °C/min	✗	✗
3B	180 °C	25 mins	5 °C/min	✓	✗
3C	180 °C	25 mins	5 °C/min	✗	✓
3D	180 °C	25 mins	5 °C/min	✓	✓
4A	210 °C	60 mins	5 °C/min	✗	✓
4B	210 °C	60 mins	5 °C/min	✓	✓

deposition by shadow masking and surface priming was attempted. For shadow masking, wafers were wedged in between two aluminum plates with machined cut-outs in the shape of the detector strips. After parylene-C deposition, the masks were cut away from the wafer using a sharp blade. For surface priming, a Micro-90 solution was painted onto the strip surface before parylene-C deposition. Micro-90 (Mfg: Cole-Parmer) is a soap-like solution that inhibits the Parylene-C adhesion to silicon, enabling us to peel the Parylene-C from the selectively primed surfaces [205]. After vapor deposition, the Parylene-C was mechanically removed from the electrodes by scraping and pulling with electrostatic discharge safe polyvinylidene fluoride tipped tweezers and the Micro-90 was cleaned from the detector surface using a methanol-soaked swab.

5.2.3 Adhesion Testing & Results

5.2.3.1 Adhesion Testing Method & Success Criteria

Adhesion testing was performed on test samples using an ASTM D3359 cross hatch adhesion test [206]. Using a razor blade, an X-shape cut was notched into the polymer coating. Elcometer

99 tape was pressed and smoothed down onto the coating surface, on top of the X-cut. Within 90 ± 30 seconds of applying the tape, the tape was pulled off, pulling it back upon itself at a 180° angle. After pulling, the coating was inspected for blemishes, and the tape was inspected for residue from the coating. The degree of polymer removal due to the pull test is graded on a 0-5 scale (5 indicates no polymer removed, 0 indicates a majority of the polymer was removed). In order to pass adhesion testing, a coating had to pass the 180° pull test with a score greater than four.

5.2.3.2 Adhesion Testing Results

No difference in adhesion strength was noted between neat and dilute samples of a given PI. PI samples without APS failed all adhesion tests, while PI samples with an APS pre-coating passed all adhesion tests, for both neat and dilute PI-1388 and U-Varnish-S. Without an APS adhesion layer, VTEC PI-1388 demonstrated stronger adhesion properties than Ube U-Varnish-S, as U-Varnish-S samples demonstrated a higher degree of PI removal after adhesion testing, regardless of dilution. All samples prepared with the final PI application protocol (Sample Code 4B) passed adhesion tests with a grade of 5.

Conformally coated parylene-C samples passed all adhesion tests, with and without a silane base layer. Thus, for noise testing, parylene-C samples were not prepared with a silane pre-coating, while PI samples were primed with an APS / DI solution.

5.2.4 Thermal Testing & Results

5.2.4.1 Thermal Cycling Testing Method & Success Criteria

Samples were thermal cycled in a custom testing setup that consisted of dry ice and EPS foam insulation. The testing setup was assembled to cycle the samples between room temperature and $-50\,^{\circ}\mathrm{C}$, with a ramp rate $< 5\,^{\circ}\mathrm{C/min}$. This temperature profile is consistent with the cooling used during laboratory calibration and expected during the LDB flight. During thermal cycling, the wafers were kept in polypropylene carrying cases, to avoid condensation on the wafer surfaces

when opening the chamber. After each thermal cycle, the coatings were inspected visually and under a microscope for cracking and delamination. A sample was required to survive twelve thermal cyclings without exhibiting delamination or cracking to be deemed successful.

5.2.4.2 Thermal Cycling Results

Parylene-C coatings were extremely robust to thermal stresses, and did not demonstrate any delamination or cracking through 12 thermal cycles.

Initially, PI samples were cured at 120 °C for 25 minutes (Sample Codes 1A-1B), based on previous successful passivation work [196, 202]. However, these samples exhibited delamination and cracking through successive thermal cyclings, and the cure temperature was subsequently increased to 180 °C (Code 2A-3D). PI applied 'neat' to the grooves demonstrated poor reproducibility, as the neat PI precursor had a high contact angle with the Si surface and aggregated during curing, leaving bare silicon surfaces exposed. Therefore, dilute PI application was selected for noise testing. Rapidly cured samples, cured in an oven pre-heated to the cure temperature, demonstrated higher failure rates than slow cured samples because slow curing promotes better solvent removal and prevents thermal shock in the coating [204]. The PI samples primed with APS and slow cured at $\geq$180 °C for $\geq$10 mins (Sample Codes 2D, 3D, 4B) were robust to thermal cycling (see Fig. 5.1).

5.3 Noise Testing

5.3.1 Motivation

After tuning the application protocols to produce coatings with acceptable adhesion and thermal properties (see Sec. 5.2), the passivation coatings were applied to Si(Li) detectors, and detector noise performance was assessed before and after passivation. The main requirement is that GAPS Si(Li) detectors must provide $\lesssim 4$ keV energy resolution to 20–100 keV X-rays. Calibration measurements are made using a discrete preamplifier, whereas during final calibration and the LDB flight a custom ASIC will be used [169]. Therefore, it is essential to understand the noise charac-

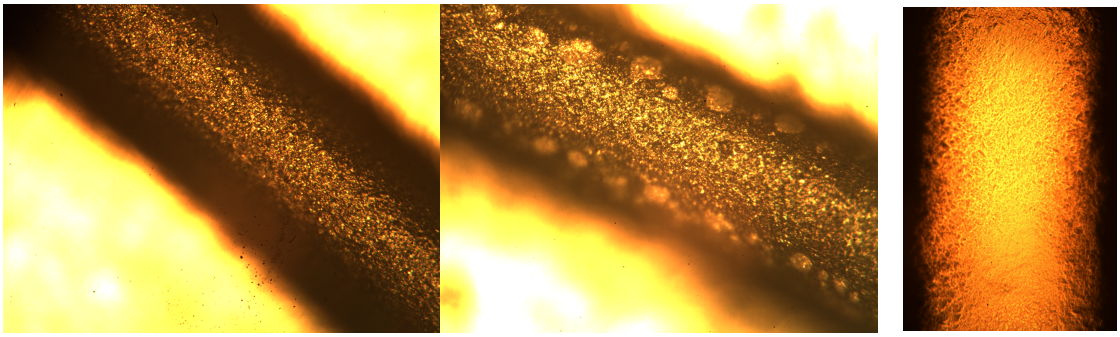

Figure 5.1: *Left/Center:* Microscope images of grooves of thermal test sample before (left) and after (center) two thermal cycles. After two thermal cycles, spots appeared at bottom of groove. These spots are indicative of delamination of the PI from the silicon surface, due to CTE mismatch. This sample was cured at 120 °C for 25 minutes, a cure cycle that was found to be insufficient to produce a robust coating. *Right:* Microscopic images of a PI coated groove, passivated using the final procedure. No delamination or cracking was observed after twelve thermal cyclings in PI coatings using the final passivation procedure.

teristics of each detector (leakage current, capacitance, resistance, etc.) to simulate detector energy resolution with the ASIC design parameters for the LDB flight. A noise model was used, and the noise model fit parameters were included in the success criteria, which are outlined in Sec. 5.3.3.

5.3.2 Detector Preparation

A detector's grooves and top hat were cleaned before passivation. The standard cleaning protocol consists of applying methanol to the tip of a cleanroom swab, and gently swabbing the detector's bare silicon surfaces. This cleaning protocol removes any particulate contamination from the surfaces and sets the surface state of the silicon to be lightly n-type. The cleaning must be performed in a low-humidity environment (<10% relative humidity), specifically a N2 purged glove box, to yield consistently good results. Detectors fabricated in-house at Columbia University (TDxxxx) and at Shimadzu (Shxxxx) were passivated and tested. There are some differences in the fabrication protocols [165, 167]. Typically, the in-house detectors were used to demonstrate proof of concept, whereas the success criteria were ultimately applied to Shimadzu detectors.

Parylene-C and PI passivation coatings were applied to in-house detectors as proof of concept. Parylene-C was applied using Micro-90 to mask the electrodes and enable readout (see

Sec. 5.3.4.1). PI was applied using an APS adhesion promoter and a diluted VTEC PI-1388 polyimide precursor solution. The diluted PI was degassed under rough vacuum for 10 minutes prior to application. For initial testing purposes, the APS and PI cure conditions were varied to produce optimal passivated detector noise performance. The minimal cure temperature and time that produced coatings with acceptable adhesion and thermal properties were 85 °C for 30 minutes for APS curing, and 180 °C for 10 minutes for PI curing (see Sec. 5.2.2.2). These cure conditions were compared to higher temperature cures that were chosen to exceed the boiling point of the solvent in the APS and PI precursor solution. To improve the solvent removal and degree of PI imidization, PI was cured at 210 °C for 1 hour, and APS was cured at 110 °C for 20 minutes. Based on the initial testing results, where lower temperature cures resulted in degraded leakage current and energy resolution, the final PI passivation protocol used the 110 °C APS cure and 210 °C PI cure (see Sec. 5.3.4.1).

Temperature testing was conducted to ensure that the substrate temperature reached >100 °C during the APS cure and >204 °C during the PI cure. A dummy substrate was placed in the oven and on the hot plate used for curing passivation coatings. Thermocouples were used measure the substrate's surface temperature. A MicroDAQ USB-TEMP temperature data acquisition module was used to log the substrate temperature at each second during the cure cycles. During APS curing, the substrate equilibrated to ∼ 110 °C after 10 minutes. In the oven, the substrate reached ∼ 210 °C at the end of the 1 hour cure cycle, and the temperature ramp rate was kept below 5 °C/min to avoid thermally shocking the PI coating.

5.3.3 Noise Testing Setup

To assess the success of a passivation coating, room temperature leakage current and cold (∼ –37 °C) spectral measurements were performed on a detector before and after applying the passivation coating. Per-strip leakage current was measured directly using a Keithley 487 Picoammeter / Voltage source with all other strips and guard ring grounded. The Keithley 487 ramped the voltage applied to the *p*-side from 0 V to −400 V in 25 V increments while measuring the resulting leakage

current from a given strip on the n^+ side.

Energy resolution measurements were performed at MIT in a custom vacuum testing chamber outlined in [166] or in a SUN EC13 Temperature Chamber. Both chambers were cooled using LN2. To avoid condensation on the detector surface, the custom chamber was pumped to ~0.1 Torr during operation, whereas the SUN chamber was purged with nitrogen. Detector temperature was monitored using a calibrated diode, and spectral measurements were recorded in the typical operating temperature range, $-35\,^{\circ}\mathrm{C} > \mathrm{T} > -45\,^{\circ}\mathrm{C}$. In the chambers, the detectors were uniformly irradiated with a 100 µCi ^{241}Am radioactive source. During operation, the p-side of a detector was biased to −250 V using a Tennelac 953 HV supply in the vacuum chamber, and a CAEN N1471 in the SUN chamber. The signal was readout from the n^+ side by a custom 8-channel discrete-component charge-sensitive preamplifier board, which was pressure mounted to the strips via spring-loaded pins. In the vacuum chamber, signal from one preamplifier was processed by a Canberra 2020 Spectroscopy Amplifier at various peaking times and digitized by an Ortec Ametek Easy MCA module. In the SUN chamber, signals are shaped and digitized using a CAEN N6725 digitizer.

A noise model is used to characterize each detector, identify each noise source that contributes to the overall energy resolution, and determine if the noise arises from intrinsic detector performance or from the readout chain [166, 207]. The equivalent noise charge (ENC) from the detector and readout chain, and the FWHM energy resolution can be estimated as follows [173, 208]:

$$ENC^2 = \left(2eI_{leak} + \frac{4kT}{R_p}\right)\tau F_i + 4kT\left(R_s + \frac{1}{g_m}\right)\frac{C_{tot}^2}{\tau}F_v + A_f C_{tot}^2 F_{vf} \tag{5.1}$$

$$FWHM = 2.35\epsilon\frac{ENC}{e} \tag{5.2}$$

In Eqs. (5.1) and (5.2), e is the electron charge, k is the Boltzmann constant, ϵ is the ionization energy of silicon (3.6 eV per electron-hole pair), R_p is the parallel resistance ($R_p \sim R_g$, where R_g is the gate resistance of the FET), and g_m is the FET's input transconductance. The dependence of

each noise term on the pulse shaping system is parameterized by the form factors F_i, F_v, and F_{vf}, and are calculated as $F_i = 0.367$, $F_v = 1.15$, and $F_{vf} = 3.287$ for the Sin^4 semi-Gaussian Canberra shaper used in this work, following [166, 209].

The most relevant parameters in this study are I_{leak}, C_{tot}, A_f, and R_s, which are fit to characterize the noise performance of the detector. I_{leak} is the temperature-dependent per-strip leakage current. The total input capacitance (C_{tot}) is the sum of all parallel capacitances including the individual strip capacitance (C_{det}), the capacitance of the FET input stage ($C_{FET} \sim 10\,\text{pF}$), the interelectrode capacitance of adjacent strips and the grounded guard ring (C_{int}), and any stray capacitance ($C_{stray} \sim 5\,\text{pF}$). R_s is the sum of all series resistances that can arise from the detector and preamplifier mounting. A_f is the coefficient of 1/f noise which may arise from surface effects or (ideally just) preamplifier noise.

Energy resolution was measured as a function of peaking time for detectors at a given operational temperature before and after applying a passivation coating. The peaking time (τ) vs. energy resolution (FWHM) data is used with Eq. (5.2) to find a best fit for I_{leak}, C_{tot}, A_f, and R_s while keeping the other noise model parameters fixed. Since, C_{tot}, A_f, and R_s are degenerate, they cannot be fit simultaneously, so an iterative approach is used, which is described in [166]. The fitted values for each strip are compared before and after passivation, and we assess the success criteria based on the overall energy resolution and fit parameters.

The following success criteria were imposed on passivated detector energy resolution and noise model fit parameters:

1. FWHM energy resolution at optimal peaking time $\lesssim 4\,\text{keV}$
2. $I_{leak} \lesssim 4\,\text{nA}$
3. $A_f \lesssim 2.5 \times 10^{-13}\,\text{V}^2$.

The fitted I_{leak} and A_f cutoffs were chosen based on measurements of unpassivated GAPS Si(Li) detectors reported in [166] that found detectors with noise parameters below these cutoffs satisfy the GAPS requirements.

5.3.4 Noise Testing Results

5.3.4.1 Passivation Protocol Optimization

Before passivating Shimadzu flight detectors, in-house fabricated detectors were passivated and tested to validate a passivation method that passed adhesion and thermal testing. Parylene-C was applied to an in-house fabricated Si(Li) detector, TD0087. After applying the parylene-C coating using selective deposition with Micro-90, the detector's leakage current saturated the picoammeter's current limit (2.5 mA) at ~30 V. Since the leakage current from the active area was <1 μA during this test, it indicated a large leakage current through the guard ring due the passivation coating. Based on this result and concerns about the reproducibility of the coating method, Parylene-C was not further explored.

An in-house fabricated Si(Li) detector, TD0093, was passivated with PI cured at 180 °C for 10 minutes. After passivation, the detector's leakage current was an order of magnitude higher than its pre-passivation value at room temperature, −36 °C, and −48 °C. Re-baking the detector at 180 °C for 25 minutes reduced the detector leakage current to its pre-passivation values. Therefore, we determined that the elevated leakage current was caused by an insufficient cure cycle that did not drive out the solvent and imidize the PI precursor, and all subsequent detectors passivated with PI were cured at 210 °C for 1 hour. The heating involved in this cure cycle did not significantly affect the detector's lithium distribution, and did not degrade detector energy resolution when operated at 250 V. We note that the voltage required to deplete and operate the detector increases from ~80 V before passivation, to ~150 V after passivation; however, this is acceptable since the detectors are operated at 250 V.

To isolate the effects of the APS application procedure, APS was applied to an eight-strip Shimadzu detector, Sh0075, following the protocol used for thermal and adhesion samples. After curing at 85 °C for 30 minutes, the detector's spectral performance degraded due to 1/f noise (see Fig. 5.2). Re-heating the detector at 110 °C for 20 minutes improved the detector's spectral performance so that no degradation was noted compared to pre-passivation measurements. Therefore,

the 85 °C cure was deemed insufficient to dry the APS solution, and APS was cured at 110 °C for all subsequent passivations.

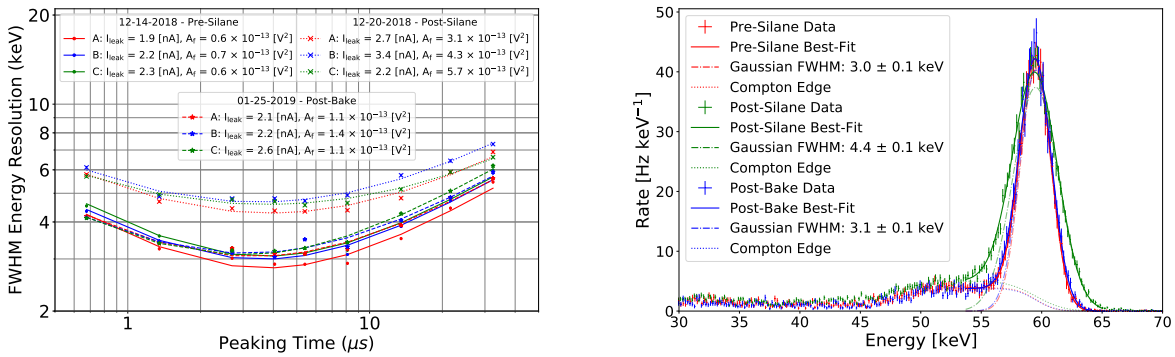

Figure 5.2: *Left:* Energy resolution (FWHM) as a function of peaking time for three strips of the 8-strip detector Sh0075, measured at ∼ –37 °C. Baseline measurements were taken after cleaning the detector strips as outlined in Sec. 5.3.2. Post-silane measurements were taken after applying the APS adhesion promoter to the detector's grooves and top hat and curing on a hot plate at 85 °C for 30 minutes. After this APS cure cycle, the detector's energy resolution degraded and 1/f noise component increased. After re-baking the detector at 110 °C, the energy resolution and 1/f noise component recovered to pre-passivation levels. *Right:* Corresponding spectra for strip A of Sh0075 at the optimal peaking time (4 µs). Each spectra shows a photopeak and a low-energy tail. The data is fit to a Gaussian (dash-dotted) plus an error function (dotted) as discussed in [166]. Pre-silane and post-bake measurements were performed using a preamplifier with higher attenuation than the preamplifier used for post-silane measurements, so the post-silane count rate was scaled to make the difference in spectral shape more evident.

Based on these results, the PI passivation protocol was refined by increasing the APS and PI cure temperatures. The final PI passivation protocol is as follows:

- Mix 0.1% (v/v) solution of APS in de-ionized water for 1 hour
- Apply APS solution to detector grooves and top hat using pipette
- Bake detector in open glass petri dish on hotplate at 110 °C for 20 minutes
- Let detector cool, mix 1:1 dilution of PI precursor in NMP by hand with teflon applicator
- Degas PI in rough vacuum for 10 minutes to remove bubbles
- Apply PI precursor solution to detector grooves and top hat using pipette
- Cure in oven at 210 °C set point temperature for 1 hour with 5 °C/min heating rate
- After 1 hour at 210 °C set point, prop oven open to decrease temperature gradually
- When oven temperature reaches 70 °C (∼ 40 min), remove detector and place in dry box

5.3.4.2 Energy Resolution Testing and Large-Scale Validation

Detectors passivated with the final PI passivation protocol demonstrated good leakage current characteristics and indicated no degradation in X-ray energy resolution. The optimized passivation procedure was applied to a batch of 12 eight-strip flight detectors. Given time-constraints, these detectors were not tested for energy resolution before passivation, and not all strips were measured after passivation. At least four strips per detector were randomly sampled for post-passivation energy resolution measurements. Each measured detector strip had $\lesssim 4\,\mathrm{keV}$ energy resolution, and was determined to have suitably low 1/f noise (see Fig. 5.3). A small fraction of detector strips demonstrated fitted leakage current above the acceptance criteria, but were deemed successful based on their energy resolution and 1/f noise.

5.4 Effectiveness in Protecting Detectors

5.4.1 Motivation

GAPS is scheduled for three LDB science flights. Therefore, the mission's success relies on passivated detector performance remaining stable for several years. Even with a passivation coating, precautions are taken to ensure that detectors have minimal exposure to humidity and organics. For long-term storage, detectors are stored in a vacuum sealed antistatic bag with desiccant in a freezer, which has been demonstrated to produce an environment with <5% relative humidity (RH) at $-20\,^{\circ}\mathrm{C}$. During routine calibration and processing, lab spaces are maintained at $< 30\%$ RH at room temperature. During integration, the modules will be purged continuously with N2 to mitigate humidity and organic outgassing.

Accelerated lifetime testing was conducted to assess the PI passivated detector's robustness to contamination from humidity (see Sec. 5.4.2) and organic materials (see Sec. 5.4.3) used in detector assemblies. Furthermore, a long-term detector performance monitoring program is ongoing to track detector performance over time (see Sec. 5.4.4).

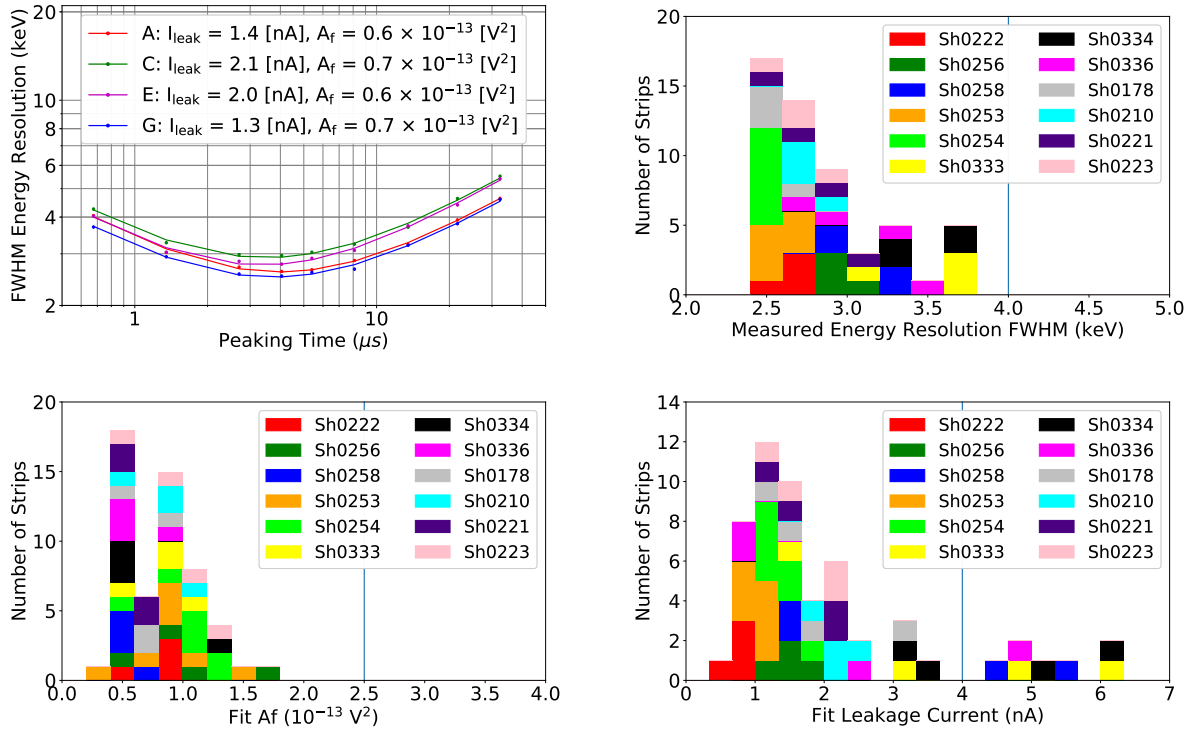

Figure 5.3: *Top Left:* Energy Resolution (FWHM) as a function of peaking time for strips A, C, E, and G of Sh0221, a GAPS flight detector after passivation with VTEC PI-1388 polyimide using final protocol (see Sec. 5.3.2). Measurements were performed at −37 °C in the vacuum testing setup outlined in Sec. 5.3.3. *Top Right:* Energy resolution (FWHM) at the optimal peaking time after passivation for each measured strip of the 12 eight-strip flight detectors, using optimized passivation procedure. *Bottom Left:* Best-fit A_f component (V^2) of the $1/f$ noise for the strips of these detectors. *Bottom Right:* Best-fit leakage current (nA) for the strips of these detectors.

5.4.2 Accelerated Humidity Exposures

5.4.2.1 Success Criteria

Acceleration factors were computed by examining water vapor barrier penetration. The acceleration factor for humidity exposures is proportional to the number of water molecules hitting the detector surface at a given temperature and humidity, and can be expressed as [210]:

$$a = \frac{hP_w^v(T)}{h_0 P_w^v(T_0)} e^{-\frac{E_p}{R}(\frac{1}{T}-\frac{1}{T_0})} \tag{5.3}$$

where $P_w^v(T)$ is the water saturation vapor pressure, E_p is the activation energy for water diffusion into the polymer film, and R is the gas constant. T and h are the temperature (Kelvin) and RH under test conditions, while T_0 and h_0 are the temperature (K) and RH during normal field use. $E_p \simeq 11$ kJ/mol was used to compute the humidity acceleration factor, based on an empirical measurement of water diffusion into polymer films [211].

The success criteria for accelerated humidity exposures was motivated by the foreseen processing and storage conditions. To be deemed successful, a detector was required to undergo humidity exposures equivalent to 14 days at 50% RH. This exposure is equivalent to ~1 month of active work on a detector in typical lab conditions (~ 30% RH at room temperature), and ~20 years in a desiccated bag in a freezer at ~ –20 °C.

5.4.2.2 Experimental Setup

Accelerated humidity exposures were performed by placing a detector in an airtight chamber with a small water dish. The entire chamber was heated to 60 °C for 3 hours, and the humidity in the chamber increased to ~80% RH. Each exposure is equivalent to ~ 2 days at 23 °C and 50% RH. The chamber temperature and humidity was measured each minute using a logging hygrometer, and the temperature and humidity data was used to compute the acceleration factor and equivalent time of the exposure.

5.4.2.3 Results

Three detectors fabricated in-house were subjected to humidity exposures. Two detectors (TD0090 and TD0093) were passivated following the passivation protocol (see Sec. 5.3.4.2) before being exposed to humidity. One detector (TD0094) was left unpassivated as control. Detector room temperature leakage current was measured before and after exposure to humidity. The passivated detectors demonstrated no degradation in leakage current, while the unpassivated detector's leakage current increased significantly (see Fig. 5.4).

Furthermore, a passivated 8-strip GAPS flight detector, Sh0070, was subjected to similar hu-

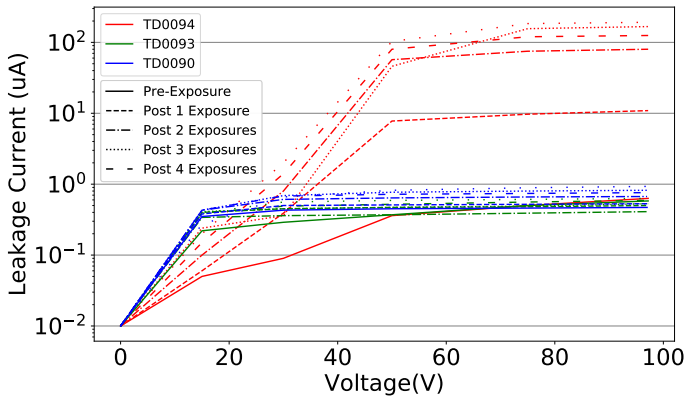

Figure 5.4: Room temperature leakage current measurement of TD0090 (passivated), TD0093 (passivated), and TD0094 (unpassivated) through successive humidity exposures. Solid lines indicate leakage current before exposure to humidity, whereas dashed and dotted lines indicate successive humidity exposures. In this test, the total accelerated exposure was comparable to 7 days at 50% RH during field use, following Eq. (5.3). The passivated detector performance was stable through all exposures, while the unpassivated detector leakage current degraded significantly.

midity testing and was resilient against degradation due to humidity. This detector's leakage current was stable through humidity exposures equivalent to 14 days at 50% RH at room temperature.

5.4.3 Accelerated Organics Exposures

5.4.3.1 Success Criteria

Once integrated, the detector modules consist of four eight-strip Si(Li) detectors, an ASIC board, and fluorosilicone and G10 detector retaining parts fastened into an aluminum frame. The modules are sealed on both sides with an aluminized polypropylene window. In this study, detectors were exposed to outgassing from organics from materials that are constituent in a detector module.

Assuming diffusion as the dominant source of outgassing, the outgassed material at a time t is given by:

$$\Delta m(t,T) = f_m m_0 \sqrt{\frac{t}{t_r}} e^{\frac{E_a}{R}\left(\frac{1}{T_r}-\frac{1}{T}\right)} \tag{5.4}$$

where m_0 is the initial mass of the organic, E_a is the activation energy of the organic material,

R is the gas constant, and f_m is the fractional mass loss at a reference time (t_r) and temperature (T_r) [212]. Since we are mainly concerned with finding an acceleration factor, we note that the total mass loss (TML) $\propto t^{\frac{1}{2}} e^{-\frac{E_a}{RT}}$, where T and t are the accelerated exposure temperature and time during lab testing, and T_0 and t_0 are the temperature and time of exposure during normal field use. An acceleration factor for the lab exposures to organics can be found using the scaling relation:

$$a \equiv \frac{t_0}{t} = e^{\frac{2E_a}{R}(\frac{1}{T_0}-\frac{1}{T})} \tag{5.5}$$

In this study, detectors were exposed to a FR-4 circuit board, G10, fluorosilicone, and vacuum grease that will be used to install and seal the detector modules. The activation energies for these materials are not well measured, so to compute an acceleration factor, $E_a = 10\,\text{kJ/mol}$ was used, based on the typical activation energy for diffusion driven outgassing [212]. To mitigate outgassing, the modules are equipped for N2 purge, however N2 purge is not always feasible. The success criteria was motivated by the approximate amount of time that detector surfaces will be exposed to organics when not being purged. Detectors were exposed to organics equivalent to > 6 months of field use at room temperature, and were required to demonstrate no degradation in leakage current or energy resolution to be deemed successful.

5.4.3.2 Experimental Setup

Accelerated organics exposures were performed by placing a detector in a chamber next to a hot plate, and heating the organic material on a hot plate to increase its TML. For each exposure, the organic material was heated to ~70 °C for 6 hours, an equivalent exposure of ~30 days, using Eq. (5.5). Before and after each exposure, the detector's room temperature leakage current was measured. After achieving an equivalent exposure >6 months, the detector was sent to MIT for energy resolution testing.

5.4.3.3 Testing

Two passivated 8-strip detectors, Sh0079 and Sh0161, were selected for exposure to organics. Both detectors demonstrated no change in room temperature leakage current characteristics through exposures to organics equivalent to >6 months field exposure to the materials in the GAPS detector modules at room temperature. After exposures, X-ray energy resolution was measured and no increase in energy resolution or 1/f noise was observed (see Fig. 5.5).

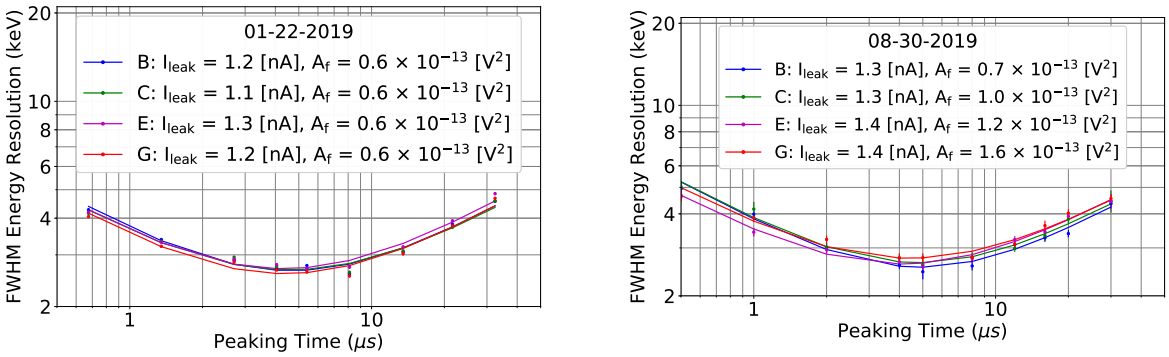

Figure 5.5: *Left:* Energy resolution (FWHM) as a function of peaking time for strips B, C, E, and G of Sh0079, an eight-strip flight detector. Measurements were performed at ∼–35 °C immediately after passivation. *Right:* Energy resolution (FWHM) as a function of peaking time for same strips of Sh0079, after organics exposures equivalent to 6 months of field use. No degradation in noise performance was observed, and the fit parameters of the noise model were consistent.

5.4.4 Long-Term Monitoring

A long-term monitoring program is ongoing to ensure detector stability. Over the course of a year, the energy resolution of passivated GAPS flight detectors was measured in the SUN chamber. Between measurements, detectors were stored in a dry box or in a vacuum-sealed bag with desiccant in a freezer at ∼–20 °C. No detector degradation has been noted over the course of twelve months (see Fig. 5.6).

In conjunction with accelerated lifetime testing, the results of the long-term monitoring program are promising. They indicate that storing the passivated GAPS flight detectors in a vacuum sealed bag with desiccant in a freezer at ∼–20 °C is sufficient to maintain stable detector perfor-

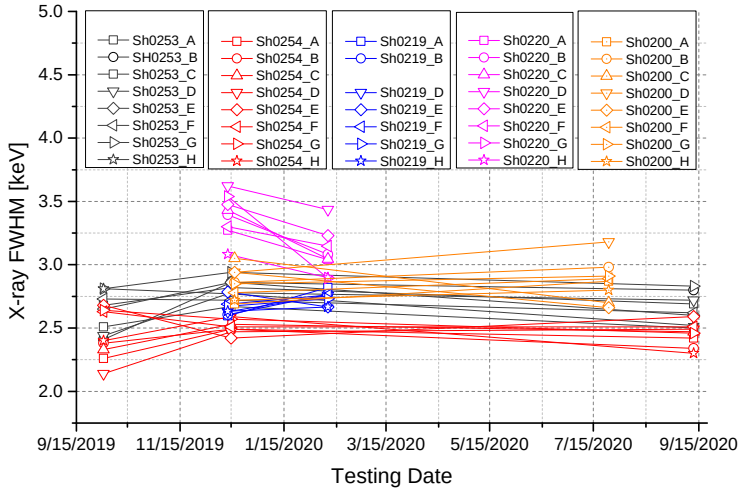

Figure 5.6: Energy resolution (FWHM) at optimal peaking time for strips of five GAPS flight detectors, measured on different dates as part of long-term detector stability monitoring program. Passivated Si(Li) detectors demonstrate stable performance over year-long timescales.

mance for the lifetime of the GAPS experiment. Moreover, it is not necessary to store these Si(Li) detectors under bias to mitigate Li re-distribution, which simplifies the long-term storage scheme needed to maintain detector performance. More details will be presented elsewhere.

Chapter 6: Detector Response Simulation

As discussed in Sec. 4.1.4, there are several effects that can cause "ballistic deficit" in the energy recorded by a semiconductor radiation detector, including incomplete charge collection and pulse shaping effects. Understanding the detector performance at each position in the tracker is crucial to properly interpret events in the GAPS instrument. As outlined in Sec. 5.3, GAPS Si(Li) detector calibration consists of measuring the spectral response of a detector to a ^{241}Am or ^{109}Cd source. While the ^{241}Am (^{109}Cd) source produces 59.5 keV (88 keV) gamma-rays, the measured spectral line width from a detector strip is not always symmetric and it is common to observe a 'low-energy tail' below the line energy. The low-energy tail is ideally only due to photons that are not fully absorbed in the detector volume due to Compton scattering, but it also could be due to ballistic deficit.

Fig. 6.1 shows an example of the spectral response of a GAPS Si(Li) detector strip during calibration. The low energy feature to the left of each photopeak — called the 'low-energy tail' — is primarily due to Compton scattering from the surrounding materials. The minimum scattered energy $E_{\gamma'}$ for a 59.5 keV photon is 48.3 keV — corresponding to a 180° backscatter. For the 59.5 keV source, the low-energy tail clearly cuts off at ~48 keV, which suggests that the feature is largely due to photons that Compton scatter once in passive material and then are fully absorbed in the detector volume. However, a contribution from charge trapping to this feature cannot be ruled out by visual inspection.

The main objective of this study is to investigate whether the low-energy tail observed in the GAPS Si(Li) detector spectra was due to solely to Compton scattering, or if there was also a contribution from ballistic deficit. To disentangle these two effects, I developed a simulation and analysis framework to model the GAPS Si(Li) detector's spectral response during calibration. The simulated spectra are compared to experimental spectra to identify the contributing factors to the

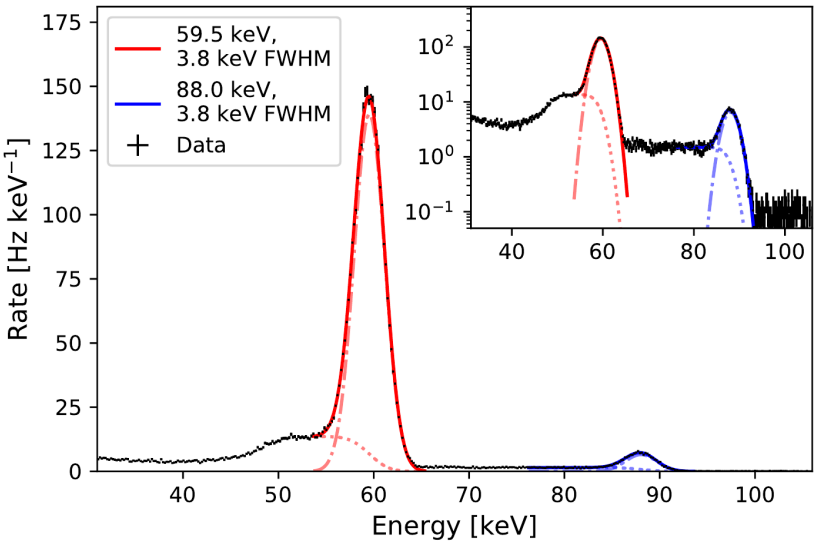

Figure 6.1: Example spectrum of ^{241}Am and ^{109}Cd, recorded with one strip of GAPS Si(Li) detector Sh0025 at –35 °C, processed with 4 µs peaking time. The data show each photopeak together with a low-energy tail (modeled in this figure by the dotted lines). Simulation studies presented in this chapter aim to identify contribution of Compton scattering and charge trapping to the low-energy tail. Figure from Ref. [166].

low-energy tail. In this work, only the ballistic deficit due to incomplete charge collection is modeled, and the deficit due to the dead layer will be included in future work. Section 6.1 describes the simulation and analysis tools used to produce MC spectra. Section 6.2 compares the simulated and experimental spectra. Section 6.3 summarizes the conclusions and planned next steps for this work.

6.1 Simulation Framework

In order to isolate the root cause of the low-energy tail of the photopeak in GAPS Si(Li) detectors, I developed a `Geant4`-based simulation and analysis framework to model the GAPS Si(Li) detector and calibration chamber geometry, and produce Monte Carlo (MC) spectra. `Geant4` [213] encodes the physics of the photon interactions (absorption and scattering cross sections) in the detector and passive material (Fig. 4.2), providing the true spectrum of the energy depositions in the detector before convolving the detector response. Since a large contribution to the low-energy tail comes from photons that Compton scatter once in passive material before

being fully absorbed in the detector, it is important to faithfully model the chamber geometry, particularly the high-Z materials. The veracity of the MC truth in the simulation is mainly limited by the accuracy of the modeling of the detector and chamber geometry, which was implemented judiciously to provide an accurate representation of the experimental setup.

6.1.1 Simulation Tools

To simulate the irradiation of the detector by a radioactive source during calibration, a 3D model of the GAPS Si(Li) detector and calibration chamber was built in `Geant4` [214]. The simulated detector matches the GAPS flight detector geometry, including eight strips, a guard ring, and a top hat. The chamber geometry includes the Fe and Al chamber walls, detector mount, cooling plate, preamplifier, Faraday cage, and X-ray source. To replicate the ^{241}Am source used during calibration, 10^8 monoenergetic 59.5 keV X-rays are generated isotropically from a source centered above the detector at a distance of 5.5 cm from the top surface of the detector. A visualization of the detector and chamber geometry in `Geant4` is shown alongside a photograph of a detector mounted in the chamber in Fig. 6.2.

To estimate the charge collection efficiency in the Si(Li) detectors, a 2D electrostatic model of the GAPS Si(Li) detectors was constructed using `KDetSim` [215]. `KDetSim` is a software package that uses the finite-difference method to solve Poisson's equation and simulate charge transport in semiconductor detectors. The simulated geometry was designed to match a 2D cross-section of the GAPS flight detectors' active area and guard ring. In particular, the measured rounded profile of the grooves that segment the readout strips and guard ring was implemented (see right panel of Fig. 4.13) to evaluate the impact of this unique geometry on charge collection efficiency.

Based on the input detector geometry, space charge density, and bias voltage, `KDetSim` solves Poisson's equation to calculate the electric potential and field in the detector bulk and the weighting potential and field for each electrode. The weighting field is the electric field that would exist at charge q's instantaneous position $\mathbf{x}$ with (1) the readout electrode at unit potential, (2) all other electrodes at zero potential, and (3) all other charges removed from the detector bulk. Following the

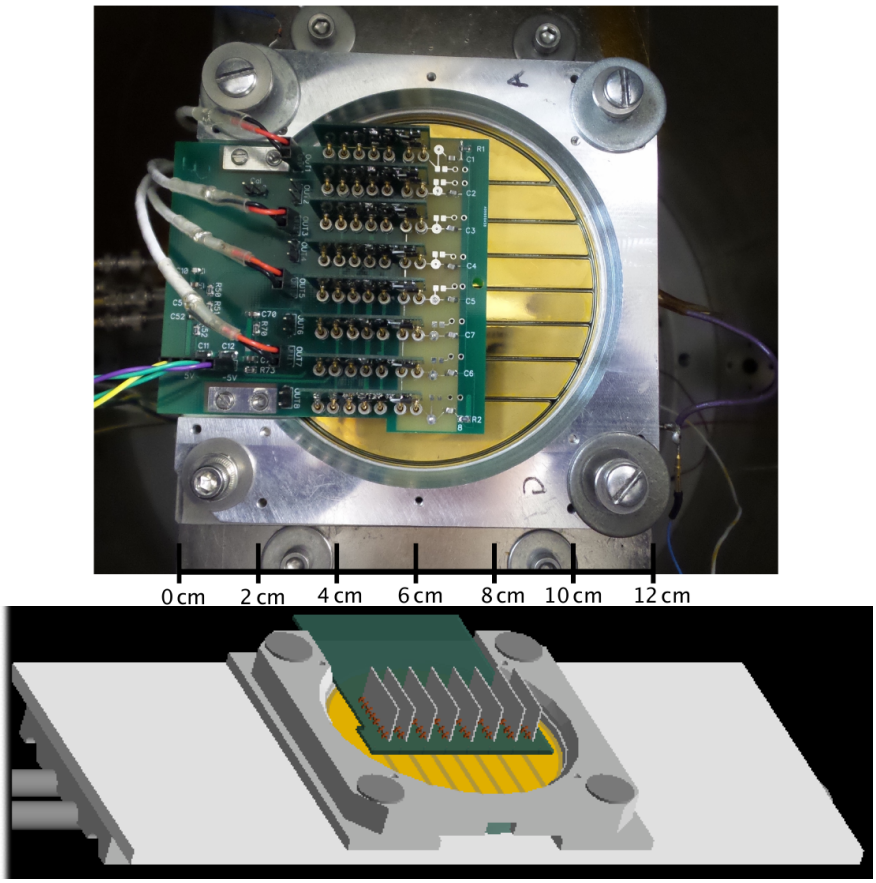

Figure 6.2: *Top:* An eight-strip detector mounted in the calibration chamber (Faraday cage not shown to display detector, preamplifier, and mount) for energy resolution measurements. *Bottom:* Simulated geometry of GAPS Si(Li) detector, preamplifier, and cooling plate in `Geant4`. The Faraday cage and the chamber's top, bottom, and sidewalls are not shown.

Shockley-Ramo theorem, the current i induced on electrode j are calculated using the weighting field $\mathbf{E_j}$ as [179]

$$i = q\mathbf{v} \cdot \mathbf{E_j}(\mathbf{x}) \tag{6.1}$$

where $\mathbf{v}$ is the instantaneous velocity of charge q.

To determine the electric and weighting field, Poisson's equation was solved on a two-dimensional discrete uniform mesh of size $\Delta x = 50\,\mu\text{m} \times \Delta z = 25\,\mu\text{m}$. The weighting field was calculated for all eight strips individually, and was used to determine the induced charge on each electrode during charge transport following Eq. (6.1).

The effective space charge density eN_{eff} used in the source term of Poisson's equation was

determined based on C-V measurements that found an empirically measured depletion voltage $V_d \simeq 100\,\text{V}$. By solving Eq. 4.8 for eN_{eff}, the effective space charge density is

$$eN_{eff} = \frac{2\epsilon_0\epsilon_{Si}V_d}{W^2}, \tag{6.2}$$

where W is the detector thickness and ϵ_{Si} is the DC dielectric constant of silicon. Using the GAPS Si(Li) detector's thickness and depletion voltage, Eq. (6.2) yields $N_{eff} \approx 2{\times}10^{10}\,\text{cm}^{-3}$. By inspection of the resulting electric field, we confirmed that the simulated detector was fully depleted at 100 V for $N_{eff} = 2{\times}10^{10}\,\text{cm}^{-3}$. The simulated electric field at 250 V bias and $N_{eff} = 2{\times}10^{10}\,\text{cm}^{-3}$ is shown in Fig. 6.3. In this study, N_{eff} was held constant throughout the detector bulk; future studies will investigate the effect of an uncompensated dead layers by varying the N_{eff} value throughout the detector volume.

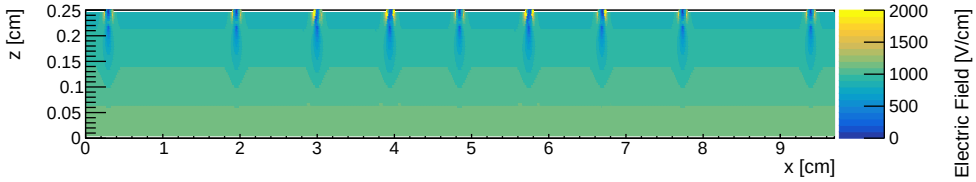

Figure 6.3: Simulated electric field of GAPS Si(Li) detector in `KDetSim` at 250 V bias.

6.1.2 Charge Collection Efficiency

In `KDetSim`, an ionizing event is simulated by creating electron-hole pairs at a point-like region in the detector bulk. The amount of charge created by the ionizing event is parameterized in arbitrary units, called 'buckets.' The calculated electric and weighting fields are used to simulate the drift of electrons and holes through the detector bulk, determining the induced current on each electrode as a function of time. Since the charge collection time is much smaller than the fall time of the preamplifier, it is sufficient to simply integrate the current to determine the total induced charge in the event, and we do not expect any ballistic deficit due to pulse shaping effects. This model provides an estimate of the incomplete charge collection due to charge sharing and inter-electrode charge collection.

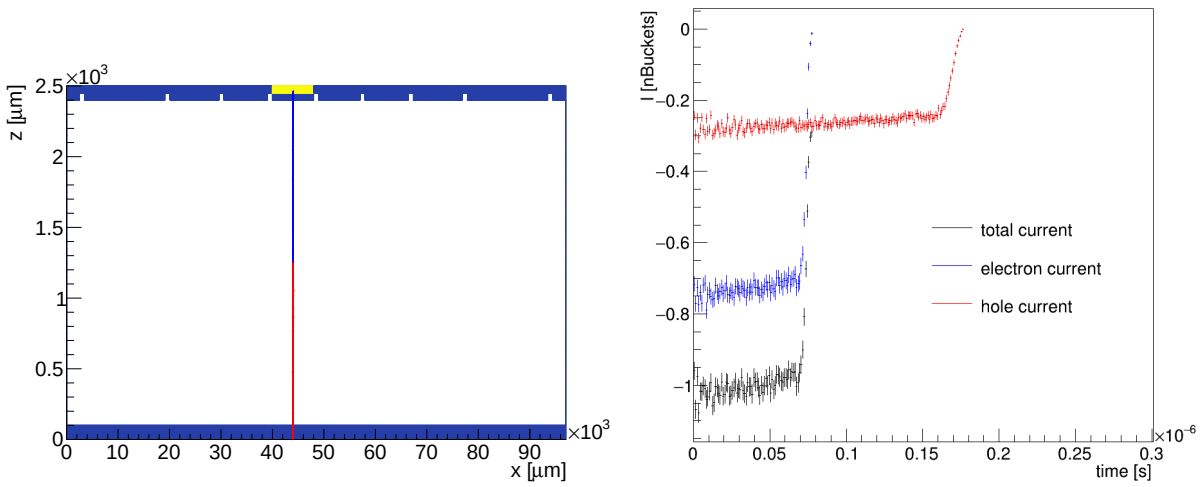

Figure 6.4: *Left:* Drift of electrons (blue) and holes (red) through simulated detector geometry. Readout electrode is indicated by yellow shading. The weighting field is calculated to determine the induced current on the readout electrode. *Right:* Induced current on readout electrode as a function of time as found by `KDetSim`. Current is reported in arbitrary units that correspond to the initial amount of charge created in the ionizing event. Total current is indicated in black, whereas the current due to electrons and holes are shown in blue and red, respectively. The difference in the electron and hole currents and charge collection times is due to their carrier mobility, which is about three times larger for electrons than for positive holes.

The charge collection efficiency (CCE) to strip j for charge created at position (x, z) is calculated as follows:

$$\epsilon_{CCE,j}(x, z) = \frac{Q_j}{Q_i(x, z)} \tag{6.3}$$

where $Q_i(x, z)$ is the initial amount of charge created in the detector bulk at position (x, z) and Q_j is the amount of charge collected to strip j.

A look-up table of the charge collection efficiency $\epsilon_{CCE,j}(x, z)$ to each strip was generated in increments of $\Delta x = 25\,\mu\text{m} \times \Delta z = 50\,\mu\text{m}$ throughout the detector bulk. The `Geant4` positional information was coupled to this look-up table to determine the energy measured by a strip including charge transport effects.

6.1.3 Simulating Spectral Response

To simulate the spectra recorded by each strip during a calibration run, the `Geant4` data is coupled to the CCE look-up table described in Eq. (6.3). Each photon interaction in the detector is

associated with a position in the look-up table to determine the CCE to each strip. The strip noise is included by Gaussian smearing the measured energy. This process can be summarized in the equation

$$E_j = E_{dep}(x, y, z) * \epsilon_{CCE,j}(x, z) + \text{Rand}(\mu = 0, \sigma_E), \tag{6.4}$$

where E_j is the energy measured by strip j, $E_{dep}(x, y, z)$ is the energy deposited at position (x, y, z) in `Geant4`, and $\text{Rand}(\mu = 0, \sigma_E)$ is a random number selected from a Gaussian distribution centered at 0 and σ_E the strip's energy resolution. Since the measured energy resolution is dominated by electronic noise with $\sigma_E \approx 1\,\text{keV}$, fluctuations in the signal charge due to Fano noise ($\sigma_F \approx 0.1\,\text{keV}$ for 20–100 keV X-rays) is negligible.

To check the reliability of the CCE model, the simulated spectra using the CCE look-up table were compared to spectra generated without CCE effects. To populate the spectra without CCE effects, each energy deposition was fully added ($\epsilon_{CCE} = 1$) to the strip closest to its hit position. The simulated spectra for strips A, C, E, and G of a detector with ~2.8 keV (FWHM) energy resolution are shown with and without CCE effects in Fig. 6.5. The simulated spectra are binned to match the binning of the experimental spectra. Solid lines indicate that CCE effects were not included ($\epsilon_{CCE} = 1$), whereas dashed lines included CCE. The relative difference in counts between each strip's spectra reflects the source-to-strip distance, with the central strip (E) having the highest count rate and the outside strip (A) having the lowest.

For the same strip, the spectra with CCE included demonstrate a reduced peak height and broadened peak width, due to ionizing events directly underneath a groove. These events exhibit charge sharing between neighboring strips and inter-electrode charge collection, resulting in the full-energy not being recorded by the individual strip. To assess the impact of the CCE on the full-energy peak efficiency, we compare the main photopeaks in simulated spectra with and without CCE effects. By integrating the number of counts in each spectrum within about ±1.5 keV of the ^{241}Am line energy, we estimate that charge sharing and inter-electrode charge collection will cause $\lesssim$6% additional fully absorbed photons to fall outside of one FWHM of the main photopeak for a detector with ~3 keV (FWHM) energy resolution.

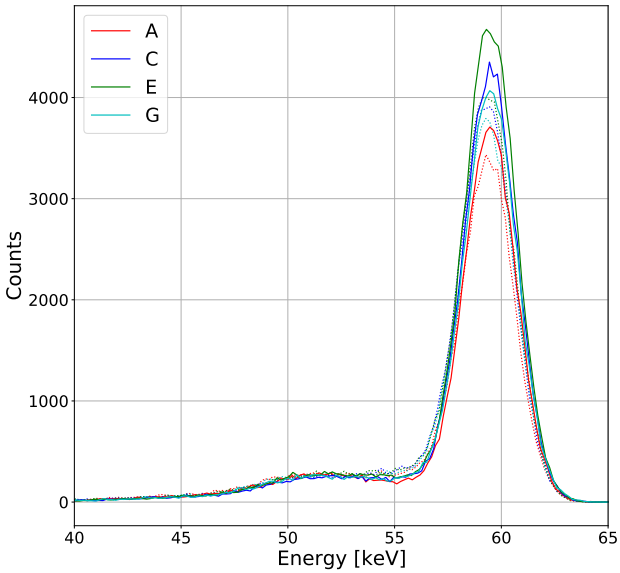

Figure 6.5: Simulated spectra of strips A, C, E, and G overlaid. Solid lines indicate that CCE effects were neglected ($\epsilon_{CCE} = 1$). Dashed lines indicate that CCE effects were included. The relative difference in counts observed in each strip reflects the source-to-strip distance, which results in a larger solid angle subtended by the central strips compared to the perimeter strips.

6.2 Comparison of Experimental and Simulated Spectra

The simulated spectra, with and without CCE effects, were compared to experimental spectra to validate the model. Simulated spectra were generated and convolved with a range of energy resolution values close to the best-fit experimental energy resolution. For each spectra, the simulated counts were normalized by fitting the upper half of the main photopeak to the experimental data with a floating normalization factor, and scaling the simulated counts by the best-fit normalization factor. After normalization, the simulated and experimental spectra were compared and a reduced chi-squared statistic was calculated to assess the goodness of fit in the 48–65 keV range. Fig. 6.6 shows example spectra for strip A of a simulated detector, with and without CCE effects, that provided the best fit to experimental spectra.

Comparing experimental data with the simulated spectra, we observe a similar spectral shape, notably in the low-energy tail. The simulated spectra including CCE effects, convolved with 2.7 keV (FWHM) energy resolution, provided an excellent fit to the experimental data, with a reduced chi-squared $\chi^2_\nu \sim 1$. Without CCE effects, the best-fit spectra was generated with 2.8 keV

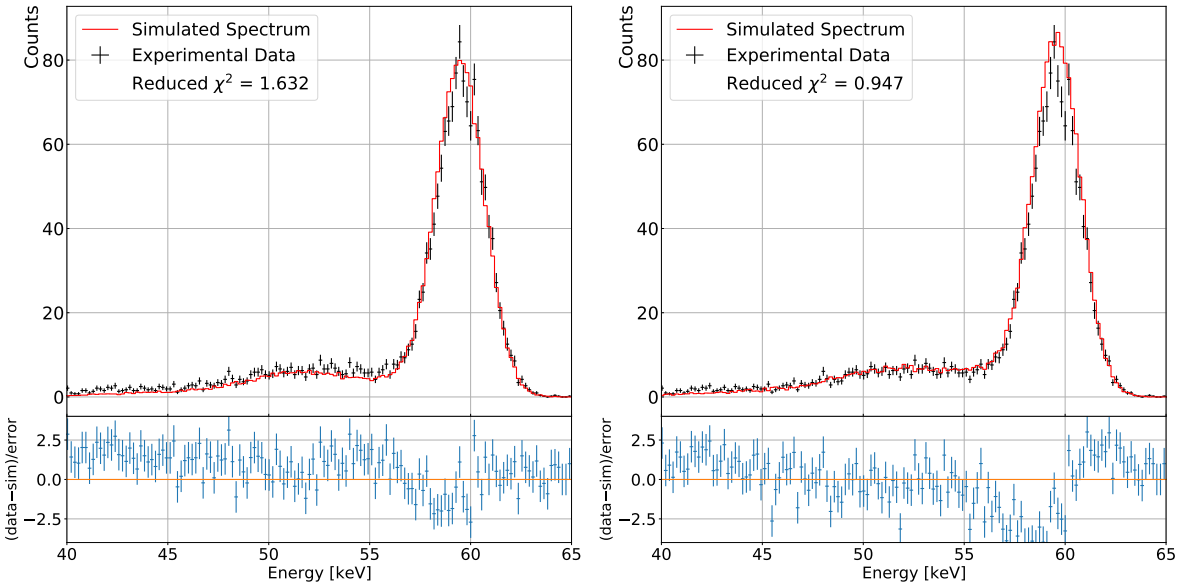

Figure 6.6: Overlaid simulated and experimental spectra for strip A of Sh0222, a GAPS flight detector. The simulated spectra were generated with (right) and without (left) CCE effects. The simulated spectrum including CCE effects accurately represents the shape of the detector spectrum, particularly the low-energy tail.

(FWHM) energy resolution, giving $\chi^2_\nu \approx 1.6$. This indicates that the inter-electrode CCE is necessary to accurately model the low-energy tail in the spectrum down to 48 keV. Furthermore, it shows that the CCE effects tend to broaden the FWHM of the spectra by ~0.1 keV, in comparison to the expected spectral line width solely due to detector noise.

6.3 Conclusions and Outlook

These studies indicate that the low-energy tail observed during GAPS Si(Li) detector calibration can be fully attributed to Compton scattering in passive material, charge sharing between adjacent electrodes, and charge collection to the inter-electrode gap; and there is no necessity for any contribution from charge trapping. Future work will aim to refine the model and increase the sample size by comparing the model to more experimentally measured spectra. The planned refinements to the simulated model include creating a 3D CCE look-up table to account for ionizing events under the circumference of the guard ring groove, and including the effects of the dead layers on the charge collection efficiency and measured energy.

Chapter 7: Benchmarking of Hadronic Annihilation Products

A key component of the GAPS identification technique is the multiplicity of charged hadrons emerging from the antinucleus-nucleus annihilation vertex (see Sec. 3.2). To optimize the design and determine the performance capabilities of the GAPS instrument, simulation studies were conducted using the `GEANT4` toolkit [213]. In `Geant4`, a unified model of antiproton, antiproton-nucleus, and light antinucleus-nucleus interactions is implemented in the Fritiof (FTF) model. This model determines the multiplicity, energy, and angular distribution of the hadronic annihilation products, and subsequently dictates the annihilation event topology in GAPS simulation studies.

A key contribution I made to the GAPS simulation efforts was benchmarking the hadronic annihilation products in each `Geant4` release to ensure the simulation results matched expectation. This chapter summarizes the expected properties of the antinucleus-nucleus annihilations, the implemented `Geant4` physics processes used to simulate antinucleus-nucleus interactions, and compares the simulated results to experimental data and theoretical predictions.

7.1 Properties of Antinucleus-nucleus Annihilation at Rest

Since the discovery of the antiproton in 1955 [216], the properties of antiproton-proton annihilation at rest has been studied in detail. Bubble chamber experiments in the 1960s analyzed final states with charged mesons, but were unable to identify neutral pions due to the lack of gamma-ray detection [217]. At CERN, the Low Energy Antiproton Ring (LEAR) enabled the the study of antiproton annihilations by several experimental groups before being decomissioned in 1996. In particular, the CRYSTAL BARREL experiment was capable of identifying events with multiple neutral pions in the final state, and provided precise measurements of the branching fractions in antiproton-proton annihilation at rest. For a comprehensive review of the nucleon-antinucleon

results obtained at LEAR, see Ref. [218].

To first approximation, the general properties of the antiproton-proton annihilation process can be described by the fireball model. In the fireball model, the energy deposited in the annihilation excites the nucleus. The density of states of the nuclear energy levels can be parameterized by a fireball temperature T_F of the compound nucleus, and particles are emitted by evaporation from the excited system. The probability of a particle of mass m evaporating from the nucleus scales with $\exp(-mc^2/kT_F)$, so that pions are evaporated more abundantly than nucleons. The energy spectrum of pions produced in $\bar{p}p$ annihilation is well described by a fireball temperature of $T \sim 100\,\mathrm{MeV}$ [219]. The total pion multiplicity $n = n_{\pi^-} + n_{\pi^+} + n_{\pi^0}$ follows a Gaussian distribution [220]. This model predicts that for a given total pion multiplicity n in the final state, the branching ratios are distributed according to the factorial law with weight $\frac{1}{n_{\pi^-}!n_{\pi^+}!n_{\pi^0}!}$ [221].

The Intra-Nuclear Cascade (INC) model is another framework that successfully describes the global properties of antiproton annihilations on nuclei. In the INC model, the antiproton annihilates on a single nucleon at the surface of the nucleus, producing a few primordial pions. Some of the primordial pions are emitted towards the interior of the nucleus, where they interact with the nucleons, ejecting some fast nucleons. The residual nucleus is highly excited after this fast ejection process and its energy density distribution is non-thermal. Therefore, the nucleus can fragment and produce pre-equilibrium emission. Following this stage, the energy distribution of the nucleus reaches thermal equilibrium and the remaining excitation energy is dissipated by nuclear evaporation.

The INC model was extended by Cugnon [222] to describe antideuteron annihilation on nuclei. Two models were configured, one in which the antideuteron annihilates as a whole at a single point (model A), and another in which the consituent antinucleons interact independently (model B). In model B, after the first antinucleon annihilates, the remaining antinucleon may scatter on pions produced in the first annihilation or target nucleons before annihilating, but it also may escape the nucleus. In the INC model, the pion multiplicity follows a Gaussian distribution and can be estimated based on the center of mass energy of the antinucleus-nucleus system.

Since the 1980s, the prevailing view is that the antinucleon-nucleon annihilation should be understood at the quark level [223]. Since baryons and mesons are composite particles, their annihilation is distinct from electron-positron annihilations, in which the initial consituents disappear. Instead, an antinucleon-nucleon annihilation can be modeled as a mere rearrangement of quarks. In Geant4 the annihilation is modeled in this regard — based on the interactions of quarks and antiquarks — following the main assumptions of the Dual-Parton or Quark-Gluon String model.

Geant4 uses the FTFP model to simulate antinucleus-nucleus interactions, which is a combination of the Fritiof (FTF) and Precompound (P) models. The FTF model encodes the annihilations of antinuclei and nuclei, including the interaction cross-sections, annihilation branching fractions, and the excitation energies of residual nuclei. This is coupled to the Precompound model which handles the de-excitation of the residual nucleus. The Glauber approach [224, 225] is used to calculate the antinucleus-nucleus cross sections. The Quark-Gluon String model is used to determine the possible quark flow diagrams and estimate the cross section of each annihilation process at the quark level [226]. The implementation of the FTFP model in GEANT4, as well as its comparison to experimental data is described in Ref. [227].

In the Quark-Gluon String model, hadrons are treated as excitations of strings with confined quarks at their ends: a meson being a quark and antiquark, a baryon being a quark and a diquark. Following this approach, Geant4 treats the annihilation of an antinucleus with a nucleus based on the interactions of antiquarks in the antinucleons interacting with quarks in the target nucleons. As such, the annihilation of antideuterons in Geant4 is treated as two independent nucleon-antinucleon annihilations, corresponding to model B in Cugnon's terminology [222].

7.2 Antiproton-proton Annihilation in Hydrogen

The most studied antinucleon-nucleon annihilation system is antiproton-proton ($\bar{p}p$) annihilations, with experimental datasets arising from antiproton beams incident on hydrogen targets. These datasets provide a way to validate the annihilation processes implemented in Geant4. At LEAR, the CRYSTAL BARREL experiment collected a high-statistics sample of $\bar{p}p$ annihilation

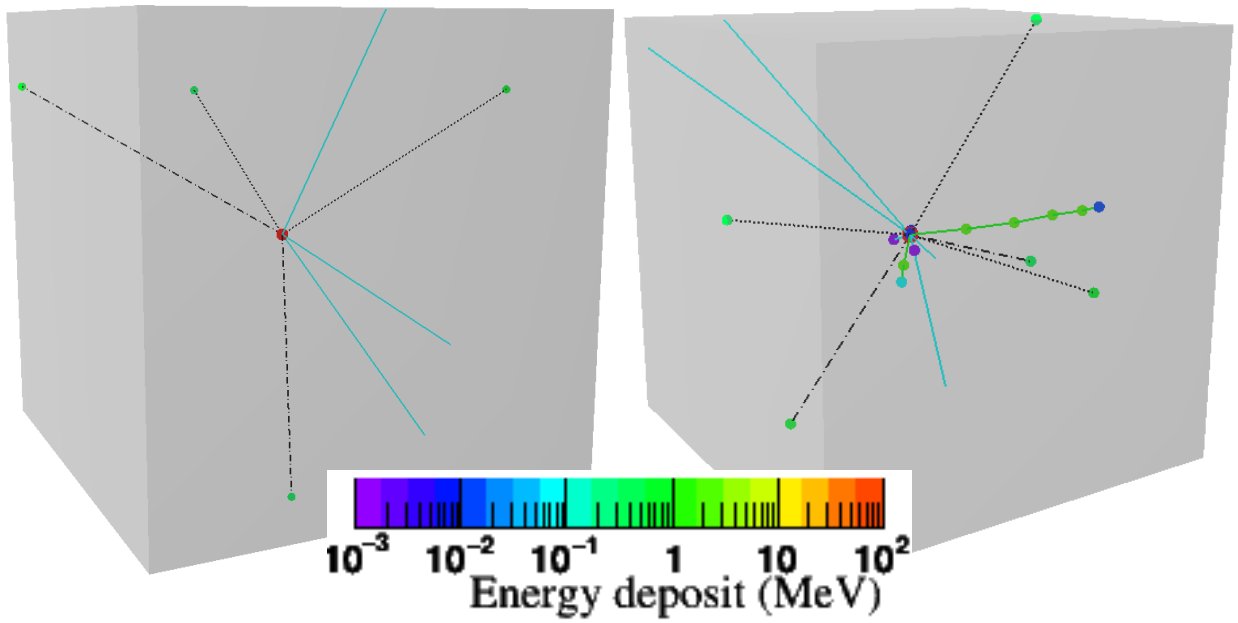

Figure 7.1: Event display of antiproton annihilating in 2.5 mm^3 cube of hydrogen (left) and silicon (right) in `Geant4`. Green lines represent secondary protons, cyan lines indicate secondary photons, and black lines indicate secondary pions, with dashed lines representing π^- and dot-dashed lines representing π^+. The color of dots on each track indicate the energy deposited by a particle in the corresponding step, with the energy scale shown in the color bar.

events in a liquid hydrogen target. CRYSTAL BARREL measured the branching fractions of annihilation channels for antiproton annihilations in hydrogen. To test the `FTFP_BERT_HP` model, antiproton annihilation at rest in hydrogen was simulated using `GEANT4v10.7.1` and compared to the CRYSTAL BARREL results.

In the simulation, 10^6 antiprotons were generated at the center of a 2.5 mm^3 cube of hydrogen. The antiprotons were generated with 1 keV energy directed in the $-\hat{z}$ direction. The incident primary energy of 1 keV was recommended by `Geant4` developers to ensure that the primary particle takes a step in the material to initiate the `FTF` capture at rest process.

The subsequent data analysis follows the approach used to verify the Chiral Invariant Phase Space (CHIPS) model, which was used to model nucleon-antinucleon annihilation at rest in previous `Geant4` versions [228]. The annihilation branching fraction to channels with pions in the final state was determined in the simulated data and compared to the CRYSTAL BARREL results [229, 230] (Fig. 7.2). The final states listed on the x-axis were selected exclusively, meaning that no

other hadronic secondaries were produced in the event unless explicitly noted. The accuracy of the FTFP_BERT_HP model has improved in subsequent Geant4 versions, as can be seen by inspection of successive panels (a)-(d) in Fig. 7.2.

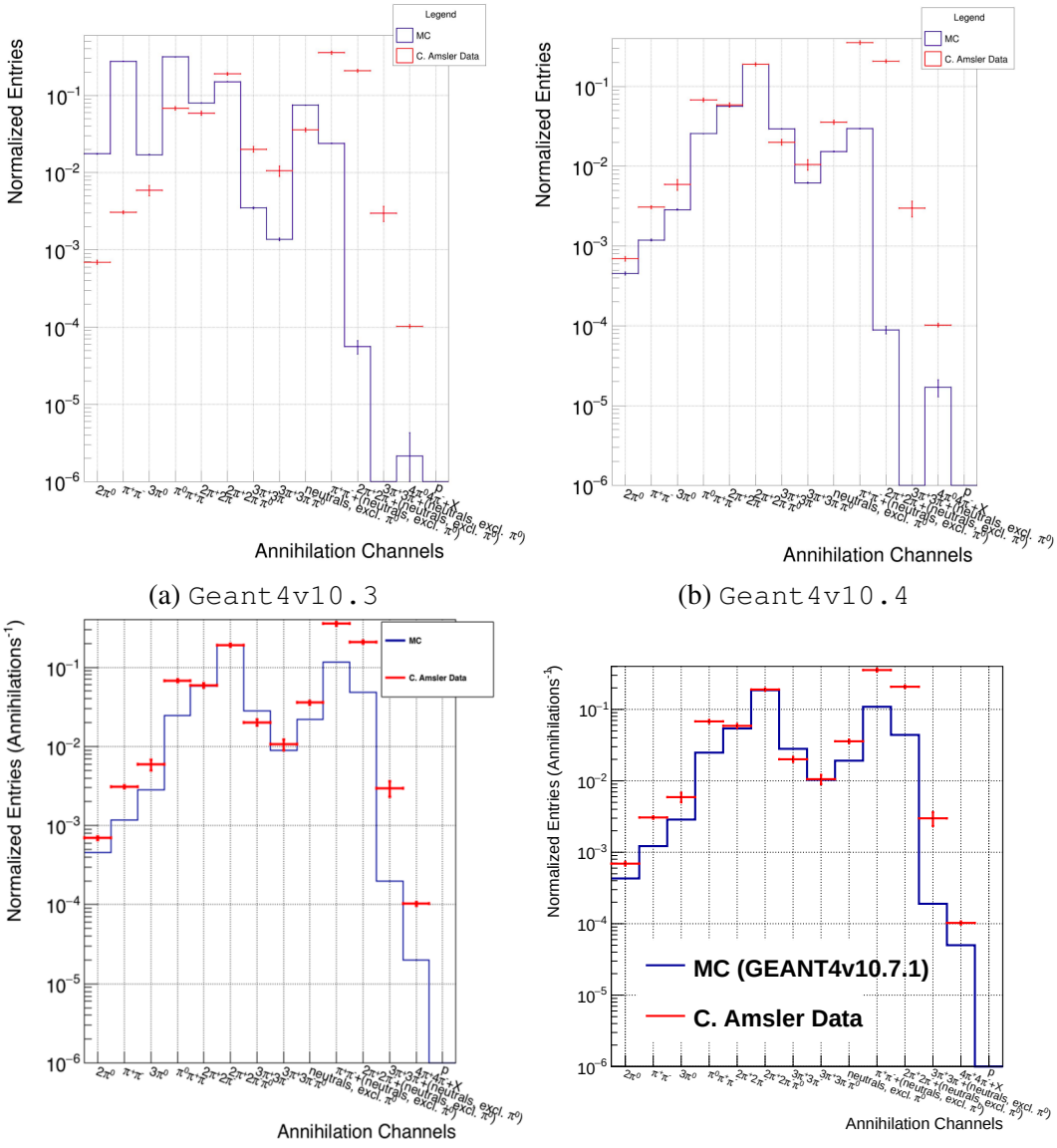

(a) Geant4v10.3 (b) Geant4v10.4

(c) Geant4v10.5 (d) Geant4v10.7.1

Figure 7.2: Per event annihilation branching fractions using different versions of the GEANT4 FTFP_BERT_HP physics list, compared to experimental data. Note the general improvement in the consistency between MC results and experimental data in subsequent Geant4 versions.

7.3 Hadronic Products of Antiproton, Antideuteron, and Antihelium-3 Annihilations

7.3.1 Motivation

While antiproton-nucleus annihilation products can be cross-checked with an array of experimental results from LEAR and other accelerator-based experiments, there is a limited experimental dataset to verify the properties of antideuteron annihilations. To verify the implementation of antideuterons in the `FTF` model, the calculated cross-sections were compared to experimental measurements of the antideuteron-nucleus absorption at 13.3 and 25 GeV/c [231], and the multiplicity and energy distribution of particles produced in antideuteron-nucleus interactions at 12.2 GeV/c [232, 233].

For GAPS, the main motivation for benchmarking each `Geant4` release is to check the multiplicity and energy of charged secondaries (primarily pions) produced in annihilations of antiproton, antideuteron, and antihelium nuclei in target materials that comprise the GAPS instrument. Another motivation is to inspect the event topologies of antiproton, antideuteron and antihelium annihilations. As mentioned in Sec. 7.1, the annihilation of antideuterons and antihelium in `Geant4` is modeled based on the annihilations of the constituent antinucleons on target nucleons, according to their quark content. As such, there is a chance that only a subset of the constituent antinucleons annihilate in the initial annihilation vertex, while the other antinucleons escape the nucleus and continue propagating through the target material. A main part of my `Geant4` benchmarking work was identifying these 'antinucleus breakup' events and determining their implications for GAPS.

7.3.2 Simulation Setup

To assess the hadronic annihilation products in each `Geant4` release, I simulated annihilation at rest of antiproton, antineutron, antideuteron, and antihelium-3 nuclei using the `FTFP_BERT_HP` physics list. 10^5 primary antinuclei were generated with 1 keV energy directed in the $-\hat{z}$ direction at the center of a 2.5 m^3 cube of different target materials. The following target materials were used: hydrogen, deuterium, tritium, helium, carbon, aluminum, silicon, and tantalum. These materials

were selected to examine the dependence of the annihilation products on the target material's atomic number (Z) and mass number (A). Carbon, aluminum, and silicon were specifically chosen because these elements constitute the majority of the GAPS instrument. The data analysis focused on checking the charged pion multiplicity produced in annihilations, as well as determining the fraction of antideuteron and antihelium-3 nuclei that annihilate on a single target nucleus.

7.3.3 Antiproton and Antineutron Annihilation Properties

Examining the results of antiproton and antineutron annihilation in hydrogen and deuterium illustrates the properties of antinucleon-nucleon annihilations in `Geant4`, in particular the conservation of charge and strangness. In analyzing the simulated data, only charged pions daughter to the primary antinucleus were included in the selection criteria, as these will produce ionizing tracks in the GAPS instrument. Since the primary had an initial energy of 1 keV, all primary antiprotons and antineutrons annihilated within the 2.5 mm^3 cube. Annihilation in hydrogen shows 'primordial' pions produced in $\bar{p}p$ and $\bar{n}p$ annihilations (Fig. 7.3), since the secondaries do not

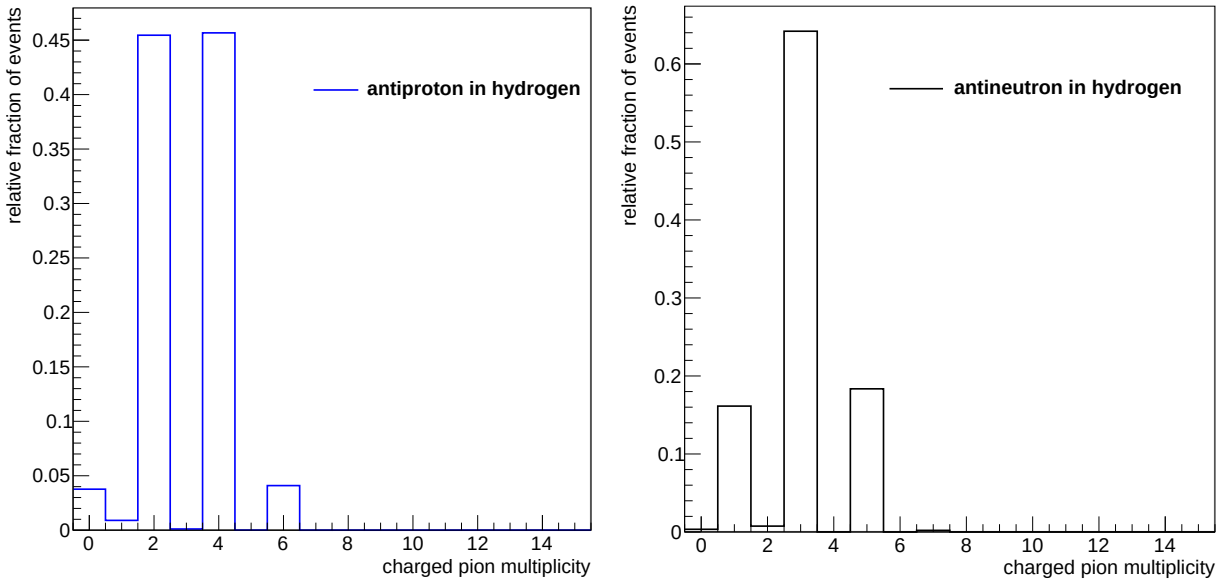

Figure 7.3: Charged pion multiplicity per event for $\bar{p}p$ (left) and $\bar{n}p$ (right) annihilations in Geant4. Charge conservation requires that the charged pions are mostly produced in $\pi^{\pm}$ pairs in $\bar{p}p$ annihilations, and one excess π^{+} is produced in $\bar{n}p$ annihilations. In the small of fraction of events that are exceptions to this rule, kaons are produced such that charge and strangeness are conserved.

cascade through a residual nucleus. Charge conservation requires that charged pions are produced in $\pi^{\pm}$ pairs in $\bar{p}p$ annihilations, and one excess π^{+} is produced in $\bar{n}p$ annihilations. This is shown in the even (odd) parity of the charged pion multiplicity in $\bar{p}p$ ($\bar{n}p$) annihilations. In the small fraction of $\bar{p}p$ ($\bar{n}p$) events that have odd (even) parity, a charged and neutral kaon were produced so that charge and strangeness are conserved.

For annihilations in deuterium, the primary antiproton or antineutron can annihilate on either nucleon in the nucleus, and the charged pion multiplicity has a Gaussian distribution with a mean multiplicity of three (Fig. 7.4).

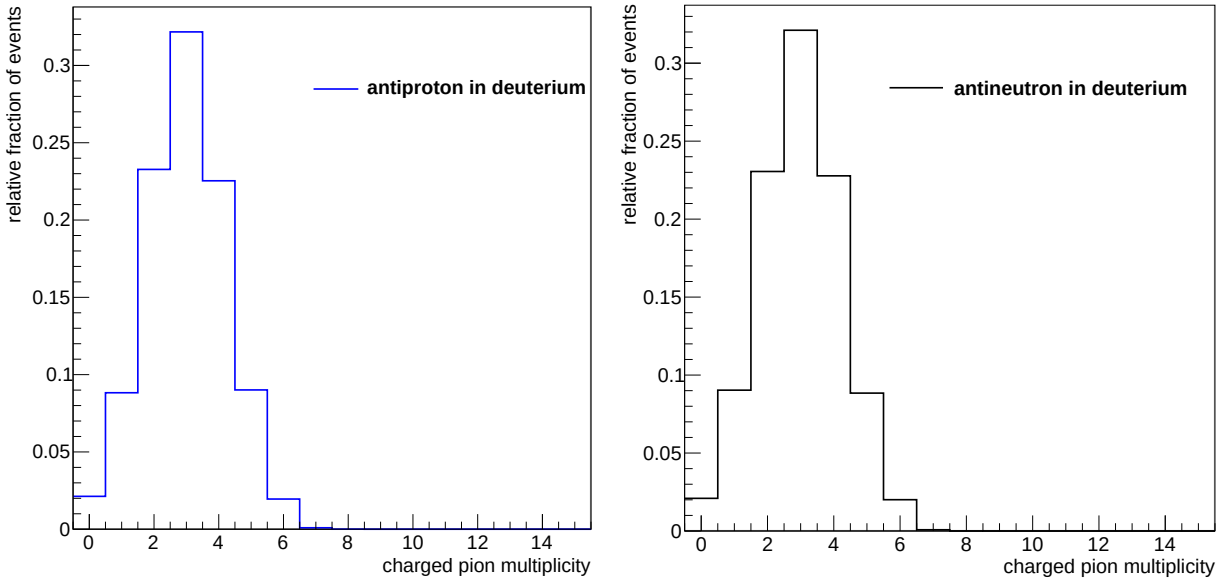

Figure 7.4: Charged pion multiplicity per event for antiproton and antineutron annihilation in deuterium. Since the deuterium nucleus consists of a proton and a neutron, the annihilation can take place with either nucleon, resulting in a Gaussian distribution in the charged pion multiplicity.

Figures 7.3 and 7.4 demonstrate the properties of the antinucleon-nucleus annihilation in the most basic configurations. For antiproton annihilations with heavier nuclei, the charged pion multiplicity matches the experimental and theoretical expectations, having a Gaussian distribution with a mean of three. Fig. 7.5 shows the charged pion multiplicity for antiproton annihilations in carbon, aluminum, and silicon — the materials that comprise the GAPS tracker.

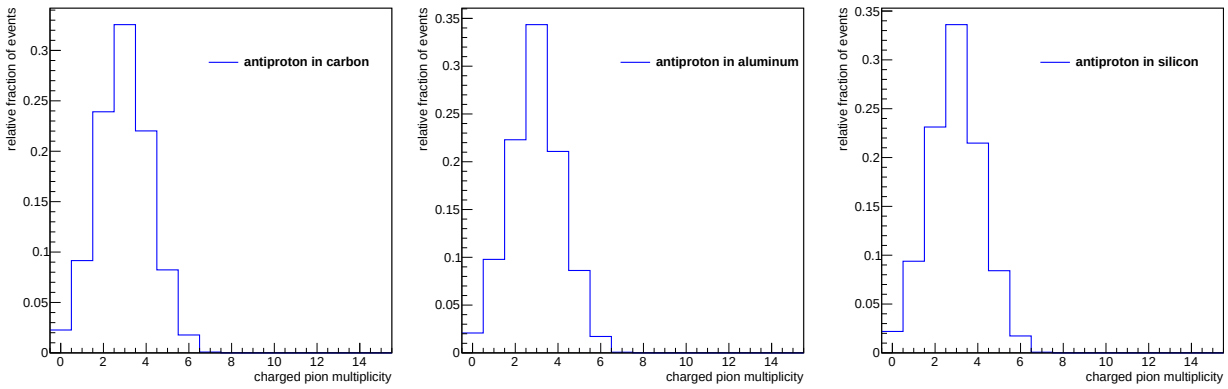

Figure 7.5: Charged pion multiplicity per event for antiproton annihilation in target materials that comprise the GAPS instrument.

7.3.4 Antideuteron and Antihelium-3 Annihilation Properties

Antideuteron and antihelium annihilations are described by the same model as antiproton annihilations in `Geant4`. Since the antinuclei are composed of multiple antinucleons, the model samples the antinucleus and nucleus wavefunctions to determine which (anti)nucleons participate in the annihilation. If one of the antinucleons does not participate in the annihilation, it can emerge from the initial annihilation vertex as a projectile.

In GAPS, antinucleus breakup events produce a different event topology than events where the antinucleus annihilates as a single unit. Breakup events can result in a 'double bang' event topology, where the remaining antinucleus annihilates at a position spatially separated from the initial annihilation vertex. If the residual antinucleus escapes the instrument without annihilating, the event would have a lower secondary multiplicity and could be misidentified.

To study the implications of 'antinucleus breakup' in antideuteron and antihelium-3 events, I selected charged pions daughter to the primary antinucleus and any residual antinuclei that emerged from the initial annihilation vertex. For antideuterons and antihelium-3 nuclei, the charged pion multiplicity distributions are plotted according to the residual antinuclei that emerged from the initial annihilation vertex.

The charged pion multiplicity in antideuteron annihilations in carbon, aluminum, and silicon are shown in Fig. 7.6. The black line indicates events where the both antinucleons annihilated on

one nucleus, and the red and green lines indicate events where antineutron or antiproton emerged from the initial annihilation vertex. Pions daughter to residual antiprotons or antineutrons are shown in the green and red histogram, respectively. This indicates that when an antiproton emerges from the initial annihilation vertex, it will slow down via ionization losses and also annihilate within a 2.5 mm^3 volume. On the contrary, when an antineutron emerges from the initial annihilation vertex, it does not undergo ionization losses and can escape from the volume. At energies below about 50 MeV, the antineutron-nucleon annihilation is described by an S-wave annihilation cross section with $\sigma_{ann} \propto 1/v$ [234]. Therefore, if the antineutron emerges with sufficient velocity, it will not annihilate in the GAPS instrument.

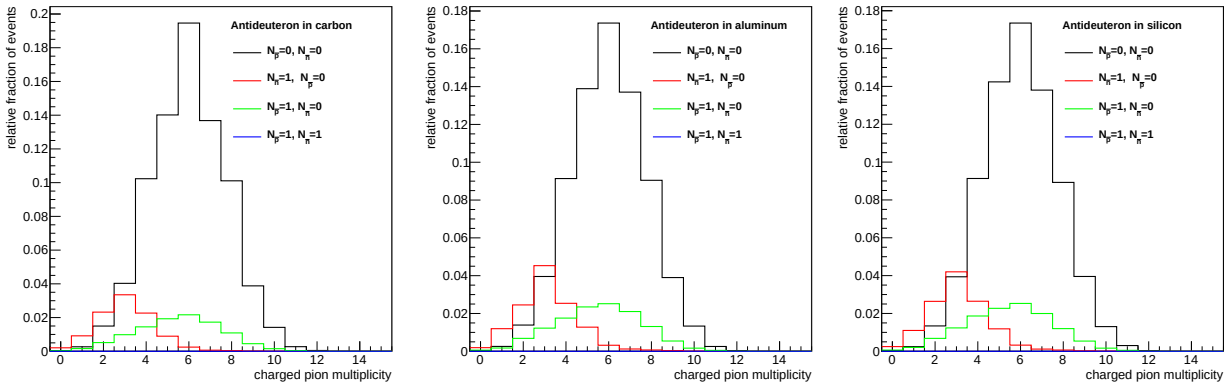

Figure 7.6: Charged pion multiplicity per event for antideuteron annihilation in carbon (left), aluminum (center), and silicon (right), the target nuclei that comprise the GAPS payload. The black line indicates the antideuterons that annihilated as a single unit. The green (red) line indicates events where only one antinucleon in the antinucleus annihilated in the target material, and an antiproton (antineutron) is produced as daughter to the primary. Each histogram is normalized by the total number of generated events.

The effect of antineutrons emerging from the initial annihilation vertex was bounded by examining the fraction of annihilation events that the antinucleus breaks up. Table 7.1 shows the fraction of events that an antinucleon emerges from the initial annihilation vertex. In ~13% of antideuteron annihilations carbon, aluminum, and silicon, an antineutron emerges as a secondary with non-zero kinetic energy.

Similar to antideuteron annihilations, antihelium-3 annihilations are governed by the interactions of the individual antinucleons and nucleons in the antinucleus-nucleus system. The mean

Table 7.1: Fraction of antideuteron annihilations in which one constituent antinucleon annihilates with a target nucleus, and the other antinucleon escapes from the nucleus, shown for a range of target materials.

Material	Z	A	ρ [g/cm^3]	Breakup Fraction	1 Escaped $\bar{p}$	1 Escaped $\bar{n}$
Hydrogen	1	1	1	100%	50%	50%
Deuterium	1	2	1	59.5%	30.2%	29.3%
Tritium	1	1	3	42.6%	22.4%	20.2%
Helium	2	4	1	36.6%	18.5%	18.1%
Carbon	6	12	1.6	21%	10.7%	10.3%
Aluminum	13	27	2.7	25.6%	12.9%	12.7%
Silicon	14	28	2.3	25.4%	12.8%	12.5%
Tantalum	73	181	16.7	24.7%	12.6%	12.1%

charged pion multiplicity in antihelium-3 annihilations is about 9, as shown in Fig. 7.7. About 60% of the antihelium-3 nuclei annihilate as a single unit at the primary annihilation vertex, whereas about 40% of primary antihelium-3 nuclei breakup in the target materials that comprise the GAPS tracker (see Table 7.2). However, antineutrons only emerge from the initial annihilation vertex in 10% of events, which reduces the expected charged pion multiplicity in this fraction of events as shown in the pink and red curves in Fig. 7.7.

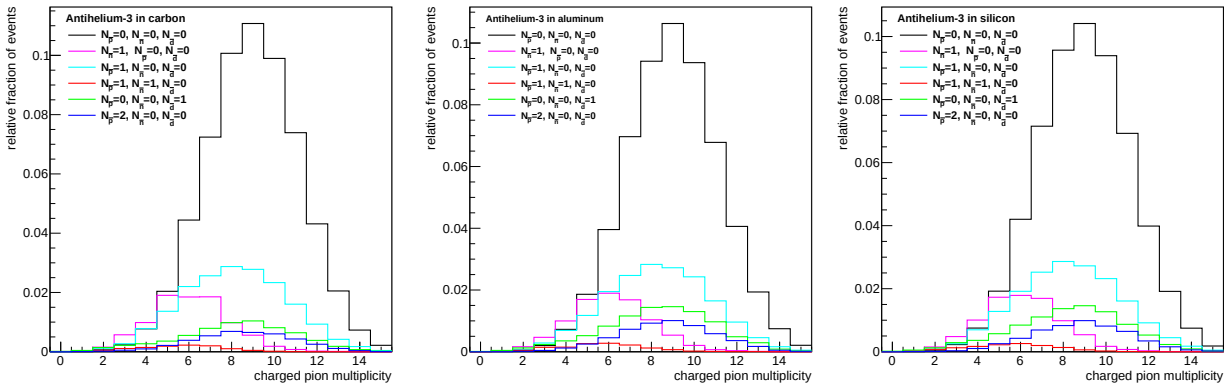

Figure 7.7: Charged pion multiplicity per event for antihelium-3 annihilation in target nuclei that comprise the GAPS tracker.

Table 7.2: Branching fraction of residual antinuclei emerging from the initial antihelium-3 annihilation vertex for a range of target materials.

Material	Breakup Fraction	1 $\bar{p}$	1 $\bar{n}$	2 $\bar{p}$	1 $\bar{d}$	1 $\bar{p}$ & 1 $\bar{n}$
Hydrogen	100%	0.004%	0.004%	33.5%	66.5%	0.006%
Deuterium	100%	35.4%	18.1%	16.0%	13.4%	16.7%
Tritium	74.1%	31.4%	15.3%	10.1%	8.1%	9.0%
Helium	62.3%	26.9%	13.2%	7.6%	11.6%	2.9%
Carbon	39.4%	18.4%	9.2%	4.1%	6.5%	1.1%
Aluminum	43.0%	17.9%	8.8%	5.6%	9.3%	1.3%
Silicon	42.5%	17.9%	8.7%	5.4%	9.2%	1.3%
Tantalum	40.8%	18.2%	8.6%	4.9%	7.3%	1.8%

7.4 Conclusions and Outlook

Overall, we find that the global properties of nucleus-antinucleus annihilations are modeled acceptably in `Geant4`. The `FTFP_BERT_HP` model demonstrates the expected properties of antiproton annihilations, and appropriately extends the relevant nuclear physics to describe antideuteron and antihelium annihilations. In the future, each `Geant4` release will be benchmarked following a similar approach, and the results will be presented to `Geant4` developers to improve the accuracy of the software package.

This chapter has focused on benchmarking the hadronic annihilation products of the annihilation process. Currently, the exotic atom de-excitation X-rays are not implemented in the out-of-the-box `Geant4` source code, but a patch has been developed by the GAPS simulation team for antiprotons and antideuterons. The following section will detail the cascade model used to determine the exotic atom de-excitation X-ray energies and yields, its extension to describe antihelium exotic atoms, and its planned integration into `Geant4`.

Chapter 8: Cascade Model of Exotic Atom De-excitation

As discussed in Sec. 3.2, the X-rays produced in exotic atom de-excitation play an important role in the GAPS identification technique, providing identification power to distinguish antinuclei and reject positively charged particles. X-rays from antiprotonic exotic atoms have been studied at particle accelerators with increasing precision since their first observation in 1970 [235]. For GAPS, a series of accelerator tests at KEK in 2004 and 2005 measured the X-ray yields of antiprotonic exotic atoms in aluminum and sulfur, providing proof-of-concept for GAPS to use a solid target [158–160]. Using these measurements and other experimental data, a comprehensive cascade model was developed and validated that accurately describes the X-ray yields of muonic and antiprotonic exotic atoms [160]. This model was extended to estimate the X-ray energies and yields for antideuteronic exotic atoms, and the antideuteronic X-rays were used in the event selection criteria to reject antiprotons in the GAPS antideuteron sensitivity study [156].

Recently, interest in cosmic antihelium has surged due to the report of antihelium candidate events by AMS-02 [236, 237]. A major part of my work was determining the sensitivity of GAPS to measure cosmic antihelium nuclei, which is presented in Chapter 9. The identification technique used in the antihelium sensitivity study focused on tracking charged annihilation products, and did not include the exotic atom X-rays from antihelium in the selection criteria. Due to larger strong interactions between the antihelium and target nuclei, it was not clear that the X-ray yields from antihelium exotic atoms would be high in the 20–100 keV range — the optimal energy range for efficient X-ray detection in the Si(Li) tracker. If the antihelium X-ray yields are high in this energy range, they would provide an additional event signature to identify antihelium nuclei with GAPS.

To this end, I extended the cascade model to describe the de-excitation of exotic atoms formed by the capture of antihelium nuclei. Prior to this work, the X-rays produced in the de-excitation of antihelium exotic atoms were not studied in the cascade model. This chapter describes the

theoretical basis of the cascade model and predicts the X-ray yields for antihelium exotic atoms in silicon. Sec. 8.1 reviews the cascade model. Sec. 8.2 describes the modifications to the cascade model that were implemented to simulate antihelium exotic atoms. Sec. 8.3 shows the predicted X-ray yields for antihelium exotic atoms in the cascade model. Sec. 8.4 demonstrates the integration of antiprotonic and antideuteronic exotic atoms into `Geant4`, providing a blueprint for similarly incorporating the antihelium X-rays into `Geant4`. Conclusions and future work are presented in Sec. 8.5.

8.1 Overview of Cascade Model

An exotic atom is a system in which a negatively charged particle heavier than an electron is captured into an atomic orbit by the Coulomb field of a nucleus. Exotic atoms were theoretically predicted in the 1940s [238, 239], and first observed experimentally based on the emission of Auger electrons [240] and characteristic X-rays from muonic [241] and pionic [242] exotic atoms in the early 1950s. Since their discovery, X-ray emission from a wide array of exotic atoms has been established. For a detailed review of exotic atoms see Refs. [243, 244].

A negatively charged particle (μ^-, π^-, K^-, $\bar{p}$, $\bar{d}$, etc., hereafter called a "cascader") will be captured into a target atom if its kinetic energy is comparable to the binding energy of an electron [243, 244]. The kinetic energy of the cascader is absorbed by electron emission or electron excitation to unoccupied atomic states.

To leading order, the Bohr model describes the energy levels of the exotic atom, which are proportional to the reduced mass of the cascader and nucleus. The energy difference between an initial state n_1 and final state n_2 is given by

$$\Delta E_{n_1,n_2} = hcR_y \mu Z_c^2 Z^2 \left(\frac{1}{n_1^2} - \frac{1}{n_2^2} \right), \tag{8.1}$$

where R_y is the Rydberg constant, Z is the atomic number of the nucleus, Z_c is the charge number of the cascader, and μ is the ratio of the reduced masses of the nucleus-cascader and nucleus-

electron systems ($\mu \approx m_c/m_e$). The effective Bohr radius and the expectation value of the orbital radii are proportional to the reciprocal of the reduced mass of the nucleus-cascader system. Specifically, the effective Bohr radius a_{eff} is given by

$$a_{eff} = \left(\frac{\hbar^2}{m_e e^2}\right)\left(\frac{1}{\mu Z|Z_c|}\right) = \frac{a_0}{\mu Z|Z_c|}, \tag{8.2}$$

where a_0 is the Bohr radius of the hydrogen atom.

Based on the Bohr model and energy conservation, the cascader will be captured into a highly excited state. For $Z_c = -1$ cascaders, the initial principal quantum number n_i for the exotic atom can be estimated as [243, 244]

$$n_i \sim n_e\sqrt{\frac{M_c}{M_e}}. \tag{8.3}$$

Here, n_e is the principal quantum number of the capturing electron shell of the target atom ($n_e = 1$ for K shell), M_e is the reduced mass of an electron and the nucleus of the target atom, and M_c is the reduced mass of the cascader-nucleus system. The cascade model starts at the electron K shell ($n_e = 1$ in Eq. (8.3)). Using Eq. (8.3), the principal quantum number n_i is approximately 14 for μ^-, 16 for π^-, 31 for K^-, 40 for $\bar{p}$, and 60 for $\bar{d}$.

For target atoms with $Z > 2$, the two leading de-excitation mechanisms are Auger (emission of an Auger electron) and radiative (emission of a photon) transitions. Auger transitions dominate at high n states, and radiative transitions dominate at lower n states. At very low n states, the strong interaction between a hadronic cascader and the nucleus is very large, and nuclear capture can occur. Fig. 8.1 shows a schematic of Auger emission, radiative transitions, and nuclear capture in the de-excitation of an antiprotonic exotic atom.

The cascade model calculates the transition rates for each process between each (n,l) state, where l is the orbital angular momentum. After calculating the transition rates, it iteratively simulates the de-excitation of the cascader. Each cascade starts at n_i based on Eq. (8.3), and the orbital angular momentum l is selected following a modified statistical distribution, $P_l \propto (2l+1)e^{\alpha l}$ [244]. The results of each cascade are tabulated to determine probability per event of a transition occuring

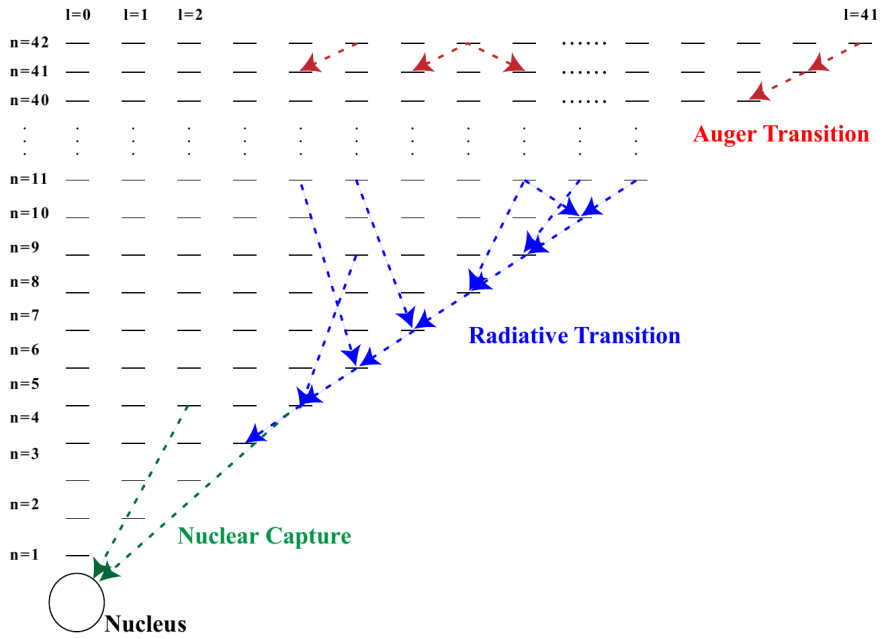

Figure 8.1: Schematic of the cascade model for the de-excitation of an antiprotonic exotic atom. Auger emission dominates at high n states, whereas radiative transitions dominate at intermediate n states. At low n, nuclear capture occurs. Figure from [160].

via a certain de-excitation process. This provides the X-ray yields for each radiative transition per exotic atom.

8.1.1 Auger Transitions

In antiprotonic exotic atoms, Auger transitions dominate at the beginning of the cascade, occuring when the energy difference between the exotic atom levels exceeds the ionization energy for an electron. The Auger transitions emit shell electrons, depleting the electron shell and leaving a "hydrogenic atom" with the cascader as the sole bound negative charge. The Auger transition rate for K shell and L shell electrons can be estimated as [245]

$$\begin{aligned}
\Gamma^{Aug,K}_{n_1,l_1\to n_2,l_2} &= \frac{32\pi\alpha c}{a_0\mu^2}\left(\frac{Z^*}{Z}\right)^2 \frac{\max(l_1,l_2)}{3(2l_1+1)}\frac{y^2}{1+y^2}\frac{\exp[y(4\arctan(y-\pi))]}{\sinh(\pi y)}I^2 \\
\Gamma^{Aug,L}_{n_1,l_1\to n_2,l_2} &= \frac{16\pi\alpha c}{a_0\mu^2}\left(\frac{Z^*}{Z}\right)^2 \frac{\max(l_1,l_2)}{3(2l_1+1)}\frac{y^2(4+5y^2)(4+3y^2)}{(4+y^2)^3}\frac{\exp[y(4\arctan(y-\pi))]}{\sinh(\pi y)}I^2.
\end{aligned} \tag{8.4}$$

Here, $\Gamma^{Aug,K}_{n_1,l_1\to n_2,l_2}$ ($\Gamma^{Aug,L}_{n_1,l_1\to n_2,l_2}$) is the Auger transition rate emitting K shell (L shell) electrons between initial state (n_1, l_1) and final state (n_2, l_2), α is the fine structure constant, Z^* is the effective nuclear charge seen by the electron, and I is the dipole matrix element. I and y are defined as follows:

$$\begin{aligned} I &\equiv \int_0^\infty drrR(n_1, l_1)R(n_2, l_2) \\ y &\equiv \frac{Z^*\alpha}{\sqrt{(T/m_ec^2)^2 + (2T/m_ec^2)}} \\ T &= \Delta E_{n_1,n_2} - E_{ioniziation} \end{aligned} \tag{8.5}$$

where $R(n, l)$ are the normalized radial wavefunctions and T is the kinetic energy of the emitted Auger electron. Due to the transition selection rules, Auger transitions with $\Delta l = \pm 1$ dominate.

After the electrons are depleted by Auger emission, the electrons can be filled from adjacent atoms with a refilling rate Γ_{ref}, and from higher shells by fluorescence with transition rate Γ_{flu}. The refilling rate can be estimated as

$$\Gamma_{ref} = \rho_n \cdot \sigma \cdot v, \tag{8.6}$$

where ρ_n is the number density of target atoms, σ is the cross section for charge transfer, and v is the relative velocity of the exotic atom with respect to other atoms in the medium. In solids and metals the refilling rate is $O(10^{16}\,\mathrm{s}^{-1})$ [243].

The Auger transition rate is much higher than the refilling rate, so the shell electrons are depleted in the initial stages of the cascade. Since Auger transitions can only occur if an electron occupies a shell state, the refilling rate bottlenecks the rate of Auger transitions [246]. Therefore, the modified Auger transition rate

$$\Gamma^{Aug,K,mod}_{n_1,l_1\to n_2,l_2} = \left(\frac{1}{\Gamma^{Aug,K}_{n_1,l_1\to n_2,l_2}} + \frac{1}{\Gamma_{ref}} + \frac{1}{\Gamma_{flu}}\right)^{-1} \tag{8.7}$$

is used in the cascade model. This modified Auger transition rate will not effect the X-ray yields

at low n states, because the radiative transition rate dominates at low n.

8.1.2 Radiative Transitions

Radiative transitions dominate in the intermediate stage of the cascade, particularly once all electron shells are emptied through Auger emission. The radiative transition rate can be estimated with a perturbation method in the dipole approximation as [245]

$$\Gamma^{Rad}_{n_1,l_1\to n_2,l_2} = \frac{4e^2}{3\hbar^4 c^3}\left(\frac{a_0}{\mu Z}\right)(\Delta E_{n_1,n_2})^3 \frac{\max(l_1,l_2)}{2l_1+1} I^2. \tag{8.8}$$

Here, $\Gamma^{Rad}_{n_1,l_1\to n_2,l_2}$ is the radiative transition probability between the initial state (n_1, l_1) and the final state (n_2, l_2) and $\Delta E_{n_1,n_2}$ is given by Eq. (8.1). Due to the selection rules for radiative transitions, the $\Delta l = \pm 1$ dominate this process. The radiative transition rate increases as n decreases ($\Delta E_{n_1,n_2}$ increases), becoming the dominant de-excitation process at low n until nuclear capture takes over.

8.1.3 Nuclear Capture

At low n states, the strong interaction between the cascader and the nucleus becomes large, which can result in nuclear capture of the cascader before it reaches the ground state. To simulate the effects of strong interactions in exotic atoms, a macroscopic optical model is used. An optical potential is defined that represents the strong interaction between the nucleus and the hadronic cascader, and the imaginary part of the optical potential encodes the nuclear capture rate at each step of the cascade.

The strong interaction causes a measurable shift in the energy of the lowest atomic level and broadens the X-ray transitions to this level. By adjusting the parameters of the optical potential, the optical model is capable of fitting experimental measurements of the strong interaction shift and width values for exotic atoms for a wide range of nuclei. The optical potential between the

nucleus and cascader can be defined as [247, 248]

$$\begin{aligned} U(r) &= -\frac{2\pi}{M_c}\left(1+\frac{M_c}{m_N}\right)\bar{a}\rho(r) \\ &\equiv -(V+iW)\frac{\rho(r)}{\rho(0)}. \end{aligned} \tag{8.9}$$

Here, m_N is the mass of a nucleon, $\bar{a}$ is the average complex effective hadron-nucleus scattering length, and $\rho(r)$ is the Fermi distribution:

$$\rho(r) = \frac{\rho(0)}{1+e^{\frac{r-c}{z}}} \tag{8.10}$$

with the parameters $\rho(0) = 0.122\,\mathrm{fm}^3$, $c = 1.07 \times A^{1/3}$, and $z = 0.55\,\mathrm{fm}$ [247–249]. W is the imaginary part of the optical potential and can be written as

$$W = \left(\frac{2\pi}{M_c}+\frac{2\pi}{m_N}\right)\bar{a}_I\rho(0) \tag{8.11}$$

where $\bar{a}_I$ is the imaginary part of $\bar{a}$.

The nuclear capture rate can be found using Fermi's golden rule [250] and Eqs. (8.9)–(8.11) as

$$\begin{aligned} \Gamma^{Cap}_{n_1,l_1} &= \frac{2}{\hbar}\int \mathrm{Im}(U(r))(R(n_1,l_1))^2 r^2 dr \\ &= \frac{2W}{\hbar}\int \frac{R(n_1,l_1)^2 r^2}{1+e^{\frac{r-c}{z}}} dr\,, \end{aligned} \tag{8.12}$$

where $R(n_1, l_1)$ is the hydrogenic radial wavefunction of the cascader and W is found by fitting the complex scattering length to experimental data [251].

8.2 Modifications to Cascade Model for Antihelium Nuclei

To predict the X-rays produced in the capture of antihelium nuclei, I extended the cascade model to accommodate antihelium nuclei as cascaders. In the following section, I describe the relevant changes to the cascade model that were implemented to predict the X-ray yields for

antihelium-3 nuclei. Future work will implement the antihelium exotic atom de-excitation X-rays into `Geant4` and assess their feasibility for antihelium identification, as outlined in Sec. 8.4.

In comparison to the cascaders previously described in the cascade model, the main difference for antihelium nuclei is their charge ($Z_c = -2$) and mass. The energy level spacing (8.1) and effective Bohr radius (8.2) of the nucleus-cascader system both depend on the cascader's mass and charge. The cascader mass dependence was already included in the inherited model. The cascader charge dependence was added by changing $Z \rightarrow |Z_c|Z$ in the relevant Bohr formulae, which are shown in Eqs. (8.1) and (8.2). After determining the energy level and orbital structure of the antihelium exotic atom, the main aspects of the calculation requiring modification were the initial principal quantum number (Sec. 8.2.1), the radiative transition rate (Sec. 8.2.3), and the optical potential between the antihelium cascader and nucleus (Sec. 8.2.4).

8.2.1 Initial Principal Quantum Number

The initial principal quantum number n_i of the cascader is estimated by assuming the antinucleus is captured when its kinetic energy is comparable to the binding energy of the nucleus, and requiring that angular momentum is conserved. From these assumptions it follows that:

$$n_i \sim n_e |Z_c| \sqrt{\frac{M_c}{M_e}} \tag{8.13}$$

using the same nomenclature as Eq. (8.3). Using Eq. (8.13), n_i is about 126 for antihelium-3 nuclei and 160 for antihelium-4 nuclei.

8.2.2 Auger Transitions

The Auger transition rate does not depend on the cascader charge, so Eq. (8.4) remains unchanged for antihelium exotic atoms. However, the initial state n_i and the energy difference between states (Eq. (8.1)) are larger for antihelium cascaders. This affects the condition that Auger transitions can only occur when $\Delta E_{n_1,n_2} > E_b$ where E_b is the binding energy of the electron. For

antihelium cascaders, this means that at the initial stage of the cascade that Auger transitions ejecting K shell electrons in Si ($E_b = 1.839\,\text{keV}$) are forbidden until $n \sim 70$. Therefore, the Auger emission of M shell ($E_b \sim 0.01\,\text{keV}$) and L shell electrons ($E_b \sim 0.1\,\text{keV}$) will dominate at the beginning of the cascade, until the Auger transitions provide enough energy to liberate K shell electrons. This does not affect the radiative transitions of interest for GAPS that occur at $n \lesssim 17$.

8.2.3 Radiative Transitions

The radiative transition probability depends on the cascader charge, which is reflected in Eqs. (8.1) and (8.8). Plugging Eq. (8.1) into Eq. (8.8), we find $\Gamma^{Rad}_{n_1,l_1\rightarrow n_2,l_2} \propto Z_c^4$, which indicates that the radiative transition probability is enhanced for $Z_c = -2$ cascaders. This cascader charge dependence was implemented into the cascade model to enable the simulation of antihelium exotic atoms.

8.2.4 Optical Potential for Nuclear Capture

Compared to previously studied cascaders, the nuclear capture probability is larger for antihelium cascaders because the cascader mass is larger and the effective Bohr radius is smaller. To modify the cascade model for antihelium cascaders, the radial wavefunctions $R(n, l)$ were updated to include the dependence of the effective Bohr radius on the cascader charge. Furthermore, W was selected based on its dependence on $\bar{a}_I$, and $\bar{a}_I$'s predicted scaling with the mass of the cascader. W has been determined for antiprotons in a variety of materials, and previous studies found that a cascade model with $W \sim 10\,\text{MeV}$ best fit the X-ray yields of antiprotonic exotic atoms in Al and S targets [160]. Following Ref. [252], the average scattering length is directly proportional to the reduced mass of the cascader-nucleus system M_c. Combining this proportionality with Eq. (8.11), we find $W \propto (1 + \frac{M_c}{m_N})$. This indicates that $W_{\bar{d}} \sim 1.5 W_{\bar{p}} = 15\,\text{MeV}$ and $W_{\overline{^3He}} \sim 2W_{\bar{p}} = 20\,\text{MeV}$ are the optimal W values for cascade simulations.

8.3 Exotic Atom X-rays from Antihelium-3

After extending the cascade model to accomodate antihelium cascaders, the cascade of antihelium-3 exotic atoms was simulated. The Auger transition, radiative transition, and nuclear capture probabilities were calculated for each state, and the cascade was simulated 10^6 times starting at $n_i = 126$, with the angular momentum state l following a modified statistical distribution $P(l) \propto (2l+1)e^{\alpha l}$. 10^6 iterations was sufficient to reduce the statistical error on the reported yields to an acceptable level.

The X-ray yield's dependence on the cascade model parameters are shown in the tables below. Table 8.1 demonstrates the X-ray yields in Si for different values of α with $W = 20\,\text{MeV}$ and $\Gamma_{ref} = 10^{16}\,\text{s}^{-1}$. Table 8.2 shows the X-ray yields for different values of W with $\alpha = 0.16$ and $\Gamma_{ref} = 10^{16}\,\text{s}^{-1}$.

Transition	**Energy [keV]**	α					
		0	0.04	0.08	0.12	0.16	0.2
$16 \rightarrow 15$	28.6	0.267	0.434	0.482	0.496	0.498	0.500
$15 \rightarrow 14$	34.9	0.347	0.565	0.630	0.646	0.652	0.651
$14 \rightarrow 13$	43.3	0.419	0.682	0.760	0.781	0.787	0.788
$13 \rightarrow 12$	54.5	0.478	0.770	0.857	0.879	0.885	0.887
$12 \rightarrow 11$	70.1	0.520	0.828	0.917	0.939	0.945	0.946
$11 \rightarrow 10$	92.1	0.552	0.863	0.950	0.970	0.976	0.977
$10 \rightarrow 9$	124.5	0.572	0.874	0.954	0.972	0.976	0.978
$9 \rightarrow 8$	174.0	0.370	0.530	0.564	0.572	0.574	0.573
$8 \rightarrow 7$	253.8	0.059	0.039	0.0271	0.0234	0.023	0.022

Table 8.1: X-ray yields from the cascade of antihelium-3 ($m_{casc} = 2814$) in Si target with $W = 20\,\text{MeV}$, for α in the 0–0.2 range.

For GAPS, the main antihelium-3 X-rays of interest for event discrimination are 70.1 keV ($12 \rightarrow 11$), 54.5 keV ($13 \rightarrow 12$), 43.3 keV ($14 \rightarrow 13$), and 34.9 keV ($15 \rightarrow 14$). As seen in Table 8.1, the X-ray yields in Si of these transitions are relatively insensitive changes in α for $\alpha \gtrsim 0.08$. Table 8.2 shows the dependence of the X-ray yields on W (which determines the nuclear capture rate). As W increases, the X-ray yields of lower n transitions are quenched. However, the transitions of interest for GAPS are not affected up to $W \sim 500\,\text{MeV}$, an order of magnitude above

Transition	Energy [keV]	W [MeV]							
		10	20	30	50	100	200	300	500
$16 \rightarrow 15$	28.6	0.499	0.498	0.499	0.499	0.499	0.498	0.499	0.498
$15 \rightarrow 14$	34.9	0.650	0.652	0.652	0.651	0.651	0.651	0.650	0.651
$14 \rightarrow 13$	43.3	0.786	0.787	0.786	0.786	0.786	0.786	0.786	0.787
$13 \rightarrow 12$	54.5	0.885	0.885	0.885	0.884	0.885	0.885	0.884	0.885
$12 \rightarrow 11$	70.1	0.945	0.945	0.945	0.945	0.945	0.945	0.944	0.945
$11 \rightarrow 10$	92.1	0.975	0.976	0.976	0.975	0.975	0.974	0.973	0.971
$10 \rightarrow 9$	124.5	0.983	0.976	0.970	0.957	0.925	0.869	0.818	0.733
$9 \rightarrow 8$	174.0	0.728	0.574	0.472	0.346	0.204	0.108	0.0712	0.040
$8 \rightarrow 7$	253.8	0.054	0.0225	0.0128	0	0	0	0	0

Table 8.2: X-ray yields from the cascade of antihelium-3 ($m_{casc} = 2814\,\mathrm{MeV}/c^2$) in Si target with $\alpha = 0.16$ for W in the 0–200 MeV range.

the expected value $W \sim 20\,\mathrm{MeV}$.

For antihelium-3 exotic atoms, the optimized parameters $\alpha = 0.16$, $W = 20\,\mathrm{MeV}$, and $\Gamma_{ref} = 10^{16}\,\mathrm{s}^{-1}$ were selected based on scaling the optimal parameters for antiprotonic exotic atoms. The expected X-ray yields for antihelium-3 exotic atoms in Si with the optimized parameters is shown in Table 8.3. The antihelium-3 X-rays have high yields in the 20–100 keV range, and could be used to confirm a potential GAPS antihelium-3 candidate event. These X-rays will be incorporated into `Geant4` to enable studies that assess their feasibility for antihelium identification, as discussed in the following section.

Transition	Energy (keV)	Yield
$8 \rightarrow 7$	253.8	0.022
$9 \rightarrow 8$	174.0	0.574
$10 \rightarrow 9$	124.5	0.976
$11 \rightarrow 10$	92.1	0.976
$12 \rightarrow 11$	70.1	0.945
$13 \rightarrow 12$	54.5	0.885
$14 \rightarrow 13$	43.3	0.787
$15 \rightarrow 14$	34.9	0.652
$16 \rightarrow 15$	28.6	0.498
$17 \rightarrow 16$	23.7	0.356

Table 8.3: X-rays from de-excitation of antihelium-3 exotic atom, as predicted with the cascade model with optimized parameters $W = 20\,\mathrm{MeV}$, $\alpha = 0.16$, and $\Gamma_{ref} = 10^{16}\,\mathrm{s}^{-1}$.

8.4 Integration of Antiprotonic and Antideuteronic Exotic Atoms into Geant4

The previous chapters demonstrated that antihelium exotic atoms will produce exotic atom X-rays that can be detected in the GAPS tracker. This section will outline the previous work that integrated antiprotonic and antideuteronic X-rays into `Geant4`, providing a blueprint of the next steps to similarly implement the antihelium exotic X-rays in `Geant4` in order to assess their impact on the GAPS antihelium identification technique.

Until recent years, exotic atom physics was not included in the `Geant4` software package. In previous GAPS sensitivity studies, the simulation was conducted in two parts: (1) determining the stopping positions of the incoming antinuclei, and (2) generating the atomic X-rays and from the stopping position to estimate the energy spectrum in the instrument due to exotic atom de-excitation. Recently, the `Geant4` team added a package to simulate the X-rays produced in muonic exotic atoms. This package was extended to simulate the X-rays produced in the de-excitation of antiprotonic and antideuteronic exotic atoms by adding a table of the X-ray energies and yields found by the cascade model. This enabled a full simulation of the slow-down, capture, de-excitation, and annihilation of incoming antiprotons and antideuterons.

The implementation of antiprotonic and antideuteronic exotic atom de-excitation X-rays in `Geant4` was validated through a benchmarking simulation similar to the studies reported in Ch. 7. 10^5 antiprotons and antideuterons were generated with 1 keV kinetic energy in a 2.5 mm^3 cube (Fig. 7.1) of silicon or aluminum — the materials that comprise the GAPS tracker. Each event was analyzed to determine the X-ray yields in the 20–120 keV range, and the `Geant4` yields were compared to the expected results of the cascade model. The `Geant4` simulation precisely reproduced the expected X-ray yields and energies in silicon and aluminum, as shown in Fig. 8.2 and Table 8.4.

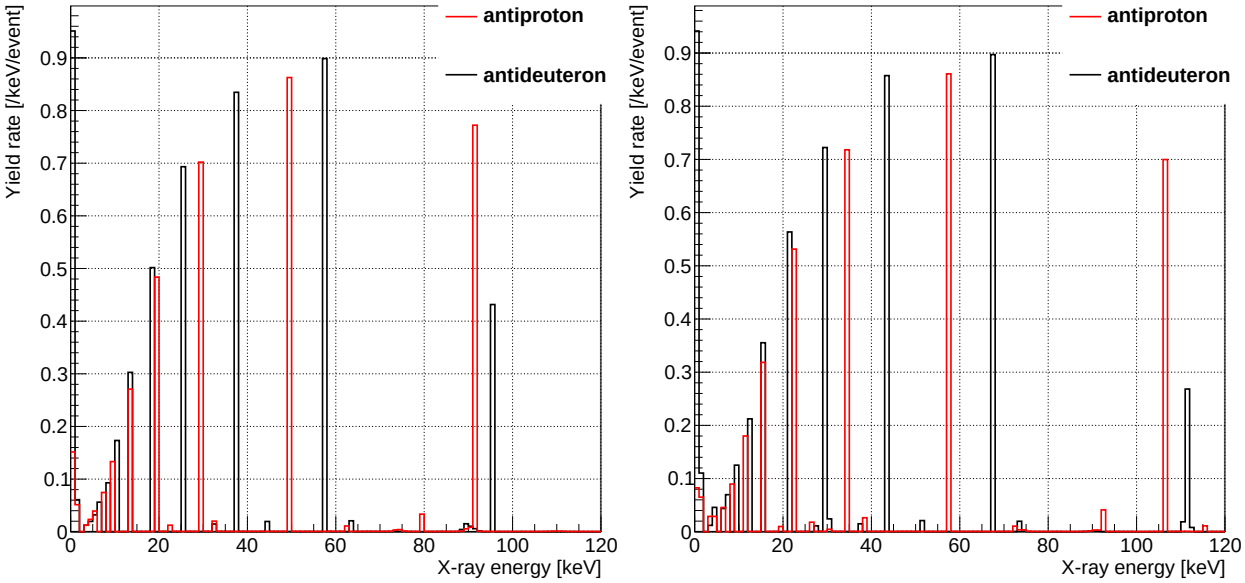

Figure 8.2: Observed energies and yields of 0–120 keV photons produced in antiproton and antideuteron annihilations in aluminum (left) and silicon (right) in `Geant4.10.7.1`.

Table 8.4: Characteristic energies and yields of antiprotonic and antideuteronic exotic atom X-rays produced in aluminum and silicon targets. Each table shows the energy of a characteristic X-ray transition, its predicted yield from the cascade model, and the observed yield in `Geant4.10.7.1`.

Antiproton in silicon		
Energy [keV]	Yield (Model)	Yield (MC)
15.5	0.317	0.318
22.6	0.531	0.531
34.8	0.719	0.718
57.8	0.827	0.861
106.4	0.698	0.700

Antideuteron in silicon		
Energy [keV]	Yield (Model)	Yield (MC)
21.4	0.563	0.564
30.0	0.742	0.723
43.7	0.857	0.858
67.5	0.897	0.897
111.7	0.273	0.269

Antiproton in aluminum		
Energy [keV]	Yield (Model)	Yield (MC)
13.4	0.272	0.271
19.5	0.484	0.484
30.0	0.702	0.702
49.5	0.862	0.863
91.6	0.765	0.772

Antideuteron in aluminum		
Energy [keV]	Yield (Model)	Yield (MC)
18.4	0.502	0.502
25.8	0.694	0.693
37.6	0.835	0.835
57.9	0.899	0.899
96.1	0.432	0.432

8.5 Conclusions and Future Work

The cascade model was successfully extended to describe antihelium exotic atom de-excitation, and used to predict the X-ray energies and yields produced by antihelium-3 exotic atoms. The key modifications to the model incorporated the cascader charge dependence into the relevant calculations, including the exotic atom's energy level spacings, effective Bohr radius, and initial principal quantum number, as well as the radiative transition rate and nuclear capture rate at each state in the cascade. Antihelium-3 exotic atoms produce several X-rays in the 20–100 keV range with high yields that can be used to identify antihelium-3 nuclei with GAPS. The predicted X-ray energies and yields will be implemented into the `Geant4` simulation toolkit, following the approach used to integrate antiprotons and antideuterons outlined in Sec. 8.4. Future studies will predict the X-ray energies and yields of antihelium-4 exotic atoms using the extended cascade model, and investigate the feasibility of using the antihelium X-rays in the GAPS identification technique.

Chapter 9: Antihelium Sensitivity Study

As discussed in Sec. 2.3.1, cosmic antinuclei provide a promising avenue to probe beyond the Standard Model (BSM) physics. The GAPS experiment is optimized to detect low-energy antideuterons, as well as to provide unprecedented sensitivity to low-energy antiprotons and antihelium nuclei. A major part of my work on GAPS was developing an antihelium identification technique and estimating the GAPS sensitivity to antihelium nuclei. This sensitivity study was largely motivated by the report of antihelium candidate events by AMS-02 [236], which generated considerable interest in antihelium nuclei as probes of DM and other beyond the Standard Model theories.

Generally, the flux of cosmic antinuclei can be attributed to:

(1) exotic sources such as DM decay or annihilation or primordial black hole evaporation,

(2) secondary antinuclei, produced in collisions of cosmic rays with interstellar gas or supernova shells, or

(3) primordial antinuclei, created in the early Universe through nonhomogeneous baryosynthesis, that evolve in antimatter domains and currently exist in the form of macroscopic antimatter objects like antimatter stars.

While low-energy antideuterons are widely considered to be a smoking-gun signal of DM annihilation or decay, the detection of cosmic antihelium could have another interpretation. Several authors have claimed that the discovery of a single cosmic antihelium nucleus would point toward the existence of antimatter stars or even antimatter galaxies (e.g. [253]). Interestingly, these objects are not predicted to produce antideuterons, because antideuterons are burned in nuclear reactions within the antistars [142].

Gamma-ray observations are used to constrain the abundance of nearby antistars [254]. If ordinary matter in the interstellar medium (ISM) makes contact with the antistar it would annihilate, producing neutral pions that subsequently decay to gamma-rays. The characteristic spectrum of this annihilation signature peaks at approximately half the mass of the neutral pion at ~70 MeV and cuts off around the mass of the proton at 938 MeV [255]. Previous gamma-ray observations have nearly excluded large antimatter domains in the Universe [256, 257]; however smaller anti-objects such as antistars or anticlouds remain feasible [258]. Recent observations with the Fermi Large Area Telescope set upper limits on the local antistar fraction, indicating that a region of size $O(1\,\mathrm{pc})$ around the solar system should be free of antistars [259]. Within these constraints, antistars still provide a viable explanation for the AMS-02 antihelium candidate events, as is discussed in detail in Ref. [260].

Prior to AMS-02, BESS-Polar set an exclusion limit on the antihelium to helium flux ratio of $1.0 \cdot 10^{-7}$ in the range of 1.6–14 GV [261], the most stringent upper limit on the antihelium flux before the tantalizing AMS-02 reports. Naively, any DM model explaining the AMS-02 antihelium nuclei candidate events would overproduce both antiprotons and antideuterons. Attempts to explain the AMS-02 antihelium candidate events predict fluxes in the GAPS energy range covering many orders of magnitude. These range from standard cosmic rays with heavily-tuned formation models [262, 263], to new DM annihilation channels [138, 264–268], or the existence of an antistar within our Galaxy [260, 269].

Data taking, analyses, and interpretation of AMS-02 candidate antihelium nuclei events are still ongoing. Given the transformative nature of such a discovery, verification with a complementary experimental technique is important. GAPS will be complementary to AMS-02, as it has orthogonal systematic uncertainties and operates in the lower-energy range where the predicted contribution from new-physics models compared to astrophysical background is highest. One key advantage of the Antarctic flight path of GAPS, which BESS-Polar similarly benefited from, is the low geomagnetic cutoff compared to the trajectory of AMS-02 on the International Space Station. The GAPS antihelium measurement will provide crucial information to constrain these models,

and the detection of low-energy antihelium nuclei would be an exciting sign of new physics.

This chapter will report the GAPS antihelium sensitivity calculation that I led. The GAPS flight time-of-flight geometry has been slightly modified since this calculation was performed; however, an identical study using the new geometry demonstrated a flux sensitivity that is consistent with the results shown below, and will be presented in a forthcoming publication. The simulation framework is described in Sec. 9.1. The instrument simulations and identification technique are presented in Sec. 9.2. The atmospheric simulations used to estimate background fluxes and the antihelium nuclei sensitivity of GAPS are presented in Sec. 9.3. Conclusions and the outlook for the GAPS experiment are presented in Sec. 9.4.

9.1 Simulation Framework

A dedicated `Geant4`-based simulation [214, 270] and analysis framework was developed to model the GAPS payload and its interactions with cosmic-rays. The simulated geometry includes active detector components (Si(Li) detectors in the tracker, plastic scintillator paddles in the TOF) and their electronics response, and the passive structural components.

The simulation assumes a time-of-flight resolution of 300 ps – the target timing resolution for the GAPS TOF system. The identification analysis is insensitive to the TOF resolution to the extent that using the demonstrated TOF resolution does not change the result. To simulate the physics processes, the `FTFP_BERT_HP` physics list was used in `Geant4v10.6.p02`. The implemented `Geant4` physics processes for antiproton annihilations at-rest, as described by the Fritiof model [227], were validated by comparison to available data from accelerator-based experiments [229] (see Ch. 7).

Primary antihelium-3 nuclei and their dominant backgrounds (antiprotons, protons, and α-particles) were generated from the top of the instrument (TOI). The simulated primary particles were generated with a uniform velocity distribution ($0.1 < \beta_{\mathrm{TOI,gen}} < 1$) and an isotropic angular distribution from the surface of a 4.4 m side-length cube encapsulating the GAPS instrument. The geometrical acceptance of the instrument is calculated following the standard approach from [271].

For this study, 10^{11} protons, $6 \cdot 10^9$ α-particles, $5 \cdot 10^8$ antiprotons, and $2 \cdot 10^8$ antihelium-3 nuclei were generated. The simulations made use of the intended GAPS trigger scheme that is designed to reject high-velocity and high-charge particles. Identification studies focused on rejecting the dominant $|Z| = 1$ and $|Z| = 2$ backgrounds, since the trigger and preselection (Sec. 9.2.2) criteria reliably reject background contamination from heavier nuclei, such as carbon and boron. The trigger scheme requires that the TOF energy depositions are in the range of slow-moving $|Z| = 1$ or $|Z| = 2$ to reject minimally ionizing (high-velocity) and high-charge particles. In addition, at least eight hits in the combined TOF system, with at least three hits each in the TOF umbrella and TOF cube, are required to focus the data taking on annihilating antinuclei and reject non-annihilating positively charged particles with low secondary multiplicity. The trigger algorithm provides a rejection factor of approximately 700 and 50 for protons and α-particles, respectively, while retaining a significant fraction (>50%) of incoming antinuclei [164].

9.2 Particle Identification

9.2.1 Event Reconstruction

As illustrated in the right panel of Fig. 9.1, the reconstruction algorithm reconstructs the primary particle's trajectory, its stopping vertex, and secondary tracks emerging from the vertex. The GAPS algorithm starts by identifying the earliest hits in the TOF and then iteratively adds hits from the tracker that are spatially and energetically consistent with the primary track. In the next step, a search for the annihilation star signature is performed along the primary particle trajectory to identify secondary tracks emerging from the stopping vertex. In the final step, a minimization procedure is performed to find the most likely stopping vertex. This algorithm has an efficiency of >80% to identify antinuclei that stopped inside the tracker volume and reconstructs the stopping vertex to within 60 mm for about 70% of the events. The identification analysis (Sec. 9.2.3) takes into account the typical energy loss in the instrument to determine the primary particle's reconstructed velocity at TOI, $\beta_{\mathrm{TOI,rec}}$. The combination of the reconstruction algorithm with the energy loss correction achieves a velocity resolution of less than 5% in the relevant velocity range

$(0.1 < \beta_{\mathrm{TOI,gen}} < 0.6)$.

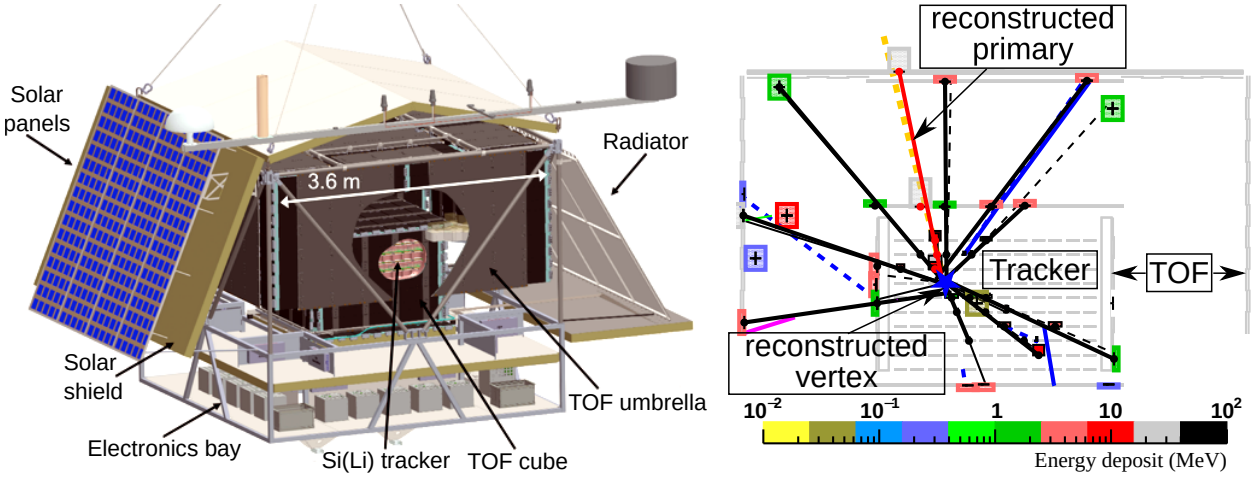

Figure 9.1: *Left:* Schematic overview of the GAPS instrument: two layers of plastic scintillator form the inner TOF "cube" and outer TOF "umbrella". The inner TOF cube encapsulates a tracker composed of 10 layers of 100 Si(Li) detectors. *Right:* Antihelium-3 nucleus event topology: the orange dashed and red solid line indicate the simulated and the reconstructed primary antihelium-3 nuclei, respectively. The blue star designates the reconstructed stopping vertex. The thick solid black lines demonstrate the reconstructed tracks emerging from the stopping vertex. Thin black solid (dashed) lines represent secondary π^+ (π^-), blue solid (dashed) lines represent secondary positrons (electrons), and magenta solid (dashed) lines represent secondary μ^+ (μ^-) from the simulation. The colored boxes show the energy depositions of the registered hits. The color of the box indicates the amount of energy deposited, and the size of the boxes correspond to the estimated error in position.

9.2.2 Analysis Preselection

Before the identification analysis, preselection criteria (or cuts) are applied to select well-reconstructed events. These preselection cuts require at least one hit from the reconstructed primary track in each of the TOF umbrella and TOF cube, a reconstructed stopping vertex in the tracker, no more than one active volume on the reconstructed primary track without a registered hit, and the energy depositions on the primary track consistent with a $|Z| = 1$ or $|Z| = 2$ particle at the reconstructed velocity. This last cut is essential to suppress events, typically of low velocity, where the primary particle annihilates in the TOF. This charge cut is applied using the truncated mean energy deposition event variable, which gives a measure of the primary's $\mathrm{d}E/\mathrm{d}x$ and is described in detail in the following section. Fig. 9.2 shows the upper and lower bounds on

the truncated mean energy deposition as a function of $\beta_{\mathrm{TOI,rec}}$ for $|Z| = 2$ particles, which was defined using a sample of antihelium-3 nucleus events. A similar process was performed with a sample of antiproton events to define the $|Z| = 1$ cut.

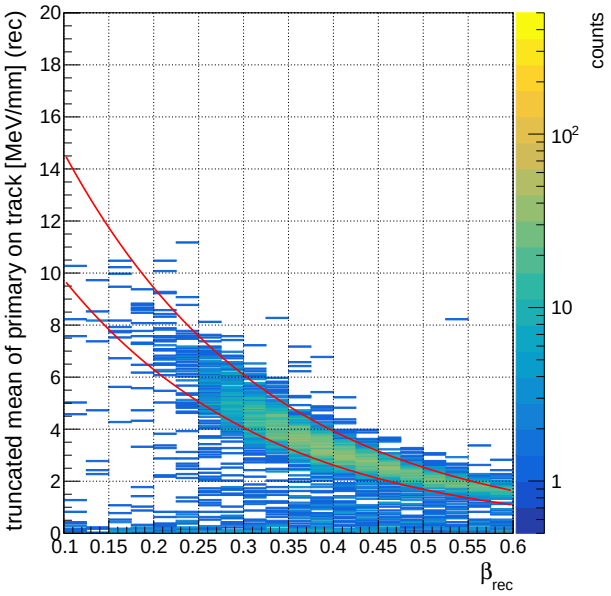

Figure 9.2: Truncated mean energy deposition as a function of $\beta_{\mathrm{TOI,rec}}$ for a sample of antihelium-3 events used to define preselection criteria. Red lines indicate the upper and lower bounds on the truncated mean energy deposition used to select $|Z| = 2$ particles.

Fig. 9.3 compares the GAPS antiproton and antihelium-3 nucleus acceptance for events that trigger (solid lines), have a reconstructed stopping vertex in the tracker (dashed lines), and pass the preselection criteria outlined above (dot-dashed lines). For the stopping and preselection acceptances shown in Fig. 9.3, events were required to have a reconstructed velocity $\beta_{\mathrm{TOI,rec}}$ in the range of 0.3–0.6 to ensure that the primary could stop in the TOF cube.

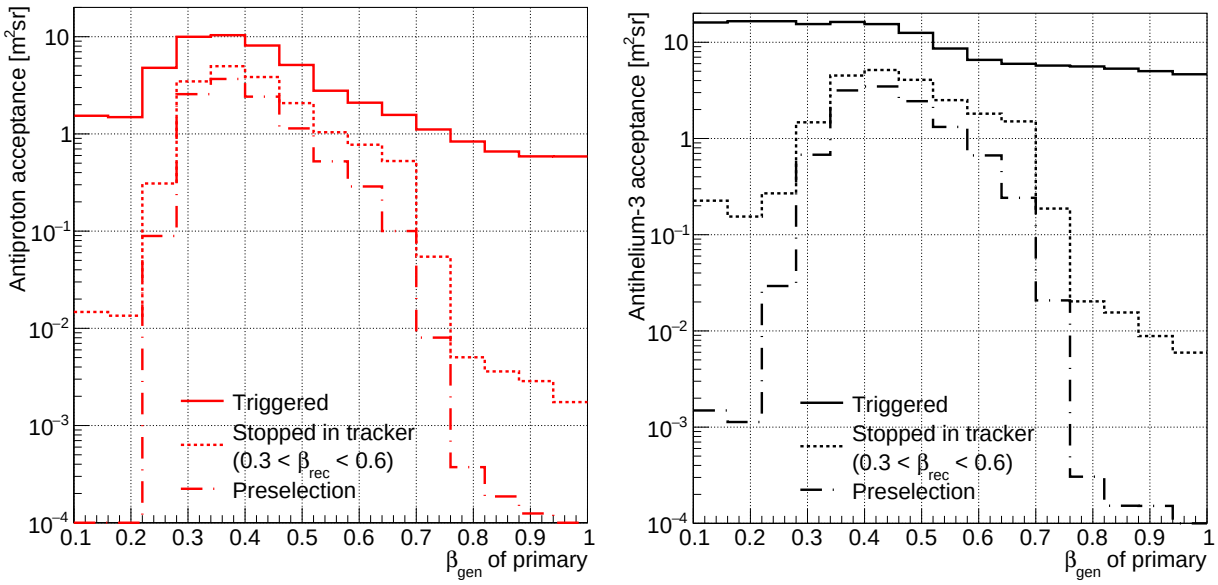

Figure 9.3: Acceptance as a function of generated β at TOI for antiproton (left) and antihelium-3 nuclei (right) for different filtering criteria. Stopping and preselection criteria required that that the reconstructed beta $\beta_{\text{TOI,rec}}$ was in the range of 0.3–0.6. The preselection criteria helps select well-reconstructed events, which can be seen in the difference between the stopping and preselection acceptances with β_{gen} outside of the 0.3–0.6 range.

9.2.3 Identification Analysis

Using the information from the event reconstruction (Sec. 9.2.1), the following seven variables are combined in an identification analysis to identify antihelium-3 nuclei:

Truncated mean energy deposition: this variable is calculated by sorting the primary particle's energy depositions normalized to the pathlength in the corresponding volume ($\mathrm{d}E/\mathrm{d}x$) in ascending order, followed by averaging the lower half of the $\mathrm{d}E/\mathrm{d}x$ values. Since $\mathrm{d}E/\mathrm{d}x$ scales with Z^2/β^2, selecting the primary hits with lower $\mathrm{d}E/\mathrm{d}x$ values ensures that energy depositions close to the stopping vertex, when the particle's β has decreased from ionization losses, are not included in the $\mathrm{d}E/\mathrm{d}x$ calculation. This allows determining the magnitude of the primary particle's charge $|Z|$ when combining it with the reconstructed primary particle's velocity $\beta_{\text{TOI,rec}}$ (Fig. 9.4, right). It provides major rejection power to distinguish antihelium-3 nuclei events from $|Z| = 1$ particles (antiprotons and protons) as well as carbon and other heavier nuclei.

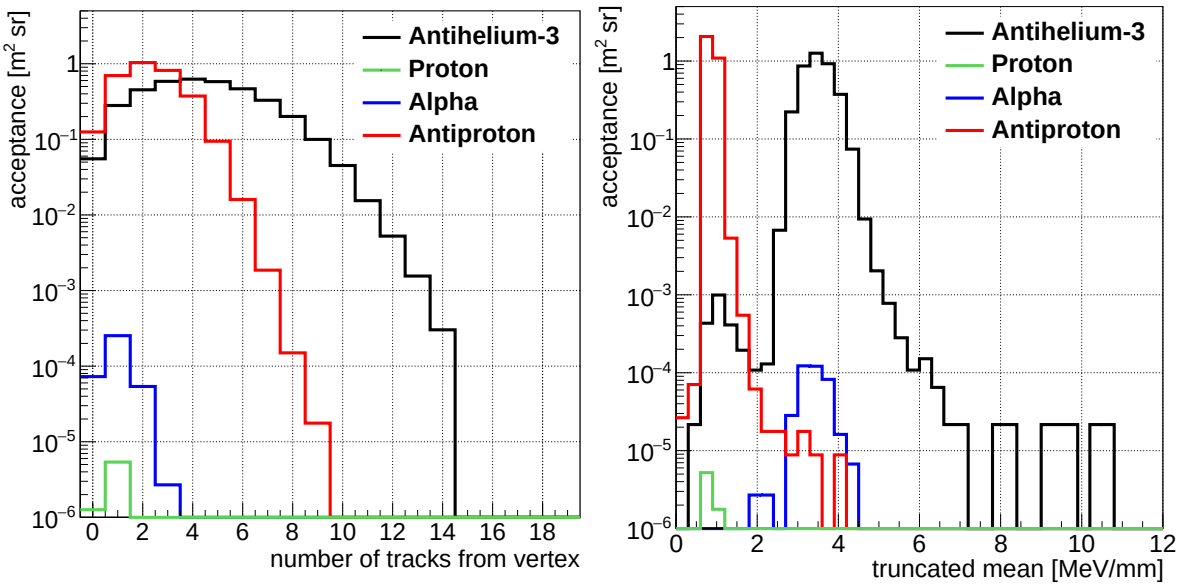

Figure 9.4: Examples of the estimated acceptance for two identification variables for antihelium-3 nuclei, antiprotons, protons, and α-particles passing trigger and quality cuts (velocity range $0.39 < \beta_{\mathrm{TOI,gen}} < 0.41$): *Left:* Number of reconstructed tracks from the stopping vertex. *Right:* Truncated mean energy deposition on the primary track.

Number of secondary tracks from the vertex: this is determined using the multiplicity of reconstructed secondary tracks emerging from the vertex. For positively charged particles that pass the trigger, the secondary multiplicity is much lower than for antihelium-3 nuclei (Fig. 9.4, left).

Total number of hits: this variable is determined by counting the total number of registered hits in the TOF and tracker. Similar to the number of secondary tracks from the vertex, the total number of hits provides means to assess the secondary multiplicity. The number of hits for antihelium-3 nuclei annihilation events is much higher than for positively charged particles.

Total energy deposition: this variable is calculated by summing all energy depositions in the TOF and tracker during an event. Antinuclei that annihilate in the tracker deposit a large amount of energy in the instrument.

Average velocity of secondary tracks: the velocity of each secondary track emerging from the vertex is determined using the timing information associated with the reconstructed stopping

vertex and the successive hits in the TOF. The average velocity of the secondary tracks is higher for antinuclei than for nuclei because the annihilation process enables the formation of relativistic pions, whereas inelastic collisions of particles must conserve baryon number and are more likely to produce lower-velocity protons.

Isotropy of secondary tracks: this variable is determined by averaging the cosine of the angle between the primary particle's direction and the direction reconstructed between individual tracker hits and the stopping vertex. Antinuclei annihilation at-rest has a more isotropic secondary signature while inelastic collisions of high-velocity protons and α-particles are more forward-boosted.

Primary column density: this variable evaluates the grammage traversed by the primary particles from the top of the instrument to the stopping vertex. For the same primary velocity, antihelium-3 nuclei will typically traverse 25% less grammage than antiprotons, protons, and α-particles before stopping.

Next, probability distributions of these variables for the different particle types are created as a function of the primary particle's generated velocity $\beta_{\mathrm{TOI,gen}}$ and the cosine of the generated zenith angle $\cos(\theta_{\mathrm{TOI,gen}})$. The construction of these probability distributions accounts for velocity resolution effects by introducing a Gaussian smearing of the probability distributions, which depends on the β resolution as a function of the primary's velocity. The probability distributions are used to perform an identification analysis to determine the likelihood of each event being a signal event relative to a background event. The likelihood identifier $\mathcal{P}^a$ describing the likelihood for a given event to be a particular particle species a is calculated as:

$$\mathcal{P}^a = \sqrt[N]{\prod_i^N P_i^a \left(\beta_{\mathrm{TOI,rec}}, \cos(\theta_{\mathrm{TOI,rec}})\right)}. \tag{9.1}$$

Here, $P_i^a(\beta_{\mathrm{TOI,rec}}, \cos(\theta_{\mathrm{TOI,rec}}))$ is a probability distribution for one of the $N = 7$ identification variables, indexed by i and evaluated at an event's $\beta_{\mathrm{TOI,rec}}$ and $\cos(\theta_{\mathrm{TOI,rec}})$ for a certain particle

species a. These $\mathcal{P}^a$ values are used to construct the likelihood ratio L:

$$L = \frac{\mathcal{P}^{^3\overline{\mathrm{He}}}}{\mathcal{P}^{^3\overline{\mathrm{He}}} + \mathcal{P}^{\overline{p}} + \mathcal{P}^{p} + \mathcal{P}^{\alpha}} \tag{9.2}$$

In the analysis that follows, the natural logarithm of the ratio $-\ln(L)$ is used as the identification variable. A low $-\ln(L)$ value indicates a high probability of being an antihelium-3 nucleus event. Before evaluating the likelihood ratio, two additional cuts were applied. Candidate antihelium-3 nucleus events are required to have a truncated mean energy deposition (Figs. 9.2 and 9.4, right) corresponding to a charge of $|Z| = 2$, to ensure an unambiguous charge measurement of the primary. Furthermore, candidate events are required to have a reconstructed velocity $\beta_{\mathrm{TOI,rec}}$ in the range of 0.3–0.6 to assure that a candidate antihelium-3 nucleus could stop inside the TOF cube. This analysis was conducted for three different $\cos(\theta_{\mathrm{TOI,rec}})$ ranges ($\cos(\theta_{\mathrm{TOI,rec}}) = [0, 1/3]$, $[1/3, 2/3]$, $[2/3, 1]$). For each angular range, cuts on $-\ln(L)$ were optimized to reject background events while maximizing GAPS's antihelium-3 nuclei acceptance (Sec. 9.3.1).

9.3 Sensitivity Calculation

9.3.1 Atmospheric Simulations

To determine the number of background events passing antihelium-3 nuclei selection, the identification acceptance calculation for antihelium-3 nuclei and the various background channels at the TOI need to be combined with the anticipated background flux levels. For this purpose, the TOI background fluxes were determined using a separate `Geant4` simulation, based on `PLANETOCOSMICS` [272], that propagates geomagnetically- and solar-modulated cosmic-ray fluxes [145] from the top-of-the-atmosphere (TOA) to TOI. The background fluxes were simulated for the expected LDB float altitude of 37 km above Antarctica during December. The antiproton fluxes include a contribution from atmospherically produced antiprotons. This model was validated with available data, including the 2012 pGAPS flight [161], and it determines the energy loss and survival probability of antihelium-3 nuclei traversing the atmosphere as well as the energy

and angular distributions of background particles.

Combining the TOI background fluxes with measurement time and their corresponding acceptances to pass all antihelium-3 nucleus selection criteria determines the required background rejection level. The $-\ln(L)$ selection criterion for each angular range was chosen such that one detected antihelium-3 nucleus provides an unambiguous discovery. Fig. 9.5 compares the acceptance for antihelium-3 nuclei after preselection cuts with the acceptance after all identification cuts. The antihelium-3 nuclei identification efficiency is on the level of about 50% for the peak region around $\beta_{\mathrm{TOI,gen}} \approx 0.34 - 0.52$. To estimate the number of background events passing cuts, the background acceptances after all identification cuts are integrated with the TOI background fluxes. A detailed publication on the atmospheric studies is forthcoming.

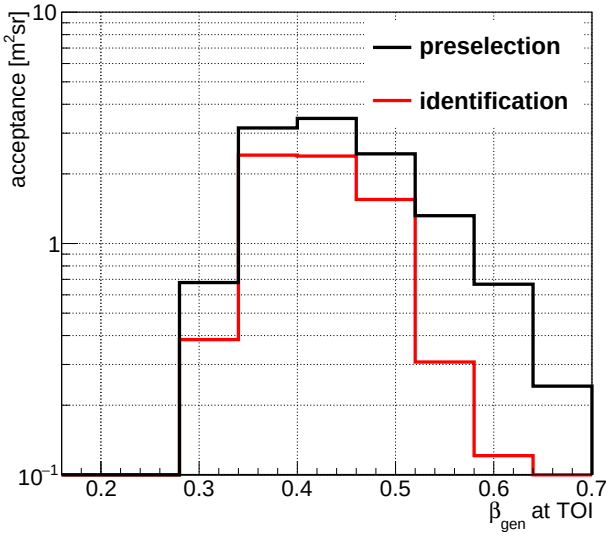

Figure 9.5: The GAPS acceptance as a function of $\beta_{\mathrm{TOI,gen}}$ for antihelium-3 nuclei after preselection and identification cuts.

9.3.2 Sensitivity Estimate

The number of predicted mean background events (spurious events that pass the antihelium-3 nuclei cuts) after trigger, preselection, and identification cuts is on the order of about 10^{-3} for one LDB flight of 35 days. The subsequent estimation of sensitivity was done with a Bayesian analysis [273]. Combining the number of background events b with the expectation of one de-

tected antihelium-3-nucleus-like event ($n = 1$), the antihelium-3 flux sensitivity S of the GAPS experiment can be calculated for a given confidence interval. The mean value of S is calculated from:

$$S = \frac{n - b}{\bar{A}_{\mathrm{id}} T \Delta E \epsilon_{\mathrm{geo}} \epsilon_s}. \tag{9.3}$$

Here, T is the observation time (three 35-day LDB flights = 105 days). $\bar{A}_{\mathrm{id}}$ is the average antihelium-3 nuclei identification acceptance in the TOA kinetic energy range of 0.11–0.3 GeV/n. To determine the GAPS acceptance in this TOA energy range, the antihelium-3 nuclei identification acceptance as a function of $\beta_{\mathrm{TOI,gen}}$ was mapped to the TOA kinetic energy per nucleon using the results of the atmospheric studies described in Sec. 9.3.1. ϵ_{geo} is the geomagnetic cutoff efficiency for antihelium-3 nuclei (≈0.85 in the TOA energy range) [274]. ϵ_s is the atmospheric survival probability for antihelium-3 nuclei, which describes the probability of an antihelium-3 nucleus to traverse the atmosphere without being absorbed (≈0.5 averaged across the TOA energy range). The corresponding antihelium-3 nuclei single event sensitivity is $1.3^{+4.5}_{-1.2} \cdot 10^{-6}\,\mathrm{m^{-2}sr^{-1}s^{-1}(GeV/}n\mathrm{)^{-1}}$ (95% confidence level). For one 35-day LDB flight, the projected GAPS antihelium-3 nuclei sensitivity is $4.0^{+13.3}_{-3.8} \cdot 10^{-6}\,\mathrm{m^{-2}sr^{-1}s^{-1}(GeV/}n\mathrm{)^{-1}}$ (95% confidence level). The uncertainties in the projected sensitivities are estimated using the upper and lower limits of true antihelium-3 nuclei detections from the 95% confidence interval, based on the calculated mean number of background events. Fig. 9.6 shows the three-flight sensitivity in comparison with antihelium-3 fluxes predicted by a variety of dark matter [138, 262, 266–268] and astrophysical background [275–277] models. Within the 95% confidence interval, three GAPS flights have the potential to discover dark matter models annihilating into W^+W^- [266].

9.3.3 Future Work

The presented identification technique does not exploit the rejection power associated with exotic-atom de-excitation X-rays, which are an important component of the GAPS antideuteron detection concept [156]. As discussed in Chapter 8, the exotic atom cascade model [160] was extended to include antihelium-3 nuclei. This model indicates high yields for the relevant antihelium-

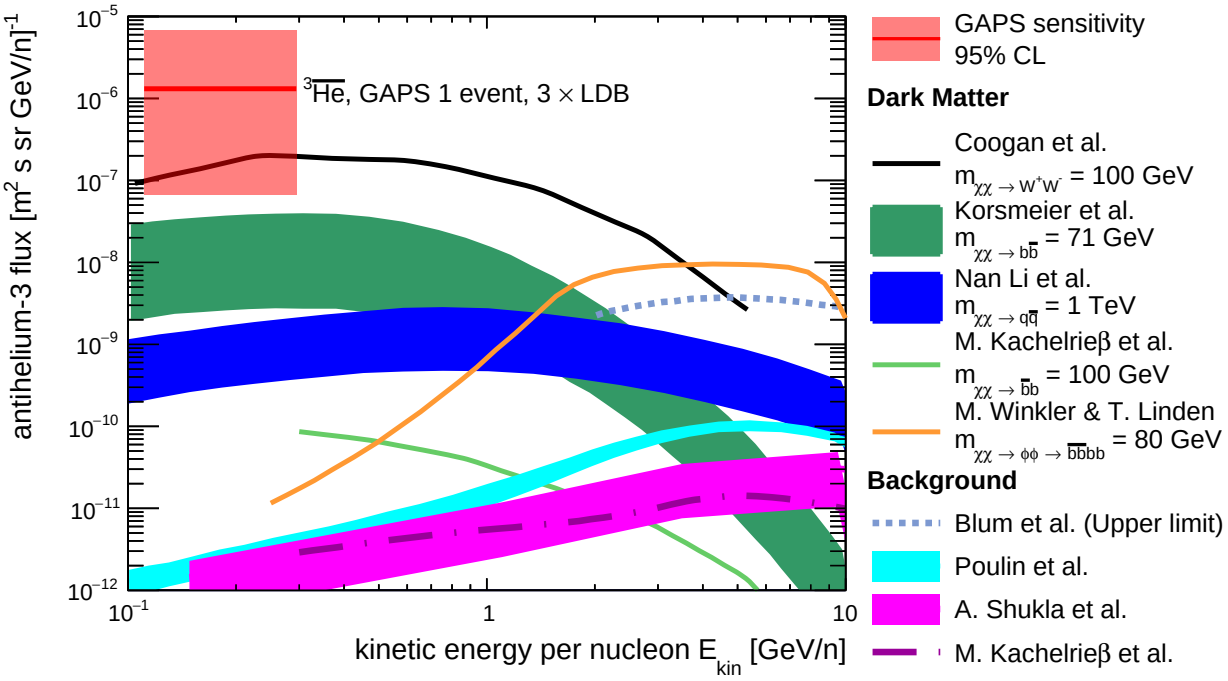

Figure 9.6: The solid red line shows the single event sensitivity of GAPS to antihelium-3 nuclei (95% confidence level) for three LDB flights of 35 days each. The red box indicates the upper and lower bounds of the 95% confidence level. Also shown are the antihelium-3 flux predicted by a variety of dark matter [138, 262, 266–268] and standard astrophysical background [275–277] models. For theoretical predictions, the error bands illustrate uncertainties in the coalescence momentum, but also include propagation uncertainties.

3 X-rays (34.9, 43.3, 54.5, 70.1 keV). Efforts are currently underway to improve the rejection power by exploiting this X-ray signature of antihelium-3 nuclei stopping in the GAPS tracker.

Studies are also planned to determine the sensitivity of GAPS to cosmic antihelium-4 nuclei. Due to the higher secondary multiplicity in antihelium-4 nuclei events, the event variables used to identify antihelium-3 nuclei are expected to provide even stronger rejection of background particles when applied to antihelium-4 nuclei.

9.4 Conclusion and Outlook

Low-energy cosmic antihelium nuclei provide an ultra-low background signature of dark matter. Based on full instrument simulation, event reconstruction, and realistic atmospheric influence simulations, a projected GAPS flux sensitivity to antihelium-3 nuclei, assuming the detection of

one event in three 35-day LDB flights, was determined to be $1.3^{+4.5}_{-1.2} \cdot 10^{-6}$ $m^{-2}sr^{-1}s^{-1}(GeV/n)^{-1}$ (95% confidence level) in the energy range of 0.11–0.3 GeV/n. The GAPS sensitivity to antihelium-3 nuclei extends to lower energies than any previous experiment, complementing the exclusion limits set by BESS-Polar and ongoing searches with AMS-02. Due to its orthogonal systematic uncertainties and sensitivity to the lower-energy range, where the predicted contribution from new-physics models is highest, GAPS will provide crucial input to interpret the AMS-02 candidate events. This unique sensitivity can be further enhanced by increasing the tracker active area (instrumenting with more Si(Li) detectors), increasing flight times, and improving the background suppression techniques. Future GAPS missions, such as through the NASA Pioneer program, would allow expanding this sensitivity to the $O(10^{-7})$ $m^{-2}sr^{-1}s^{-1}(GeV/n)^{-1}$ flux range.

References

[1] N. Aghanim, Y. Akrami, M. Ashdown, J. Aumont, C. Baccigalupi, M. Ballardini, A. J. Banday, R. B. Barreiro, N. Bartolo, and et al., "Planck 2018 results," *Astronomy and Astrophysics*, vol. 641, A6, 2020.

[2] D. E. S. Collaboration, "Dark Energy Survey year 1 results: Cosmological constraints from galaxy clustering and weak lensing," *Physical Review D*, vol. 98, no. 4, 043526, p. 043 526, Aug. 2018. arXiv: 1708.01530 [astro-ph.CO].

[3] B. Kelvin, *Baltimore Lectures on Molecular Dynamics and the Wave Theory of Light*, ser. Cambridge Library Collection - Physical Sciences. Cambridge University Press, 2010.

[4] F. Zwicky, "Die Rotverschiebung von extragalaktischen Nebeln," *Helvetica Physica Acta*, vol. 6, pp. 110–127, Jan. 1933.

[5] ——, "On the Masses of Nebulae and of Clusters of Nebulae," *Astrophysical Journal*, vol. 86, p. 217, Oct. 1937.

[6] V. C. Rubin and J. Ford W. Kent, "Rotation of the Andromeda Nebula from a Spectroscopic Survey of Emission Regions," *Astrophysical Journal*, vol. 159, p. 379, Feb. 1970.

[7] M. S. Roberts, "A High-Resolution 21-CM Hydrogen-Line Survey of the Andromeda Nebula," *Astrophysical Journal*, vol. 144, p. 639, May 1966.

[8] B. Paczynski, "Gravitational Microlensing by the Galactic Halo," *Astrophysical Journal*, vol. 304, p. 1, May 1986.

[9] T. Lasserre, "Not enough stellar mass machos in the galactic halo," *Astron. Astrophys.*, vol. 355, pp. L39–L42, 2000. arXiv: astro-ph/0002253.

[10] M. Milgrom, "A modification of the Newtonian dynamics as a possible alternative to the hidden mass hypothesis.," *Astrophysical Journal*, vol. 270, pp. 365–370, Jul. 1983.

[11] M. Milgrom and R. H. Sanders, "Modified Newtonian Dynamics Rotation Curves of Very Low Mass Spiral Galaxies," *Astrophysical Journal*, vol. 658, no. 1, pp. L17–L20, Mar. 2007. arXiv: astro-ph/0611494 [astro-ph].

[12] Y. Mellier, "Probing the Universe with Weak Lensing," *Annual Review of Astronomy and Astrophysics*, vol. 37, no. 1, pp. 127–189, 1999. eprint: https://doi.org/10.1146/annurev.astro.37.1.127.

[13] D. Clowe, A. Gonzalez, and M. Markevitch, "Weak-Lensing Mass Reconstruction of the Interacting Cluster 1E 0657-558: Direct Evidence for the Existence of Dark Matter," *Astrophysical Journal - ASTROPHYS J*, vol. 604, pp. 596–603, Apr. 2004.

[14] D. Clowe, M. Bradač, A. H. Gonzalez, M. Markevitch, S. W. Randall, C. Jones, and D. Zaritsky, "A Direct Empirical Proof of the Existence of Dark Matter," *The Astrophysical Journal*, vol. 648, no. 2, pp. L109–L113, 2006.

[15] R. H. Miller, K. H. Prendergast, and W. J. Quirk, "Numerical Experiments on Spiral Structure," *Astrophysical Journal*, vol. 161, p. 903, Sep. 1970.

[16] F. Hohl, "Numerical Experiments with a Disk of Stars," *Astrophysical Journal*, vol. 168, p. 343, Sep. 1971.

[17] J. P. Ostriker and P. J. E. Peebles, "A Numerical Study of the Stability of Flattened Galaxies: or, can Cold Galaxies Survive?" *Astrophysical Journal*, vol. 186, pp. 467–480, Dec. 1973.

[18] J. R. Bond, G. Efstathiou, and J. Silk, "Massive Neutrinos and the Large-Scale Structure of the Universe," *Phys. Rev. Lett.*, vol. 45, pp. 1980–1984, 24 1980.

[19] P. J. E. Peebles, "Primeval adiabatic perturbations - Effect of massive neutrinos," *Astrophysical Journal*, vol. 258, pp. 415–424, Jul. 1982.

[20] M. Davis, J. Huchra, D. W. Latham, and J. Tonry, "A survey of galaxy redshifts. II. The large scale space distribution.," *Astrophysical Journal*, vol. 253, pp. 423–445, Feb. 1982.

[21] S. D. M. White, C. S. Frenk, and M. Davis, "Clustering in a neutrino-dominated universe," *Astrophysical Journal*, vol. 274, pp. L1–L5, Nov. 1983.

[22] M. Davis, G. Efstathiou, C. S. Frenk, and S. D. M. White, "The evolution of large-scale structure in a universe dominated by cold dark matter," *Astrophysical Journal*, vol. 292, pp. 371–394, May 1985.

[23] J. F. Navarro, C. S. Frenk, and S. D. M. White, "The Structure of Cold Dark Matter Halos," *Astrophysical Journal*, vol. 462, p. 563, May 1996. arXiv: `astro-ph/9508025 [astro-ph]`.

[24] S. Gillessen, F. Eisenhauer, S. Trippe, T. Alexander, R. Genzel, F. Martins, and T. Ott, "Monitoring stellar orbits around the massive black hold in the galactic center," *The Astrophysical Journal*, vol. 692, no. 2, 1075–1109, 2009.

[25] E. Hubble, "A Relation between Distance and Radial Velocity among Extra-Galactic Nebulae," *Proceedings of the National Academy of Science*, vol. 15, no. 3, pp. 168–173, Mar. 1929.

[26] A. A. Penzias and R. W. Wilson, "A Measurement of Excess Antenna Temperature at 4080 Mc/s.," *Astrophysical Journal*, vol. 142, pp. 419–421, Jul. 1965.

[27] A. G. Riess, "The expansion of the universe is faster than expected," *Nature Reviews Physics*, vol. 2, no. 1, 10–12, 2019.

[28] B. P. Schmidt, N. B. Suntzeff, M. M. Phillips, R. A. Schommer, A. Clocchiatti, R. P. Kirshner, P. Garnavich, P. Challis, B. Leibundgut, J. Spyromilio, and et al., "The high-z supernova search: Measuring cosmic deceleration and global curvature of the universe using type ia supernovae," *The Astrophysical Journal*, vol. 507, no. 1, 46–63, 1998.

[29] C. Amsler *et al.*, "Review of particle physics," *Physics Letters B*, vol. 667, no. 1, pp. 1–6, 2008, Review of Particle Physics.

[30] V. Springel *et al.*, "Simulations of the formation, evolution and clustering of galaxies and quasars," *Nature*, vol. 435, no. 7042, pp. 629–636, Jun. 2005. arXiv: astro-ph/0504097 [astro-ph].

[31] R. Laha, "Primordial Black Holes as a Dark Matter Candidate Are Severely Constrained by the Galactic Center 511 keV γ-Ray Line," *Physical Review Letters*, vol. 123, no. 25, 2019.

[32] R. Laha, J. B. Muñoz, and T. R. Slatyer, "*INTEGRAL* constraints on primordial black holes and particle dark matter," *Phys. Rev. D*, vol. 101, p. 123 514, 12 2020.

[33] M. Boudaud and M. Cirelli, "Voyager 1 $e^{\pm}$ Further Constrain Primordial Black Holes as Dark Matter," *Physical Review Letters*, vol. 122, no. 4, 2019.

[34] M. H. Chan and C. M. Lee, "Constraining primordial black hole fraction at the galactic centre using radio observational data," *Monthly Notices of the Royal Astronomical Society*, vol. 497, no. 1, 1212–1216, 2020.

[35] H. Niikura, M. Takada, N. Yasuda, R. H. Lupton, T. Sumi, S. More, T. Kurita, S. Sugiyama, A. More, M. Oguri, and et al., "Microlensing constraints on primordial black holes with subaru/hsc andromeda observations," *Nature Astronomy*, vol. 3, no. 6, 524–534, 2019.

[36] P. Pani and A. Loeb, "Tidal capture of a primordial black hole by a neutron star: Implications for constraints on dark matter," *Journal of Cosmology and Astroparticle Physics*, vol. 2014, no. 06, 026–026, 2014.

[37] B. Carr and F. Kühnel, "Primordial black holes as dark matter: Recent developments," *Annual Review of Nuclear and Particle Science*, vol. 70, no. 1, 355–394, 2020.

[38] M. Viel, J. Lesgourgues, M. G. Haehnelt, S. Matarrese, and A. Riotto, "Constraining warm dark matter candidates including sterile neutrinos and light gravitinos with wmap and the lyman-α forest," *Physical Review D*, vol. 71, no. 6, 2005.

[39] E. W. Kolb and M. S. Turner, *The early universe*, ser. Frontiers in physics. Boulder, CO: Westview Press, 1990.

[40] S. Dimopoulos and H. Georgi, "Softly broken supersymmetry and su(5)," *Nuclear Physics B*, vol. 193, no. 1, pp. 150–162, 1981.

[41] R. Barbier, C. Bérat, M. Besançon, M. Chemtob, A. Deandrea, E. Dudas, P. Fayet, S. Lavignac, G. Moreau, E. Perez, and et al., "R-parity-violating supersymmetry," *Physics Reports*, vol. 420, no. 1-6, 1–195, 2005.

[42] G. Servant and T. M. Tait, "Is the lightest kaluza–klein particle a viable dark matter candidate?" *Nuclear Physics B*, vol. 650, no. 1, pp. 391–419, 2003.

[43] E. W. Kolb and R. Slansky, "Dimensional reduction in the early universe: Where have the massive particles gone?" *Physics Letters B*, vol. 135, no. 5, pp. 378–382, 1984.

[44] L. Randall and R. Sundrum, "Large mass hierarchy from a small extra dimension," *Physical Review Letters*, vol. 83, no. 17, pp. 3370–3373, 1999.

[45] A. Barrau, P. Salati, G. Servant, F. Donato, J. Grain, D. Maurin, and R. Taillet, "Kaluza-klein dark matter and galactic antiprotons," *Phys. Rev. D*, vol. 72, p. 063 507, 6 2005.

[46] D. Hooper and G. Servant, "Indirect detection of dirac right-handed neutrino dark matter," *Astroparticle Physics*, vol. 24, no. 3, pp. 231–246, 2005.

[47] E. Aprile, J. Aalbers, F. Agostini, M. Alfonsi, F. D. Amaro, M. Anthony, B. Antunes, F. Arneodo, M. Balata, and et al., "The XENON1T dark matter experiment," *The European Physical Journal C*, vol. 77, no. 12, 2017.

[48] D. Akerib *et al.*, "Results from a search for dark matter in the complete lux exposure," *Physical Review Letters*, vol. 118, no. 2, 2017.

[49] A. Sirunyan *et al.*, "Search for dark matter particles produced in association with a top quark pair at $\sqrt{s} = 13\,\text{tev}$," *Physical Review Letters*, vol. 122, no. 1, 2019.

[50] G. Arcadi, M. Dutra, P. Ghosh, M. Lindner, Y. Mambrini, M. Pierre, S. Profumo, and F. S. Queiroz, "The waning of the wimp? a review of models, searches, and constraints," *The European Physical Journal C*, vol. 78, no. 3, 2018.

[51] R. K. Leane, T. R. Slatyer, J. F. Beacom, and K. C. Ng, "Gev-scale thermal wimps: Not even slightly ruled out," *Physical Review D*, vol. 98, no. 2, 2018.

[52] M. Battaglieri *et al.*, *Us cosmic visions: New ideas in dark matter 2017: Community report*, 2017. arXiv: 1707.04591 [hep-ph].

[53] D. Hooper, R. K. Leane, Y.-D. Tsai, S. Wegsman, and S. J. Witte, "A systematic study of hidden sector dark matter: Application to the gamma-ray and antiproton excesses," *Journal of High Energy Physics*, vol. 2020, no. 7, 2020.

[54] J. Baur, N. Palanque-Delabrouille, C. Yèche, C. Magneville, and M. Viel, "Lyman-alpha forests cool warm dark matter," *Journal of Cosmology and Astroparticle Physics*, vol. 2016, no. 08, 012–012, 2016.

[55] R. D. Peccei and H. R. Quinn, "CP conservation in the presence of pseudoparticles," *Phys. Rev. Lett.*, vol. 38, pp. 1440–1443, 25 1977.

[56] C. Abel *et al.*, "Measurement of the permanent electric dipole moment of the neutron," *Phys. Rev. Lett.*, vol. 124, p. 081 803, 8 2020.

[57] S. Weinberg, "A new light boson?" *Phys. Rev. Lett.*, vol. 40, pp. 223–226, 4 1978.

[58] F. Wilczek, "Problem of Strong P and T Invariance in the Presence of Instantons," *Phys. Rev. Lett.*, vol. 40, pp. 279–282, 1978.

[59] K. J. Bae, J.-H. Huh, and J. E. Kim, "Update of axion CDM energy," *JCAP*, vol. 09, p. 005, 2008. arXiv: 0806.0497 [hep-ph].

[60] P. Sikivie, "Axion cosmology," in *Axions: Theory, Cosmology, and Experimental Searches*, M. Kuster, G. Raffelt, and B. Beltrán, Eds. Berlin, Heidelberg: Springer Berlin Heidelberg, 2008, pp. 19–50, ISBN: 978-3-540-73518-2.

[61] P. W. Graham, I. G. Irastorza, S. K. Lamoreaux, A. Lindner, and K. A. van Bibber, "Experimental searches for the axion and axion-like particles," *Annual Review of Nuclear and Particle Science*, vol. 65, no. 1, pp. 485–514, 2015. eprint: https://doi.org/10.1146/annurev-nucl-102014-022120.

[62] G. G. Raffelt, "Astrophysical axion bounds," in *Axions: Theory, Cosmology, and Experimental Searches*, M. Kuster, G. Raffelt, and B. Beltrán, Eds. Berlin, Heidelberg: Springer Berlin Heidelberg, 2008, pp. 51–71, ISBN: 978-3-540-73518-2.

[63] H. Primakoff, "Photo-production of neutral mesons in nuclear electric fields and the mean life of the neutral meson," *Phys. Rev.*, vol. 81, pp. 899–899, 5 1951.

[64] L. Hui, J. P. Ostriker, S. Tremaine, and E. Witten, "Ultralight scalars as cosmological dark matter," *Phys. Rev. D*, vol. 95, no. 4, p. 043 541, 2017. arXiv: 1610.08297 [astro-ph.CO].

[65] L. Hui, *Wave dark matter*, 2021. arXiv: 2101.11735 [astro-ph.CO].

[66] D. H. Weinberg, J. S. Bullock, F. Governato, R. Kuzio de Naray, and A. H. G. Peter, "Cold dark matter: Controversies on small scales," *Proceedings of the National Academy of Sciences*, vol. 112, no. 40, pp. 12 249–12 255, 2015. eprint: https://www.pnas.org/content/112/40/12249.full.pdf.

[67] J. Kleyna, M. I. Wilkinson, N. W. Evans, G. Gilmore, and C. Frayn, "Dark matter in dwarf spheroidals ii. observations and modelling of draco," *Monthly Notices of the Royal Astronomical Society*, vol. 330, no. 4, 792–806, 2002.

[68] J. R. Jardel and K. Gebhardt, "VARIATIONS IN a UNIVERSAL DARK MATTER PROFILE FOR DWARF SPHEROIDALS," *The Astrophysical Journal*, vol. 775, no. 1, p. L30, 2013.

[69] A. Fattahi, J. F. Navarro, T. Sawala, C. S. Frenk, L. V. Sales, K. Oman, M. Schaller, and J. Wang, *The cold dark matter content of galactic dwarf spheroidals: No cores, no failures, no problem*, 2016. arXiv: 1607.06479 [astro-ph.GA].

[70] J. S. Bullock, A. V. Kravtsov, and D. H. Weinberg, "Reionization and the abundance of galactic satellites," *The Astrophysical Journal*, vol. 539, no. 2, pp. 517–521, 2000.

[71] L. Evans and P. Bryant, "LHC machine," *Journal of Instrumentation*, vol. 3, no. 08, S08001–S08001, 2008.

[72] A. A. Prinz, R. Baggs, J. Ballam, S. Ecklund, C. Fertig, J. A. Jaros, K. Kase, A. Kulikov, W. G. J. Langeveld, R. Leonard, and et al., "Search for millicharged particles at slac," *Physical Review Letters*, vol. 81, no. 6, 1175–1178, 1998.

[73] O. Buchmueller, M. J. Dolan, S. A. Malik, and C. McCabe, "Characterising dark matter searches at colliders and direct detection experiments: Vector mediators," *Journal of High Energy Physics*, vol. 2015, no. 1, 2015.

[74] ATLAS Collaboration, "Search for dark matter in association with an energetic photon in pp collisions at $\sqrt{\{s\}}$ = 13 TeV with the ATLAS detector," *Journal of High Energy Physics*, vol. 2021, no. 2, 226, p. 226, Feb. 2021. arXiv: 2011.05259 [hep-ex].

[75] E. Aprile *et al.*, "Xenon1t dark matter data analysis: Signal and background models and statistical inference," *Physical Review D*, vol. 99, no. 11, 2019.

[76] M. Schumann, "Direct detection of wimp dark matter: Concepts and status," *Journal of Physics G: Nuclear and Particle Physics*, vol. 46, no. 10, p. 103 003, 2019.

[77] R. Essig *et al.*, "Direct detection of sub-gev dark matter with semiconductor targets," *Journal of High Energy Physics*, vol. 2016, no. 5, p. 46, 2016.

[78] L. Barak *et al.*, "Sensei: Direct-detection results on sub-gev dark matter from a new skipper ccd," *Phys. Rev. Lett.*, vol. 125, p. 171 802, 17 2020.

[79] A. F. Pacheco and D. Strottman, "Nuclear-structure corrections to estimates of the spin-dependent wimp-nucleus cross section," *Phys. Rev. D*, vol. 40, pp. 2131–2133, 6 1989.

[80] J. Ellis and R. A. Flores, "Elastic supersymmetric relic-nucleus scattering revisited," *Physics Letters B*, vol. 263, no. 2, pp. 259–266, 1991.

[81] C. Amole *et al.*, "Dark matter search results from the complete exposure of the pico-60 C_3F_8 bubble chamber," *Phys. Rev. D*, vol. 100, p. 022 001, 2 2019.

[82] R Bernabei, P Belli, F Montecchia, W Di Nicolantonio, A Incicchitti, D Prosperi, C Bacci, C. Dai, L. Ding, H. Kuang, and J. Ma, "Searching for wimps by the annual modulation signature," *Physics Letters B*, vol. 424, no. 1, pp. 195–201, 1998.

[83] R. Bernabei, P. Belli, F. Cappella, R. Cerulli, C. J. Dai, A. d'Angelo, H. L. He, A. Incicchitti, H. H. Kuang, J. M. Ma, and et al., "First results from dama/libra and the combined results with dama/nai," *The European Physical Journal C*, vol. 56, no. 3, 333–355, 2008.

[84] R. Bernabei, P. Belli, F. Cappella, R. Cerulli, C. J. Dai, A. d'Angelo, H. L. He, A. Incicchitti, H. H. Kuang, X. H. Ma, and et al., "New results from dama/libra," *The European Physical Journal C*, vol. 67, no. 1-2, 39–49, 2010.

[85] J. Amare, S. Cebrian, D. Cintas, I. Coarasa, E. Garcia, M. Martinez, M. A. Olivan, Y. Ortigoza, A. O. de Solorzano, J. Puimedon, A. Salinas, M. L. Sarsa, and P. Villar, *Annual modulation results from three years exposure of anais-112*, 2021. arXiv: 2103.01175 [astro-ph.IM].

[86] P. Sikivie, "Experimental tests of the "invisible" axion," *Phys. Rev. Lett.*, vol. 51, pp. 1415–1417, 16 1983.

[87] K. Van Bibber, N. R. Dagdeviren, S. E. Koonin, A. K. Kerman, and H. N. Nelson, "Proposed experiment to produce and detect light pseudoscalars," *Phys. Rev. Lett.*, vol. 59, pp. 759–762, 7 1987.

[88] S. J. Asztalos, G. Carosi, C. Hagmann, D. Kinion, K. van Bibber, M. Hotz, L. J Rosenberg, G. Rybka, J. Hoskins, J. Hwang, and et al., "Squid-based microwave cavity search for dark-matter axions," *Physical Review Letters*, vol. 104, no. 4, 2010.

[89] T. Braine *et al.*, "Extended search for the invisible axion with the axion dark matter experiment," *Phys. Rev. Lett.*, vol. 124, p. 101 303, 10 2020.

[90] "New cast limit on the axion–photon interaction," *Nature Physics*, vol. 13, no. 6, 584–590, 2017.

[91] E Armengaud *et al.*, "Conceptual design of the international axion observatory (iaxo)," *Journal of Instrumentation*, vol. 9, no. 05, T05002–T05002, 2014.

[92] A. Abeln *et al.*, *Conceptual design of babyiaxo, the intermediate stage towards the international axion observatory*, 2021. arXiv: 2010.12076 [physics.ins-det].

[93] J. E. Gunn, B. W. Lee, I. Lerche, D. N. Schramm, and G. Steigman, "Some astrophysical consequences of the existence of a heavy stable neutral lepton.," *Astrophysical Journal*, vol. 223, pp. 1015–1031, Aug. 1978.

[94] F. W. Stecker, "The cosmic gamma -ray background from the annihilation of primordial stable neutral heavy leptons.," *Astrophysical Journal*, vol. 223, pp. 1032–1036, Aug. 1978.

[95] J. Silk and M. Srednicki, "Cosmic-ray antiprotons as a probe of a photino-dominated universe," *Phys. Rev. Lett.*, vol. 53, pp. 624–627, 6 1984.

[96] L. M. Krauss, K. Freese, D. N. Spergel, and W. H. Press, "Cold dark matter candidates and the solar neutrino problem," *Astrophysical Journal*, vol. 299, pp. 1001–1006, Dec. 1985.

[97] K. Freese, "Can scalar neutrinos or massive dirac neutrinos be the missing mass?" *Physics Letters B*, vol. 167, no. 3, pp. 295–300, 1986.

[98] L. M. Krauss, M. Srednicki, and F. Wilczek, "Solar system constraints and signatures for dark-matter candidates," *Phys. Rev. D*, vol. 33, pp. 2079–2083, 8 1986.

[99] K. Abazajian, G. M. Fuller, and W. H. Tucker, "Direct detection of warm dark matter in the x-ray," *The Astrophysical Journal*, vol. 562, no. 2, pp. 593–604, 2001.

[100] K. van Bibber, P. M. McIntyre, D. E. Morris, and G. G. Raffelt, "Design for a practical laboratory detector for solar axions," *Phys. Rev. D*, vol. 39, pp. 2089–2099, 8 1989.

[101] M. Cirelli *et al.*, "Pppc 4 dm id: A poor particle physicist cookbook for dark matter indirect detection," *Journal of Cosmology and Astroparticle Physics*, vol. 2011, no. 03, pp. 051–051, 2011.

[102] O. Adriani *et al.*, "PAMELA Results on the Cosmic-Ray Antiproton Flux from 60 MeV to 180 GeV in Kinetic Energy," *Phys. Rev. Lett.*, vol. 105, p. 121 101, 12 2010.

[103] Accardo, L. and others, "High Statistics Measurement of the Positron Fraction in Primary Cosmic Rays of 0.5-500 GeV with the Alpha Magnetic Spectrometer on the International Space Station," *Physical Review Letters*, vol. 113, p. 121 101, 12 2014.

[104] M. Aguilar *et al.*, "First result from the alpha magnetic spectrometer on the international space station: Precision measurement of the positron fraction in primary cosmic rays of 0.5–350 gev," *Phys. Rev. Lett.*, vol. 110, p. 141 102, 14 2013.

[105] ——, "Towards understanding the origin of cosmic-ray positrons," *Phys. Rev. Lett.*, vol. 122, p. 041 102, 4 2019.

[106] D. Hooper and T. Linden, "On The Origin Of The Gamma Rays From The Galactic Center," *Phys. Rev. D*, vol. 84, p. 123 005, 2011. arXiv: 1110.0006 [astro-ph.HE].

[107] T. Daylan, D. P. Finkbeiner, D. Hooper, T. Linden, S. K. Portillo, N. L. Rodd, and T. R. Slatyer, "The characterization of the gamma-ray signal from the central milky way: A case for annihilating dark matter," *Physics of the Dark Universe*, vol. 12, pp. 1–23, 2016.

[108] D. Hooper and T. Linden, "Millisecond pulsars, tev halos, and implications for the galactic center gamma-ray excess," *Physical Review D*, vol. 98, no. 4, 2018.

[109] ——, *Evidence of tev halos around millisecond pulsars*, 2021. arXiv: 2104.00014 [astro-ph.HE].

[110] M. Ackermann *et al.*, "Searching for dark matter annihilation from milky way dwarf spheroidal galaxies with six years of fermi large area telescope data," *Phys. Rev. Lett.*, vol. 115, p. 231 301, 23 2015.

[111] L. Goodenough and D. Hooper, *Possible evidence for dark matter annihilation in the inner milky way from the fermi gamma ray space telescope*, 2009. arXiv: 0910.2998 [hep-ph].

[112] S. W. Barwick, J. J. Beatty, A. Bhattacharyya, C. R. Bower, C. J. Chaput, S. Coutu, G. A. de Nolfo, J. Knapp, D. M. Lowder, S. McKee, D. Müller, J. A. Musser, S. L. Nutter, E. Schneider, S. P. Swordy, G. Tarlé, A. D. Tomasch, and E. Torbet, "Measurements of the cosmic-ray positron fraction from 1 to 50 g[CLC]e[/CLC]v," *The Astrophysical Journal*, vol. 482, no. 2, pp. L191–L194, 1997.

[113] O. Adriani, G. C. Barbarino, G. A. Bazilevskaya, R. Bellotti, A. Bianco, M. Boezio, E. A. Bogomolov, M. Bongi, V. Bonvicini, S. Bottai, and et al., "Cosmic-ray positron energy spectrum measured by pamela," *Physical Review Letters*, vol. 111, no. 8, 2013.

[114] D. Hooper, P. Blasi, and P. D. Serpico, "Pulsars as the sources of high energy cosmic ray positrons," *Journal of Cosmology and Astroparticle Physics*, vol. 2009, no. 01, pp. 025–025, 2009.

[115] A. U. Abeysekara, A. Albert, R. Alfaro, C. Alvarez, J. D. Álvarez, R. Arceo, J. C. Arteaga-Velázquez, D. Avila Rojas, H. A. Ayala Solares, A. S. Barber, and et al., "Extended gamma-ray sources around pulsars constrain the origin of the positron flux at earth," *Science*, vol. 358, no. 6365, pp. 911–914, 2017.

[116] S. Profumo, J. Reynoso-Cordova, N. Kaaz, and M. Silverman, "Lessons from hawc pulsar wind nebulae observations: The diffusion constant is not a constant; pulsars remain

the likeliest sources of the anomalous positron fraction; cosmic rays are trapped for long periods of time in pockets of inefficient diffusion," *Physical Review D*, vol. 97, no. 12, 2018.

[117] D. Hooper and T. Linden, "Measuring the local diffusion coefficient with h.e.s.s. observations of very high-energy electrons," *Physical Review D*, vol. 98, no. 8, 2018.

[118] R. L. Golden, S. Horan, B. G. Mauger, G. D. Badhwar, J. L. Lacy, S. A. Stephens, R. R. Daniel, and J. E. Zipse, "Evidence for the existence of cosmic-ray antiprotons," *Phys. Rev. Lett.*, vol. 43, pp. 1196–1199, 16 1979.

[119] E. A. Bogomolov, N. D. Lubyanaya, V. A. Romanov, S. V. Stepanov, and M. S. Shulakova, "A STRATOSPHERIC MAGNETIC SPECTROMETER INVESTIGATION OF THE SINGLY CHARGED COMPONENT SPECTRA AND COMPOSITION OF THE PRIMARY AND SECONDARY COSMIC RADIATION.," in *16th International Cosmic Ray Conference*, 1979.

[120] A. Buffington, S. M. Schindler, and C. R. Pennypacker, "A measurement of the cosmic-ray antiproton flux and a search for antihelium," *Astrophysical Journal*, vol. 248, pp. 1179–1193, Sep. 1981.

[121] A. Moiseev, K. Yoshimura, I. Ueda, K. Anraku, R. Golden, M. Imori, S. Inaba, B. Kimbell, N. Kimura, Y. Makida, H. Matsumoto, H. Matsunaga, J. Mitchell, M. Motoki, J. Nishimura, M. Nozaki, S. Orito, J. Ormes, T. Saeki, E. S. Seo, S. Stochaj, R. Streitmatter, J. Suzuki, K. Tanaka, N. Yajima, T. Yamagami, A. Yamamoto, and T. Y. and, "Cosmic-ray antiproton flux in the energy range from 200 to 600 MeV," *The Astrophysical Journal*, vol. 474, no. 1, pp. 479–489, 1997.

[122] A. Yamamoto *et al.*, "Search for cosmic-ray antiproton origins and for cosmological antimatter with BESS," *Advances in Space Research*, vol. 51, no. 2, pp. 227 –233, 2013, The Origins of Cosmic Rays: Resolving Hess's Century-Old Puzzle.

[123] K. Abe *et al.*, "Measurement of the Cosmic-Ray Antiproton Spectrum at Solar Minimum with a Long-Duration Balloon Flight over Antarctica," *Phys. Rev. Lett.*, vol. 108, p. 051 102, 5 2012.

[124] D. Bergstrøm *et al.*, "First mass-resolved measurement of high-energy cosmic-ray antiprotons," *The Astrophysical Journal*, vol. 534, no. 2, pp. L177–L180, 2000.

[125] O. Adriani *et al.*, "Measurement of the flux of primary cosmic ray antiprotons with energies of 60 MeV to 350 GeV in the PAMELA experiment," *JETP Letters*, vol. 96, pp. 621–627, Jan. 2013.

[126] M. Aguilar *et al.*, "Antiproton Flux, Antiproton-to-Proton Flux Ratio, and Properties of Elementary Particle Fluxes in Primary Cosmic Rays Measured with the Alpha Magnetic

Spectrometer on the International Space Station," *Phys. Rev. Lett.*, vol. 117, p. 091 103, 9 2016.

[127] M.-Y. Cui, Q. Yuan, Y.-L. S. Tsai, and Y.-Z. Fan, "Possible dark matter annihilation signal in the ams-02 antiproton data," *Physical Review Letters*, vol. 118, no. 19, 2017.

[128] I. Cholis, T. Linden, and D. Hooper, "A robust excess in the cosmic-ray antiproton spectrum: Implications for annihilating dark matter," *Phys. Rev. D*, vol. 99, p. 103 026, 10 2019.

[129] A. Cuoco, J. Heisig, L. Klamt, M. Korsmeier, and M. Krämer, "Scrutinizing the evidence for dark matter in cosmic-ray antiprotons," *Phys. Rev. D*, vol. 99, p. 103 014, 10 2019.

[130] A. Cuoco, J. Heisig, M. Korsmeier, and M. Krämer, "Probing dark matter annihilation in the galaxy with antiprotons and gamma rays," *Journal of Cosmology and Astroparticle Physics*, vol. 2017, no. 10, pp. 053–053, 2017.

[131] M. Boudaud, Y. Génolini, L. Derome, J. Lavalle, D. Maurin, P. Salati, and P. D. Serpico, "Ams-02 antiprotons' consistency with a secondary astrophysical origin," *Physical Review Research*, vol. 2, no. 2, 2020.

[132] J. Heisig, M. Korsmeier, and M. W. Winkler, "Dark matter or correlated errors: Systematics of the ams-02 antiproton excess," *Phys. Rev. Research*, vol. 2, p. 043 017, 4 2020.

[133] T. Sjöstrand *et al.*, "An introduction to PYTHIA 8.2," *Computer Physics Communications*, vol. 191, 159–177, 2015.

[134] G. Corcella *et al.*, "Herwig 6: An event generator for hadron emission reactions with interfering gluons (including supersymmetric processes)," *Journal of High Energy Physics*, vol. 2001, no. 01, 010–010, 2001.

[135] H. Baer and S. Profumo, "Low energy antideuterons: Shedding light on dark matter," *Journal of Cosmology and Astroparticle Physics*, vol. 2005, no. 12, pp. 008–008, 2005.

[136] P. Chardonnet, J. Orloff, and P. Salati, "The production of anti-matter in our galaxy," *Physics Letters B*, vol. 409, no. 1-4, 313–320, 1997.

[137] F. Donato, N. Fornengo, and P. Salati, "Antideuterons as a signature of supersymmetric dark matter," *Physical Review D*, vol. 62, no. 4, 043003, p. 043 003, Aug. 2000. eprint: hep-ph/9904481.

[138] M. Korsmeier, F. Donato, and N. Fornengo, "Prospects to verify a possible dark matter hint in cosmic antiprotons with antideuterons and antihelium," *Physical Review D*, vol. 97, no. 10, 2018.

[139] N Fornengo, L Maccione, and A Vittino, "Dark matter searches with cosmic antideuterons: Status and perspectives," *Journal of Cosmology and Astroparticle Physics*, vol. 2013, no. 09, 031–031, 2013.

[140] S. Acharya *et al.*, "Production of deuterons, tritons, ^{3}He nuclei, and their antinuclei in *pp* collisions at $\sqrt{s}$ = 0.9, 2.76, and 7 tev," *Phys. Rev. C*, vol. 97, p. 024 615, 2 2018.

[141] R. Duperray, B. Baret, D. Maurin, G. Boudoul, A. Barrau, L. Derome, K. Protasov, and M. Buénerd, "Flux of light antimatter nuclei near earth, induced by cosmic rays in the galaxy and in the atmosphere," *Phys. Rev. D*, vol. 71, p. 083 013, 8 2005.

[142] P. v. Doetinchem, K. Perez, T. Aramaki, S. Baker, S. Barwick, R. Bird, M. Boezio, S. Boggs, M. Cui, A. Datta, and et al., "Cosmic-ray antinuclei as messengers of new physics: Status and outlook for the new decade," *Journal of Cosmology and Astroparticle Physics*, vol. 2020, no. 08, pp. 035–035, 2020.

[143] F. Donato, N. Fornengo, and D. Maurin, "Antideuteron fluxes from dark matter annihilation in diffusion models," *Physical Review D*, vol. 78, no. 4, 2008.

[144] F. Donato, N. Fornengo, D. Maurin, P. Salati, and R. Taillet, "Antiprotons in cosmic rays from neutralino annihilation," *Phys. Rev. D*, vol. 69, p. 063 501, 6 2004.

[145] A. W. Strong, I. V. Moskalenko, and V. S. Ptuskin, "Cosmic-Ray Propagation and Interactions in the Galaxy," *Annual Review of Nuclear and Particle Science*, vol. 57, no. 1, pp. 285–327, 2007.

[146] J. Lavalle, D. Maurin, and A. Putze, "Direct constraints on diffusion models from cosmic-ray positron data: Excluding the minimal model for dark matter searches," *Physical Review D*, vol. 90, no. 8, 2014.

[147] E. Parker, "The passage of energetic charged particles through interplanetary space," *Planetary and Space Science*, vol. 13, no. 1, pp. 9–49, 1965.

[148] L. J. Gleeson and W. I. Axford, "Solar Modulation of Galactic Cosmic Rays," *Astrophysical Journal*, vol. 154, p. 1011, Dec. 1968.

[149] M. J. Boschini, S. D. Torre, M. Gervasi, D. Grandi, G. Jóhannesson, M. Kachelriess, G. L. Vacca, N. Masi, I. V. Moskalenko, E. Orlando, S. S. Ostapchenko, S. Pensotti, T. A. Porter, L. Quadrani, P. G. Rancoita, D. Rozza, and M. Tacconi, "Solution of heliospheric propagation: Unveiling the local interstellar spectra of cosmic-ray species," *The Astrophysical Journal*, vol. 840, no. 2, p. 115, 2017.

[150] M. J. Boschini, S. D. Torre, M. Gervasi, D. Grandi, G. Jóhannesson, G. L. Vacca, N. Masi, I. V. Moskalenko, S. Pensotti, T. A. Porter, L. Quadrani, P. G. Rancoita, D. Rozza, and M.

Tacconi, "HelMod in the works: From direct observations to the local interstellar spectrum of cosmic-ray electrons," *The Astrophysical Journal*, vol. 854, no. 2, p. 94, 2018.

[151] O. P. M. Aslam, D. Bisschoff, M. S. Potgieter, M. Boezio, and R. Munini, "Modeling of heliospheric modulation of cosmic-ray positrons in a very quiet heliosphere," *The Astrophysical Journal*, vol. 873, no. 1, p. 70, 2019.

[152] A. Ibarra and S. Wild, "Prospects of antideuteron detection from dark matter annihilations or decays at ams-02 and gaps," *Journal of Cosmology and Astroparticle Physics*, vol. 2013, no. 02, pp. 021–021, 2013.

[153] A. Cuoco, M. Krämer, and M. Korsmeier, "Novel dark matter constraints from antiprotons in light of ams-02," *Physical Review Letters*, vol. 118, no. 19, 2017.

[154] H. Fuke, T. Maeno, K. Abe, S. Haino, Y. Makida, S. Matsuda, H. Matsumoto, J. W. Mitchell, A. A. Moiseev, J. Nishimura, M. Nozaki, S. Orito, J. F. Ormes, M. Sasaki, E. S. Seo, Y. Shikaze, R. E. Streitmatter, J. Suzuki, K. Tanaka, K. Tanizaki, T. Yamagami, A. Yamamoto, Y. Yamamoto, K. Yamato, T. Yoshida, and K. Yoshimura, "Search for cosmic-ray antideuterons," *Phys. Rev. Lett.*, vol. 95, p. 081 101, 8 2005.

[155] T. Aramaki, S. Boggs, S. Bufalino, L. Dal, P. von Doetinchem, F. Donato, N. Fornengo, H. Fuke, M. Grefe, C. Hailey, B. Hamilton, A. Ibarra, J. Mitchell, I. Mognet, R. Ong, R. Pereira, K. Perez, A. Putze, A. Raklev, P. Salati, M. Sasaki, G. Tarle, A. Urbano, A. Vittino, S. Wild, W. Xue, and K. Yoshimura, "Review of the theoretical and experimental status of dark matter identification with cosmic-ray antideuterons," *Physics Reports*, vol. 618, pp. 1 –37, 2016, Review of the theoretical and experimental status of dark matter identification with cosmic-ray antideuterons.

[156] T. Aramaki, C J. Hailey, S E. Boggs, P. Doetinchem, H. Fuke, S I. Mognet, R A. Ong, K. Perez, and J Zweerink, "Antideuteron sensitivity for the gaps experiment," *Astroparticle Physics*, vol. 74, pp. 6–13, Jun. 2015.

[157] K. Mori, C. J. Hailey, E. A. Baltz, W. W. Craig, M. Kamionkowski, W. T. Serber, and P. Ullio, "A novel antimatter detector based on x-ray deexcitation of exotic atoms," *The Astrophysical Journal*, vol. 566, no. 1, pp. 604–616, 2002.

[158] C. J. Hailey, T Aramaki, W. W. Craig, L Fabris, F Gahbauer, J. E. Koglin, N Madden, K Mori, H. T. Yu, and K. P. Ziock, "Accelerator testing of the general antiparticle spectrometer; a novel approach to indirect dark matter detection," *Journal of Cosmology and Astroparticle Physics*, vol. 2006, no. 01, pp. 007–007, 2006.

[159] J. Koglin, T. Aramaki, W. Craig, L. Fabris, F. Gahbauer, C. Hailey, F. Jou, N. Madden, K. Mori, H. Yu, and K. Ziock, "Indirect dark matter search with antideuterons: Progress and future prospects for general antiparticle spectrometer (gaps)," *Nuclear Physics B - Proceed-*

ings Supplements, vol. 173, pp. 75–78, 2007, Proceedings of the 7th UCLA Symposium on Sources and Detection of Dark Matter and Dark Energy in the Universe.

[160] T. Aramaki, S. K. Chan, W. W. Craig, L. Fabris, F. Gahbauer, C. J. Hailey, J. E. Koglin, N. Madden, K. Mori, H. T. Yu, and K. P. Ziock, "A measurement of atomic X-ray yields in exotic atoms and implications for an antideuteron-based dark matter search," *Astroparticle Physics*, vol. 49, pp. 52–62, Sep. 2013. arXiv: 1303.3871 [astro-ph.IM].

[161] P. von Doetinchem, T. Aramaki, N. Bando, S. Boggs, H. Fuke, F. Gahbauer, C. Hailey, J. Koglin, S. Mognet, N. Madden, and et al., "The flight of the gaps prototype experiment," *Astroparticle Physics*, vol. 54, pp. 93–109, 2014.

[162] H. Fuke, R. Ong, T. Aramaki, N. Bando, S. Boggs, P. Doetinchem, F. Gahbauer, C. Hailey, J. Koglin, N. Madden, and et al., "The pgaps experiment: An engineering balloon flight of prototype gaps," *Advances in Space Research*, vol. 53, no. 10, 1432–1437, 2014.

[163] S. Mognet, T. Aramaki, N. Bando, S. Boggs, P. von Doetinchem, H. Fuke, F. Gahbauer, C. Hailey, J. Koglin, N. Madden, and et al., "The prototype gaps (pgaps) experiment," *Nuclear Instruments and Methods in Physics Research Section A: Accelerators, Spectrometers, Detectors and Associated Equipment*, vol. 735, 24–38, 2014.

[164] S. Quinn, *Recent progress on the gaps time of flight system*, 2020. arXiv: 1912.01675 [astro-ph.IM].

[165] K. Perez *et al.*, "Fabrication of low-cost, large-area prototype Si(Li) detectors for the GAPS experiment," *Nucl. Instrum. Meth.*, vol. A905, pp. 12–21, 2018. arXiv: 1807.07912 [astro-ph.IM].

[166] F. Rogers, M. Xiao, K. Perez, S. Boggs, T. Erjavec, L. Fabris, H. Fuke, C. Hailey, M. Kozai, A. Lowell, N. Madden, M. Manghisoni, S. McBride, V. Re, E. Riceputi, N. Saffold, and Y. Shimizu, "Large-area Si(Li) detectors for X-ray spectrometry and particle tracking in the GAPS experiment," *Journal of Instrumentation*, vol. 14, no. 10, P10009–P10009, 2019.

[167] M. Kozai *et al.*, "Developing a mass-production model of large-area Si(Li) detectors with high operating temperatures," *Nucl. Instrum. Meth. A*, vol. 947, p. 2695, 2019. arXiv: 1906.05577 [physics.ins-det].

[168] N. Saffold, F. Rogers, M. Xiao, R. Bhatt, T. Erjavec, H. Fuke, C. Hailey, M. Kozai, D. Kraych, E. Martinez, and et al., "Passivation of Si(Li) detectors operated above cryogenic temperatures for space-based applications," *Nuclear Instruments and Methods in Physics Research A*, p. 165 015, 2021.

[169] V. Scotti, A. Boiano, L. Fabris, M. Manghisoni, G. Osteria, E. Riceputi, F. Perfetto, V. Re, and G. Zampa, "Front-end electronics for the GAPS tracker," *PoS*, vol. ICRC2019, p. 136, 2020. arXiv: 1909.01682 [astro-ph.IM].

[170] H. FUKE, T. ABE, T. DAIMARU, T. INOUE, A. KAWACHI, H. KAWAI, Y. MASUYAMA, H. MATSUMIYA, D. MATSUMOTO, Y. MIYAZAKI, J. MORI, H. NAGAI, T. NONOMURA, H. OGAWA, S. OKAZAKI, T. OKUBO, S. OZAKI, D. SATO, K. SHIMIZU, K. TAKAHASHI, S. TAKAHASHI, N. YAMADA, and T. YOSHIDA, "Development of a cooling system for gaps using oscillating heat pipe," *TRANSACTIONS OF THE JAPAN SOCIETY FOR AERONAUTICAL AND SPACE SCIENCES, AEROSPACE TECHNOLOGY JAPAN*, vol. 14, no. ists30, $Pi_1$7–$Pi_2$6, 2016.

[171] S. Okazaki, H. Fuke, H. Ogawa, Y. Miyazaki, K. Takahashi, and N. Yamada, "Meter-scale multi-loop capillary heat pipe," *Applied Thermal Engineering*, vol. 141, pp. 20 –28, 2018.

[172] H. Fuke, S. Okazaki, H. Ogawa, and Y. Miyazaki, "Balloon flight demonstration of an oscillating heat pipe," *Journal of Astronomical Instrumentation*, vol. 06, no. 02, p. 1 740 006, 2017. eprint: https://doi.org/10.1142/S2251171717400062.

[173] F. Goulding, "Semiconductor detectors for nuclear spectrometry, i," *Nuclear Instruments and Methods*, vol. 43, no. 1, pp. 1–54, 1966, Proceedings of the Tenth Summer Meeting of Nuclear Physicists.

[174] W. R. Leo, *Techniques for Nuclear and Particle Physics Experiments: A How to Approach*. Springer-Verlag Berlin Heidelberg, 1987, ISBN: 978-3-540-57280-0.

[175] R. Griffiths, "Calculated total efficiencies of coaxial Ge(Li) detectors," *Nuclear Instruments and Methods*, vol. 91, no. 3, pp. 377–379, 1971.

[176] J. L. Campbell, G. Cauchon, T. Lakatos, M. C. Lépy, L. McDonald, T. Papp, J. Plagnard, P. Stemmler, and W. J. Teesdale, "Experimental K-shell fluorescence yield of silicon," *Journal of Physics B Atomic Molecular Physics*, vol. 31, no. 21, pp. 4765–4779, Nov. 1998.

[177] W. Shockley, "Currents to Conductors Induced by a Moving Point Charge," *Journal of Applied Physics*, vol. 9, no. 10, pp. 635–636, Oct. 1938.

[178] S. Ramo, "Currents induced by electron motion," *Proceedings of the IRE*, vol. 27, no. 9, pp. 584–585, 1939.

[179] Z. He, "Review of the shockley–ramo theorem and its application in semiconductor gamma-ray detectors," *Nuclear Instruments and Methods in Physics Research Section A: Accelerators, Spectrometers, Detectors and Associated Equipment*, vol. 463, no. 1, pp. 250–267, 2001.

[180] Q. Looker, "Fabrication process development for high-purity germanium radiation detectors with amorphous semiconductor contacts," Copyright - Database copyright ProQuest LLC; ProQuest does not claim copyright in the individual underlying works; Last updated - 2021-05-20, PhD thesis, 2014, p. 177, ISBN: 978-1-321-26013-7.

[181] B. W. Loo, F. S. Goulding, and D. Gao, "Ballistic deficits in pulse shaping amplifiers," *IEEE Transactions on Nuclear Science*, vol. 35, no. 1, pp. 114–118, 1988.

[182] R. Lothrop and H. Smith, "Lithium-Drifted Silicon Radiation Detector Production Process," Lawrence Berkeley National Laboratory, Tech. Rep. UCRL-16190, 1965.

[183] D. Protic, T. Krings, and R. Schleichert, "Development of double-sided microstructured Si(Li) detectors," *IEEE Transactions on Nuclear Science*, vol. 49, no. 4, pp. 1993–1998, 2002.

[184] D. Protic and T. Krings, "Development of transmission Si(Li) detectors," *IEEE Transactions on Nuclear Science*, vol. 50, no. 4, pp. 1008–1012, 2003.

[185] D. Protic, E. L. Hull, T. Krings, and K. Vetter, "Large-volume Si(Li) orthogonal-strip detectors for Compton-effect-based instruments," *IEEE Transactions on Nuclear Science*, vol. 52, no. 6, pp. 3181–3185, 2005.

[186] B. Lowe and R. Sareen, *Semiconductor X-ray Detectors*, 1st ed. CRC Press, 2013, ISBN: 9780429088247.

[187] E. M. Pell, "Ion drift in an n-p junction," *Journal of Applied Physics*, vol. 31, no. 2, pp. 291–302, 1960. eprint: https://doi.org/10.1063/1.1735561.

[188] G. Dearnaley and J. Lewis, "A lithium-drifted silicon surface-barrier detector for nuclear radiations," *Nuclear Instruments and Methods*, vol. 25, pp. 237–243, 1963.

[189] R. Ristinen, D. Lind, and J. Homan, "The manufacture of thick lithium-drifted silicon detectors," *Nuclear Instruments and Methods*, vol. 56, no. 1, pp. 55–60, 1967.

[190] A. Lauber, "The theory of compensation in lithium drifted semiconductor detectors," *Nuclear Instruments and Methods*, vol. 75, no. 2, pp. 297–308, 1969.

[191] J. T. Walton, G. S. Hubbard, E. E. Haller, and H. A. Sommer, "A Two-Dimensional Position Sensitive Si(Li) Detector," *IEEE Transactions on Nuclear Science*, vol. 26, no. 1, pp. 334–337, 1979.

[192] J. Llacer, "Study of surface effects in thick lithium drifted silicon radiation detectors," *IEEE Transactions on Nuclear Science*, vol. 11, no. 3, pp. 221–231, 1964.

[193] P. J. Whoriskey, "Two chemical stains for marking p-n junctions in silicon," *Journal of Applied Physics*, vol. 29, no. 5, pp. 867–868, 1958. eprint: https://doi.org/10.1063/1.1723306.

[194] J. Llacer, "Geometric control of surface leakage current and noise in lithium drifted silicon radiation detectors," *IEEE Transactions on Nuclear Science*, vol. 13, no. 1, pp. 93–103, 1966.

[195] P. J. Serlemitsos, "The broad band x-ray telescope (bbxrt) on astro-1," in *Observatories in Earth Orbit and Beyond*, Y. Kondo, Ed., Dordrecht: Springer Netherlands, 1990, pp. 294–294, ISBN: 978-94-011-3454-5.

[196] M. Jantunen and S. A. Audet, "Surface passivated Si(Li) detectors for an X-ray detector array," *Nuclear Instruments and Methods in Physics Research A*, vol. 353, pp. 89–92, Dec. 1994.

[197] J. T. Walton, R. H. Pehl, Y. K. Wong, and C. P. Cork, "Si(Li) X-Ray Detectors with Amorphous Silicon Passivation," *IEEE Transactions on Nuclear Science*, vol. 31, no. 1, pp. 331–335, 1984.

[198] X. Meng, Y.-C. Byun, H. S. Kim, J. S. Lee, A. T. Lucero, L. Cheng, and J. Kim, "Atomic Layer Deposition of Silicon Nitride Thin Films: A Review of Recent Progress, Challenges, and Outlooks," *Materials*, vol. 9, no. 12, 2016.

[199] O. H. Kim, "Atomic layer deposition of gallium nitride and tantalum nitride," PhD thesis, Doctoral Dissertations Available from Proquest, 2009, p. 130.

[200] A. E. Kaloyeros, F. A. Jové, J. Goff, and B. Arkles, "Review—Silicon Nitride and Silicon Nitride-Rich Thin Film Technologies: Trends in Deposition Techniques and Related Applications," *ECS Journal of Solid State Science and Technology*, vol. 6, no. 10, P691–P714, 2017.

[201] W. L. Hansen, E. E. Haller, and G. S. Hubbard, "Protective surface coatings on semiconductor nuclear radiation detectors," *IEEE Transactions on Nuclear Science*, vol. 27, no. 1, pp. 247–251, 1980.

[202] C. S. Rossington, P. M. Fine, and N. W. Madden, "Large area, low capacitance si(li) detectors for high rate x-ray applications," *IEEE Transactions on Nuclear Science*, vol. 40, no. 4, pp. 354–359, 1993.

[203] K. C. Sheth, "Stress, mechanical and thermal characterization of anisotropic polyimide thin films and coatings," AAI9709653, PhD thesis, UMass Amherst, Doctoral Dissertations Available from Proquest, 1996.

[204] T.-C. J. Hsu and Z.-L. Liu, "Solvent effect on the curing of polyimide resins," *Journal of Applied Polymer Science*, vol. 46, no. 10, pp. 1821–1833, 1992.

[205] B. J. Kim and E. Meng, "Micromachining of parylene c for biomems," *Polymers for Advanced Technologies*, vol. 27, no. 5, pp. 564–576, 2016.

[206] A. International, "ASTM D3359-17 Standard Test Methods for Rating Adhesion by Tape Test," ASTM International, West Conshohocken, PA, Standard, 2017.

[207] T. Aramaki, S. K. Chan, C. J. Hailey, P. A. Kaplan, T. Krings, N. Madden, D. Protić, and C. Ross, "Development of large format Si(Li) detectors for the GAPS dark matter experiment," *Nuclear Instruments and Methods in Physics Research A*, vol. 682, pp. 90–96, Aug. 2012.

[208] H. Spieler, *Semiconductor Detector Systems*, ser. Series on Semiconductor Science and Technology. OUP Oxford, 2005.

[209] F. S. Goulding and D. A. Landis, "Signal processing for semiconductor detectors," *IEEE Transactions on Nuclear Science*, vol. 29, no. 3, pp. 1125–1141, 1982.

[210] W. Nelson, *Accelerated Testing: Statistical Models, Test Plans, and Data Analysis*, ser. Wiley series in probability and mathematical statistics: Applied probability and statistics. John Wiley & Sons, 1990.

[211] T. Ogawa, T. Nagata, and Y. Hamada, "Determination of diffusion coefficient of water in polymer films by tga," *Journal of Applied Polymer Science*, vol. 50, no. 6, pp. 981–987, 1993.

[212] A. C. Tribble, B. Boyadjian, J. Davis, J. Haffner, and E. McCullough, "Contamination control engineering design guidelines for the aerospace community," Rockwell International Corporation, NASA Contractor Report 4740, 1996.

[213] S. Agostinelli and others, "Geant4—a simulation toolkit," *Nuclear Instruments and Methods in Physics Research A*, vol. 506, no. 3, pp. 250 –303, 2003.

[214] S. Agostinelli *et al.*, "Geant4–a simulation toolkit," *Nucl. Instrum. Meth. A*, vol. 506, no. 3, pp. 250 –303, 2003.

[215] G Kramberger, V Cindro, and M Mikuž, "Signals in non-irradiated and irradiated single-sided silicon detectors," *Nuclear Instruments and Methods in Physics Research Section A: Accelerators, Spectrometers, Detectors and Associated Equipment*, vol. 457, no. 3, pp. 550–557, 2001.

[216] O. Chamberlain, E. Segrè, C. Wiegand, and T. Ypsilantis, "Observation of antiprotons," *Phys. Rev.*, vol. 100, pp. 947–950, 3 1955.

[217] J. Díaz, P. Gavillet, G. Labrosse, L. Montanet, W. Swanson, P. Villemoes, M. Bloch, P. Frenkiel, C. Ghesquière, E. Lillestøl, and A. Volte, "Pp annihilations at rest into four pions," *Nuclear Physics B*, vol. 16, no. 2, pp. 239–271, 1970.

[218] C. Amsler, *Nucleon-antinucleon annihilation at lear*, 2019. arXiv: 1908.08455 [hep-ph].

[219] M. Kimura and S. Saito, "A model of the absorptive potential in nn scattering," *Nuclear Physics B*, vol. 178, no. 3, pp. 477–490, 1981.

[220] S. Orfanidis and V. Rittenberg, "Nucleon-antinucleon annihilation into pions," *Nuclear Physics B*, vol. 59, no. 2, pp. 570–582, 1973.

[221] A. Pais, "The many pi-meson problem," *Annals Phys.*, vol. 9, pp. 548–602, 1960.

[222] J. Cugnon, "Antideuteron annihilation on nuclei," *Nuclear Physics A*, vol. 542, no. 4, pp. 559–578, 1992.

[223] J.-M. Richard, "Antiproton physics," *Frontiers in Physics*, vol. 8, p. 6, 2020.

[224] R.J. Glauber, *Lectures on Theoretical Physics*. N.Y.: Intersci. Publishers, 1959, vol. 1.

[225] V. Franco and R. J. Glauber, "High-energy deuteron cross sections," *Phys. Rev.*, vol. 142, pp. 1195–1214, 4 1966.

[226] A. Capella, U. Sukhatme, C.-I. Tan, and J. Tran Thanh Van, "Dual parton model," *Phys. Rept.*, vol. 236, pp. 225–329, 1994.

[227] A. Galoyan, "Dynamics of interactions of anti-protons and anti-nuclei with nuclei in Geant4," *PoS*, vol. BaldinISHEPPXXII, p. 049, 2015.

[228] P. V. Degtyarenko, M. V. Kossov, and H. P. Wellisch, "Chiral invariant phase space event generator," *European Physical Journal A*, vol. 8, no. 2, pp. 217–222, Feb. 2000.

[229] C. Amsler, "Proton-antiproton annihilation and meson spectroscopy with the crystal barrel," *Rev. Mod. Phys.*, vol. 70, pp. 1293–1339, 4 1998.

[230] C Amsler and F Myhrer, "Low energy antiproton physics," *Annual Review of Nuclear and Particle Science*, vol. 41, no. 1, pp. 219–267, 1991.

[231] S. Denisov, S. Donskov, Y. Gorin, V. Kachanov, V. Kutjin, A. Petrukhin, Y. Prokoshkin, E. Razuvaev, R. Shuvalov, and D. Stojanova, "Measurements of antideuteron absorption and stripping cross sections at the momentum 13.3 gev/c," *Nuclear Physics B*, vol. 31, no. 2, pp. 253–260, 1971.

[232] B. V. Batyunya *et al.*, "The study of inclusive characteristics of anti-d d interactions at 12 GeV/c," Dec. 1987.

[233] V. F. Andreyev, P. S. Baranov, S. V. Levonian, Y. S. Pol, L. V. Filkoy, E. S. Golubeva, and A. S. Ilinov, "Multiplicities and correlations of secondary charged particles in the interactions of anti-neutrons and anti-deuterons with a momentum of 6.1-GeV/c per nucleon with tantalum nuclei," *Nuovo Cim. A*, vol. 103, pp. 1163–1176, 1990.

[234] T. Bressani and A. Filippi, "Antineutron physics," *Physics Reports*, vol. 383, no. 4, pp. 213–297, 2003.

[235] A. Bamberger *et al.*, "Observation of antiprotonic atoms," *Physics Letters B*, vol. 33, no. 3, pp. 233–235, 1970.

[236] S. Ting, "The first five years of the alpha magnetic spectrometer on the international space station," Press Conference at CERN, 8.

[237] V. A. Choutko, "Ams heavy antimatter," La Palma, Spain, 8.

[238] S. Tomonaga and G. Araki, "Effect of the nuclear coulomb field on the capture of slow mesons," *Phys. Rev.*, vol. 58, pp. 90–91, 1 1940.

[239] E. Fermi and E. Teller, "The capture of negative mesotrons in matter," *Phys. Rev.*, vol. 72, pp. 399–408, 5 1947.

[240] W. F. Fry, "The capture and decay of mesons in photographic emulsions," *Phys. Rev.*, vol. 83, pp. 594–597, 3 1951.

[241] V. L. Fitch and J. Rainwater, "Studies of x-rays from mu-mesonic atoms," *Phys. Rev.*, vol. 92, pp. 789–800, 3 1953.

[242] M. Camac, A. D. McGuire, J. B. Platt, and H. J. Schulte, "X-rays from mesic atoms," *Phys. Rev.*, vol. 88, pp. 134–134, 1 1952.

[243] F. J. Hartmann, "Exotic atom cascade processes in atoms with z>2," in *Electromagnetic Cascade and Chemistry of Exotic Atoms*, L. M. Simons, D. Horváth, and G. Torelli, Eds. Boston, MA: Springer US, 1990, pp. 127–139, ISBN: 978-1-4899-3701-8.

[244] D. Gotta, "Precision spectroscopy of light exotic atoms," *Prog. Part. Nucl. Phys.*, vol. 52, pp. 133–195, 2004.

[245] Y. Eisenberg and D. Kessler, "On the μ-mesonic atoms," *Il Nuovo Cimento (1955-1965)*, vol. 19, pp. 1195–1210, 1961.

[246] T. Koike, T. Harada, and Y. Akaishi, "Cascade calculation of k^--p and k^--d atoms," *Phys. Rev. C*, vol. 53, pp. 79–87, 1 1996.

[247] C. Batty, "Optical-model analysis of exotic atom data: (i). kaonic atoms," *Nuclear Physics A*, vol. 372, no. 3, pp. 418–432, 1981.

[248] ——, "Optical-model analysis of exotic atom data: (ii). antiprotonic and sigma atoms," *Nuclear Physics A*, vol. 372, no. 3, pp. 433–444, 1981.

[249] C. E. Wiegand, "Measurement of K^--mesonic x-ray spectra of medium and heavy elements," *Phys. Rev. Lett.*, vol. 22, pp. 1235–1238, 23 1969.

[250] Enrico Fermi, *Nuclear Physics: Course Notes*. University of Chicago Press, 1949.

[251] C. J. Batty, "Antiprotonic-hydrogen atoms," *Reports on Progress in Physics*, vol. 52, no. 10, pp. 1165–1216, 1989.

[252] P. Roberson *et al.*, "Strong Interaction and Mass Measurements Using anti-Protonic Atoms," *Phys. Rev. C*, vol. 16, pp. 1945–1962, 1977.

[253] P. Salati, P. Chardonnet, and J. Orloff, "The anti-nuclei production of our galaxy," *Nuclear Physics B - Proceedings Supplements*, vol. 70, no. 1, pp. 492–494, 1999, Proceedings of the Fifth International Workshop on topics in Astroparticle and Underground Physics.

[254] G. Steigman, "Observational tests of antimatter cosmologies," *Annual Review of Astronomy and Astrophysics*, vol. 14, no. 1, pp. 339–372, 1976. eprint: https://doi.org/10.1146/annurev.aa.14.090176.002011.

[255] G. Backenstoss, M. Hasinoff, P. Pavlopoulos, J. Repond, L. Tauscher, D. Tröster, P. Blüm, R. Guigas, H. Koch, M. Meyer, H. Poth, U. Raich, B. Richter, L. Adiels, I. Bergström, K. Fransson, A. Kerek, M. Suffert, and K. Zioutas, "Proton-antiproton annihilations at rest into $\pi^0\omega$, $\pi^0\eta$, $\pi^0\gamma$, $\pi^0\pi^0$, and $\pi^0\eta'$," *Nuclear Physics B*, vol. 228, no. 3, pp. 424–438, 1983.

[256] F. C. Adams *et al.*, "Constraints on the Intergalactic Transport of Cosmic Rays," *Astrophysical Journal*, vol. 491, no. 1, pp. 6–12, Dec. 1997. arXiv: astro-ph/9710113 [astro-ph].

[257] A. G. Cohen, A. D. Rújula, and S. L. Glashow, "A matter-antimatter universe?" *The Astrophysical Journal*, vol. 495, no. 2, pp. 539–549, 1998.

[258] S. Blinnikov, A. Dolgov, and K. Postnov, "Antimatter and antistars in the universe and in the galaxy," *Physical Review D*, vol. 92, no. 2, 2015.

[259] S. Dupourqué, L. Tibaldo, and P. von Ballmoos, "Constraints on the antistar fraction in the Solar System neighborhood from the 10-year Fermi Large Area Telescope gamma-ray source catalog," *Physical Review D*, vol. 103, no. 8, 2021.

[260] V. Poulin, P. Salati, I. Cholis, M. Kamionkowski, and J. Silk, "Where do the ams-02 antihelium events come from?" *Physical Review D*, vol. 99, no. 2, 2019.

[261] K. Abe *et al.*, "Search for Antihelium with the BESS-Polar Spectrometer," *Phys. Rev. Lett.*, vol. 108, p. 131 301, 13 2012.

[262] K. Blum, K. C. Y. Ng, R. Sato, and M. Takimoto, "Cosmic rays, antihelium, and an old navy spotlight," *Physical Review D*, vol. 96, no. 10, 2017.

[263] N. Tomassetti and A. Oliva, "Production of cosmic-ray antinuclei in the galaxy and background for dark matter searches," *Proceedings of The European Physical Society Conference on High Energy Physics — PoS(EPS-HEP2017)*, 2017.

[264] M. Cirelli, N. Fornengo, M. Taoso, and A. Vittino, "Anti-helium from dark matter annihilations," *Journal of High Energy Physics*, vol. 2014, no. 8, 2014.

[265] E. Carlson, A. Coogan, T. Linden, S. Profumo, A. Ibarra, and S. Wild, "Antihelium from dark matter," *Physical Review D*, vol. 89, no. 7, 2014.

[266] A. Coogan and S. Profumo, "Origin of the tentative ams antihelium events," *Physical Review D*, vol. 96, no. 8, 2017.

[267] Y.-C. Ding, N. Li, C.-C. Wei, Y.-L. Wu, and Y.-F. Zhou, "Prospects of detecting dark matter through cosmic-ray antihelium with the antiproton constraints," *Journal of Cosmology and Astroparticle Physics*, vol. 2019, no. 06, p. 004, 2019.

[268] M. W. Winkler and T. Linden, "Dark matter annihilation can produce a detectable antihelium flux through $\overline{\Lambda}_b$ decays," *Physical Review Letters*, vol. 126, no. 10, 2021.

[269] K. M. Belotsky *et al.*, "Anti-helium Flux As a Signature for Antimatter Globular Clusters in Our Galaxy," *Physics of Atomic Nuclei*, vol. 63, no. 2, pp. 233–239, Feb. 2000.

[270] J. Allison *et al.*, "Geant4 developments and applications," *IEEE Transactions on Nuclear Science*, vol. 53, no. 1, pp. 270–278, Feb. 2006.

[271] J. D. Sullivan, "Geometrical factor and directional response of single and multi-element particle telescopes," *Nuclear Instruments and Methods*, vol. 95, p. 5, Jan. 1971.

[272] L. Desorgher, E. O. Flückiger, and M. Gurtner, "The PLANETOCOSMICS Geant4 application," in *36th COSPAR Scientific Assembly*, vol. 36, Jan. 2006, p. 2361.

[273] G. J. Feldman and R. D. Cousins, "Unified approach to the classical statistical analysis of small signals," *Physical Review D*, vol. 57, no. 7, pp. 3873–3889, 1998.

[274] P. Doetinchem and B. Yamashiro, "Geomagnetic cutoff calculations for the interpretation of low-rigidity cosmic-ray antiparticle measurements," vol. ICRC2017, Aug. 2017, p. 151.

[275] V. Poulin, P. Salati, I. Cholis, M. Kamionkowski, and J. Silk, "Where do the AMS-02 antihelium events come from?" *Physical Review D*, vol. 99, no. 2, p. 023 016, 2019. arXiv: 1808.08961 [astro-ph.HE].

[276] M. M. Kachelrieß, S. Ostapchenko, and J. Tjemsland, "Revisiting cosmic ray antinuclei fluxes with a new coalescence model," *Journal of Cosmology and Astroparticle Physics*, vol. 2020, no. 08, pp. 048–048, 2020.

[277] A. Shukla, A. Datta, P. von Doetinchem, D.-M. Gomez-Coral, and C. Kanitz, "Large-scale simulations of antihelium production in cosmic-ray interactions," *Physical Review D*, vol. 102, no. 6, 2020.